UNIVERSITY of TASMANIA

AMC
AUSTRALIAN MARITIME COLLEGE

Cavity Flow Over a Wall-Mounted Fence

Luka Barbaca
M.Eng (Mechanical Engineering)
National Centre for Maritime Engineering and Hydrodynamics
Australian Maritime College

Submitted in fulfilment of the requirements
for the degree of Doctor Of Philosophy,
University of Tasmania

May, 2018

Declarations

Authority of Access

The publishers of the papers comprising Chapters 2-5 hold the copyright for that content, and access to the material should be sought from the respective journals. The remaining non-published content of this thesis may be made available for loan and limited copying and communication in accordance with the Copyright Act 1968.

Statement of Originality

This thesis contains no material which has been accepted for a degree or diploma by the University or any other institution, except by way of background information and as duly acknowledged in the text, and to best of my knowledge and belief no material previously published or written by another person except where due acknowledgement is made in the text of the thesis, nor does the thesis contain any material that infringes copyright.

Signed: _____ Date: 24/05/2018

Luka Barbaca

Statement of Co-Authorship

Chapters 2-5 of this thesis have been written as scientific papers. All experimental design, numerical simulation, data analysis and manuscript preparation were the primary responsibility of the candidate, however, work was performed in collaboration with supervisors and co-authors. Details of these contributions are outlined below:

Chapter 2

An Experimental Study of Cavity Flow Over a 2-D Wall-Mounted Fence in Variable Boundary Layer

Paul Brandner and Bryce Pearce contributed to experiment design, data interpretation and manuscript preparation.

Contribution Percentage: L. Barbaca 70% , P.A. Brandner 15% , B.W. Pearce 15%

Chapter 3

On the Unsteady Behaviour of Cavity Flow Over a 2-D Wall-Mounted Fence

Paul Brandner and Bryce Pearce contributed to experiment design, data interpretation and manuscript preparation. Harish Ganesh and Steven Ceccio contributed to design of the experiments performed during the candidate's research visit to University of Michigan and X-ray data interpretation.

Contribution Percentage: L. Barbaca 55% , P.A. Brandner 15% , B.W. Pearce 15% , H. Ganesh 10% , S.L. Ceccio 5%

Chapter 4

Numerical Analysis of Ventilated Cavity Flow Over a 2-D Wall-Mounted Fence

Paul Brandner and Bryce Pearce contributed to development of numerical simulations, data interpretation and manuscript preparation.

Contribution Percentage: L. Barbaca 70% , P.A. Brandner 15% , B.W. Pearce 15%

Chapter 5

Experimental Study of Ventilated Cavity Flow Over a 3-D Wall-Mounted Fence

Paul Brandner and Bryce Pearce contributed to experiment design, data interpretation and manuscript preparation.

Contribution Percentage: L. Barbaca 70% , P.A. Brandner 15% , B.W. Pearce 15%

We the undersigned confirm the above stated "proportion of work undertaken" for each of the above published or submitted peer-reviewed manuscripts contributing to this thesis.

Signed: _____ Date: 24/05/2018

Prof Paul Brandner
Supervisor
National Centre for Maritime Engineering and Hydrodynamics
Australian Maritime College, University of Tasmania

Signed: _____ Date: 24/05/2018

Dr Bryce Pearce
Supervisor
National Centre for Maritime Engineering and Hydrodynamics
Australian Maritime College, University of Tasmania

Acknowledgements

As my PhD thesis takes its final shape it is with deepest gratitude and thankfulness that I wish to acknowledge those who provided the support and encouragement along the way.

I wish to thank my Supervisors, Professor Paul Brandner and Dr Bryce Pearce for giving me the opportunity to do a PhD project in a world-class fluid mechanics laboratory. Your advice, wealth of knowledge and limitless enthusiasm have been invaluable contribution to this thesis, and moreover to the development of my research skills. It was a great pleasure to have your guidance and friendship along the way.

I would like to thank Mr Robert Wrigley and Mr Steven Kent for the technical support par-excellence, patience with the endless tunnel setup changes and general banter around the lab. I would also like to thank all the post-doctoral staff and PhD students at CRL and AMC HDR hub for their support and encouragement.

I want to thank all my friends, both in Tasmania and back home in Croatia, for their support in everything that led to this achievement.

I wish to thank Claire for being her loving and caring self, and for her support and understanding throughout what was seemingly an endless sequence of long working days. As I finally reach the illusive light at the end of cavitation tunnel, I promise we will spend much more time adventuring in the future.

None of this would be possible without limitless support and love from my family. For all the sacrifices they made in enabling me to pursue my goals, even though it meant that I am moving to the other side of the world, I will be eternally indebted.

Finally, I want to thank Huey for keeping me sane by providing wind and waves every time I needed to clear my mind.

Abstract

Ventilated cavity flow over a wall mounted fence is experimentally investigated in a cavitation tunnel. The flow over a 2-D fence, attached to the tunnel test section ceiling, is examined for a range of free-stream conditions. The dependence of cavity topology, cavitation number, upstream wall pressure distribution and drag on several parameters, including ventilation rate, fence height based Froude number (Fr), vapour pressure based cavitation number (σ_v) and degree of fence immersion in the oncoming wall boundary layer, is investigated. Three different flow regimes are identified throughout the range of cavitation numbers for a particular set of free-stream conditions: shear layer cavitation, fully developed cavity and 'blocked' flow. The cavity exhibits a typical re-entrant jet closure and the re-entrant jet intensity is found to be a function of Fr. The high intensity re-entrant jet, present at high Fr, leads to an increase in drag. Drag decreases significantly with an increase in fence immersion in the oncoming boundary layer. Complementary measurements for a naturally cavitating flow are obtained for comparison.

A more detailed examination of the topology and unsteady behaviour of ventilated and natural cavity flows over a 2-D wall-mounted fence was undertaken for fixed length cavities with varying free-stream velocity using high-speed and still imaging, X-ray densitometry and dynamic surface pressure measurements in two experimental facilities. Two main unsteady features are observed, the irregular small-scale shedding of structures at the cavity closure and a larger-scale re-entrant jet oscillation. Small-scale cavity break-up was associated with a high-frequency broad-band peak in the wall pressure spectra, found to be governed by the overlying turbulent boundary layer characteristics, similar to observations from single-phase flow over a forward-facing step. A low-frequency peak reflecting the oscillations in size of re-entrant jet, analogous to the 'flapping' motion in single-phase flow, was found to be modulated by gravity effects (i.e. a Froude number dependency). Likewise, a significant change in cavity behaviour was observed as the flow underwent transition analogous to the transition from sub- to super- critical regime in open-channel flow.

A companion numerical study is undertaken to provide additional insight into particular flow features such as the separated flow region upstream of the fence and to assess the influence of blockage. An implicit unsteady compressible solver is used with a RANS

$k-\omega$ SST turbulence model and VOF approach to capture the cavity interface. The numerical results are found to compare reasonably with the experimental data, additionally showing a significant influence of blockage on the studied flow.

Along with the 2-D fence, a 3-D wall mounted fence, spanning nominally a quarter of the tunnel test section, is investigated. The impact that 3-D effects have on the cavity topology and the relations between the parameters characterizing the flow is observed. The most notable effect of 3-D flow is a change in the closure mechanism observed for low Fr. Following a decrease in Fr the closure topology transforms from a well defined single re-entrant jet regime, through a phase of gradual re-entrant jet widening to a completely split re-entrant jet separated into two branches. Generally, the 2-D and 3-D flows exhibited similar trends with any significant difference attributable to differing levels of flow confinement due to lesser width of 3-D fence.

Contents

List of Figures

List of Tables

Nomenclature

Symbol	Definition	Unit
α	void fraction	-
α_{in}	interior angle between split re-entrant jet cavity branches and centre-line	^{o}
α_{out}	angle between split re-entrant jet cavity side boundary and centre-line	^{o}
β	cavity detachment angle	^{o}
C_D	drag coefficient	-
$C_{D_{min}}$	minimum drag coefficient	-
C_L	lift coefficient	-
C_P	pressure coefficient	-
$C_{P_{max}}$	maximum pressure coefficient	-
$C_{P_{RMS}}$	root-mean-square value of pressure coefficent	-
C_{Qv}	volumetric flow-rate coefficient	-
D	drag	N
δ	boundary layer thickness	m
$\Delta t_1'$	non-dimensional lag between two signals	-
f	frequency	Hz
Fr	Froude number	-
Fr_0	re-entrant jet extinction Froude number	-
Fr_c	critical Froude number	-
Fr_h	fence height based Froude number	-
Fr_H	test-section depth based Froude number	-
g	gravitational acceleration	m/s^2
h	fence height	m
H	test-section depth	m
L	lift	N
l_c	cavity length	m

l_{cr}	critical cavity length	m
l_{ns}	no-slip boundary condition wall length	m
l_{rj}	re-entrant jet length	m
l_{st}	largest structure length scale	m
l_{wall}	length of upstream wall influenced by the fence	m
ν	kinematic viscosity	m^2/s
p	local pressure	Pa
p'	normalized pressure	-
p_c	cavity pressure	Pa
p_v	vapour pressure	Pa
p_∞	reference free-stream pressure	Pa
Q_m	air mass flow-rate	kg/s
Re	Reynolds number	-
Re_h	fence height based Reynolds number	-
ρ	water density	kg/m^3
ρ_{12}	cross-correlation function value	-
ρ_{air}	air density	kg/m^3
S	fence front face surface area	m^2
S_c	cavity cross-sectional area	m^2
St_h	fence height based Strouhal number	-
St_{rj}	re-entrant jet length based Strouhal number	-
σ_c	cavity pressure based cavitation number	-
σ_{min}	minimum cavitation number	-
σ_v	vapour pressure based cavitation number	-
t	time	s
t'	non-dimensionalised time	-
t_c	cavity thickness	m
U	local velocity	m/s
U_{adv}	advective structure velocity	m/s
U_{rj}	re-entrant jet velocity	m/s
U_∞	reference free-stream velocity	m/s
w_c	maximum cavity width	m
w_{cr}	cavity width at the location of bifurcation point	m
w_{st}	width of the cross-correlation peak	-
x	stream-wise position	m
x_L	representative wall length	m
y	vertical position	m
y^+	dimensionless wall distance	-

Abbreviations

ALDR	Air Layer/Film Drag Reduction
AMC	Australian Maritime College
BEM	Boundary Element Method
BDR	Bubble Drag Reduction
BFS	Backward-Facing Step
CFD	Computational Fluid Dynamics
CRL	Cavitation Research Laboratory
FFS	Forward-Facing Step
PCC	Pearson Correlation Coefficient
PCDR	Partial Cavity Drag Reduction
POD	Proper Orthogonal Decomposition
PSD	Power Spectral Density
RANS	Reynolds Averaged Navier-Stokes
RMS	Root-Mean-Square
SCDR	Supercavity Drag Reduction
SLPM	Standard Litres Per Minute
SLR	Single-Lens Reflex
SST	Shear Stress Transport
TBL	Turbulent Boundary Layer
VOF	Volume of Fluid
WMF	Wall-Mounted Fence

Chapter 1

General Introduction

Cavitation is a phenomenon defined as a change of phase from liquid to vapour when the local pressure in the flow approaches the vapour pressure. The presence of a geometric discontinuity will generally induce flow separation in the wake, which in high-speed flows may be susceptible to cavitation inception. A further reduction in free-stream pressure or an increase in flow velocity will result in an increase in number and size of cavitation bubbles, eventually leading to the formation of a large continuous cavity. The existence of such cavities in high-speed marine applications generally has a detrimental effect on performance, observed through a loss of lift on the lifting surfaces, increased flow instability, noise, vibration and surface erosion. However, if the cavity is extended downstream of the cavitating body, termed 'supercavitation', these negative effects can be largely diminished. The existence of a gaseous bubble/layer between the body and surrounding water will result in decrease in skin friction and, consequently, reduced viscous drag (Acosta, 1973). To form a cavity applicable for drag reduction purposes naturally (i.e. due to phase change), the flow velocity has to be impractically high, usually in excess of 100 knots (Kawakami and Arndt, 2011). However, similar cavities, termed 'ventilated', can be formed artificially at lower flow velocities by admission or forced injection of incondensible gas into the separated flow region (May, 1975; Kunz et al., 1999).

Ventilated cavities have been extensively investigated in the context of drag reduction via creation of gaseous bubble/layer separating the cavitating body from the water since mid-last century (Swanson and O'Neill, 1951; Schiebe and Wetzel, 1961). Prominent examples of the use of this technique include axisymmetric ventilated super-cavitating underwater projectiles (Brennen, 1995; Semenenko, 2002) and 'air-lubrication' of ship hulls through use of ventilated cavity flow over a backward-facing step (Ceccio, 2010). Alternatively, with the technique referred to as 'base-ventilation' (Franc and Michel, 2004), air injection through the downstream face of the body can be used to increase the wake pressure. This results in a decrease of the stream-wise pressure gradient, and consequent

reduction of the form drag.

A basic flow that has potential to be used in a range of high-speed marine applications is the cavity flow over a wall-mounted fence immersed in a turbulent boundary layer. Although, this particular geometry has been comprehensively studied in single-phase flow (Good and Joubert, 1968; Durst and Rastogi, 1980; Yaragal et al., 1997; Kim and Lee, 2001), a considerable gap in knowledge for the cavitating/ventilated configuration can be identified. An example of fence geometry investigated in the multi-phase flow context is the use of interceptors fitted to the bottom and sides of a ship transom (Brizzolara, 2003).

The interest in cavity flow over a wall-mounted fence originates from the potential use of a retractable fence ('interceptor') attached to the trailing edge of a base-ventilated hydrofoil for a rapid generation of bi-directional lift with a minimum drag penalty (Elms, 1999). As the fence is attached to a flat wall (i.e. isolated from the foil), the present study is also relevant for flow over a fence attached to a ship hull, either used for lift generation, or ventilated cavity drag reduction. The case studied is a canonical flow, with a nominal zero stream-wise pressure gradient, suitable for comparison of behaviour of vaporous (i.e. natural) and gaseous (i.e. ventilated) cavities. Furthermore, the simple geometry makes the flow well suited for comparison of results from experimental and computational analysis.

The present thesis follows on from work undertaken over recent years at the Australian Maritime College (AMC) Cavitation Research Laboratory (CRL). As a part of research on intercepted base-ventilated hydrofoils (Pearce and Brandner, 2015b,c), comprehensive numerical studies on cavity flow over a wall-mounted fence using potential flow based Boundary Element Method (BEM) analysis are reported by Pearce (2011) and Pearce and Brandner (2014). The present work aims to gain further insight through experimental studies of natural and ventilated cavity flow over 2-D and 3-D wall-mounted fences in a cavitation tunnel and a Computational Fluid Dynamics (CFD) analysis for the 2-D configuration.

The research objectives of this work are:

- To gain basic understanding of the general topology and dynamics of natural and ventilated cavity flow over a wall-mounted fence immersed in a turbulent boundary layer.
- To perform experiments that show the effects of variation in flow parameters and fence immersion in a turbulent boundary layer on the cavity flow over 2-D and 3-D wall-mounted fences.
- To evaluate forces generated by the fence/wall system in context of the application of the fence as an 'interceptor' type device.

- To develop a CFD model and compare the numerical results with experiment.

The research questions to be answered by this research are:

- What is the general topology of nataural and ventilated cavity flow over a wall-mounted fence?
- What is the topology of cavity closure?
- Which mechanism(s) are controlling the cavity break-up?
- What is the spectral content of the cavity shedding?
- What are the differences between the natural and ventilated flows?
- How is the flow topology and unsteady behaviour affected by a variation of flow parameters and variable fence immersion in a turbulent boundary layer?
- What is the influence of variable flow parameters on the forces generated by fence/wall system and its hydrodynamic efficiency?
- To what extent can CFD modelling be used to analyse the flow?
- What are the differences between the cavity flows over 2-D and 3-D wall-mounted fences?

The individual chapters presented in this thesis are written in journal article form and are either published or submitted for publication. The publishing details for each article are given at the start of each chapter. An outline of the chapters, and their contribution to research objectives, is given below:

- In chapter 2, the experimental investigation of ventilated and natural cavity flow over a 2-D wall-mounted fence immersed in a turbulent boundary layer is presented. Cavity topology, upstream wall pressure distribution and the resulting hydrodynamic forces were determined as a function of ventilation rate, fence immersion in the oncoming wall boundary layer and free-stream conditions. Some comparison with the results from 3-D wall-mounted fence experiments and a comparison with numerical results from CFD analysis for 2-D configuration are given.
- In chapter 3, the topology and unsteady behaviour of ventilated and natural cavity flow over a 2-D wall-mounted fence was investigated for fixed length cavities with varying free-stream velocity using high-speed and still imaging, X-ray densitometry and dynamic surface pressure measurements in two experimental facilities.

- In chapter 4, ventilated cavity flow over a 2-D wall-mounted fence is numerically investigated using an unsteady compressible solver with RANS k - ω SST turbulence model and VOF approach to capture the cavity interface. The simulations were carried out for a fixed free-stream speed and pressure. Cavity topology, wall pressure distribution and the resulting hydrodynamic forces were determined as a function of ventilation rate, degree of fence immersion in the oncoming wall boundary layer and degree of confinement of the flow domain.

- In chapter 5, ventilated cavity flow over a fixed height 3-D wall-mounted fence is experimentally investigated for a range of free-stream conditions. The impact of 3-D effects on cavity topology is examined, along with the dependence of cavitation number and drag on volumetric flow rate coefficient, free-stream velocity and free-stream pressure.

Chapter 2

An Experimental Study of Cavity Flow Over a 2-D Wall-Mounted Fence in Variable Boundary Layer

This chapter is based on the article accepted for publication in *International Journal of Multiphase Flow*. The contributing authors are: L. Barbaca, B.W. Pearce and P.A. Brandner.

The citation for the journal paper is:

Barbaca, L., Pearce, B. W., Brandner, P. A., 2018, An Experimental Study of Cavity Flow Over a 2-D Wall-Mounted Fence in a Variable Boundary Layer, *International Journal of Multiphase Flow* (article in press)

Abstract

Ventilated and natural cavity flow over a 2-D wall-mounted fence immersed in a boundary layer is experimentally investigated in a cavitation tunnel. Cavity topology, upstream wall pressure distribution and the resulting hydrodynamic forces were determined as a function of ventilation rate, fence immersion in the oncoming boundary layer and free-stream conditions. Cavities exhibit a typical re-entrant jet behaviour, which is the primary mechanism of air/vapour entrainment into the main flow. Some entrainment is also observed via the turbulent break-up at the cavity surface, the intensity of which increases with deeper immersion of the fence within the wall boundary layer. A similar cavity topology, apart from some difference in the wake, is observed for ventilated and natural cavities

at the same flow conditions. This similarity is also present in the relations between all other parameters investigated. It was found that with a decrease in cavitation number lift (i.e. force normal to the wall) increases and drag (i.e. force normal to the fence) decreases, resulting in an increased hydrodynamic efficiency of the wall/fence system. With an increase in fence immersion in the boundary layer, lift and drag both increase at the same rate, resulting in a constant lift-to-drag ratio.

2.1 Introduction

Efficient sea transport and drag reduction of marine vehicles are interrelated topics of interest to the maritime community. Various methods based on the use of gaseous layers/bubbles for reduction of the skin friction of the wetted part of a vessel have been extensively investigated since mid-last century. With reference to the extent of gaseous layer/bubble, these methods can be categorized into four groups: bubble drag reduction (BDR); air layer/film drag reduction (ALDR); partial cavity drag reduction (PCDR) and supercavity drag reduction (SCDR) (Ceccio, 2010; Elbing et al., 2013; Mäkiharju et al., 2013a; Murai, 2014). Of particular interest for this study are the latter two, which involve creation and maintenance of large gaseous pockets covering a significant portion (i.e. partial cavity) or the whole body (i.e. supercavity). Additionally, partial cavity drag reduction techniques can be divided into those using the body designs with and without cavity lockers (also labelled as 'arrestors' or 'sloped beach') used to control the flow at the cavity closure (Kopriva et al., 2008; Mäkiharju et al., 2013a).

The origin of the gaseous cavity can be twofold. A cavity can form naturally, i.e. due to the phase change of the water to vapour, or artificially by injecting an incondensable gas (typically air) into the wake of a cavitator. The latter process is commonly referred to as 'ventilation' and the resulting cavity termed a ventilated cavity. The main parameter used to characterize these cavitating flows, both natural and ventilated, is the cavitation number, $\sigma_c = (p_\infty - p_c)/0.5\rho U_\infty^2$, where p_∞ is the reference free-stream pressure, p_c is the pressure inside the cavity, ρ is the liquid phase density and U_∞ is the reference free-stream velocity. Past studies have shown that both natural and ventilated cavities present at the same flow conditions have a largely similar behaviour except for differences in the closure physics (May, 1975; Kunz et al., 1999). To form a cavity applicable for drag reduction in high-speed applications the σ_c value usually has to be of the order of 0.1. For a naturally cavitating flow $p_c = p_v$ (where p_v is vapour pressure) and achieving such a low σ_c generally requires impractical operational speeds in excess of 90 knots (Kawakami and Arndt, 2011). In contrast, for the ventilated case p_c is also controlled by the flux of injected air and sufficiently large cavities can be formed at lower, more practical, speeds making the technique applicable to a broad range of applications. Ventilation has also

been investigated for drag reduction of low-speed ships (Butuzov et al., 1999) and lifting surfaces (Kopriva et al., 2008), where practicable cavities were achieved for somewhat different cavitation number values (i.e. negative σ_c for slow ships and $\sigma_c \approx 1$ for lifting surfaces).

The use of ventilated supercavities (SCDR) has been extensively studied in the context of axisymmetric underwater projectiles configured with a nose-mounted disk cavitator. A large catalogue of published literature exists with a comprehensive review of the principles governing this flow discussed by Semenenko (2002) and more recently by Karn et al. (2016). The main emphasis with the PCDR technique has been with the application of what has been termed 'air lubrication' to a substantial portion of the wetted surface of a ship's hull. Generally, air is injected through a backward-facing step spanning the width of the hull bottom, with a sloped beach placed in the cavity closure region to ensure a smooth cavity reattachment and minimal air loss (Arndt et al., 2009; Matveev et al., 2009; Lay et al., 2010; Mäkiharju et al., 2013a). A decrease in drag in the range of 10-30% has been reported in full-scale studies of planning and semi-displacement hulls (Latorre, 1997; Butuzov et al., 1999) and the concept has been also applied commercially on full displacement hull forms (Mizokami et al., 2010). Recently, a study of a partial cavity detaching from a wall-mounted fence (i.e. a forward facing step) of limited span has been reported by Barbaca et al. (2017a). There has also been some interest in creating partial cavities by using transverse jets of air injected into the liquid cross-flow through discrete holes. Reports on cavities formed by jet injection via a single hole have been authored by Insel et al. (2010) and Mäkiharju et al. (2017b) and via an array of holes by Lee (2015) and Mäkiharju and Ceccio (2018). The use of ventilation on low-drag partially cavitating foils with a smooth reattachment has been proposed by Kopriva et al. (2008). Apart from their use in hydrodynamics, ventilated cavities have been also utilized to prevent surface erosion on dam spillways (Chanson, 1989) and to attenuate pressure fluctuations in hydro turbines (Papillon et al., 2002).

Alternatively, air injection can be used on lifting surfaces to reduce the form drag. On a device referred to as 'base-ventilated' hydrofoil, air is injected through a blunt trailing edge, forming a supercavity in the wake of the hydrofoil. The pressure in the wake increases proportionally to the amount of injected air, leading to a decrease in the streamwise differential pressure across the foil and a reduction in the form drag (Lang and Daybell, 1961; Verron and Michel, 1984; Franc and Michel, 2004; Pearce and Brandner, 2015b). A recent comprehensive review on ventilation of lifting bodies, both natural and artificial, has been authored by Young et al. (2017). A similar flow, observed in the case of a ship's transom mounted fence (also termed an 'interceptor'), can be considered as an 'infinite' (i.e. nominally zero cavitation number) ventilated cavity flow with atmospheric pressure in the wake of the fence (Brizzolara, 2003).

An aspect of partial and supercavity flow that has not had any comprehensive focus

in the published literature is the effect of variable immersion of a cavitator in the oncoming wall boundary layer. Vigneau et al. (2001) investigated the effects of upstream wall boundary layer thickness on the development of a cavity resulting from an axisymmetric gas jet injected into a confined vertical water flow. Some numerical results on the flow around a transom mounted interceptor of a variable height immersed in a constant thickness boundary layer were reported by Molini and Brizzolara (2005) and a recent study investigating ventilated cavities detaching from a backward-facing step for a range of upstream boundary layer thicknesses has been authored by Pearce et al. (2015). The relatively sparse knowledge gained thus far for cavitating flow configurations is in contrast to the now quite well understood flow over wall-mounted fences immersed in a boundary layer in single-phase flow (see for example Good and Joubert, 1968; Fang and Wang, 1997).

In this study both ventilated and naturally cavitating flow over a 2-D wall-mounted fence is experimentally investigated in a cavitation tunnel. The effect that variable immersion of the fence in the oncoming boundary layer has on the cavity topology, upstream wall pressure distribution and hydrodynamic forces is examined. Additionally, the flow parameters are investigated with respect to the flux of injected air and variable free-stream velocity and pressure.

This study represents a continuation of a research programme on cavity flow over a wall-mounted fence at the Australian Maritime College (AMC) Cavitation Research Laboratory (CRL), which has up to date resulted in several publications reporting on both numerical (Pearce and Brandner, 2014; Barbaca et al., 2017b) and experimental results (Barbaca et al., 2017a). This project is a part of a larger research program based on a novel concept, initially proposed by Elms (1999), utilizing a retractable fence attached to the trailing edge of a base-ventilated hydrofoil for generation of bi-directional lift with a rapid response. Some results on this wider topic are reported by Pearce and Brandner (2012b) and Pearce and Brandner (2015b).

The present results contribute to the basic understanding of this canonical cavitating flow, and also provide valuable data for the practical application of wall-mounted fences in a drag reduction context (i.e. PCDR or SCDR), or as an interceptor type device with a minimal drag penalty. The studied geometry is well suited for experiment and computation and a comparison of the experimental data with CFD (Computational Fluid Dynamics) results from Barbaca et al. (2017b) is provided. The experimental data for a 2-D wall-mounted fence is compared with the experimental results for a 3-D wall-mounted fence presented in Barbaca et al. (2017a) and some new results obtained with the 3-D setup.

2.2 Experimental setup and modelling

A schematic representation of cavity flow over a wall-mounted fence is shown in Fig. 2.1. A fence, of height h, is immersed in the upstream wall boundary layer of thickness δ. The latter is defined as the distance from the wall where the local mean velocity, U, is 99% of the free-stream velocity U_∞. In the case of a ventilated cavity, air is supplied to the wake region of the resulting bluff-body flow through a manifold on the downstream face of the fence with a mass flow rate Q_m (Fig. 2.1). Alternatively, for $Q_m = 0$, a natural cavity may be formed due to phase change when the pressure in the wake of the fence, $p = p_c$, reduces to the vapour pressure, p_v (Fig. 2.1). Irrespective of its origin, the cavity detaches from the sharp fence tip and exhibits a re-entrant jet closure. The resulting notional pressure signature on the wall upstream of the fence is indicated.

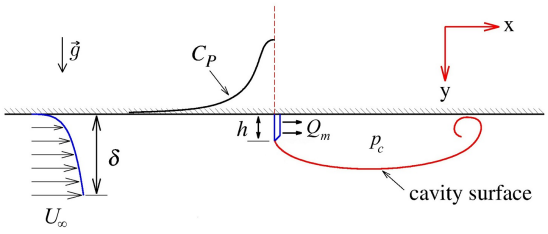

Figure 2.1: Sketch of a wall mounted fence immersed in the oncoming wall boundary layer with a cavity detaching from the sharp fence tip. For a ventilated cavity, air is supplied from the downstream face of the fence with mass flow rate Q_m. The notional pressure distribution on the upstream wall is shown. The origin of the coordinate system is at the fence upstream face/wall junction

As already mentioned, the cavitation number, σ_c, is the fundamental dimensionless parameter characterizing cavitating flows. In the case of ventilated cavities, for constant free-stream conditions (i.e. free-stream pressure, p_∞, and free-stream velocity, U_∞), p_c and hence σ_c is determined by the air injection rate. This parameter is presented in non-dimensionalised form as a volumetric flow rate coefficient, $C_{Qv} = Q_m/\rho_{air}U_\infty S$, where Q_m is the air mass flow rate, ρ_{air} is the air density at the cavity pressure and S is the fence face area. For natural cavities, with p_v nominally constant for all test conditions, σ_c is determined solely by the free-stream conditions, i.e. by varying p_∞ and/or U_∞. The dependence of cavitation number on free-stream velocity and free-stream pressure (for ventilated flow) has been quantified using a fence height based Froude number, $Fr = U_\infty/\sqrt{gh}$ (where g is the gravitational acceleration), and vapour pressure based cavitation number, $\sigma_v = (p_\infty - p_v)/0.5\rho U_\infty^2$, respectively. A Froude number based on the test section depth, $Fr_H = U_\infty/\sqrt{gH}$, is applicable for additional flow characterization. To examine the effect of the fence immersion in the oncoming wall boundary layer, a dimensionless parameter in the form of boundary layer thickness to fence height ratio, δ/h, is defined. Alongside the cavitation number, lift (L), drag (D) and lift-to-drag ratio (L/D) are

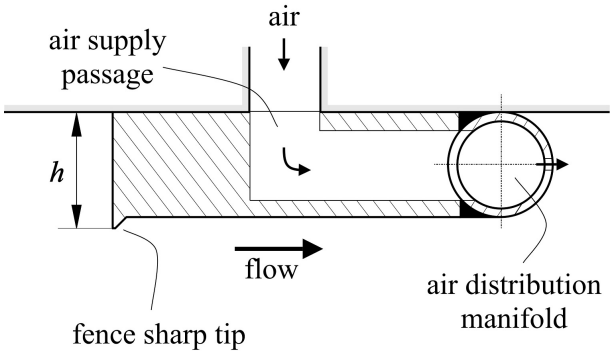

Figure 2.2: Cross-section of the fence model at the test section centreline. A sharp tip is machined on the fence front face to ensure a stable cavity detachment. Air is injected into the wake of the fence via an internal channel and distribution manifold (with 39 $\times$ ϕ2 mm equi-spaced outlets) glued to the downstream face of the fence.

investigated with the respect to the aforementioned parameters. In common with the usual convention drag is the force normal to the fence and lift has been defined as the force normal to the wall. The latter is obtained from the integral of the pressure distribution on the wall upstream of the fence $\int_{x_L}^{0} p(x)dx$, where x_L is a representative wall length. The lift and drag are non-dimensionalised using force coefficients based on the fence cross-sectional area giving: lift coefficient, $C_L = L/0.5U_\infty^2\rho S$, and drag coefficient, $C_D = D/0.5U_\infty^2\rho S$. The cavity length, l_c, dependence on σ_c is also determined.

The experiments were performed in the University of Tasmania variable pressure water tunnel. The tunnel design incorporates a large tank downstream of the test section for bubble coalescence and separation (Brandner et al., 2015). This feature, combined with the auxiliary systems for rapid degassing and continuous evacuation of the large quantities of incondensable gas, enables efficient conduct of tests involving ventilation (i.e. injection and continuous removal of large quantities of air). The tunnel test section measures 0.6×0.6 m square at the entrance, by 2.6 m long. The test section has a horizontal ceiling with the floor sloping 20 mm (i.e. test section depth of 0.62 m at the outlet) to nominally maintain constant speed and zero stream-wise pressure gradient. The operating velocity and pressure are controlled independently, with ranges from 2 to 12 m/s and 4 to 400 kPa absolute respectively. The tunnel volume is 365 m^3 and is filled with demineralised water. Optical access is provided through acrylic windows on each side of the test section.

For the present study, the experimental setup has been developed to examine ventilated and natural cavity flow over a 2-D wall-mounted fence (i.e. nominally spanning the whole test section width). The fence model incorporating an internal air supply channel is machined from a 32 $\times$ 10 mm stainless steel bar, with a manifold for air distribution, machined from an 8 mm stainless steel tube, glued to the downstream face (Fig. 2.2). The fence is 599 mm wide $\times$ 10 mm high, with a sharp tip machined on the front face to ensure a stable cavity detachment. The resulting blockage based on the fence and test section cross-sectional areas is $\approx$ 1.7%. Overall stream-wise length of the fence model

including manifold is 39 mm. As the fence body downstream of the tip is wholly immersed within the cavity, its geometry does not have any influence on the flow. To facilitate drag measurement the model is attached to a six-component force balance (Zarruk et al., 2014), and mounted to the test section ceiling with the fence located normal to the oncoming flow. The mounting disk on the force balance has an outside diameter of 160 mm and a thin plastic shim is placed between the fence and the disk to ensure that there is no contact between the fence model and the test section ceiling (i.e. to avoid drag measurement corruption). Likewise, there is a 0.5 mm gap between the fence ends and the test section sides. Air is supplied through the fore-body of the fence to the manifold (spanning the full fence width) via a ϕ6.5 mm passage located at the fence centreline 2.2. It is then distributed into the wake of the fence through 39 equi-spaced stream-wise outlets. The distance between the outlets is 15 mm, and their diameter is 2 mm. Ventilation air is provided from an external pressurized supply via a flexible tube routed through the force balance. Some additional data presented in this paper is obtained using the setup developed to study ventilated cavity flow over a 3-D wall-mounted fence, with the fence spanning approximately a quarter of the test section width. A detailed description of the 3-D setup can be found in Barbaca et al. (2017a).

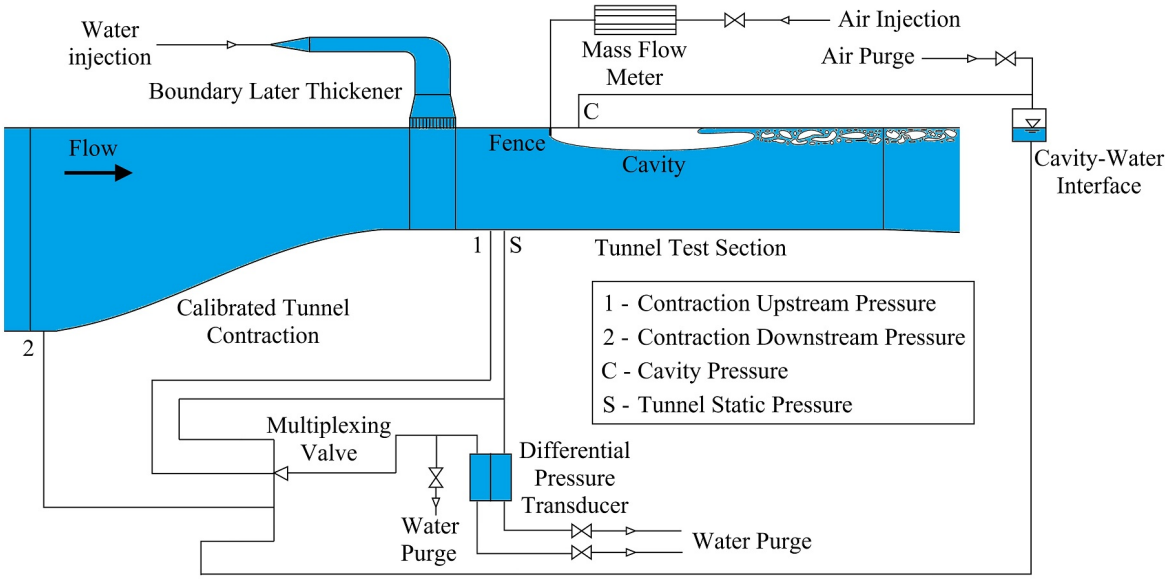

Figure 2.3: Schematic of the multiplexing valve system used to obtain the cavitation number, σ_c. Air injection is via a mass flow meter. Gas pressure measured from the taping inside the cavity is converted to a liquid pressure (necessary for the differential pressure transducer operation) using the cavity-water interface. A boundary layer control device attached upstream of the test section entrance is also shown (Belle et al., 2016).

A multiplexing valve system used for pressure measurement is represented schematically in figure 2.3. This setup allows the use of a single pressure transducer for all measurements, eliminating the need to apply corrections arising from transducer zero and

span errors. The free-stream dynamic pressure and pressure inside the cavity are measured relative to the free-stream static pressure, from which σ_c can be derived. The cavity pressure is sensed with a ϕ1 mm wall tapping located 20 mm downstream of the model, with a flexible tube routed through the force balance. The gas/liquid interface device, set at the tunnel ceiling height allows for the gas pressure (i.e. gaseous cavity) to be converted into liquid pressure (i.e. water) which can be measured with the liquid/liquid differential pressure transducer. Prior to each cavity pressure measurement the gas side is purged (i.e. vented to atmosphere) to ensure that the passage is free from liquid. The transducer and all lines containing liquid are purged using water from the tunnel prior to each set of measurements.

To facilitate the upstream wall pressure measurements the fence was mounted to the test section ceiling at 1.9 m from the entrance. Measurements were obtained from 17 $\times$ 1 mm wall tappings, located between 0.5 mm and 1000 mm upstream of the fence and spaced following a logarithmic progression. All tappings are located on the centreline, apart from tappings 2-3 and 4-5 from the fence, which are offset 5 mm and 10 mm to the side due to the spatial constraints. The tappings are connected to a 30 port sequential multiplexing valve using single differential pressure transducer as described above.

The test section absolute pressure is measured, depending on the value, from high or low range Siemens Sitransp absolute pressure transducers models 7MF4333-1FA02-2AB1 (pressure range 0-130 kPa) and 7MF4333-1GA02-2AB1 (pressure range 0-400 kPa) with estimated precision of 0.13 and 0.48 kPa respectively. The test section velocity is measured from the calibrated contraction differential pressure. Depending on the value, either high or low range Siemens Sitransp differential pressure transducers models 7MF4433-1DA02-2AB1-Z (pressure range 0-25 kPa) and 7MF4433-1FA02-2AB1-Z (pressure range 0-160 kPa) are used, with estimated precision of 0.007 and 0.018 m/s respectively. The air mass flow rate is controlled and measured using an Alicat Scientific model MCR-500-SLPM-D mass flow meter with flow rate range 0 - 500 SLPM (standard litres per minute) and an estimated precision of 3 SLPM. The cavitation number and upstream wall pressures are measured using a Validyne model DP15TL differential pressure transducer (pressure range 0-86 kPa and estimated precision of 0.2 kPa) via Swagelok model SS-43Z6FS1 7 way valve and via custom built 30 port sequencer utilizing Burkert flipper solenoid valves controlled from the data acquisition system. The force balance used to measure the model drag has a maximum rated load of 2 kN and an estimated precision of 0.15 N (for additional description see Zarruk et al. (2014)). The dissolved gas content of the water is measured using an Endress+Hauser OxyMax WCOS 41 membrane sensor. Cavity length has been obtained using still forward-lit photography as the average from at least ten images. Images were taken using a Nikon D800E SLR camera with Nikon AF Nikkor 50 mm f/1.4D lens. The exposure was controlled using a triggered stroboscopic flash (Drello 1018/LE4040).

In the case of ventilated cavities, four variables were independently prescribed to control the flow; air ventilation rate, boundary layer thickness to fence height ratio, free-stream Froude number and free-stream cavitation number. The combination of latter three, being held at particular constant values, gives a particular free-stream condition. Due to the air flow rate being measured via a mass flow meter, the volumetric flow rate coefficient could not be prescribed (it depends on the gas pressure inside the cavity and free-stream conditions), and it had to be calculated using the cavity pressure derived from the measured ventilated cavitation number. Due to the limited extent of the test section, an upper bound on the air flow rate needed to be determined (for a particular free-stream condition) where the cavity length would extend out of the test section into the diffuser (see Fig. 2.3). Approximately ten Q_m values were examined for each set of free-stream conditions.

Tests were conducted for Froude numbers (controlled with test section velocity) in the range $20.1 \leq Fr \leq 37.8$ and free-stream cavitation numbers (controlled with the test section static pressure for a particular flow velocity) in the range $0.27 \leq \sigma_v \leq 1.28$. The test section depth based Froude number was in the range $2.59 \leq Fr_H \leq 4.88$, resulting in conditions analogous to super-critical flow regime in open-channel flow, i.e. $Fr_H > 1$, in all cases.

Tests were performed for four δ/h ratios, with the fence model fully immersed in the oncoming wall boundary layer in all cases. The two lower δ/h values ($\delta/h = 1.9\,\&\,3.2$) were obtained using a natural boundary layer developed over the test section ceiling, with the fence located 0.7 m and 1.9 m from the test section entrance. The two higher δ/h values ($\delta/h = 5.6\,\&\,7.6$) were obtained using a boundary layer control system (Fig. 2.3) utilizing an array of transverse jets injected as described in Belle et al. (2016), with the fence located in the downstream position (1.9 m) along the test section ceiling. The boundary layer control system is connected to the tunnel ceiling via a 0.6 m (span-wise) by 0.124 m (stream-wise) penetration, fitted with a perforated plate. The perforated plate used in the present study had an array of 252 $\times$ 5 mm diameter holes, with a 28 mm spacing between the holes in stream-wise direction and 18.5 mm spacing in span-wise direction (designated as 'plate a' in Belle et al. (2016)). All tests were conducted with a dissolved O_2 content between 2 and 6 ppm.

The three independently controlled variables in the case of naturally cavitating flow were; free-stream cavitation number, free-stream Froude number and boundary layer thickness to fence height ratio. After Fr and δ/h values were set, a lower bound on the free-stream cavitation number (where a cavity would grow into the diffuser) had to be established. Between five and ten σ_v values were examined for each combination of Fr and δ/h. The range of test conditions involving natural cavities was reduced compared to the ventilated case. A summary of independently controlled parameters and their respective values for ventilated and natural cavity flows is given in Table 2.1.

Parameter	**Symbol**	**Ventilated**	**Natural**
Froude number (fence height based)	Fr	20.1 - 37.8	23.3 - 34.2
Froude number (test section depth based)	Fr_H	2.6 - 4.9	3 - 4.4
Vapour pressure based cavitation number	σ_v	0.45 - 1.28	$\approx 0.15 - 0.4$
Boundary layer thickness to fence height ratio	δ/h	1.9 - 7.6	1.9 - 7.6
Air ventilation rate	Q_m	0 - 500 SLPM	N/A

Table 2.1: List of independently controlled parameters with their respective values range for the ventilated and natural cavity flow experiments.

The numerical data provided for comparison is from a previous study Barbaca et al. (2017b) and was obtained using a commercial CFD software STAR-CCM+, employing a first order implicit unsteady compressible solver with Volume of Fluid (VOF) method used to capture the cavity/water interface.

2.3 Results and discussion

2.3.1 Cavity topology

A typical topology of a fully developed cavity is shown in Fig. 2.4 for (a) ventilated and (b) naturally cavitating flow at the same flow conditions ($Fr = 23.3$, $\sigma_c = 0.19$ and $\delta/h = 1.9$). Apart from the differences in the closure/wake region, the appearance of the cavities is largely similar, corresponding to the observations previously reported by May (1975) and Kunz et al. (1999) for axisymmetric ventilated and natural cavity flow. In both cases, the cavity has a stable detachment from the fence tip and two distinct regions are evident along the cavity length. The region closer to the fence is air/vapour filled with a relatively sharp cavity/water interface and a transparent appearance. A series of randomly appearing and disappearing stream-wise streaks travelling in the span-wise direction can be observed immediately downstream of the cavity detachment line (Fig 2.4c). These streaks, along with the small-scale stream-wise waves observable on the cavity surface (Fig 2.4d), can be attributed to turbulence contained within the oncoming wall boundary layer in which the fence is fully immersed.

The rear or closure of the cavity is affected by re-entrant jet flow and is observed as an opaque region. Depending on the cavity length and the free-stream conditions, the re-entrant jet can extend all the way to the fence, or be contained to only a portion of the cavity. The re-entrant jet instability is the predominant mode of gas entrainment for cavitating flows with unsteady closure and it has been comprehensively reported on in a seminal study by Callenaere et al. (2001). The re-entrant jet penetrates into the cavity, transporting liquid upstream along the wall. The liquid falls under gravity, impinging on

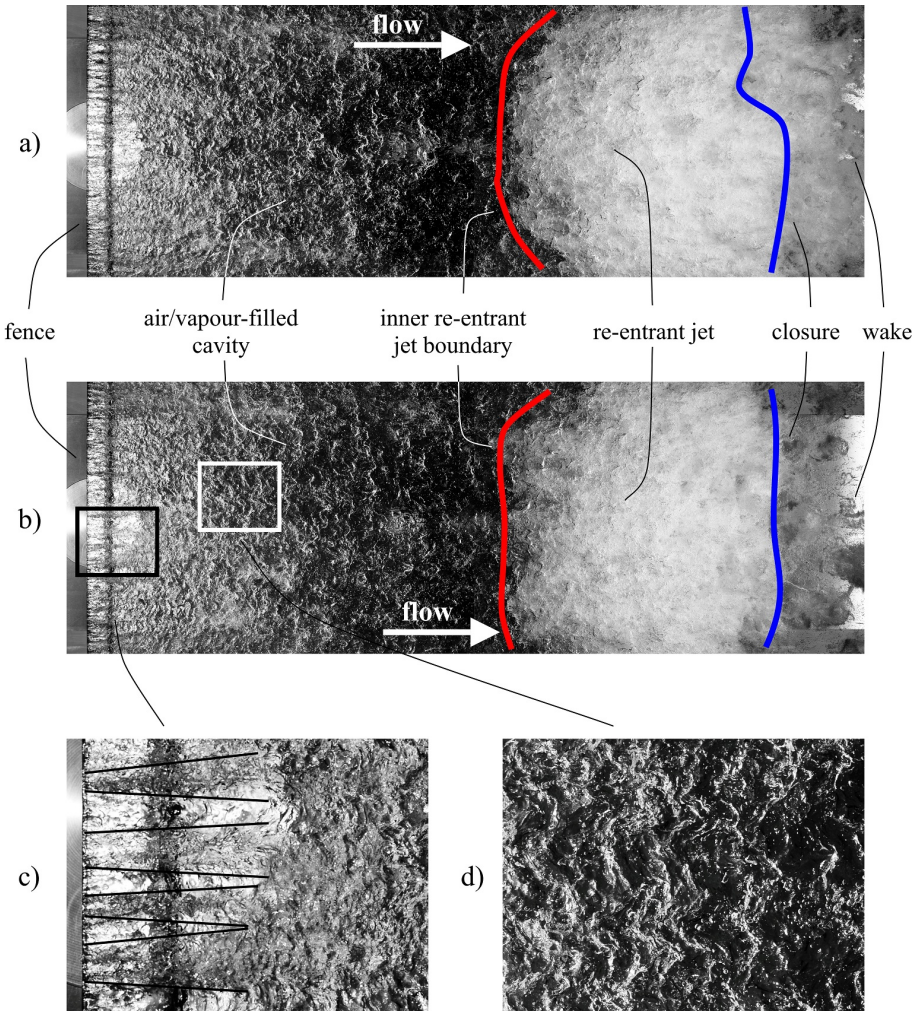

Figure 2.4: Typical topologies of developed ventilated (a) and natural (b) cavities for the same flow conditions ($Fr = 23.3$, $\sigma_c \approx 0.19$ and $\delta/h = 1.9$). Different regions along the cavity length are indicated. An enlarged view of the stream-wise streaks shown with the black lines (c) and span-wise waves (d) on the cavity surface is provided.

the cavity surface, shedding a portion of the cavity as a dense bubbly mixture into the main flow.

Unlike the periodic shedding of large scale clouds (i.e. cloud cavitation), typical for flows with a strong adverse pressure gradient in the closure region (Le et al., 1993; Brandner et al., 2010), the shedding observed for the present flow (nominally zero pressure gradient) is characterized by a larger number of varying smaller-scale cloud structures detaching randomly along the closure span. Additionally, the turbulence induced wave structures present on the cavity/water interface are, to a lesser degree, contributing to the entrainment process by pinching off fine bubbly structures from the cavity surface.

The only obvious difference in the behaviour of ventilated and natural cavities shown in Fig. 2.4 is in the wake region. The wake of a ventilated cavity in vicinity of the closure consists of a dense mixture of shed clouds and fine-scale bubbly structures. As the larger clouds are conveyed downstream by the main flow, they are progressively broken up in

the turbulent flow, eventually resulting in a dense layer of fine bubbles along the test section ceiling. In the case of a natural cavity the vapourous structures condense within a short distance from the closure and only a population of micro-bubbles containing incondensable gas remain in the far wake (Russell et al., 2016). The condensation of bubbly structures was observed to generate upstream propagating disturbances, which seem to resemble bubbly shock-wave propagation (Reisman et al., 1998; de Graaf et al., 2016; Ganesh et al., 2016a,b). Within the scope of present study this phenomena was not investigated in detail. A detailed investigation of the shock-wave phenomena, along with the study of unsteady behaviour of ventilated and natural cavity flow over a wall-mounted fence, based on the simultaneous measurements from an array of dynamic wall pressure sensors located in the cavity closure and wake region, high-speed imaging and X-ray densitometry, is planned for future work.

2.3.2 The effect of varying ventilation rate, free-stream speed and pressure

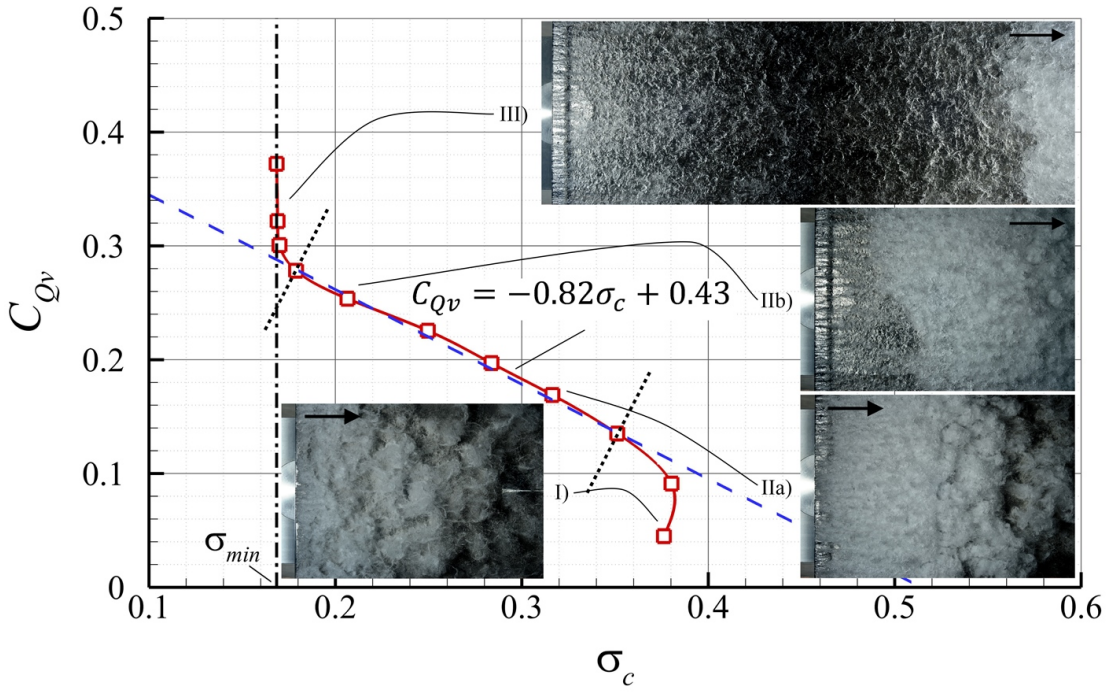

Figure 2.5: Dependence of cavitation number on the volumetric flow rate coefficient (for $Fr = 29.6$, $\sigma_v = 0.87$ and $\delta/h = 1.9$). Three regimes can be identified following an increase in C_{Qv}: I) shear layer cavitation, II) fully formed cavity with a nominally linear dependence of σ_c on C_{Qv} and III) cavity in 'blocked' conditions. Note that for a fully developed cavity, depending on the cavity length and free-stream conditions, re-entrant jet may impinge on (IIa) or be detached (IIb) from the fence. The vertical asymptote depicts the minimum cavitation number (σ_{min}) obtainable under the particular flow conditions.

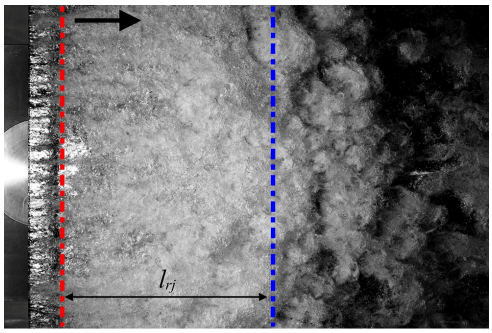

a) $C_{Qv} = 0.17$; $\sigma_c = 0.24$

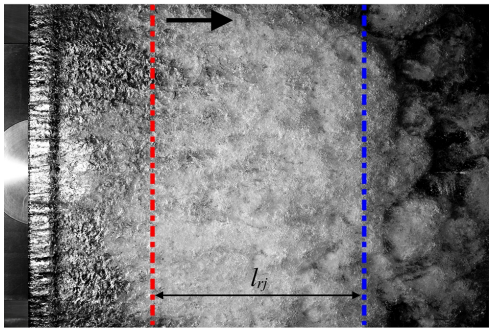

b) $C_{Qv} = 0.18$; $\sigma_c = 0.22$

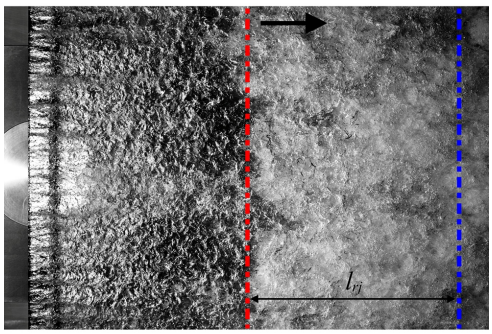

c) $C_{Qv} = 0.19$; $\sigma_c = 0.20$

Figure 2.6: Ventilated cavity development with a decrease in cavitation number is shown for constant free-stream conditions ($Fr = 29.6$, $\sigma_v = 0.87$ and $\delta/h = 1.9$). The re-entrant jet impinges on the fence for a short cavity (a), but ceases to impinge as the cavity grows (b-c). Once the re-entrant jet detaches from the fence, its length (l_{rj}) remains unchanged as σ decreases.

For ventilated cavity flow, at a particular free-stream condition (i.e. constant Fr, σ_v and δ/h), σ_c is controlled solely by the air ventilation rate, C_{Qv}. The typical dependence of σ_c on C_{Qv} (for $Fr = 29.6$, $\sigma_v = 0.87$ and $\delta/h = 1.9$) is shown in Fig 2.5. Three regimes can be identified along the curve following an increase in C_{Qv}. In regime (I), a typical unsteady shear layer type cavitation can be observed in the fence wake with several short cavities detaching across the fence span with the gaps present in-between filled with smaller air bubbles. The detachment line at the fence tip is broken and unstable.

With an increase in C_{Qv} the fragmented cavities join forming a fully developed cavity, regime (II), with a stable detachment line spanning the full fence width. In this regime σ_c has a nominally linear dependence on the ventilation rate as shown in Fig. 2.5. A re-entrant jet closure (i.e. a cavity closure with re-entrant flow) is present, which for short cavities impinges on the downstream face of the fence (IIa). With reduction in σ_c and subsequent increase in cavity length, the re-entrant jet ceases to impinge on the fence (IIb). The nominally linear dependence of σ_c on C_{Qv} is found to be unaffected by the extent of the re-entrant jet or whether it impinges on the fence or not.

In regime (III), the cavity flow is being affected by confinement (i.e. finite size of the test-section) and a vertical asymptote corresponding to a minimum cavitation number value, $\sigma_c = \sigma_{min}$, is present. When this lower bound is approached cavity growth is very sensitive to a change in ventilation rate where the length increases 'infinitely' with a slight increase in C_{Qv}. This 'blockage effect' is solely a function of the geometry of the confined flow (Brennen, 1995).

The evolution of a fully developed cavity (regime II), following a decrease in cavitation number for a constant set of free-stream conditions ($Fr = 29.6$, $\sigma_v = 0.87$ and $\delta/h = 1.9$), is shown in more detail in Fig 2.6. As stated above, during the initial phase of cavity growth, the re-entrant jet impinges on the downstream face of the fence (Fig 2.6a), but as the cavity length increases the re-entrant jet inner boundary moves downstream (Fig 2.6b-c). Once the re-entrant jet detaches from the fence its length (l_{rj}) remains constant as the overall length of the cavity increases with decreasing σ_c, resulting in a larger portion of the cavity being filled with air only. This suggests that the re-entrant jet intensity is independent of the cavitation number for a particular set of free-stream conditions.

A description of cavity topology evolution for naturally forming cavities, following a variation in σ_c, is identical to the one given above for the ventilated cavity flow. As the pressure inside a natural cavity is always close to the vapour pressure, p_v, the driving parameter governing σ_c for non-ventilated flow is the free-stream pressure p_∞, for a constant Fr (instead of C_{Qv} in the ventilated case). Apart from this dissimilarity, the preceding discussion is pertinent for both cases.

The effect of varying free-stream speed, i.e. Fr, with σ_v and δ/h held constant, on the relation between σ_c and C_{Qv} is shown in Fig. 2.7. It can been seen that with an increase in Fr more air is needed to achieve the same σ_c, however, the quantity of additional air

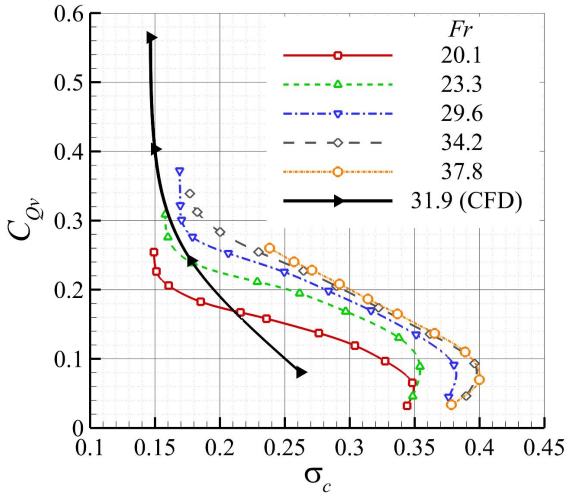

Figure 2.7: Relation between σ_c and C_{Qv} for varying Froude number, constant free-stream cavitation number ($\sigma_v = 0.87$) and boundary layer thickness to fence height ratio ($\delta/h = 1.9$). CFD data (from Barbaca et al. (2017b)) for similar flow conditions (i.e. $\sigma_v = 0.87$ and $\delta/h = 2$) is included for comparison.

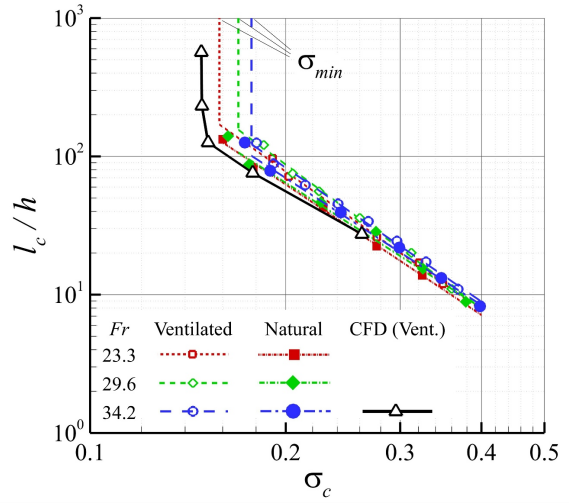

Figure 2.8: Dependence of non-dimensionalised cavity length, l_c/h, on σ_c for three Fr values for ventilated and naturally cavitating flow in a $log - log$ plot ($\sigma_v = 0.87$, $\delta/h = 1.9$). Note the vertical asymptotes corresponding to σ_{min} achievable for a particular Fr. CFD data (from Barbaca et al. (2017b)) obtained for similar flow conditions ($\sigma_v = 0.87$, $\delta/h = 2$) is included for comparison.

reduces with increasing Fr. With increase in Fr this quantity of additional air tends to zero (for $Fr > 30$), resulting in σ_c being now independent of the free-stream speed and a function of the ventilation rate only. This behaviour can be attributed to the relative contributions from boundary layer turbulence and the re-entrant flow to gas entrainment, with the former becoming insignificant at higher Fr values. C_{Qv} being independent of Fr is equivalent to the volumetric flow rate being proportional to free-stream speed. Lower σ_{min} values are achieved for lower Fr values as a consequence of less pronounced blockage resulting from decreased cavity thickness, as discussed by Barbaca et al. (2017a). For the highest Fr case, σ_{min} was not obtained due to insufficient air flow rate through the mass flow meter. The CFD results presented in Barbaca et al. (2017b) for similar flow conditions ($\sigma_v = 0.87$, $\delta/h = 2$) under-predict C_{Qv} needed to achieve a particular σ_c, but generally show a reasonable agreement with the experimental data given the limitations with capturing the unsteady entrainment mechanisms involved with the 2-D RANS method used for the numerical simulations. However, the numerical modelling does capture other aspects of the flow quite favourably as will be shown in other data following.

In Fig 2.8 the dependence of cavity length l_c on σ_c is shown in a $log-log$ plot for three Fr values (for constant $\sigma_v = 0.87$ and $\delta/h = 2$) for ventilated and naturally cavitating flows. For all Fr values, the cavity length increases with a decrease in σ_c following a power law, resembling the behaviour typically observed for unbounded flows (Franc and Michel, 2004). This behaviour changes as $\sigma_c \to \sigma_{min}$, where 'infinite' cavity growth is represented with a vertical asymptote corresponding to a particular Fr. The curves obtained for different Fr fall on top of each other, indicating that apart from the difference in σ_{min}, l_c/h dependence on σ_c is invariant of Fr. A similar behaviour is observed for ventilated and natural cavities. A greater scatter present in the data obtained for natural cavity flow is attributable to increased sensitivity of cavity length measurement on small pressure fluctuations at pressure values close to the vapour pressure. The CFD data (Barbaca et al., 2017b) compares favourably with experiment, slightly under-predicting the length for a particular σ_c.

It has been shown by Barbaca et al. (2017a) that in the case of ventilated cavity flow over a 3-D wall mounted fence a variation in Fr has a large effect on the re-entrant jet intensity. In Fig 2.9 ventilated and natural 2-D cavities of fixed length ($l_c/h \approx 60$) are shown for three Fr ($23.3, 29.6$ & 34.2). The re-entrant jet intensity may be quantified using the re-entrant jet to cavity length ratio (l_{rj}/l_c). From Fig 2.9 it is evident that l_{rj}/l_c decreases following a decrease in Fr. The earlier study (3-D) found that l_{rj}/l_c on Fr dependence is linear and that a complete extinction of the re-entrant jet for $Fr = Fr_0 > 0$. This value was found to coincide with $Fr_H \approx 1$, i.e. the transition of the flow from super-critical to sub-crtical regime. The trend presented in Fig. 2.9 for the new 2-D data suggest that a similar behaviour is expected. No difference in the re-entrant jet intensity

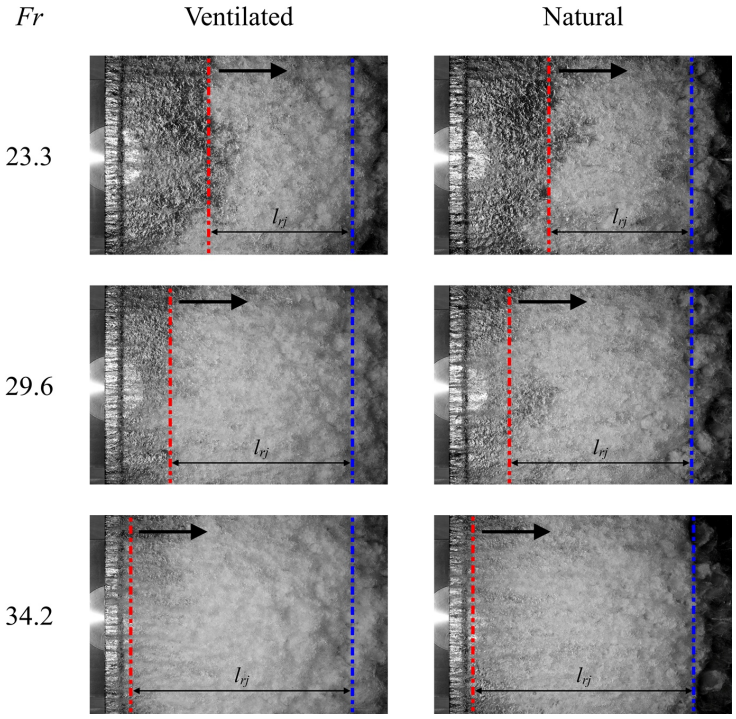

Figure 2.9: Ventilated and natural cavities of a constant length ($l_c/h \approx 60$) are shown for varying Fr ($23.3, 29.6 \,\&\, 34.2$). With a decrease in Fr the length of region affected by the re-entrant jet reduces. A similar behaviour is observed for both ventilated and natural cavities.

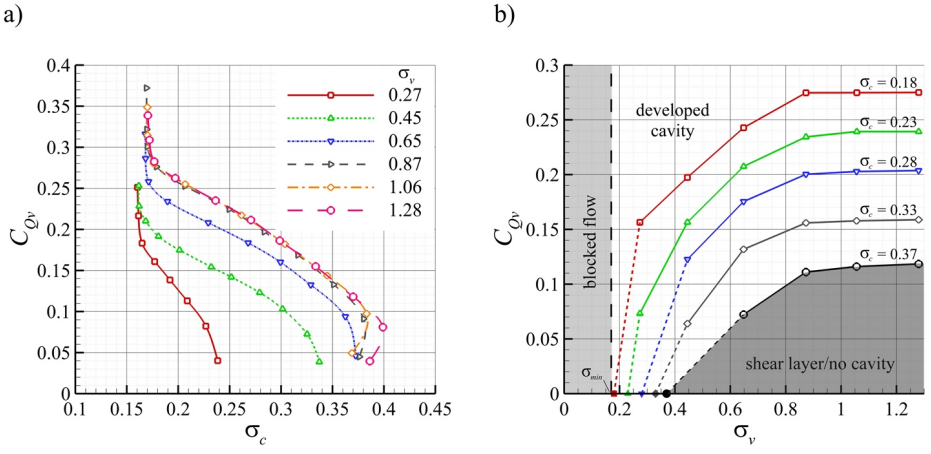

Figure 2.10: a) Relation between σ_c and C_{Qv} for varying free-stream cavitation numbers and constant Froude number and boundary layer thickness ($Fr = 29.6$, $\delta/h = 1.9$) for ventilated cavity flow. b) A cross-plot of the data from a), showing the dependence of C_{Qv} needed to achieve a constant σ_c in a fully developed cavity flow for different σ_v, encompassing the transition from naturally cavitating into ventilated flow. The natural cavity data is added as points lying along the horizontal axis (i.e. $C_{Qv} = 0$) and the various regimes are shown as shaded regions.

is observed between the ventilated and natural cavities of the same length and Fr, and the same l_{rj}/l_c on Fr dependence is present in both cases.

With ventilated cavity flow, the mass flow rate of air needed to maintain a constant σ_c is increased with an increase in free-stream cavitation number, σ_v. As C_{Qv} is in part determined by the pressure inside the cavity, the dependence of C_{Qv} on σ_v is more complicated. In Fig. 2.10a the relation between σ_c and C_{Qv} is shown for different σ_v values, while Fr and δ/h are held constant ($Fr = 29.6$, $\delta/h = 2$). For $\sigma_v < 0.87$ an increase in σ_v results in a higher C_{Qv} required to obtain the same σ_c. However, as σ_v increases, C_{Qv} tends to an asymptotic value. This behaviour can be explained by the transition of the flow from the conditions where a natural cavity (either shear layer or developed) is present with $C_{Qv} = 0$ (lowest three σ_v cases) to where a cavity only exists with ventilation (increasing σ_v), with eventual disappearance of the dependence of C_{Qv} on σ_v above a value of about 0.85. It can be noted that the maximum σ_c for the cases where a natural cavitation occurs can not be greater than the corresponding σ_v value and a decrease in σ_v leads to a shift to the left for these curves. To better illustrate the discussed behaviour, a cross-plot of the data from Fig. 2.10a is given in Fig. 2.10b for the range of σ_c values up to 0.37 for which a fully developed cavity was present. The natural cavity data points are added to Fig. 2.10b on the horizontal axis (i.e. $C_{Qv} = 0$) and they appear to connect smoothly (dashed lines) to curves obtained for the corresponding σ_c in ventilated flow. For $\sigma_v = \sigma_{min}$ the flow is 'blocked' and an 'infinite' natural cavity forms even without any ventilation. The figure is shaded to indicate the regions of differing cavitation type which occur as described in section 3.2.

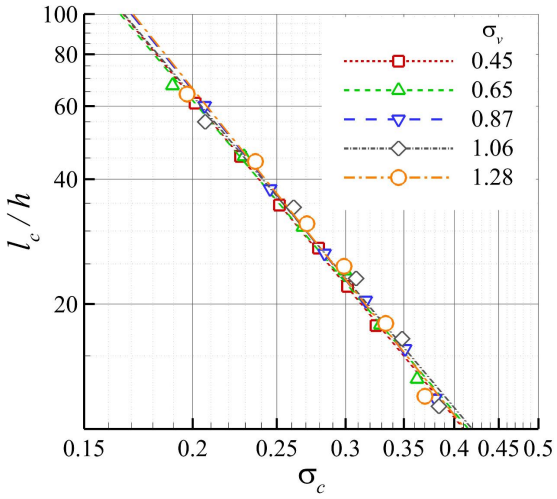

Figure 2.11: Relation between l_c/h and σ_c in case of ventilated cavity flow for five σ_v values (for constant $Fr = 29.6$, $\delta/h = 1.9$).

The dependence of l_c/h on σ_c is presented in Fig. 2.11 for five σ_v values. It can be seen that l_c/h on σ_c dependence is not a function of σ_v, i.e. no change in the length of

a cavity present for constant σ_c is observed if σ_v is varied. Together with the previously described independence of l_c/h on σ_c relation on Fr, it may be concluded that the l_c/h on σ_c dependence is completely invariant of the free-stream conditions (i.e. free-stream velocity and free-stream pressure).

2.3.3 The effect of varying boundary layer

The effect of varying immersion of a wall-mounted cavitator in an oncoming boundary layer has not been reported in any detail in the available literature. In the present study ventilated cavity flow over a 2-D and 3-D wall mounted fence is investigated for four boundary layer thickness to fence height ratios, $\delta/h = 1.9, 3.2, 5.6\,\&\,7.6$. Based on the similarity in the topologies of ventilated and naturally cavitating flow presented in previous sections, the observations made of the ventilated cavity behaviour are also taken to apply similarly for natural cavity flow in a varying boundary layer. A comprehensive discussion of the topology of 3-D ventilated cavities is reported by Barbaca et al. (2017a) and only limited details will be provided here for comparison with the 2-D results.

In figure 2.12 topologies of equal length cavities ($l_c/h \approx 60$) in 2-D and 3-D flow are shown for varying δ/h and constant free-stream conditions ($Fr = 29.6$, $\sigma_v = 0.87$). With an increase in δ/h the effect of increasing length scales of the structured turbulence contained within the oncoming wall boundary layer becomes more pronounced (magnified view in Fig 2.12). The number of stream-wise streaks observable on the cavity surface immediately after detachment decreases, resulting in increased separation between them. These streaks grow and affect a larger portion of the cavity surface for higher δ/h. Also, the stream-wise wavy perturbations on the cavity surface increase in size leading to greater entrainment through the cavity/water interface. For the two largest δ/h values, these structures can occasionally penetrate into the re-entrant jet and influence the re-entrant jet break-up dynamics. In the 3-D flow the cavity sides show an increasingly broken appearance, occasionally shedding larger gaseous clouds into the main flow. The re-entrant jet length appears to be unaffected by variation in δ/h, however, the re-entrant jet occupies a larger portion of a cavity in 3-D flow.

From Fig 2.13 it can be seen that the dependence of σ_c on C_{Qv}, as described in section 3.1, is generally unaffected by a variation in δ/h. The noticeable difference is the translation of the curves towards the lower σ_c region, i.e. a lower C_{Qv} is needed to achieve the same σ_c for a higher δ/h. Also, due to this translation, a lower σ_{min} value is obtained for a higher δ/h. Barbaca et al. (2017b) attributed this translation to a reduction in blockage effect resulting from a decrease in cavity thickness with an increase in δ/h. The small difference in trend at low σ_c between the $\delta/h = 1.9$ data and that for all other data is attributable to the differing location of the fence used for this measurement. To obtain the smallest δ/h value the fence was positioned further upstream along the test

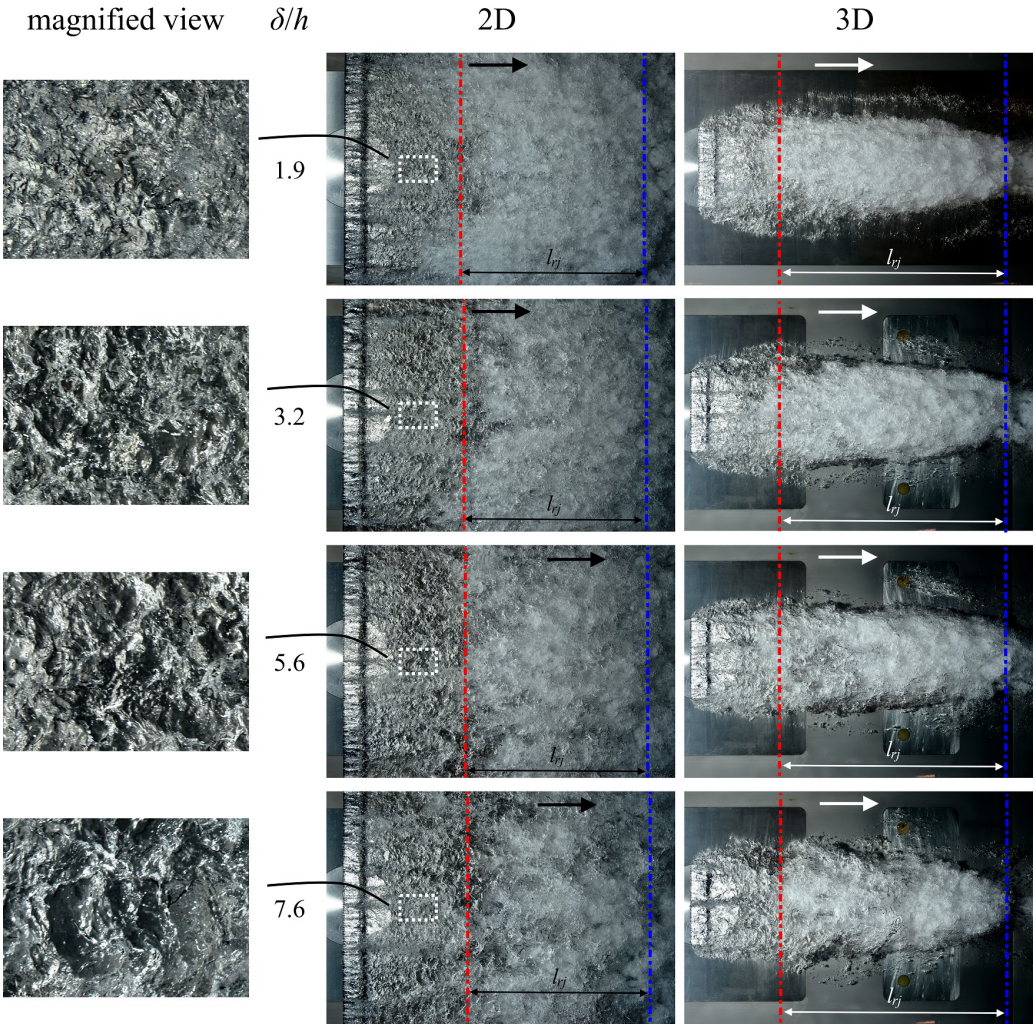

Figure 2.12: Topologies of 2-D and 3-D ventilated cavities for varying boundary layer thickness to fence height ratio, δ/h (for $Fr = 29.6$ and $\sigma_v = 0.87$). With increase in δ/h the cavity surface becomes more affected by the turbulence embedded in the boundary layer, as shown in the magnified view. Note that the re-entrant jet occupies a larger portion of the cavity in the 3-D case.

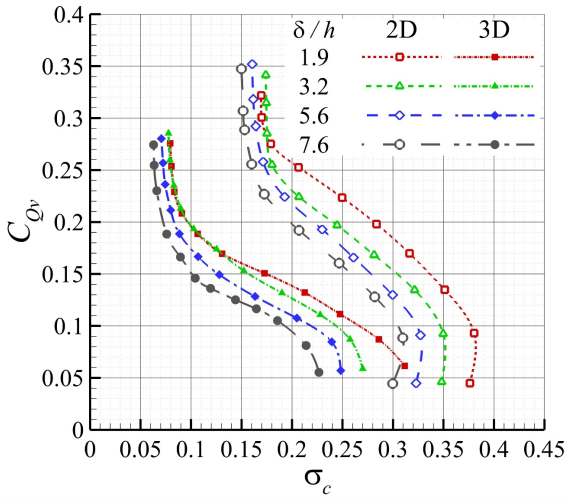

Figure 2.13: Dependence of σ_c on C_{Qv} for variable δ/h and constant free-stream conditions ($Fr = 29.6$, $\sigma_v = 0.87$). The results for 2-D and 3-D flow are shown.

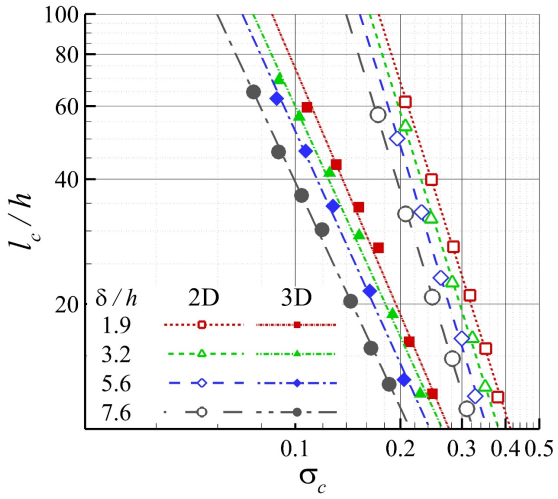

Figure 2.14: Cavity length as a function of σ_c for varying δ/h and constant free-stream conditions ($Fr = 29.6$, $\sigma_v = 0.87$) presented as $log - log$ plot for 2-D and 3-D flow.

section ceiling (at 0.7 m from the entrance) and thus further away from the diffuser. The effect due to this difference in the test geometry is most pronounced at low σ_c where the increased cavity length extends into the diffuser. The results obtained for 2-D and 3-D flow show similar behaviour, but due to a much smaller cross-sectional area of the 3-D fence model and the related decrease in blockage effect, the 3-D curves are shifted to lower ranges of σ_c.

Cavity length as a function of σ_c for varying δ/h and constant free-stream conditions ($Fr = 29.6$, $\sigma_v = 0.87$) is presented as a $log - log$ plot in Fig 2.14 for 2-D and 3-D flow. A shift towards the lower σ_c region can be observed following an increase in δ/h. This shift is a consequence of a less pronounced blockage effect for higher δ/h, as discussed in the paragraph above. Similarly, the curves obtained for 3-D flow are shifted to a lower σ_c zone, and have a lower slope than those for the 2-D case.

2.3.4 Upstream pressure distribution

In figure 2.15 the wall pressure distribution up to $100h$ upstream of the fence is shown as a $log-log$ (Fig 2.15a) and linear (Fig 2.15b) plot. The pressure distribution is presented for varying σ_c and constant free-stream conditions ($Fr = 29.6$, $\sigma_v = 0.87$ and $\delta/h = 3.2$). The pressure is expressed in non-dimensionalised form as a pressure coefficient, $C_P = (p - p_\infty)/0.5\rho U_\infty^2$. For a constant σ_c value, C_P has approximately constant value within one h upstream of the fence. The small peaks in C_P located about $0.13h$ and $0.3h$ upstream of the fence can be associated with a recirculation bubble in front of the fence and the related stagnation points present in the flow. After about one h the pressure starts to slowly decrease, eventually exhibiting a power law like reduction with increase

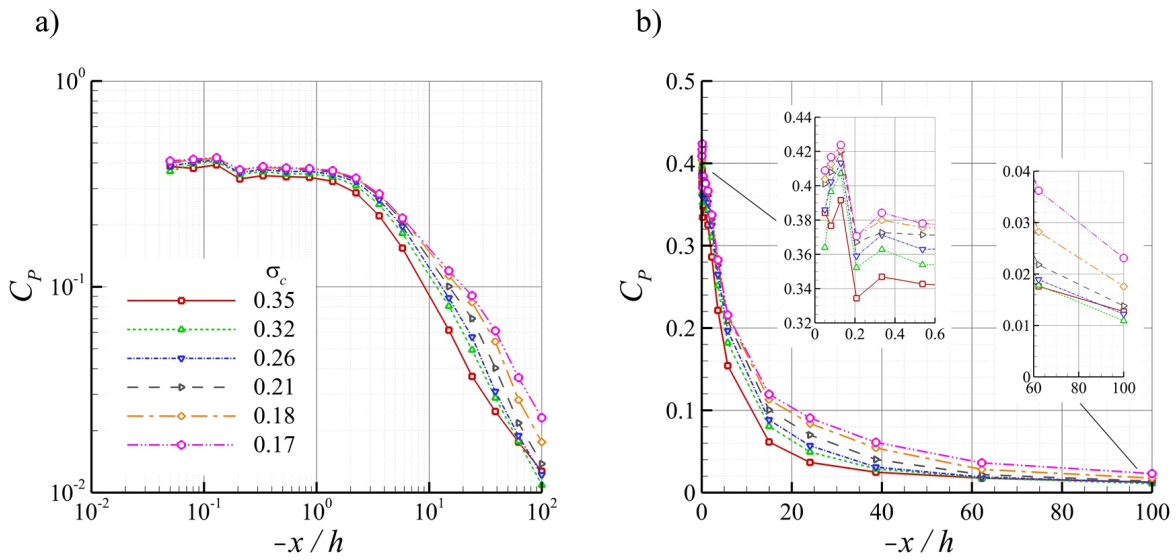

Figure 2.15: Wall pressure distribution up to $100h$ upstream of the fence shown as $log-log$ (a) and linear (b) plot for different σ_c values (for $Fr = 29.6$, $\sigma_v = 0.87$ and $\delta/h = 1.9$). Insets are provided for more detailed overview of the pressure distribution within the region up to $0.6h$ upstream of the fence and in the far upstream zone.

in the distance after $5h$ from the fence. A similar behaviour is observed by Pearce and Brandner (2014) and Barbaca et al. (2017b) in their numerical simulations.

Following a decrease in σ_c a slight increase in C_P can be observed along the whole curve. The largest increase is evident when the flow transitions from shear layer regime (i.e. for $\sigma_c = 0.35$) to a fully developed cavity regime (i.e. for $\sigma_c = 0.32$). The maximum value of the pressure coefficient ($C_{P_{max}}$) increases by about 7% for the range of achievable σ_c values, but the difference tends to zero as σ_{min} is reached. The difference in C_P in the region far upstream of the fence suggest a more pronounced influence of the fence/cavity system on the upstream flow for a lower σ_c, with a difference in C_P value $100h$ upstream of the fence of about 0.01. Similar behaviour is observed in a numerical study by (Barbaca et al., 2017b).

No significant change in the wall pressure distribution is observed if the free-stream conditions are changed and σ_c is held constant, as shown in Fig. 2.16a for the case of varying Fr and in Fig. 2.16b for varying σ_v.

The upstream wall pressure distribution for case with varying δ/h is shown as a $log-log$ in Fig. 2.17a and as a linear plot in Fig. 2.17b for a constant $\sigma_c = 0.21$ and constant free-stream conditions ($Fr = 29.6$, $\sigma_v = 0.87$). An inset is added showing a zoomed view of the C_P distribution in the zone up to $2h$ upstream of the fence. A decrease in $C_{P_{max}}$ of around 12% can be observed between the cases with lowest and highest δ/h. This decrease in $C_{P_{max}}$ is associated with a reduction in momentum acting on the fence as it is immersed deeper in the boundary layer. The curves maintain a constant offset in the C_P value in the region up to $10h$ upstream of the fence. For the two cases with a thickened boundary layer (the two larger δ/h), the C_P data becomes inconsistent in the

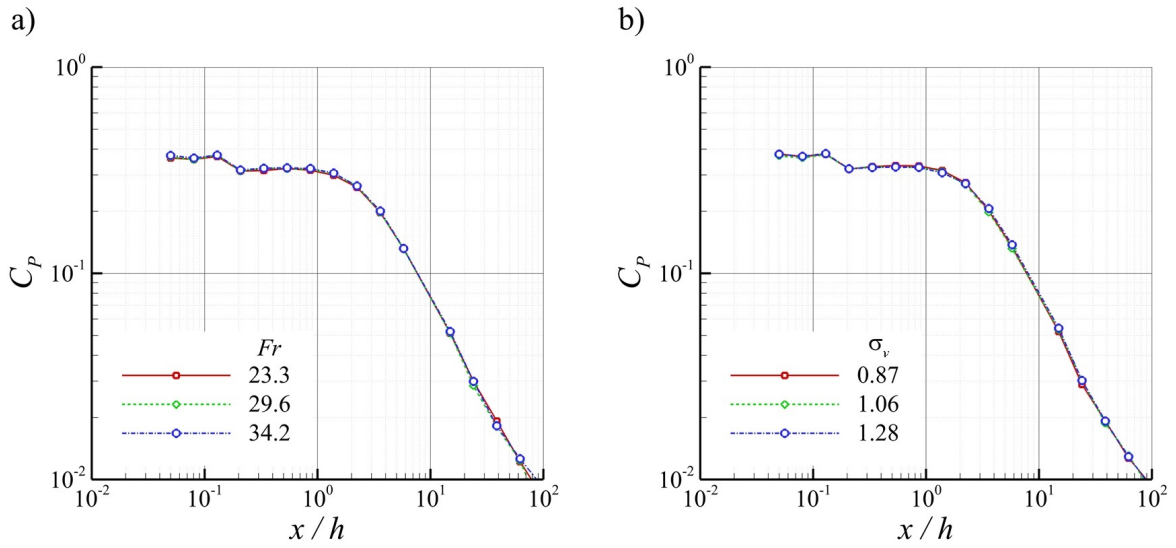

Figure 2.16: Wall pressure distribution up to $100h$ upstream of the fence shown as $log - log$ plot for different Fr (a) and σ_v (b) values (for $\sigma_c = 0.26$ and $\delta/h = 1.9$).

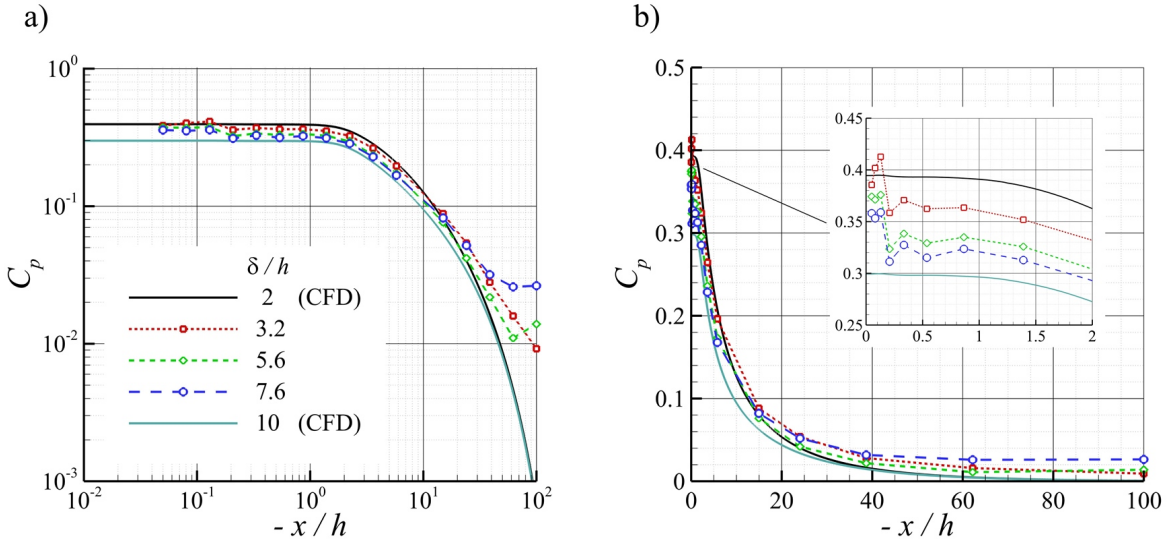

Figure 2.17: Wall pressure distribution up to $100h$ upstream of the fence shown as $log - log$ (a) and linear (b) plot for different δ/h values (for $Fr = 29.6$, $\sigma_v = 0.87$ and $\sigma_c = 0.21$). Inset is added for a more detailed insight in C_P behaviour in the region up to $2h$ upstream of the fence. The CFD data from Barbaca et al. (2017b) is provided for comparison.

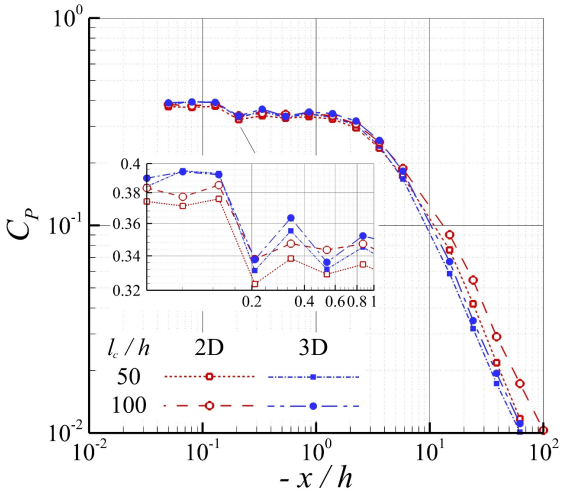

Figure 2.18: A comparison of the wall pressure distribution up to $100h$ upstream of the fence for 2-D and 3-D flow for two cavity lengths, $l_c/h = 50\,\&\,100$ (for $Fr = 29.6$, $\sigma_v = 0.87$ and $\delta/h = 1.9$) as a $log - log$ plot. A zoomed in view of the pressure distribution in the zone up to one h upstream of the fence is provided.

far upstream region due to the presence of the boundary layer thickening device. CFD data from Barbaca et al. (2017b) is provided for comparison and although the δ/h values examined computationally are outside of the range investigated in the experiment, a good agreement with the experimental data in shape of the C_P distribution and magnitude can be seen.

A comparison of the wall pressure distributions for 2-D and 3-D flow is provided in Fig. 2.18 for two cavity lengths, $l_c/h = 50\,\&\,100$ (for $Fr = 29.6$, $\sigma_v = 0.87$ and $\delta/h = 2$). Due to a large offset in the achievable σ_c values for 2-D and 3-D flow stemming from different blockage conditions, instead of σ_c, equivalent cavity length was chosen to compare between the two different flows. A small difference in the $C_{P_{max}}$ is present, with a slightly greater $C_{P_{max}}$ measured in the 3-D case. A magnified view of the pressure distribution in the zone up to one h upstream of the fence is provided for a clearer depiction of this difference. Although a large difference in the pressure distribution across the span of the fence exist between the 2-D and 3-D flow (i.e. $C_P \rightarrow 0$ towards the edges of 3-D fence), the small difference in the measured C_P suggests that the 3-D flow exhibits a largely 2-D behaviour in the vicinity of the test section centreline. As expected, the full span 2-D fence has a greater influence on the pressure distribution further upstream as it doesn't allow for pressure relief around the fence sides.

2.3.5 Hydrodynamic forces

The influence of variation in the governing flow parameters on the hydrodynamic forces is of interest in the context of using a cavitating wall-mounted fence as an 'interceptor' type device for ride control of marine craft. In Fig 2.19a the dependence of drag coefficient,

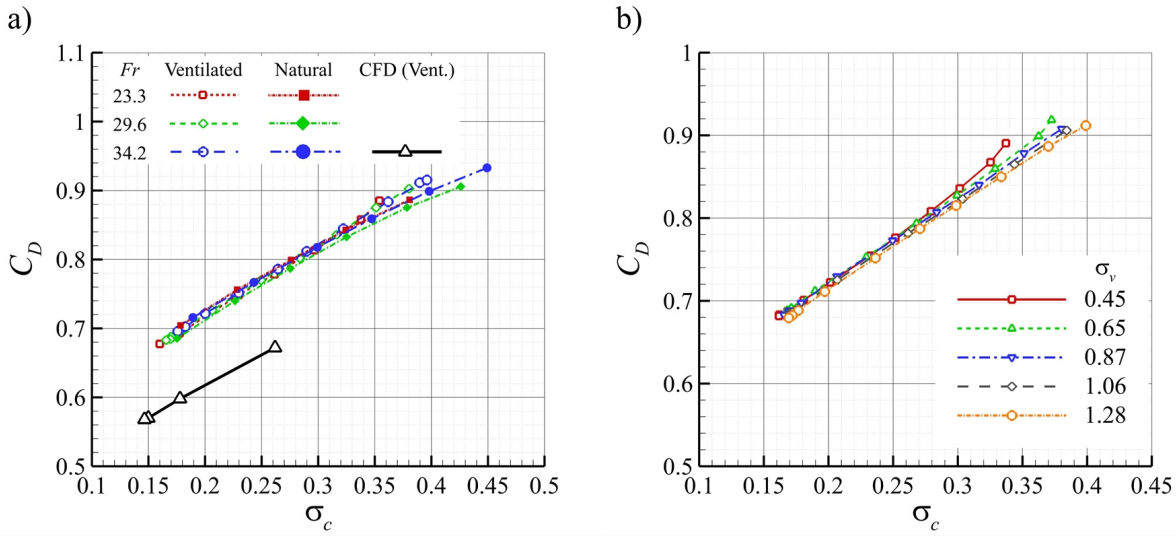

Figure 2.19: a) Dependence of C_D on σ_c for variable Fr, with $\sigma_v = 0.85$ and $\delta/h = 1.9$ for ventilated and naturally cavitating flow. The CFD data from Barbaca et al. (2017b) obtained for the similar flow conditions is given for comparison. b) Dependence of C_D on σ_c for variable σ_v, with $Fr = 29.6$ and $\delta/h = 2$, for ventilated flow.

C_D, on σ_c is presented for three Fr values for ventilated and naturally cavitating flow. In both cases, the drag decreases linearly following a decrease in σ_c converging to a minimum value for $\sigma_c \to \sigma_{min}$. The difference in C_D across the range of achievable σ_c values is around 26%. For a constant σ_c the same C_D value is measured irrespective of Fr, with only a small change in the minimum C_D value observed due to a slightly lower σ_{min} occurring for a lower Fr. The curves obtained for ventilated and naturally cavitating flow show a similar behaviour, with only a slight difference in C_D values present in the shear layer cavitation regime, where ventilated C_D is slightly larger. Again, CFD data from Barbaca et al. (2017b) is provided for comparison. The drag curve from the numerical analysis shows a linear C_D on σ_c dependence similar to one seen in experimental data, but under-predicts the C_D value, with the offset in C_D value of about 0.1 ($\approx$ 13% difference in minimal C_D).

In Fig. 2.19b a similar plot depicting the dependence of C_D on σ_c for variable σ_v in ventilated flow is provided (for $Fr = 29.6$, $\delta/h = 1.9$). From the figure it is evident that C_D on σ_c dependence is independent of σ_v. Note that curves for the lowest σ_v values have a right hand boundary at a lower σ_c value, due to the presence of a natural cavity at those σ_v values.

The dependence of C_D on σ_c for variable δ/h and constant free-stream conditions ($Fr = 29.6$, $\sigma_v = 0.87$) is shown in Fig 2.20 for 2-D and 3-D flows. In 2-D flow, the curves are offset towards the lower C_D values following a decrease in δ/h, with the difference in C_D value of about 0.08 ($\approx$ 10% difference in minimal C_D) between the extreme cases. The C_D value is decreasing at the constant rate for δ/h range investigated. Such a reduction in drag is expected, due to the lower oncoming flow velocity across the fence height with

a deeper immersion of the fence in the boundary layer.

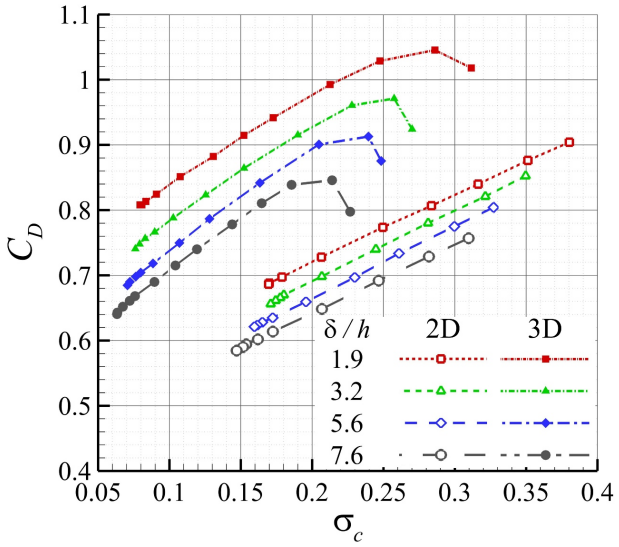

Figure 2.20: Dependence of C_D on σ_c for variable δ/h ($Fr = 29.6$, $\sigma_v = 0.87$) for 2-D and 3-D ventilated flow.

Again, due to a decrease in blockage effect the curves obtained for 3-D flow are shifted to the lower σ_c values compared to those for the 2-D case. The 2-D and 3-D flow curves exhibit a similar behaviour, differing only in the shear layer cavitation regime, where C_D decreases with an increase in σ_c in the 3-D case. The C_D values measured for 3-D flow are higher than those for the 2-D flow, with the difference of about 17% in minimal C_D value for the case with $\delta/h = 1.9$. The decrease in C_D for a constant σ_c is more rapid in the 3-D case, with the difference between the cases with smallest and largest δ/h of about 0.14 ($\approx$ 17% difference in minimal C_D).

The dependence of hydrodynamic parameters C_L, C_D and L/D on σ_c for constant $Fr = 29.6$, $\sigma_c = 0.87$ and $\delta/h = 3.2$ is shown in Fig 2.21a. The lift force is calculated as the integral of the wall pressure distribution upstream of the fence. Due to a slight scatter in the pressure data in the zone far upstream of the fence only the lift generated in the zone up to $25h$ upstream of the fence was calculated, i.e. $L = \int_{-25h}^{0} p(x)dx$. In Barbaca et al. (2017b) it was shown that the lift contribution from this area is around 80% of the total lift generated by the fence/wall system. It can be seen that C_L increases linearly with a decrease in σ_c, up to a maximum value reached for $\sigma_c = \sigma_{min}$. The lift increase is slightly larger when the flow transitions from shear layer to fully developed cavity regime, as expected from the upstream wall pressure distribution analysis provided above. The difference in C_L across the range of achievable σ_c values is about 45%. The increase in C_L, coupled with the decrease in C_D, contributes to an increase in the fence/wall system hydrodynamic efficiency, with an increase in lift-to-drag ratio, L/D, of about 85% across the range of achieved σ_c values.

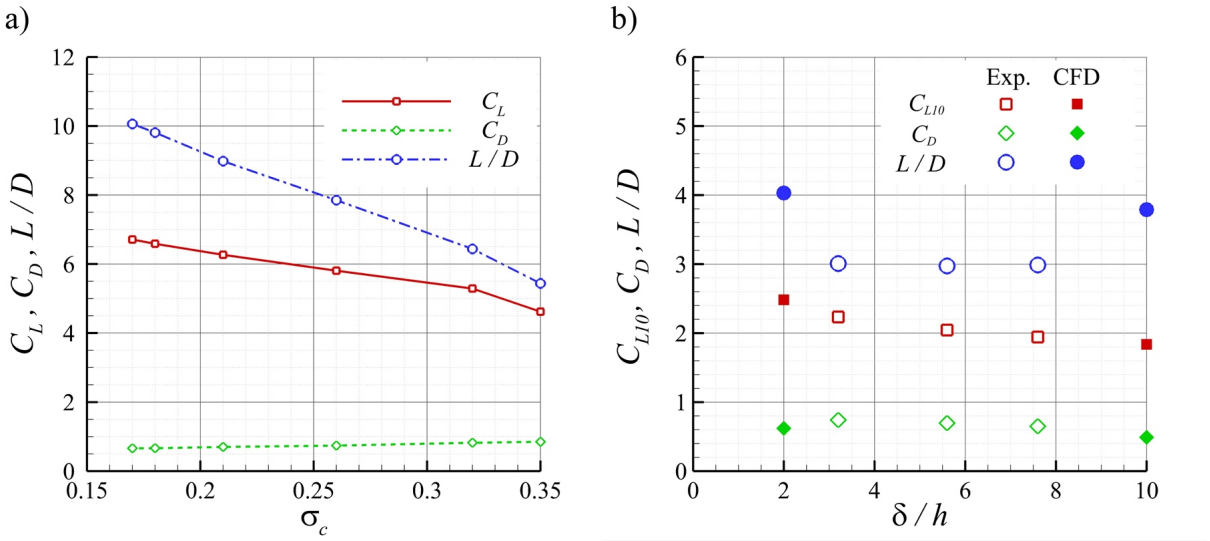

Figure 2.21: a) Dependence of hydrodynamic parameters C_L, C_D and L/D on σ_c for constant $Fr = 29.6$, $\sigma_v = 0.87$ and $\delta/h = 3.2$. b) Dependence of hydrodynamic parameters C_L, C_D and L/D on δ/h for constant $\sigma_c = 0.21$, $Fr = 29.6$ and $\sigma_v = 0.87$. Data points from the numerical study (Barbaca et al., 2017b) are provided for comparison.

In Fig 2.21b the change in C_L, C_D and L/D with the variation in δ/h is shown. Due to the increased influence of the boundary layer thickening system on the upstream wall pressure distribution (increase in C_P of about 0.01 at the most upstream position due to additional water volume injected through thickening system), to provide comparable lift values for all δ/h cases, the region used for pressure integration is reduced to $10h$ upstream of the fence (with the lift coefficient now defined as C_{L10} and lift calculated as $L_{10} = \int_{-10h}^{0} p(x)dx$). In Barbaca et al. (2017b) it was found that this zone contributes about 60% of the total lift. It can be seen that, both C_{L10} and C_D decrease approximately linearly following an increase in δ/h. The relative rate of decrease is similar for both coefficients, with a 12% decrease in C_L and C_D between the extreme cases. As C_{L10} and C_D change at the same rate, L/D remains approximately constant across the range of examined δ/h values. Data points from CFD analysis for $\delta/h = 2$ and 10, and otherwise similar flow conditions, are provided for comparison. It can be seen that the CFD data for C_{L10} follows the trend obtained from the experiment. The under-prediction in C_D (shown in Fig. 2.19a) values from the computation compared to the experiment gives the differing result in L/D between the two.

2.4 Conclusions

Ventilated and natural cavity flow over a fixed height 2-D wall-mounted fence has been investigated experimentally in a cavitation tunnel. Cavity topology, upstream wall pressure distribution and hydrodynamic forces have been examined with the respect to varying fence immersion in the oncoming wall boundary layer, flux of injected air and free-

stream conditions (i.e. speed and pressure). Two distinct regions are evident along the length of a fully developed cavity: transparent air/vapour filled zone closer to the fence and an opaque, re-entrant jet flow affected, closure region. Re-entrant jet driven shedding is the primary mode of gas entrainment into the main flow, with turbulent break up along the cavity/water interface contributing to a lesser extent. A similar cavity topology was observed for ventilated and natural cavities present for the same flow conditions, with the only difference observed in the wake. While the entrained air is conveyed downstream of the cavity as a dense bubbly mixture for the ventilated case, the vaporous structures shed from a natural cavity condense in the vicinity of closure with only a population of incondensible micro-bubbles remaining in the far wake.

Three flow regimes were identified following a decrease in σ_c value: (I) shear layer cavitation, (II) fully developed cavity and (III) blocked flow condition when $\sigma_c \to \sigma_{min}$. In ventilated cavity flow a nominally linear dependence of σ_c on C_{Qv} is observed in the fully developed cavity regime. The re-entrant jet intensity (i.e. re-entrant jet length) was found to be independent of σ_c once a fully developed cavity is established. The cavity length exhibits a power law like increase following a decrease in σ_c, up until $\sigma_c \approx \sigma_{min}$ where a vertical asymptote representing 'infinite' cavity growth is present.

It was found that C_{Qv} had to be increased following an increase in Fr to achieve the same σ_c in lower Fr range, but the σ_c on C_{Qv} dependence was independent of Fr for higher Fr values. Dependence of σ_c on C_{Qv} was found to be invariant of σ_v, for σ_v values where no natural cavity was present. A decrease in C_{Qv} value needed to achieve the same σ_c following a decrease in σ_v is observed otherwise, with a smooth transition to naturally cavitating flow (i.e. $C_{Qv} = 0$) as $\sigma_v \to \sigma_c$. The l_c/h on σ_c dependence was found to be independent of Fr and σ_v and the same behaviour was observed for the ventilated and naturally cavitating flow.

With an increase in boundary layer thickness the cavity/water interface becomes increasingly affected by the turbulence embedded in the oncoming wall boundary layer. Due to a less pronounced blockage effect present for higher δ/h values, the curves representing σ_c on C_{Qv} and l_c/h on σ_c dependencies shift towards the lower σ_c zone.

The upstream wall pressure distribution is characterized by a zone of almost constant C_P within one h of the fence followed by a slow decrease in C_P between one h and $5h$ of the fence, eventually exhibiting a power law like reduction with distance in the far field. For a particular set of free-stream conditions, an increase in C_P value following a decrease in σ_c is observed across the whole measured region, but the difference tends to zero when $\sigma_c \to \sigma_{min}$. A decrease in $C_{P_{max}}$ value of about 12% is observed between the cases with lowest and highest δ/h.

For a constant set of free-stream conditions, C_D decreases linearly following a decrease in σ_c, reaching an asymptotic value for $\sigma_c \to \sigma_{min}$. The observed difference across the achievable σ_c range is around 26%. This decrease in C_D, coupled with an increase in

C_L (around 45%), leads to an increase in hydrodynamic efficiency of fence/wall system expressed through the lift-to-drag ratio of about 85%. The drag is found to be independent of Fr and σ_v and a similar C_D on σ_c dependence observed for both ventilated and natural cavity flows. C_D decreases following an increase in δ/h, with a reduction in minimal C_D value of about 12% across the δ/h range examined. C_L decreases at a similar rate, resulting in approximately constant L/D value for all investigated δ/h values.

The experimental results obtained are compared with CFD data from an earlier numerical study (Barbaca et al., 2017b). The simplified numerical model used in CFD study is shown to have clear limitations, however, depending on the parameter of interest, a reasonable agreement between the results has been observed confirming the utility of the simulation method used. A comparison of experimental results for 2-D and 3-D flow (Barbaca et al., 2017a) is made, with the main differences originating from a less pronounced blockage effect present in the 3-D flow. Despite the significant differences observed in the 2-D and 3-D cavity geometries the general trend behaviour across various parameters was found to be quite similar. A more detailed study on the unsteady behaviour of ventilated and natural cavity flow over a wall-mounted fence is planned.

Acknowledgements

The authors wish to acknowledge the assistance of Mr Robert Wrigley and Mr Steven Kent in carrying out the experiments and the support of the Australian Maritime College.

Chapter 3

On the Unsteady Behaviour of Cavity Flow Over a 2-D Wall-Mounted Fence

This chapter is based on the manuscript submitted for publication with *Journal of Fluid Mechanics*. The contributing authors are: L. Barbaca, B.W. Pearce, P.A. Brandner, H. Ganesh and S.L. Ceccio.

Abstract

The topology and unsteady behaviour of ventilated and natural cavity flows over a 2-D wall-mounted fence are investigated for fixed length cavities with varying free-stream velocity using high-speed and still imaging, X-ray densitometry and dynamic surface pressure measurement in two experimental facilities. Cavities in both ventilated and natural flows were found to have a re-entrant jet closure, but not to exhibit large-scale oscillations, yet the irregular small-scale shedding at the cavity closure. Small-scale cavity break-up was associated with a high-frequency broad-band peak in the wall pressure spectra, found to be governed by the overlying turbulent boundary layer characteristics, similar to observations from single-phase flow over a forward-facing step. A low-frequency peak reflecting the oscillations in size of the re-entrant jet region, analogous to 'flapping' motion in single-phase flow, was found to be modulated by gravity effects (i.e. a Froude number dependence). Likewise, a significant change in cavity behaviour was observed as the flow underwent transition analogous to the transition from sub- to super-critical regime in open-channel flow. Differences in wake topology were examined using shadowgraphy and Proper Orthogonal Decomposition, from which it was found that the size and number

of shed structures increased with an increase in free-stream velocity for the ventilated case, while remaining nominally constant in naturally cavitating flow due to condensation of vaporous structures.

3.1 Introduction

Flow over a geometric discontinuity immersed in a turbulent boundary layer (TBL), such as a forward-facing step (FFS), backward-facing step (BFS) or a wall-mounted fence (WMF), will induce flow separation, on either the upstream, downstream or both sides of the discontinuity. The separation and reattachment of the flow will invariably induce some unsteadiness into the flow. These flows have been studied extensively in the single-phase case, as reviewed by Simpson (1989) and more recently by Camussi et al. (2008) and Awasthi et al. (2014). Two main components contributing to the flow unsteady behaviour have been identified as a high-frequency broadband energy peak attributed to organized turbulent structures (Farabee and Casarella, 1986) and a low-frequency oscillation related to the contraction and elongation of the re-attachment zone, also referred to as 'flapping' (Driver et al., 1987). Characterization of the unsteady behaviour through spectral analysis for the particular geometry of interest in the present study at moderate to high Reynolds numbers can be found in Dimaczek et al. (1989). In contrast to the wealth of published material on the unsteadiness related to flow separation from geometric discontinuities in single-phase flow, flows involving cavitation have not received much attention. Iyer and Ceccio (2002) showed that the unsteady flow behaviour in turbulent shear layers is altered by the presence of the shear layer cavitation. This suggests that the formation of a large-scale cavity in a separated flow zone may have a significant effect on the unsteady characteristics of the flow.

Cavitation may occur in a separated flow region as the local pressure approaches vapour pressure. At higher cavitation numbers the cavity will be limited to a number of fragmented bubbly structures within the shear layers and as the cavitation number is reduced these structures will grow and merge into a single bubble. Further reduction in the cavitation number will result in increased size of the gaseous bubble/cavity, which eventually grows beyond the original length of the separated flow region (Franc and Michel, 2004). Cavities of similar appearance and behaviour, termed 'ventilated cavities', can be formed artificially if sufficient gas (typically air) is admitted or injected into the separated flow region (May, 1975; Kunz et al., 1999). Depending on the location of the cavity closure, i.e. if the closure is on the wall of the cavitating body or rather downstream, cavities are classified as either 'partial' or 'super-cavities'. It is the condition of the cavity closure on the wall that is responsible for the emergence of significant unsteadiness in flows featuring partial cavitation. Due to the detrimental effects of unsteady flow on

the performance of hydraulic and marine equipment (such as lift reduction, vibration, noise and erosion) enquiry into the closure physics of partial cavities has been an area of interest in cavitation research lasting for more than a half of century. Despite a large body of published literature on the topic, there are many aspects that are yet to be fully understood.

The closure region of an unsteady partial cavity is found to generally exhibit a re-entrant jet behaviour, which has been identified as a predominant mechanism inducing cavity break-up and unsteady fluctuations. The formation and propagation of shock-waves have also been observed to play a prominent role in cavity dynamics for some geometries (see Reisman et al., 1998; Brandner et al., 2010; Ganesh et al., 2016a). In a seminal study Callenaere et al. (2001) give a comprehensive review of the literature reporting on characterization and modelling of the re-entrant jet and provide a systematic study of the cavitating flow over a diverging step. In their experiments, Callenaere et al. (2001) were able to independently vary the step height, flow confinement and pressure gradient at the cavity closure, providing a global map of different cavitation regimes with respect to the aforementioned parameters. They point out the existence of an adverse pressure gradient in the cavity closure region as a necessary requirement for the formation of re-entrant flow, similar to findings by Gopalan and Katz (2000) and Laberteaux and Ceccio (2001a). Furthermore, they differentiate two regimes of cavitation with the established re-entrant flow based on the re-entrant jet to cavity thickness ratio. In the case of the re-entrant jet being much thinner than the cavity, the classical cloud cavitation instability characterized by the re-entrant jet propagation up to the cavity leading edge and periodic shedding of large-scale bubbly structures is observed. Due to its severity and the large effect it has on the flow, cloud cavitation has been extensively investigated for various geometries (see for example Le et al., 1993; Leroux et al., 2004; de Graaf et al., 2016; Ganesh et al., 2016a). However, it is the second regime, labelled as 'thin non-auto-oscillating cavities with periodic re-entrant jet', that is of more interest for the present study.

In the second regime, the re-entrant jet thickness is relatively large compared to the cavity thickness, promoting interaction between the jet/cavity and the cavity/water interface. The small-scale instability resulting from this interaction induces cavity break-up at many random points, leading to irregular shedding of a large number of small-scale structures. Although, some regular shedding is still evident, the continuous break-up of the re-entrant jet curtails its penetration towards the cavity leading edge, resulting in a much smaller oscillation of the cavity length and a globally quasi-steady appearance. This second regime type behaviour has been observed in many studies, but due to the less severe effect on the flow in comparison with cloud cavitation it has not been a subject of any comprehensive study.

Perhaps the first description of this regime was provided by Furness and Hutton (1975) in their study of the flow through a two-dimensional convergent-divergent nozzle. In the

case of long and thin cavities, they observed an apparently stable cavity with oscillating re-entrant jet confined to the downstream section of the cavity. Since then the phenomenon has been briefly mentioned in a number of publications (see for example Le et al., 1993; Kawanami et al., 1998; Franc, 2001), but only in the works of de Lange et al. (1994) and Pham et al. (1999) more detailed insight has been provided. de Lange et al. (1994) relate the increase in the re-entrant jet to cavity thickness ratio to viscosity effects stopping the jet from reaching the cavity leading edge and causing the formation of a liquid layer inside the cavity. The wave disturbances on top of this layer interact with the disturbances on the cavity outer interface, resulting in the irregular small-scale shedding described above. Pham et al. (1999) investigated the power spectra of fluctuating pressure on a plano-convex hydrofoil. For the incidence less than 2° a stable cavity was observed, with the spectral content of cavity break-up distributed across a broad high-frequency low-energy peak in contrast to a much narrower intense low-frequency peak detected in the cloud cavitation regime. It is also interesting to note that large-scale shedding can be suppressed if the re-entrant jet is redirected away from the cavity interface. This can be done by introducing span-wise pressure gradients resulting in cavity behaviour more similar to the one observed in the non-auto-oscillating regime, as shown by Laberteaux and Ceccio (2001b) for the cases of a swept 2D wedge and a plano-convex hydrofoil.

A closely related flow to the one investigated in the present study is the ventilated cavity flow over a backward-facing step. This flow has been extesively studied in the context of vessel drag reduction with a comprehensive review of the topic provided by Ceccio (2010). The objective in this application is to create a long stable partial cavity with minimal gas loss (i.e. by placing a sloped beach or 'arrestor' in the cavity closure region). However, significant differences in the closure physics have been observed across the range of free-stream speeds examined. In the work of Arndt et al. (2009) and Mäkiharju et al. (2013a) it is observable that the cavities present at high free-stream speeds resemble the topology of the non-auto-oscillating regime (regime II), while for lower free-stream speeds the closure physics are largely dominated by gravity effects resulting in cavity break-up through the wave pinch-off mechanism. Additionally, from studies by Vigneau et al. (2001) and Mäkiharju et al. (2017b) looking at a gas jet injected into liquid cross-flow, a significant difference is seen in the cavity closure topology between the cases with horizontally and vertically injected jets. These observations suggest that gravity may have an important role in the present study. Similarity between the re-entrant jet behaviour and the recirculating flow observed in the case of open channel flow transition from sub- to super-critical regimes via undular jump (Ohtsu et al., 2001) further supports this premise.

Until the recent numerical and experimental studies reported by the authors (Pearce and Brandner, 2014; Barbaca et al., 2017a,b, 2018), cavity flow over a wall-mounted fence has not been reported on in the open literature. To date the mean characteristics and

global behaviour of the cavity flow over a fence immersed in an oncoming wall boundary layer of variable thickness for a range of free-stream conditions has been reported on. From these results it is evident that the flow can be classified within the 'thin cavity' regime. The next step towards a better understanding of this canonical flow with a nominally zero pressure gradient is to analyse unsteady behaviour.

Within the present study the unsteady behaviour of ventilated and natural cavity flows over a 2-D wall-mounted fence is experimentally investigated in two testing facilities. Large-scale experiments are performed in the University of Tasmania water tunnel with a 600 × 600 mm square test section, whilst smaller-scale experiments are performed in the Univeristy of Michigan 9-inch water tunnel with the test section size reduced to a 76.2 × 76.2 mm. These experimental setups are developed to utilize the complimentary capabilities from each facility, with X-ray densitometry measurements from the small-scale experiment and long-period pressure measurements from an array of six dynamic pressure sensors coupled with simultaneous high-speed imaging from the large-scale tests.

The scope of work is to examine the influence of free-stream Reynolds and Froude numbers on the cavity closure dynamics and the mechanisms of gas entrainment into the main flow for a fixed cavity length to fence height ratio. Additionally, a compariosn between ventilated and naturally cavitating flows, for the same range of flow conditions, is made. X-ray densitometry is used to gain insight into the dynamics of void fraction distribution inside the cavity, as well as in the wake. The flow spectral content is analysed using power spectral density (PSD) estimates from the Welch method, while the spatial characterization of the cavity break-up process is obtained using proper orthogonal decomposition (POD).

Within this paper the description of the flow and the governing parameters is given in §3.2.1. The experimental setup across both facilities is described in §3.2.2 and §3.2.3. Section §3.1 describes the general topology for the natural and ventilated cavity flows. In §3.3.2, the effect of change in free-stream Reynolds and Froude numbers on the cavity topology is analysed, while §3.3.3 is devoted to the analysis of the cavity wake from shadowgraphy and POD. In section §3.3.4 advective velocities are analysed using space-time plots. The spectral content of the flow is presented in section §3.3.5 and results from cross-correlation between pressure signals and high-speed imaging are given in §3.3.6. The conclusions are summarized in §3.4.

3.2 Experimental setup

3.2.1 Basic flow description and governing parameters

A schematic of cavity flow over a wall-mounted fence representative of the tests in both facilities is shown in figure 3.1. A fence of height h is immersed in the upstream

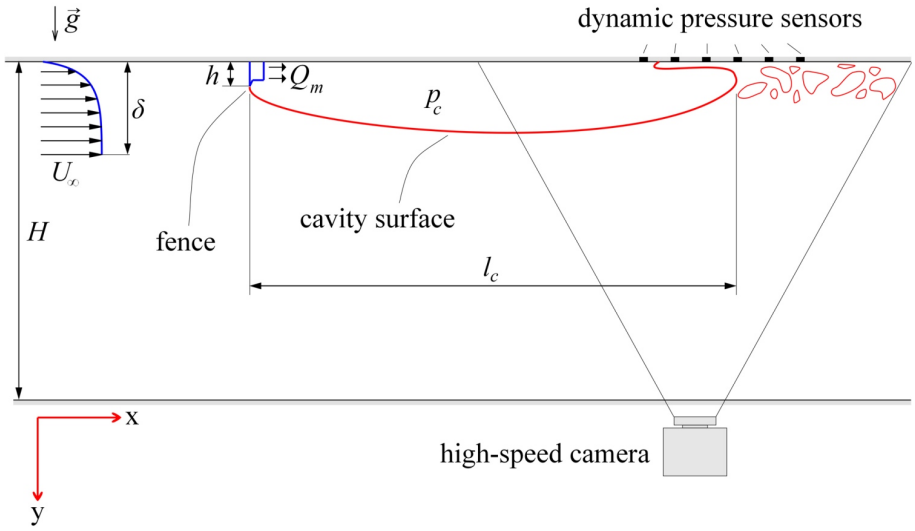

Figure 3.1: Sketch of a wall mounted fence immersed in the oncoming wall boundary layer with a cavity detaching from the sharp fence tip. For a ventilated flow, air is supplied from the downstream face of the fence with mass flow rate Q_m. With no air injection ($Q_m = 0$), a natural cavity may form due to phase change when the pressure inside the cavity, p_c, approaches vapour pressure, p_v. The location along the test-section ceiling centre-line of an array of six dynamic pressure sensors in the cavity closure region is indicated, together with the field of view of simultaneous imaging from a high-speed camera. The origin of the coordinate system is at the fence upstream face/wall junction.

wall boundary layer of thickness δ. The latter is defined as the distance from the wall to where the local mean velocity, U, is 99% of the free-stream velocity U_∞. In the case of a ventilated cavity, air is supplied to the wake region of the resulting bluff body flow through a manifold on the downstream face of the fence with a mass flow rate Q_m (figure 3.1). Alternatively, for $Q_m = 0$, a natural cavity may be formed due to phase change when the pressure in the wake of the fence, $p = p_c$, reduces to vapour pressure, p_v (figure 3.1). Irrespective of the type of formation (i.e. natural or ventilated), the cavity detaches from the sharp fence tip and exhibits a re-entrant jet closure region. The cavity length to fence height ratio, l_c/h, is held constant for all tests conducted in each facility as noted in table 1.

The fundamental dimensionless parameter characterizing cavitating flows is the cavitation number $\sigma_c = (p_\infty - p_c)/0.5\rho U_\infty^2$, where p_∞ is the reference free-stream pressure, p_c is the pressure inside the cavity, ρ is the liquid phase density and U_∞ is the reference free-stream velocity. In the case of ventilated cavities, for constant free-stream conditions (i.e. free-stream pressure, p_∞, and free-stream velocity U_∞), p_c and hence σ_c is determined by the air injection rate. This parameter is presented in non-dimensionalised form as a volumetric flow-rate coefficient, $C_{Qv} = Q_m/\rho_{air} U_\infty S$, where ρ_{air} is the air density at the cavity pressure and S is the fence face area. For natural cavities, with p_v nominally constant for all testing conditions, σ_c is determined solely by free-stream conditions, i.e. by varying p_∞ and/or U_∞.

The flow dependence on the free-stream velocity has been quantified using fence height

Dimension/Parameter	**Symbol**	**Large-scale**	**Small-scale**
Fence height	h (mm)	10	1.33
Nominal cavity length	L (mm)	~ 900	~ 80
Test-section depth	H (mm)	600	76.2
Wall boundary layer (BL) thickness	δ (mm)	15	2
Cavity length to fence height ratio	l_c/h (-)	~ 90	~ 60
Confinement	H/h (-)	60	57
BL thickness to fence height ratio	δ/h (-)	1.5	1.5
Free-stream velocity	U_∞ (m/s)	$2-12$	$6-10$
Reynolds number (fence height based)	$Re_h = \frac{U_\infty h}{\nu}$	$20000-120000$	$8000-13300$
Froude number (fence height based)	$Fr_h = \frac{U_\infty}{\sqrt{gh}}$	$6.4-38.3$	$52.5-87.6$
Froude number (test section depth based)	$Fr_H = \frac{U_\infty}{\sqrt{gH}}$	$0.8-4.9$	$6.9-11.6$
Vapour pressure based cavitation number	$\sigma_v = \frac{p_\infty - p_v}{0.5\rho U_\infty^2}$	1	1.2
Cavitation number	$\sigma_c = \frac{p_\infty - p_c}{0.5\rho U_\infty^2}$	~ 0.12	Not measured
Volumetric flow-rate coefficient	$C_{Qv} = \frac{Q_m}{\rho_{air} U_\infty S}$	$0-0.4$	Not measured

Table 3.1: List of main dimensions and non-dimensional parameters with their respective values for the large- and small-scale experiments.

based Reynolds ($Re_h = U_\infty h/\nu$, where ν is the kinematic viscosity of the water) and Froude numbers ($Fr_h = U_\infty/\sqrt{gh}$, where g is the gravitational acceleration). A Froude number based on the test section depth, $Fr_H = U_\infty/\sqrt{gH}$, is also defined to characterize the flow with consideration to finite depth effects. Several other dimensioneless parameters are held constant to ensure sufficient flow similarity for comparison of data between two facilities. These include, a vapour pressure based cavitation number (for the ventilated case), $\sigma_v = (p_\infty - p_v)/0.5\rho U_\infty^2$, the oncoming wall boundary layer thickness to fence height ratio, δ/h, and the blockage ratio, H/h, where H is the test section depth. For the characterization of unsteady behaviour of the flow a fence height based Strouhal number is used, $St_h = fh/U_\infty$, where f is the frequency of the unsteady phenomenon of interest. All spatial parameters are presented non-dimensionalised by the fence height. A list of main physical dimensions and flow parameters are listed for both facilities in table 3.1.

3.2.2 Large-scale experimental setup

The large-scale experiments were performed in the University of Tasmania variable pressure water tunnel. The tunnel design incorporates a large tank downstream of the

test section for bubble coalescence and separation (Brandner et al., 2007, 2015). This feature, combined with the auxiliary systems for rapid degassing and continuous evacuation of large quantities of incondensable gas, enables efficient long-period conduct of tests involving ventilation (i.e. injection and continuous removal of large quantities of air). The tunnel test section measures 0.6×0.6 m square at the entrance, by 2.6 m long. The test section ceiling is horizontal with the floor sloping 20 mm over the length to nominally maintain constant speed and a zero stream-wise pressure gradient. The operating velocity and pressure are controlled independently, with ranges from 2 to 12 m/s and 4 to 400 kPa absolute respectively. The tunnel volume is 365 m^3 and is filled with demineralised water. Optical access is provided through acrylic windows on each side of the test section.

The test section absolute pressure is measured, depending on the value, from high or low range Siemens Sitransp absolute pressure transducers models 7MF4333-1FA02-2AB1 and 7MF4333-1GA02-2AB1 with estimated precisions of 0.13 and 0.48 kPa respectively. The test section velocity is measured from the calibrated contraction differential pressure. Depending on the value, either high or low range Siemens Sitransp differential pressure transducers models 7MF4333-1DA02-2AB1-Z and 7MF4333-1FA02-2AB1-Z are used, with estimated precisions of 0.007 and 0.018 m/s respectively. The air mass flow rate is controlled and measured using an Alicat Scientific model MCR-500-SLPM-D mass flow meter with a flow rate range of 0-500 SLPM (Standard litres per minute) and estimated precision of 3 SLPM. A system based on a custom built 30 port sequencer utilizing Burkert flipper solenoid valves controlled from a data acquisition system is used for the cavitation number measurement. The system allows the use of a single pressure transducer (Validyne model DP15TL, estimated precision of 0.2 kPa) for all the measurements, thus eliminating the need to apply corrections arising from transducer zero and span error (for a more detailed description see Barbaca et al., 2017a, 2018). The dissolved gas content of the water is measured using an Endress+Hauser OxyMax WCOS 41 membrane sensor.

For the present study, the experimental setup used for the global characterization of the mean behaviour of natural and ventilated cavity flow over a 2-D wall-mounted fence (i.e. nominally spanning the whole test section width) described by Barbaca et al. (2018), is modified to enable unsteady measurements. The fence model incorporating an internal air supply channel is machined from a stainless steel bar, with a manifold for air distribution attached to the downstream face (figure 3.2a). The fence is 599 mm wide $\times$ 10 mm high, with a sharp tip machined on the front face to ensure a stable cavity detachment. The resulting blockage ratio is $H/h = 60$. The shape of the rear part of the fence, including the attached manifold, does not have an influence on the flow as it is located completely within the cavity. Air is supplied through the fore-body of the fence to the manifold, from which it is distributed into the wake of the fence through $39 \times \phi 2$ mm equi-spaced stream-wise outlets (figure 3.2a). The fence is attached to a 149×379 mm inter-changeable rectangular plate fitted within a test section ceiling opening, and

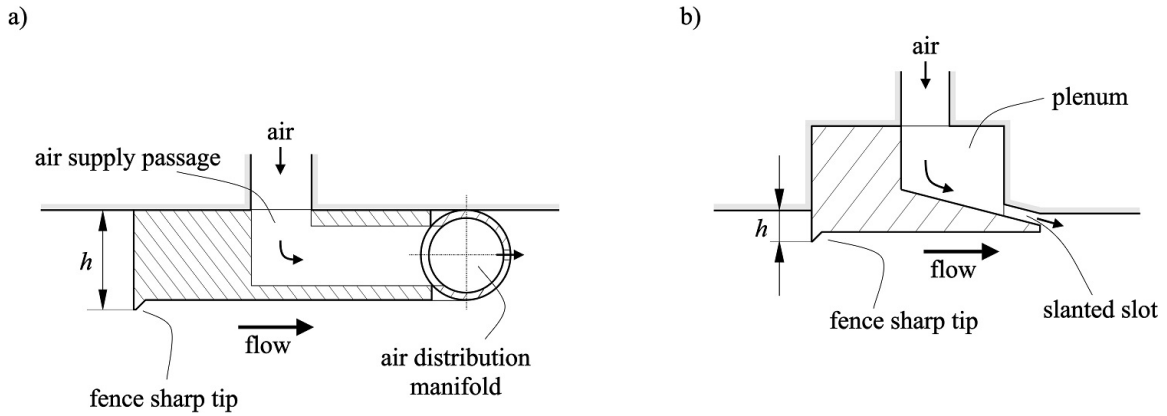

Figure 3.2: An illustration of the fence model cross-section at the test section centreline for: a) large-scale experiment and b) small-scale experiment. In a), the air is injected into the wake of the fence via an internal channel and distribution manifold, with 39 $\times\phi 2$ mm equi-spaced outlets. In b), the injection is via a plenum and a slanted slot between the fence and the test-section recess walls. Both fences are machined with a sharp tip on the front face to ensure a stable cavity detachment. Please note that these illustrations are not drawn to scale.

is located 230 mm from the test section entrance. The oncoming wall boundary layer thickness at this stream-wise position is 15 mm (Belle et al., 2016), giving the boundary layer thickness to fence height ratio of $\delta/h = 1.5$. The air is supplied to the fence through a hollow plug inserted into the rectangular plate, to which the compressed air is distributed via a flexible tube.

An array of six flush-mounted 8.1 mm diameter FUTEK PFT510 dynamic pressure sensors installed within the stainless steel test-section ceiling window was used for the measurements of unsteady pressure within the cavity closure region. The most upstream sensor was located 730 mm downstream of the fence tip, with each subsequent sensor positioned 60 mm further downstream along the test-section horizontal centre-line. The sensor range is 15 bar absolute, with the rated output of $1 - 2$ mV/V (estimated output uncertainty of 0.8%) and the sensor natural frequency of 6 kHz. A 5V excitation and signal amplification is provided through an Entran MSC6 signal conditioning box, with the data acquired simultaneously using a National Instruments PXIe-4497 card.

Forward-lit high-speed imaging was acquired simultaneously with the pressure measurements using a Photron FASTCAM SA5 high-speed camera with a Nikon Nikkor f/2.8D 24mm lens, controlled via LaVision DaVis 8.4 software. The simultaneous measurements were triggered using a BNC Model 575 delay/pulse generator and were recorded at 1 kHz for 10 s at the full image resolution (1024 $\times$ 1024 px) and at 1 kHz for 100 s at reduced resolution (64 $\times$ 8 px). Additionally, longer data series from the pressure sensors alone were recorded at 1 kHz for 1000 s. A standalone series of back-lit high-speed imaging was recorded utilizing a clear acrylic ceiling window insert with the same recording parameters as in the forward-lit case. High-resolution front- and back-lit still images were captured using a Nikon D810E camera with either a Nikon Nikkor f/2.8D 24mm or Nikon

AF-S Micro Nikkor f/2.8G 105 mm lens. The back-lit images were captured with the camera positioned both above and below the test-section. For the still imaging the exposure was controlled using three simultaneously triggered stroboscopic lights (DRELLO 3018/LE4040, DRELLO 3020/LE4040 and DRELLO 1018/HL4037).

Natural and ventilated cavities of nominally fixed length, $l_c/h \approx 90$, were investigated for a range of free-stream speeds. For the ventilated case, all tests were performed at a constant $\sigma_v = 1$. For a particular flow condition the cavity length was set to the desired length by varying the ventilation rate Q_m. Likewise, the cavity length for natural cavities, at a particular free-stream speed, was set by adjusting p_∞. Tests were conducted over the full operational range, $2 \leq U_\infty \leq 12$ m/s, resulting in Reynolds and Froude numbers varying between $0.2 \times 10^5 \leq Re_h \leq 1.2 \times 10^5$ and $6.4 \leq Fr \leq 38.3$, respectively. The test section depth based Froude number was in the range $0.8 \leq Fr_H \leq 4.9$. This resulted in super-critical flow conditions, i.e. $Fr_H > 1$, in all cases apart for the lowest free-stream speed where a transition to sub-critical flow was present and this is reflected in a change in closure behaviour as discussed in section §3.3.2. All tests were conducted with a dissolved O_2 content between 2 and 6 ppm.

3.2.3 Small-scale experiments

The small-scale experiments were performed at the University of Michigan 9-Inch Water Tunnel. The tunnel has a 6:1 round contraction leading into the test section with a diameter of 230 mm (9 inches). The test section then transitions to a square cross-section that is 210 × 210 mm with chamfered corners. The flow velocity in the tunnel test section can be varied from $U_\infty = 0$ to 18 m/s and static pressure p_∞ from near vacuum to 200 kPa. A de-aeration system enables the control of the dissolved air content. In the present experiments, the test section was further reduced in area to a conduit of 76.2 × 76.2 mm cross-section. This was done to reduce the baseline X-ray attenuation produced by the non-cavitating flow. Optical access is provided through acrylic windows on each side of the test section.

To enable flow similarity between the two facilities it was decided to have the same δ/h. This resulted in a differing model configuration due to the small scale of the fence ($h = 1.33$ mm) in the small-scale test. The fence model spanning the full test section width was machined out of a single 6 mm brass bar and is mounted inside a recess in the acrylic ceiling window (figure 3.2b). The fence is 75.2 mm wide and the in-flow height $h = 1.33$ mm results in a blockage ratio $H/h \approx 57.3$. A sharp tip is machined on the fence front tip to ensure a stable cavity detachment. A gap between the fence body and the recess walls serves as a plenum for air injection which is distributed into the fence wake through a full-span slanted slot between the angled downstream face of the fence and the ceiling window. The fence tip is located 115.6 mm downstream of the entrance

to reduced test section. The oncoming wall boundary layer thickness at this position is ≈ 2 mm, resulting in $\delta/h \approx 1.5$.

The static pressure is measured at the entrance of the reduced test section using an Omega Engineering PX-20-030A5V, 0 to 208 kPa, absolute pressure transducer with stated accuracy of 0.08 % of full scale. The pressure difference between the test section inlet and upstream of the primary contraction was measured using an Omega Engineering PX409030DWU10V, 0 to 208 kPa, differential pressure transducer with an accuracy of 0.08 % of full scale. Based on the measurement of differential pressure and the area ratios, the velocity at the entrance into the reduced test section was calculated. The air mass flow rate was controlled using an Omega Engineering FMA-5520 mass flow meter with a flow rate range of 0-10 SLPM and a manufacturer specified accuracy of $\pm 1.5\%$. The dissolved oxygen content was measured using an Orion Start A113 dissolve oxygen meter to a precision of $\pm 2\%$.

A cinematographic X-ray densitometry system was used to measure the spatial distribution of the void fraction for the ventilated and natural cavity flows over the fence. A complete description of the X-ray setup and data reduction process is provided by Mäkiharju et al. (2013b), Mäkiharju et al. (2013c) and Ganesh et al. (2016a) and for brevity it will not be presented here. The X-ray images were acquired at a sample rate of 1 kHz for ≈ 0.8 s. Forward-lit high-speed video imaging was recorded using a Vision Research Phantom v730 high-speed video camera with a Nikon f/2.8 55 mm lens. The videos were recorded at a sample rate of 4 kHz for 4 s.

Ventilated cavities of nominally fixed length, $l_c/h \approx 60$, were investigated for a range of free-stream speeds and a constant $\sigma_v = 1.2$, with the set cavity length for a particular condition achieved by varying Q_m. Test were conducted for the free-stream speeds in the range $6 \leq U_\infty \leq 10$ m/s, resulting in Reynolds and Froude numbers varying between $0.8 \times 10^4 \leq Re_h \leq 1.33 \times 10^4$ and $52.5 \leq Fr \leq 87.6$, respectively. The test section depth based Froude number was in the range $6.9 \leq Fr_H \leq 11.6$, resulting in super-critical flow conditions, i.e. $Fr_H > 1$, in all cases. A natural cavity of the same length (i.e. $l_c/h \approx 60$) was investigated for a constant free-stream speed, $U_\infty = 10$ m/s ($Re_h = 1.33 \times 10^4$, $Fr_h = 87.6$) with the length achieved by altering test section static pressure. All tests were conducted with a dissolved O_2 content between 2 and 6 ppm.

3.3 Results and Discussion

3.3.1 General cavity topology

A typical topology of a fully developed cavity ($l_c/h \approx 90$) observed in the large-scale test is shown in figure 3.3 for both ventilated and natural cavity flows for the same free-stream $Re_h = 1 \times 10^5$. In both cases, the cavity has a stable detachment from the fence tip

and two distinct regions are evident along the cavity length. Apart from the differences in the closure/wake region, the appearance of the cavities is largely similar, as previously noted for axisymmetric ventilated and natural cavities in the works of May (1975) and Kunz et al. (1999).

The region closer to the fence is air/vapour filled with a relatively sharp cavity/water interface and a transparent appearance. A series of randomly appearing and disappearing stream-wise streaks travelling in the span-wise direction can be observed immediately downstream of the cavity detachment line, as seen in figure 3.3c. These streaks, along with the small-scale stream-wise waves observable on the cavity surface (figure 3.3d), can be attributed to turbulence contained within the oncoming wall boundary layer in which the fence is fully immersed.

The rear or closure of the cavity is dominated by re-entrant jet flow and is observed as an opaque region. From the observation that the re-entrant jet does not propagate all the way upstream to the fence (consequently breaking-off a majority of the cavity), but is contained to the closure region only, the flow can be classified within the 'thin cavities' regime as distinguished by Callenaere et al. (2001). The opaque cavity surface appearance is a result of interaction between a rather thick re-entrant flow region and the cavity/water interface, inducing irregular/chaotic cavity surface break-up. The surface break-up triggers the shedding of small-scale bubbly structures into the cavity wake with consequent entrainment into the main flow. This small-scale pinch-off at the cavity closure results in a relatively small variation in the cavity length and the cavity can be considered as non-auto-oscillating. The re-entrant jet upstream or inner boundary is observed as a relatively sharp transition from opaque to transparent appearance of the cavity surface. The inner boundary exhibits irregular low-frequency oscillations of a larger-scale than those at the closure, resulting in a contraction and extension of the re-entrant flow zone. However, this oscillation does not seem to have a significant effect on the shedding behaviour. A forward-lit high-speed video of the oscillations in the cavity closure region is given in supplementary data (vid 3.1).

To provide further insight into the re-entrant jet topology, back-lit imaging (i.e. shadowgraphy) with the camera positioned below (figure 3.4b) and above (figure 3.4c) the test section is used. Topologically, the closure region of the cavity represents a recirculation bubble. As the main flow re-attaches to the wall downstream of the cavity it gives rise to a stagnation point, which causes the flow to split into two branches. The branch directed upstream, labelled as 're-entrant jet', carries the liquid into the cavity causing formation of a layer consisting of a large number of small bubbly structures (figure 3.4e). As the layer propagates into the cavity it is slowed by viscous effects (as discussed by de Lange et al., 1994) and due to gravity it eventually becomes detached from the wall. This region, where the bubbly layer is in contact with the wall may be termed an 'attached re-entrant jet', as illustrated in a cavity side-view schematic presented in figure 3.4a. The detachment

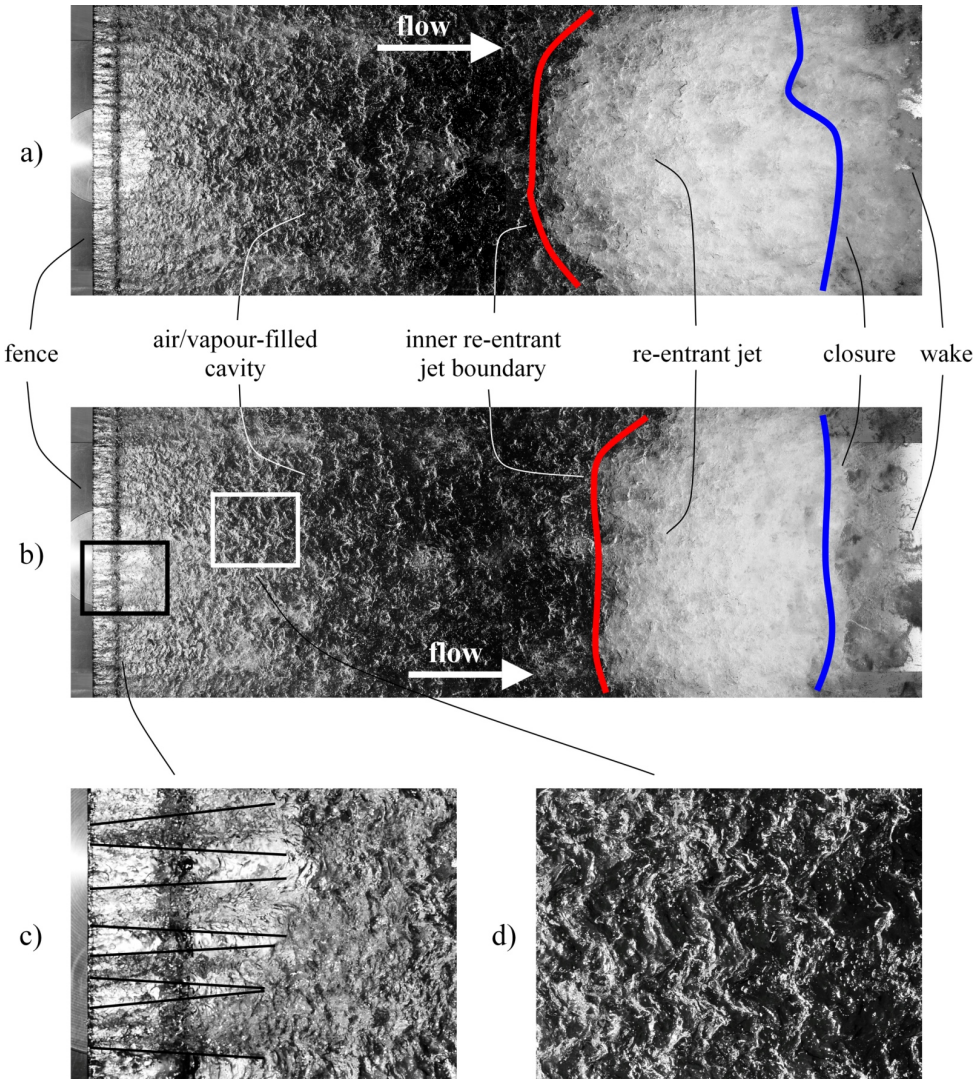

Figure 3.3: Typical topologies of ventilated (a) and natural (b) cavities in the large-scale experiments for the same $Re_h = 1 \times 10^5$. Both cavities have generally similar topology with an air/vapour filled region present closer to the fence and a re-entrant jet type closure, which can be classified within 'thin cavity' regime as specified by Callenaere et al. (2001). The observable differences between the ventilated and naturally cavitating flow topologies are a slightly shorter re-entrant jet region and a decrease in concentration of gaseous or vaporous phase in the wake due to condensation for natural cavitation. An enlarged view of the stream-wise streaks (c) and span-wise waves (d) stemming from the turbulence embedded in the overlaying boundary layer is provided. (large-scale experiment)

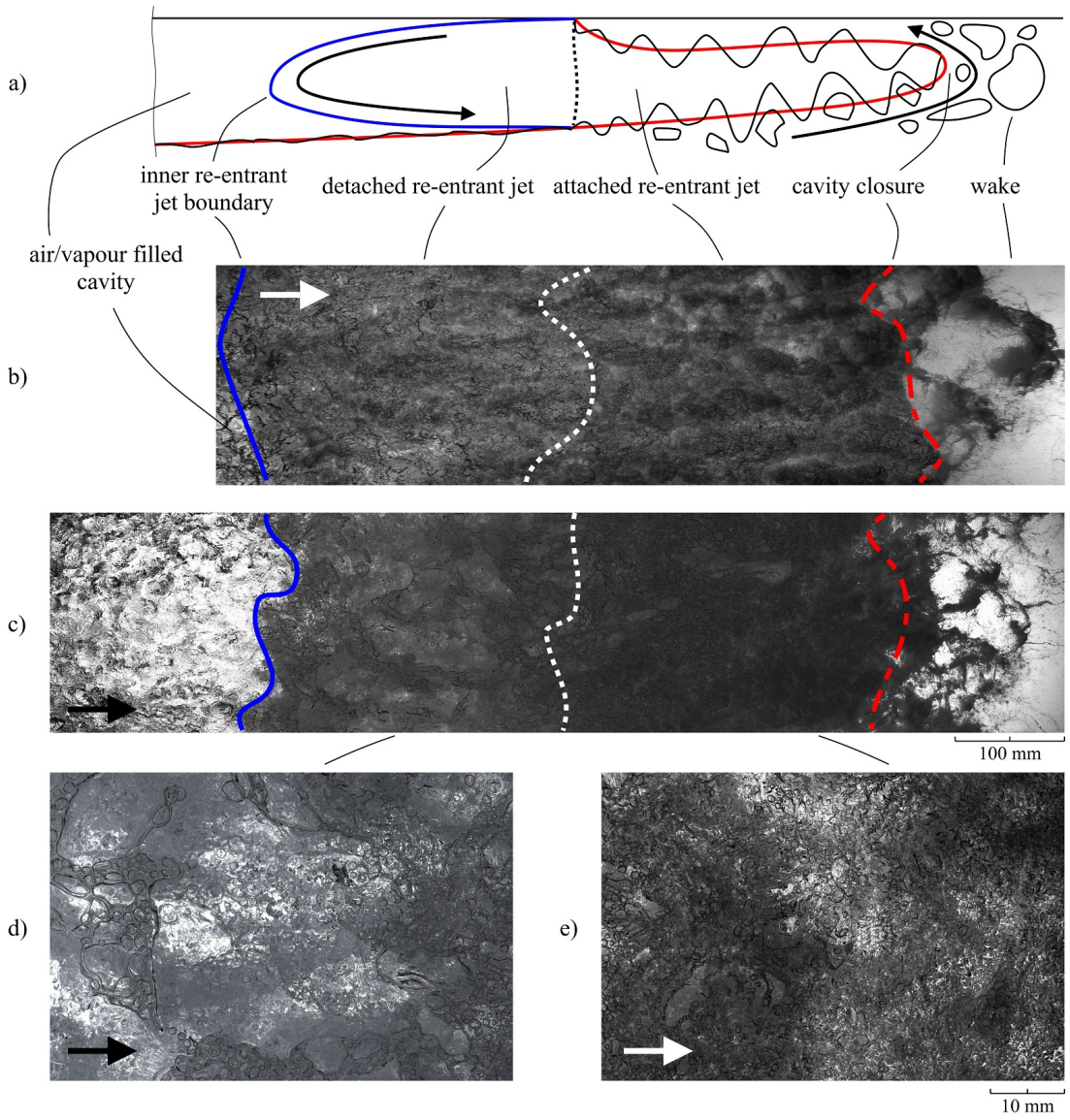

Figure 3.4: Illustration of the re-entrant jet from the ventilated flow, as a side-view schematic (a) and back-lit (shadowgraphy) images with the camera positioned below (b) and above (c) the test section. The images are from natural cavity flow for $Re_h = 1 \times 10^5$. A more detailed view of 'detached' (d) and 'attached re-entrant jet' (e) structure is provided. (large-scale experiment)

process is gradual and it includes the formation of liquid ligaments surrounding various scales of bubbles (figure 3.4d) between what may be termed a 'detached re-entrant jet' (figure 3.4a) and the wall. After detachment, the layer continues to propagate upstream, but as it falls through the cavity the flow on the cavity surface forces the layer to change direction. Eventually, the layer impinges on the cavity surface, causing the formation of small disturbances. As these disturbances are conveyed downstream they are amplified through the interaction with a disturbed/chaotic flow within the cavity, leading to the surface break-up (figure 3.4b) followed by irregular/chaotic shedding of bubbly structures.

Apart from a slightly shorter re-entrant jet length observed in a naturally cavitating flow (figure 3.4), the only obvious difference between the flows can be observed in the wake region. The wake of a ventilated cavity in the vicinity of the closure consists of a dense mixture of shed structures of variable scale. As the larger clouds are conveyed downstream they are progressively broken up in the turbulent main flow, eventually resulting in a dense layer of much finer bubbly structures along the downstream wall. In the case of a natural cavity the vaporous structures condense within a short distance from the closure and only a population of micro-bubbles containing incondensable gas remains in the far wake (Yu and Ceccio, 1997; Lee et al., 2016; Russell et al., 2016).

The break-up and condensation of bubbly structures is characterized by a series of complex physics processes which are illustrated using a sequence of extracted frames from high-speed imaging (recorded at 50 kHz) shown in figure 3.5. A large-scale bubbly cloud is broken up into a number of smaller-scale structures due to flow turbulence (b). These smaller-scale structures are then more susceptible to condensation and collapse. As a bubbly structure shrinks (c) and eventually completely collapses a shock-wave is emitted (d), followed by a bubble rebound (e). The collapse process may be complete after a single rebound, or the sequence may repeat itself several times. After the process is finished, only a population of incondensable micro-bubbles remains. This process is largely similar to the collapse of a single bubble near a solid wall (Lauterborn and Bolle, 1975). The emitted shock-wave front influences the nearby structures (f) by accelerating their collapse and inducing emission of more shock-waves (g), resulting in almost instantaneous collapse of numerous small-scale structures. However, in contrast to the well known phenomenon of bubbly shock-wave propagation inducing a large-scale cavity collapse (Reisman et al., 1998; de Graaf et al., 2016; Ganesh et al., 2016a), the observed shock-waves dissipate as soon as they reach a larger-scale (high vapour volume fraction) structure (h). A possible explanation for this discrepancy may be attributed to the role of the adverse pressure gradient in the cavity closure region. Flows strongly affected by bubbly shock-wave propagation generally have a strong adverse pressure gradient in the cavity closure region, whilst the present flow has a nominally zero pressure gradient. The existence of an adverse pressure gradient (which is favourable for upstream shock-wave propagation) may amplify the shock-wave energy enabling it to penetrate and induce collapse of a much

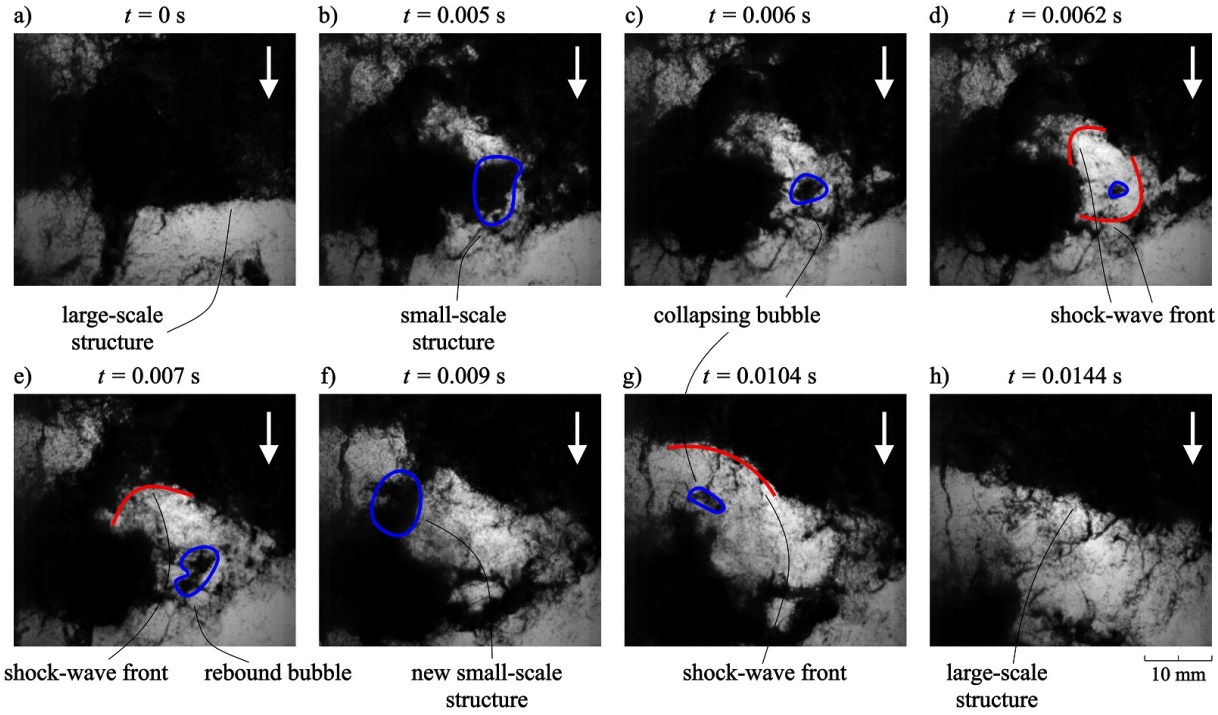

Figure 3.5: A sequence of extracted frames from high-speed imaging depicting break-up and condensation of a bubbly structure in the natural cavity wake. A large-scale structure is broken into smaller scale structures due to turbulent flow (a). A small-scale structure (b) shrinks (c), collapses and emits a shock-wave (d) and rebounds (e). A nearby small-scale structure is influenced by shock-wave front (f) which triggers its collapse and a shock-wave generation (g). The shock-waves dissipate as they reach the next large-scale structure (h). The video was recorded at 50 kHz. (large-scale experiment)

higher vapour volume fraction region, in comparison with a relatively weak non-amplified shock-wave in a zero pressure gradient flow. A high-speed video containing the sequence described in figure 3.5 is given in supplementary data (vid 3.2).

In figure 3.6 extracted frames from high-speed and X-ray imaging, along with the root-mean-square deviation (RMSD) of the X-ray sequence, are shown for the ventilated (a) and natural (b) cavity flows from the small-scale test for $l_c/h \approx 60$ and $Re_h = 1.33 \times 10^4$. Note that the scale in X-ray images is exaggerated (times two) in the vertical direction. In comparison with the flow observed in the large-scale facility, the small-scale flow is observed to be more three-dimensional in nature. This difference is manifested through a more tapered shape of the cavity closure, but more significantly through a span-wise component added to the dynamics of the re-entrant flow (supplementary video 3.3). This oblique propagation of the re-entrant jet may be due to the influence of side-wall boundary layers and/or an unstable corner flow that develops through the secondary test-section contraction. As the jets from both sides meet, a recirculation zone is formed in the horizontal plane on each side of a dividing streamline, the position of which oscillates along the cavity span. Furthermore, the cavity length for the small-scale investigation was shorter ($l_c/h = 60$ rather than 90) due to differing conditions of the small-scale tunnel giving blocked flow (i.e. unstable cavity growth beyond the test-section outlet)

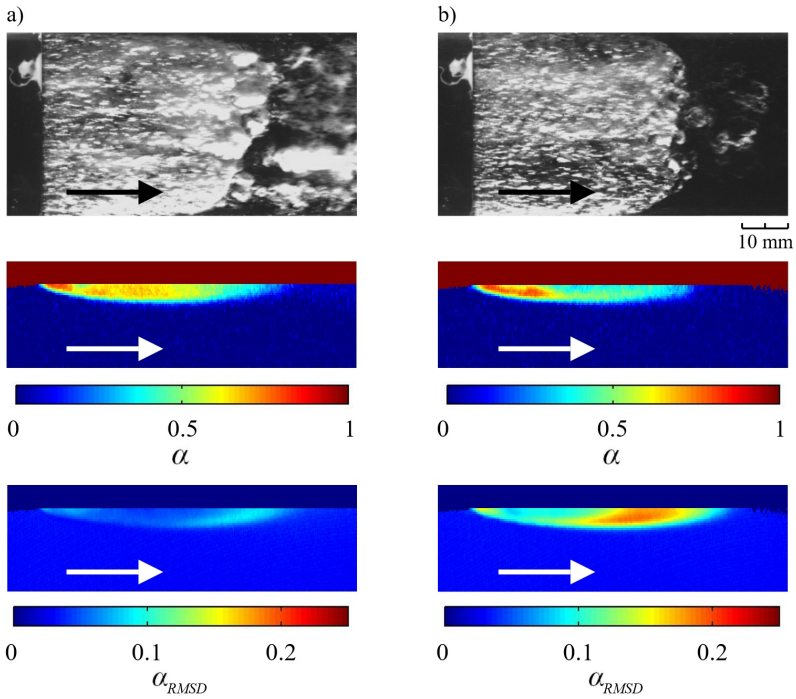

Figure 3.6: Topologies of ventilated (a) and natural (b) cavity flow from the small-scale experiment for a fixed $l_c/h \approx 60$ and $Re_h = 1.33 \times 10^4$ shown as instantaneous snap-shots from high-speed video and X-ray imaging. Additionally, the root-mean-square deviation (RMSD) of the void fraction (α) from the X-ray sequences is presented for both cases. Note that the scale in the X-ray images is shown exaggerated (times two) in the vertical direction and that X-ray and visible light instantaneous snap-shots are not of same instant in time. (small-scale experiment)

which occurred for lesser cavity lengths. Nevertheless, the shedding dynamics observed in the small-scale experiment largely resembled that described for the large-scale test and the cavity could also be classified within the 'thin-cavity' regime. Both ventilated and natural cavities also showed a largely similar behaviour, in line with the observations from the large-scale test.

The objective of the small-scale experiments is to acquire void fraction (α) measurements from cinematographic X-ray imaging. As the resulting α measurement gives a void fraction value that represents an average across the full test-section span, the three-dimensionality of re-entrant flow will have an effect on the α distribution. From the instantaneous X-ray snapshots (figure 3.6) a difference in the mean void fraction distribution can be observed between the ventilated and natural cases. While the upstream part of the cavity has a similar maximum void fraction value in both cases, a more significant difference can be seen in the closure. Firstly, the mean α value is noticeably lower in the naturally cavitating flow across the whole re-entrant jet affected region and secondly, the re-entrant jet itself has a much higher liquid content when compared with a seemingly more bubbly jet present for the ventilated flow. From the plots of void fraction RMSD it is observable that the void fraction distribution undergoes much more pronounced oscillations (approximately a 100 % increase in RMSD value) for natural cavitation. This can be linked to the more violent nature, i.e. vapour condensation and shock-wave occurrence,

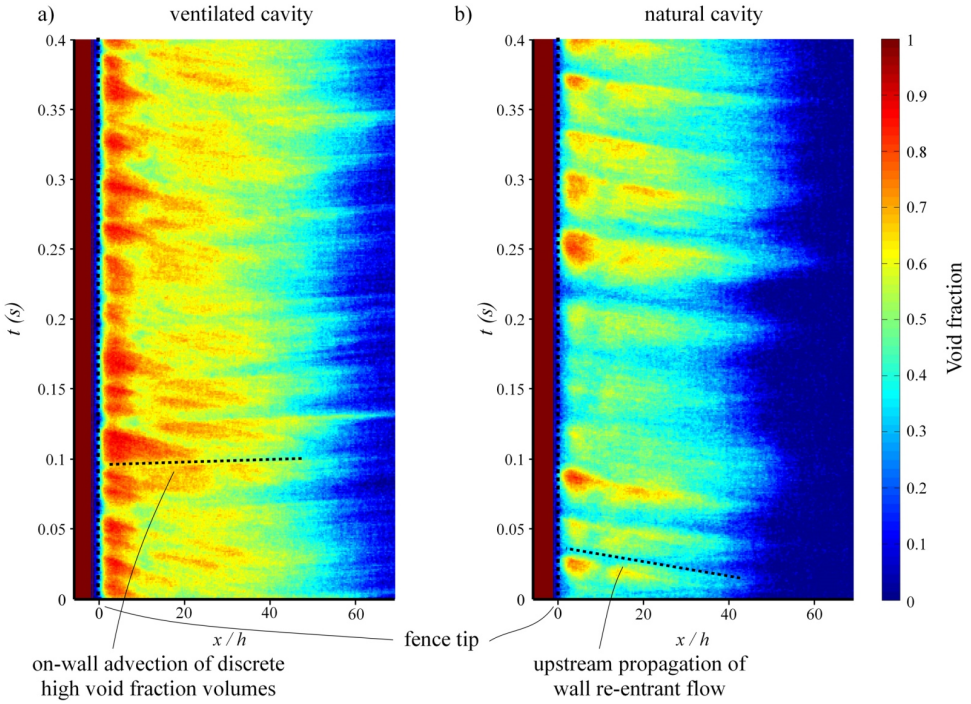

Figure 3.7: Space-time plots of void fraction distribution for ventilated (a) and natural (b) cavity flow from the X-ray imaging in the small-scale facility for $Re_h = 1.33 \times 10^4$. The data is taken from a pixel line adjacent to the test section ceiling for 0.4 seconds. The upward sloping line in (a) indicates the downstream propagation of discrete high void-fraction volumes, while the downward sloping line in (b) indicates the upstream propagation of re-entrant flow. (small-scale experiment)

of the cavity break-up in the naturally cavitating flow. This behaviour shows striking similarity in suppressed fluctuations to that observed by Mäkiharju et al. (2017a) in their study of the effect of non-condensible gas injection on the dynamics of partial cavity flow over a two-dimensional wedge.

A discussion on the void fraction oscillations can be extended using the space-time plots given in figure 3.7. The plots are obtained from the void fraction of a one-pixel stream-wise line adjacent to the wall for a time of 0.4 seconds. Space-time plots confirm that the position of cavity closure does not vary significantly in time, as concluded above from analysis of still images. In the ventilated case, a rather continuous void fraction value can be observed within the cavity at a particular distance from the fence tip, while in the natural case α variation is more pronounced (thus the greater RMSD value). As the re-entrant jet affected region has lower α values than the cavity upstream, jet upstream propagation can be seen as left to right downward sloping lines in the space-time plots. This re-entrant flow is more apparent in the natural case than the ventilated case. The jet itself always has $\alpha > 0.25$, i.e. it is never a pure liquid jet. Similar lines can be observed for the ventilated case, but due to a higher re-entrant jet α value they are less discernible. Additionally, for ventilated flow a series of upward sloping lines can be distinguished, depicting downstream advection of on-wall discrete high-void fraction volumes. A large discrepancy between the natural and ventilated cases can be seen in the wake void fraction.

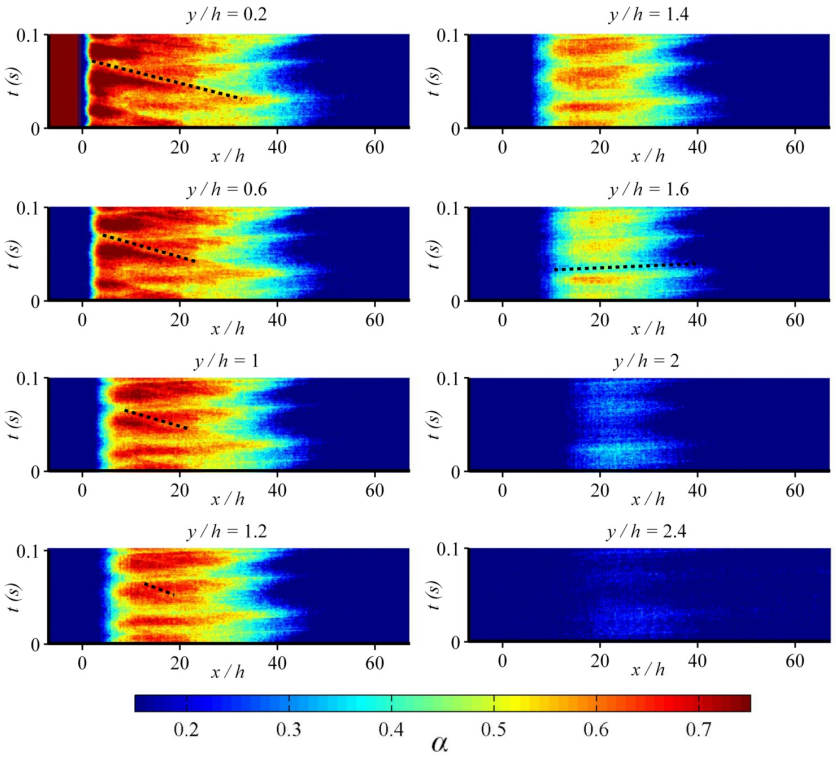

Figure 3.8: A sequence of space-time void fraction plots for pixel line locations across the cavity thickness. The data is from ventilated flow for $Re_h = 1.33 \times 10^4$ and a 0.1 seconds time-series. The dotted black lines are used to illustrate re-entrant jet propagation and flow advective velocity. (small-scale experiment)

Due to the large number of incondensible gas structures shed, the wake of the ventilated cavity has a relatively high mean void fraction in range $0.1 < \alpha < 0.4$. In contrast, the wake of the natural cavity is characterized by almost zero void fraction as shed vaporous structures mostly condense in the vicinity of the cavity closure.

A sequence of space-time plots from X-ray imaging at positions across the cavity thickness, as shown in figure 3.9, may be used to obtain an estimate of the re-entrant jet thickness. The sequence is taken from the ventilated flow imaging to avoid any ambiguity associated with the phase change phenomenon on the visualization, and to ensure that any propagating event observed has its origin in convective transport. An obvious downward sloping line can be seen for the point closest to the wall, representing a strong upstream directed flow, i.e. the re-entrant jet. As the distance from the wall is increased, the re-entrant flow weakens, eventually vanishing at $y/h \approx 1.2$. From the void fraction dynamics further away from the wall it can be seen that the flow is now directed downstream, with a sloped line now representing the advective velocity. From this crude estimate, the re-entrant jet is found to occupy about half of the cavity thickness. This observation is in agreement with the findings by Callenaere et al. (2001) on the influence of the re-entrant jet to cavity thickness ratio on the cavitation behaviour.

3.3.2 The influence of free-stream velocity on cavity topology

Following on the previous observations by the authors in a study of ventilated cavity flow over a 3-D wall-mounted fence (Barbaca et al., 2017a), it is expected that a change in free-stream velocity will also have an effect on the cavity topology in the present study. In figure 3.9, a series of shadowgraphy image pairs of the cavity closure, taken with the camera above (upper image) and below (lower image) the test section is presented for a full range of free-stream velocities investigated in the large-scale test, which are expressed through Fr_h and Re_h. It can be seen that the length of the re-entrant jet affected region (l_{rj}) increases with an increase in free-stream velocity. In the upper right corner, a plot showing the dependence of re-entrant jet length, non-dimensionalised by fence height (l_{rj}/h), on Fr_h is given for ventilated and natural cavity flow. As discussed in section §3.3.1, the re-entrant jet undergoes periodic contraction and extension, and the maximum and minimum recorded length are represented with error-bars for each investigated condition. A linear dependence of l_{rj}/h on Fr_h is evident, with a shorter re-entrant jet length observed in the naturally cavitating flow.

The justification for designation of Fr_h as a dimensionless parameter governing the re-entrant jet length can be found if the studied flow is considered as analogous to the recirculating flow associated with the undular jump phenomenon in super-critical open-channel flow. As presented in experimental work by Hager et al. (1990) and Murzyn and Chanson (2009), as well as predicted by Richard and Gavrilyuk (2013) using a conservative hyperbolic two-parameter model of shear-shallow water flow, the length of recirculating zone (termed 'roller length') has a dependence on a fixed length scale based Fr. This can be closely approximated with a linear fit function. Further rationale for this analogy emerges from the extinction of the re-entrant jet, i.e. $l_{rj}/h = 0$, for a non-zero Fr_h. This indicates that the re-entrant jet may cease to exist if the testing conditions become analogous to sub-critical open-channel flow regime, i.e. if the $Fr_H < 1$. Indeed, in the present study a significant difference was observed in the cavity flow dynamics for the lowest free-stream velocity, with a corresponding $Fr_H \approx 0.8$. Although this condition satisfies the sub-critical flow threshold, a very weak and short recirculating zone was still present, however no structured shedding was observed and the cavity break-up was characterized by random break-off of rather large distinct bubbles. This conclusion is in agreement with the closure behaviour observed in the ventilated backward facing step flow at low speeds, where the cavity break-up is associated with a gravity governed wave pinch-off mechanism (Arndt et al., 2009; Mäkiharju et al., 2013a).

In figure 3.10a, cavity pressure based cavitation number measured in the large-scale tests for a constant cavity length ($l_c/h \approx 90$) is plotted as a function of Fr_h and Re_h. Although the systematic error in measurement is eliminated, as described in §3.2.2, the variation of σ_c present in figure 3.10a is due to high cavity sensitivity to free-stream

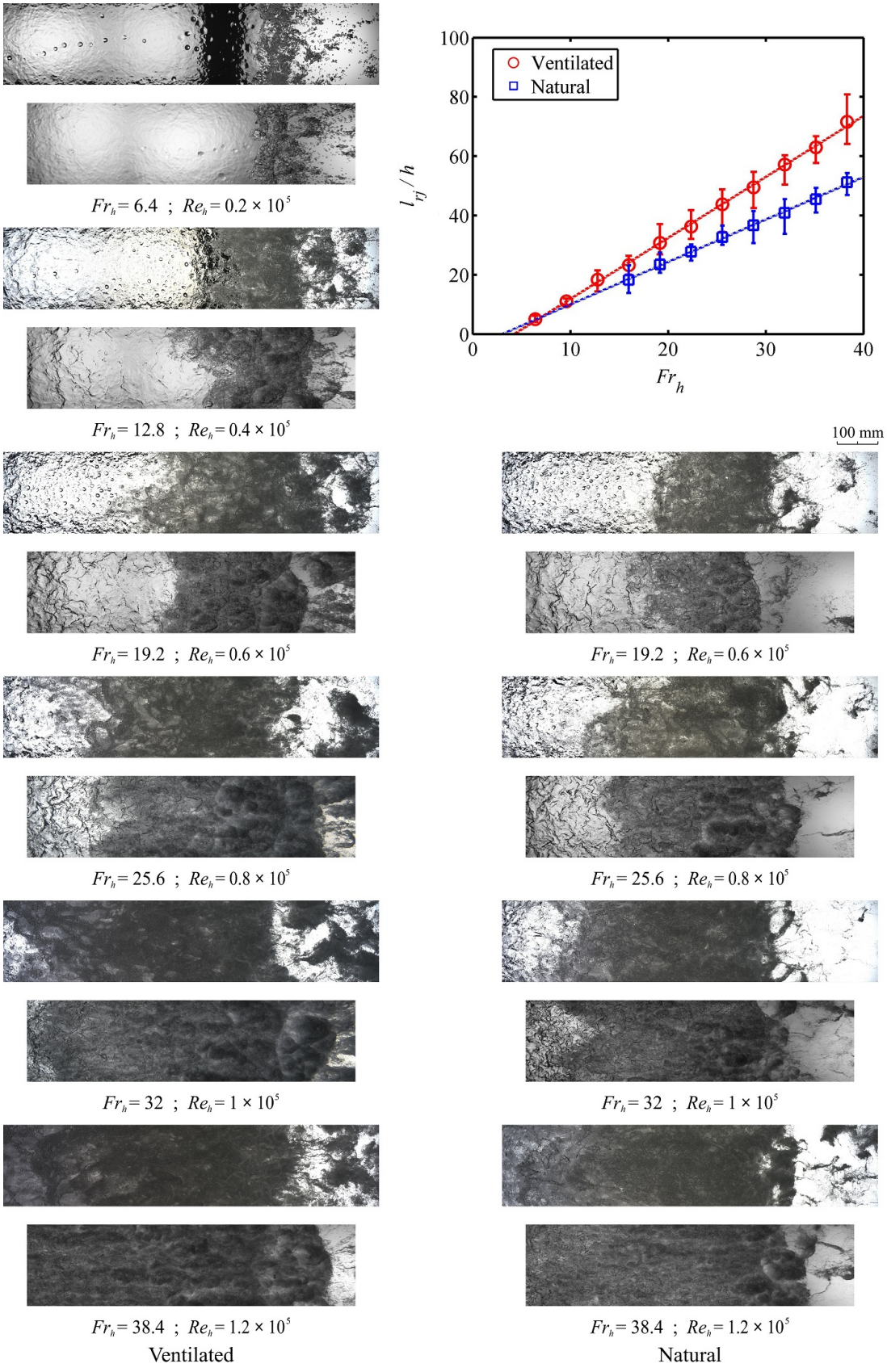

Figure 3.9: A series of shadowgraphy image pairs of the cavity closure taken with the camera positioned above (upper image) and below (lower image) the tunnel test section in the large-scale experiment. In the upper right corner a plot showing dependence of non-dimensionalised re-entrant jet length (l_{rj}/h) on Fr_h is presented. (large-scale experiment)

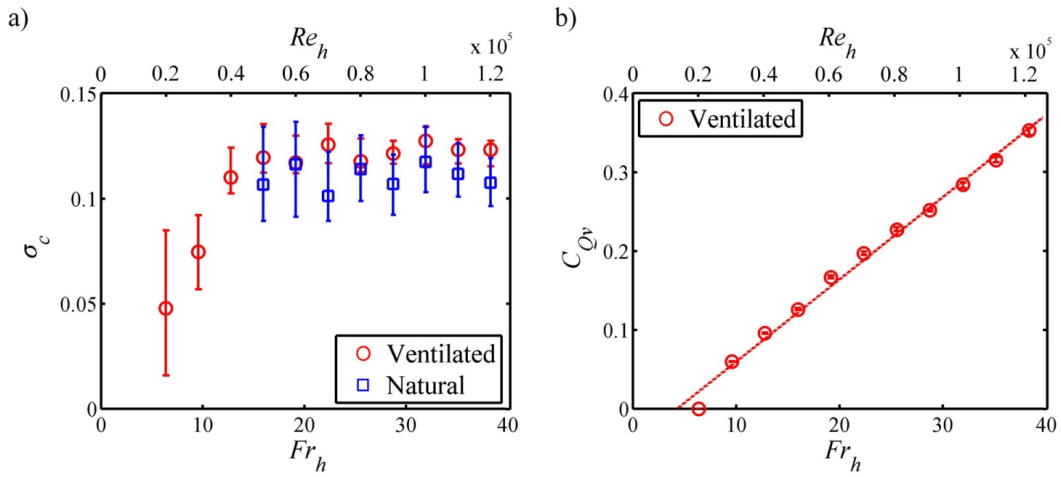

Figure 3.10: a) σ_c measured for a constant cavity length ($l_c/h \approx 90$) shown as function of Fr_h and Re_h for ventilated and natural cavity flow and b) required C_{Qv} as a function of Fr_h and Re_h for ventilated case. (large-scale experiment)

conditions close to blockage conditions. Error-bars in figure 3.10 indicate the minimum and maximum values from multiple measurements of each data point. Barbaca et al. (2018) reported for a limited range of Fr_h values that the cavitation number measured for cavities of the same length is independent of Fr_h. A similar behaviour is apparent in the present study for the conditions corresponding to $Fr_h > 15$. However, for the cases with $Fr_h < 15$, a decrease in σ_c can be observed following a decrease in Fr_h. Again, a similarity with a backward facing step flow can be noted, as σ_c values close to, or even below zero, are reported for low speed flows with a smooth cavity reattachment on the downstream wall (see for example Matveev and Miller, 2011). Slightly lower σ_c values were measured for naturally cavitating flow at the same Fr_h values, but the trend is observed to be similar.

The dependence of ventilated air volumetric flow-rate coefficient on Fr_h is presented in figure 3.10b. It is shown that the required air flux increases linearly following an increase in Fr_h. This behaviour stems from a more intense cavity break-up and shedding of bubbly structures related to increased re-entrant jet intensity (characterized by a longer re-entrant jet) with higher Fr_h. It can be noted that at the lowest $Fr_h = 6.4$ an established cavity could be maintained with zero air flux. As seen in figure 3.9, some cavity break-up is still observed for this condition, but with the absence of ventilated air flux this may be explained by the diffusion of free and dissolved gas through the cavity surface supplying the amount of gas entrained via cavity break-up.

3.3.3 The influence of free-stream velocity on the cavity wake

A qualitative analysis of spatial characteristics of the gas entrainment process through cavity break-up and shedding can be provided from the shadowgraphy images in figures 3.11 and 3.12. In figure 3.11 a set of wide view images taken with the camera located

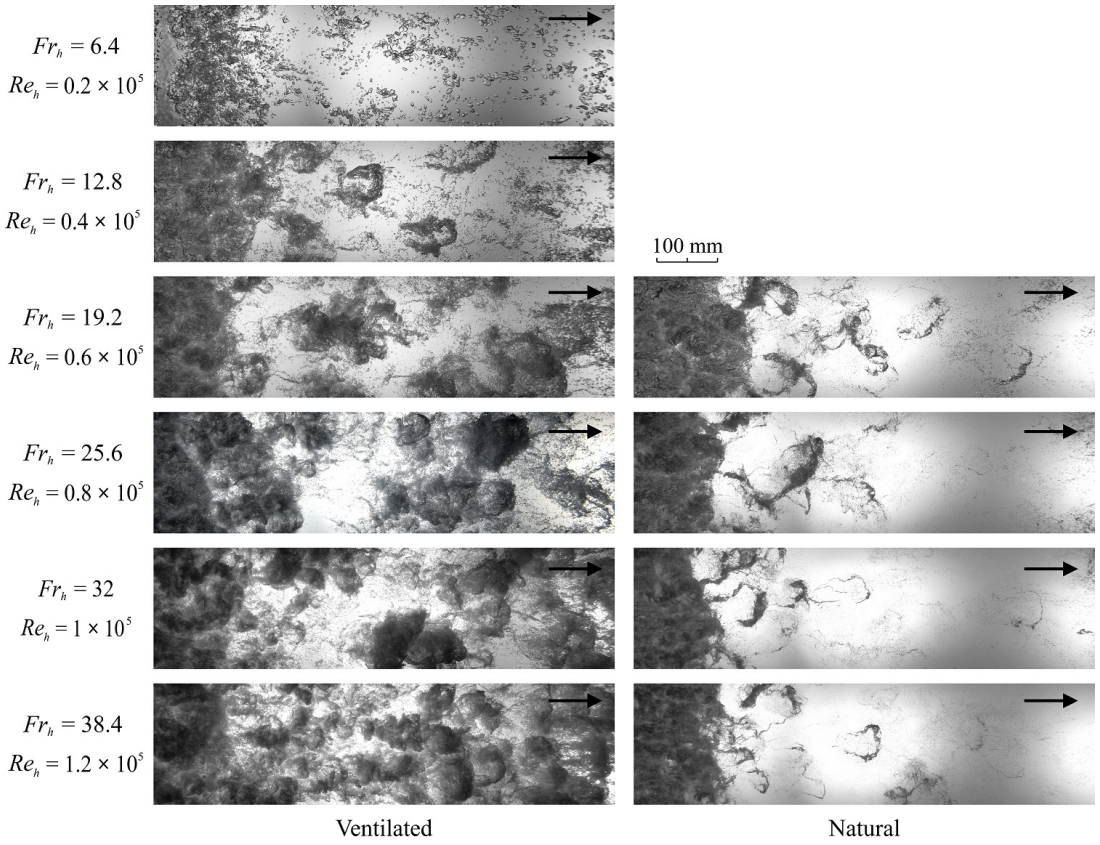

Figure 3.11: A series of wide view shadowgraphy images of the cavity wake taken with the camera positioned below the tunnel test section for ventilated and natural cavity flow across the full range of investigated Re_h. (large-scale experiment)

below the test section is shown for the complete range of Fr_h and Re_h for both ventilated and natural cavity flows. A separate set of narrow view images taken with the camera positioned above the test section for the same conditions is given in figure 3.12. Two salient flow features are apparent from the cavity wake topology. Firstly, the number and size of the shed structures, and secondly, the size and concentration of the micro-bubble population. As the sizes of structures shed into the wake are much smaller in comparison to the re-entrant jet length, it would appear that cavity break-up is governed by the turbulence scales of the overlying flow, and so Re_h will be used for characterization of free-stream speed for this discussion. This inference will be further supported in the next section.

Discussion of the first aspect (i.e. the shed structures) can be derived from the wide view images (figure 3.11). As already noted, the wake of a ventilated cavity at the lowest Re_h consists of a population of relatively large (sizes in order of a few millimetres) distinct/unclustered bubbles. As Re_h increases the bubble size decreases and they begin to cluster into larger-scale structures. At $Re_h = 0.4 \times 10^5$ shed structures are relatively small and hairpin shaped. With increase in Re_h bubble sizes reduce and start to form more spherical shaped bubble clusters. The shed structures have a transparent appearance at lower Re_h values, but become more opaque as more smaller bubbles are clustered to form

larger-scale structures at higher Re_h values. A significant increase in the gas concentration in the wake, observed as much larger areas of dark pixels in the image, can be observed with increase in Re_h. For the natural cavity flow the behaviour is quite different. No significant difference between the cavity wake across the investigated Re_h range can be observed. In all cases the hairpin shaped structures are only present in the vicinity of cavity closure. The shed hairpins for the natural cavity case remain relatively unchanged with Re_h increase. Whereas, for the ventilated case the change from hairpin to more clustered structures can be attributed to the increase of injected gas with Re_h increase.

Insight into the micro-bubble population size and concentration can be gained from narrow view images (figure 3.12). For the ventilated flow an obvious decrease in the bubble size across several orders of magnitude (from ≈ 10 mm to ≈ 10 μm) can be seen for the range of Re_h values tested. While bubble sizes decreases, the number of bubbles increases. A similar trend can be observed for the natural cavity flow with varying Re_h, however smaller bubbles are present in the wake for the natural case than for the ventilated case, for the same Re_h. This decrease in bubble size with Reynolds number increase is similar to observations made by Russell et al. (2016) for bubble sizes in the wake of a cavitating hydrofoil. The smaller micro-bubble size in the natural cavity case can be attributed to the more violent nature of natural cavity break-up, involving condensation and shock-wave generation, not present in the ventilated case.

To gain insight into shedding spatial modes and their contribution to cavity break-up energy, an analysis technique based on Proper Orthogonal Decomposition (POD) is utilized. The method has been applied in a fluid dynamics context for some time to characterize turbulence coherence (see for example Sirovich, 1987), with an application of the method to cavitating flow around a hydrofoil recently reported by Prothin et al. (2016).

In figure 3.13 the first ten spatial modes from cavity wake POD analysis of the shadowgraphy images from the large-scale measurements are shown for the ventilated and natural cavity flow cases for $Re_h = 1 \times 10^5$. These images include about one third of the full width of the flow. The POD analisys was performed on sets of 1000 images acquired with high-speed imaging at the sampling rate of 100 Hz. A scale is provided in the figure to indicate the size of structures associated with the each mode. The first mode (i.e. highest energy) represents the average value of image intensity at each pixel corresponding to mean flow conditions. The first mode of the natural cavity case contains about three times more energy than the first mode for the ventilated cavity case. This observation follows on from the presented qualitative wake analysis of the shadowgraphy images, where more large-scale gaseous structures (higher shedding energy) were observed for the ventilated cavity flow case than for the natural cavity flow case. The second and third mode represent a pair of symmetric modes with the shed structures spanning the whole field of view. As noted by Prothin et al. (2016), the quarter wave-length delay

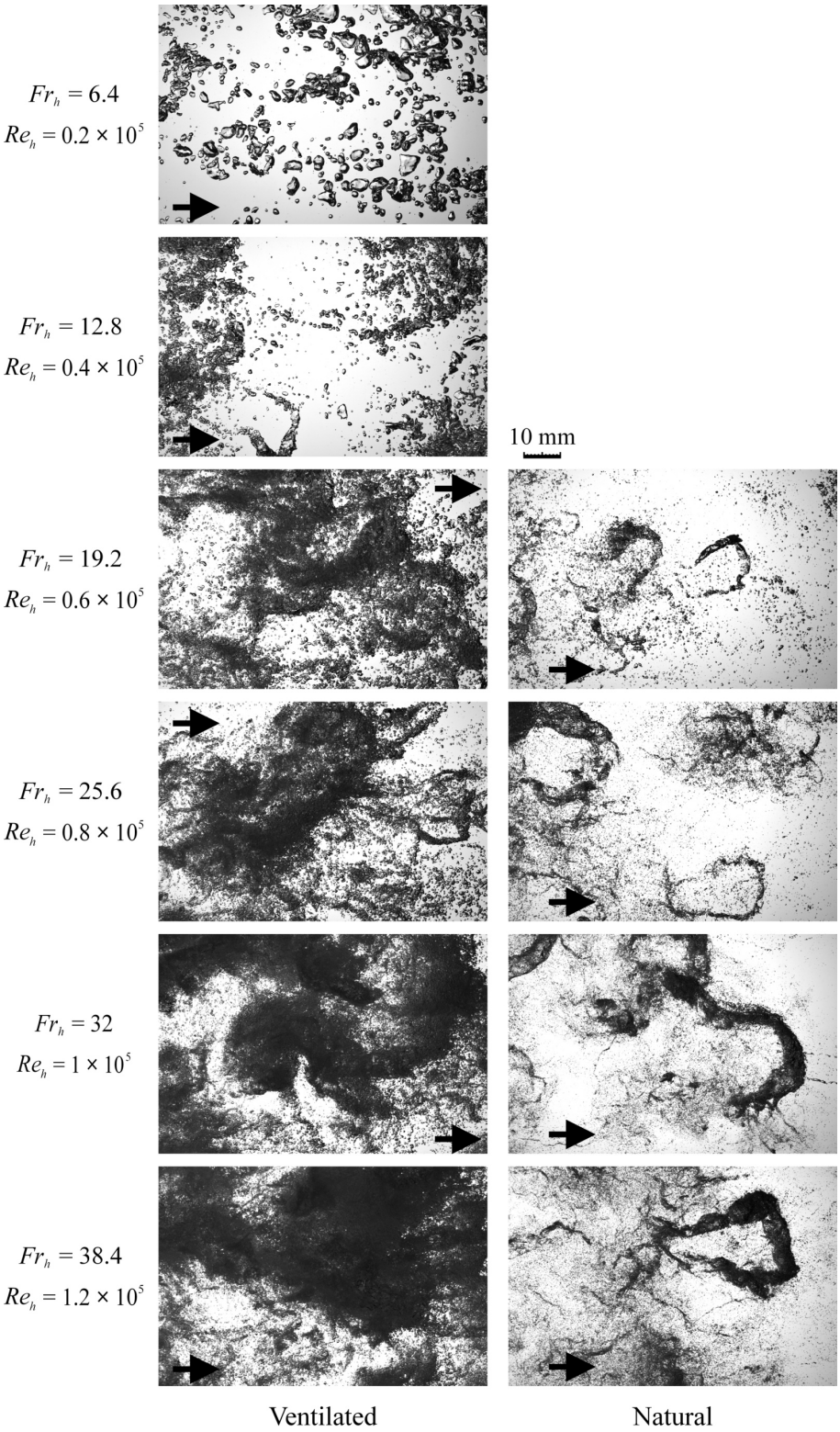

Figure 3.12: A series of narrow view shadowgraphy images of the cavity wake taken with the camera positioned above the tunnel test section for ventilated and natural cavity flow across the full range of investigated Re_h. (large-scale experiment)

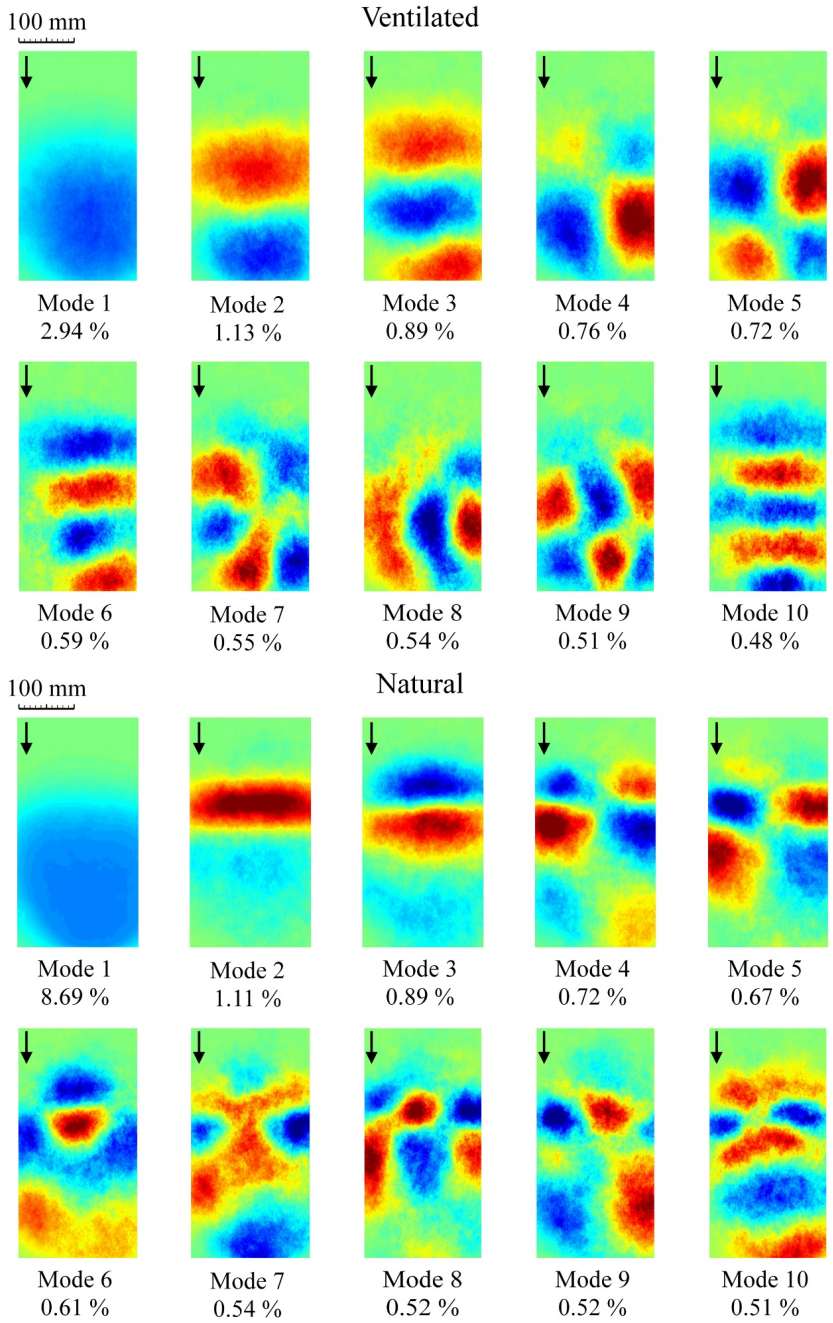

Figure 3.13: The topology and energy contribution of the first ten modes from POD analysis of 1000 shadowgraphy images of the cavity wake from the large-scale experiment at $Re_h = 1 \times 10^5$ for ventilated and natural cavity flows. The images are extracted from high-speed imaging recorded at 100 Hz sampling rate. The scale is provided to indicate the size of structures associated with each mode. (large-scale experiment)

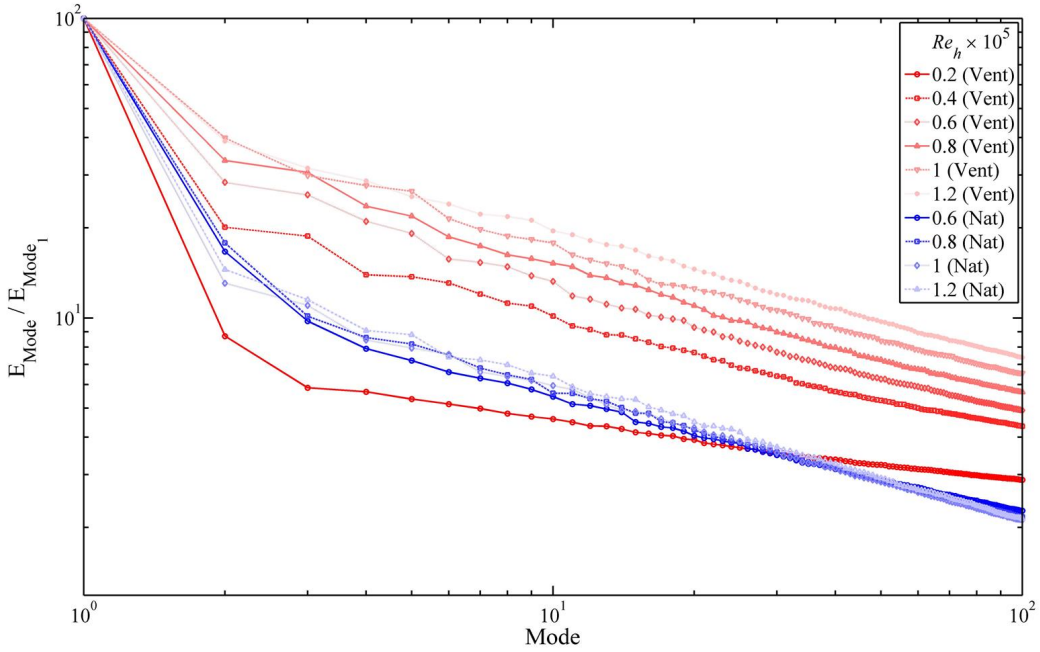

Figure 3.14: The ratio of energy of a particular POD mode to the mean flow energy for first one hundred modes presented as a *log-log* plot for the ventilated and natural cavity flows for the range of Re_h values investigated. (large-scale experiment)

between the two modes is in agreement with the results from numerical and experimental studies of bluff body wake configurations (Noack et al., 2003; Oudheusden et al., 2005). The next two modes represent a pair of antisymmetric modes with shedding events alternating about the stream-wise centre-line. Up to this point, the modes have a similar topology for the ventilated and natural cavity flows, with the smaller structures observed for natural cavitation (structure length being between 25 and 50 % less). The higher order modes are characterized by decrease in structure size, with the topology varying between symmetric to an increasingly less-structured appearance. A similar description of the mode topology is applicable for all Re_h investigated.

The distribution of energy, normalized by the energy of mean flow, across the first one hundred POD modes is given as *log-log* plot in figure 3.14 for the ventilated and natural cavity flows for the full range of Re_h. The ratio between the energy contained within the shedding modes and that of the mean flow, can provide a quantitative description of the wake area covered by the gaseous structures. The modal energy decreases with increase in modal order approximately following a power law trend, with a similar slope observed in most curves, apart from a less steep decrease present for the lowest Re_h. For the ventilated flow, an increase in shedding energy with increase in Re_h is evident, with the ratio of modal to mean flow energy having about an order of magnitude increase across the Re_h range. The energy level of a particular POD mode does not vary significantly in the naturally cavitating flow with change in Re_h, but a considerably lower amount of

energy contained within the shedding modes is noticeable in comparison to the ventilated flow at the same Re_h. These quantitative observations support the conclusions from the previously discussed qualitative analysis of the wake.

3.3.4 Advective velocities from high-speed imaging

A series of space-time plots extracted from high-speed shadowgraphy of a one second (1000 frames) time-series of a single line of stream-wise pixels is presented in figure 3.15. The space-time plots are given for the range of Re_h investigated and for both the ventilated and naturally cavitating cases. These plots are useful for analysing characteristic speeds as the propagation or transport of any feature in the space-time domain is registered as a sloping line. In the present case two distinct flow phenomena are indicated, the shedding of bubbly structures and their advection through the cavity wake, and the upstream directed propagation of the re-entrant jet. As shown in the enlarged view in the upper right corner of figure 3.15, each shed structure is represented by a downward sloping low pixel intensity band, the slope of which corresponds to the structure advective velocity (U_{adv}). As the re-entrant jet consists of a bubbly mixture, bubble tracking can be used to estimate the re-entrant jet speed. The re-entrant jet speed (U_{rj}) is visualized by a series of upward sloping streaks corresponding to distinct bubbles trapped within the re-entrant flow.

The bands in space-time plots increase in slope showing the increase in advective speed with increasing Re_h. A plot showing the dependence of U_{adv}/U_∞ on Re_h (and Fr_h) is shown in figure 3.16. The advective speed measurement is taken as an average of all downward sloping lines within the investigated time-frame. The slope is calculated from the location where a structure detaches from the cavity to the downstream boundary of the plot, giving the stream-wise spatial average of the velocity across the wake. The error-bars represent the non-uniformity in the advective speeds between specific structures, which did not appear to exhibit any regularity (i.e. the advective speed was not observed to be dependent on the structure size). From figure 3.16 it is apparent that U_{adv}/U_∞ has nearly constant value of about 0.56 across the Re_h range for ventilated flow, and about a 20% higher value of about 0.65 for the natural cavity flow.

A similar analysis of the re-entrant jet velocity for the range of Re_h can also be performed. Again, the ratio between the velocity, U_{rj}/U_∞, is plotted in figure 3.16 for additional insight. An approximately constant U_{rj}/U_∞ value of about 0.18 is observed across the range of Re_h, for both ventilated and natural cavity flow as shown in figure 3.15. A value of 0.18 compares with 0.3 reported by Callenaere et al. (2001) for flow over a diverging step in the 'thin-cavity' regime. This places the current flow further into the 'thin-cavity' regime or further away from the 'auto-oscillating/cloud cavitation' regime ($U_{rj}/U_\infty > 0.5$) as described by Callenaere et al. (2001).

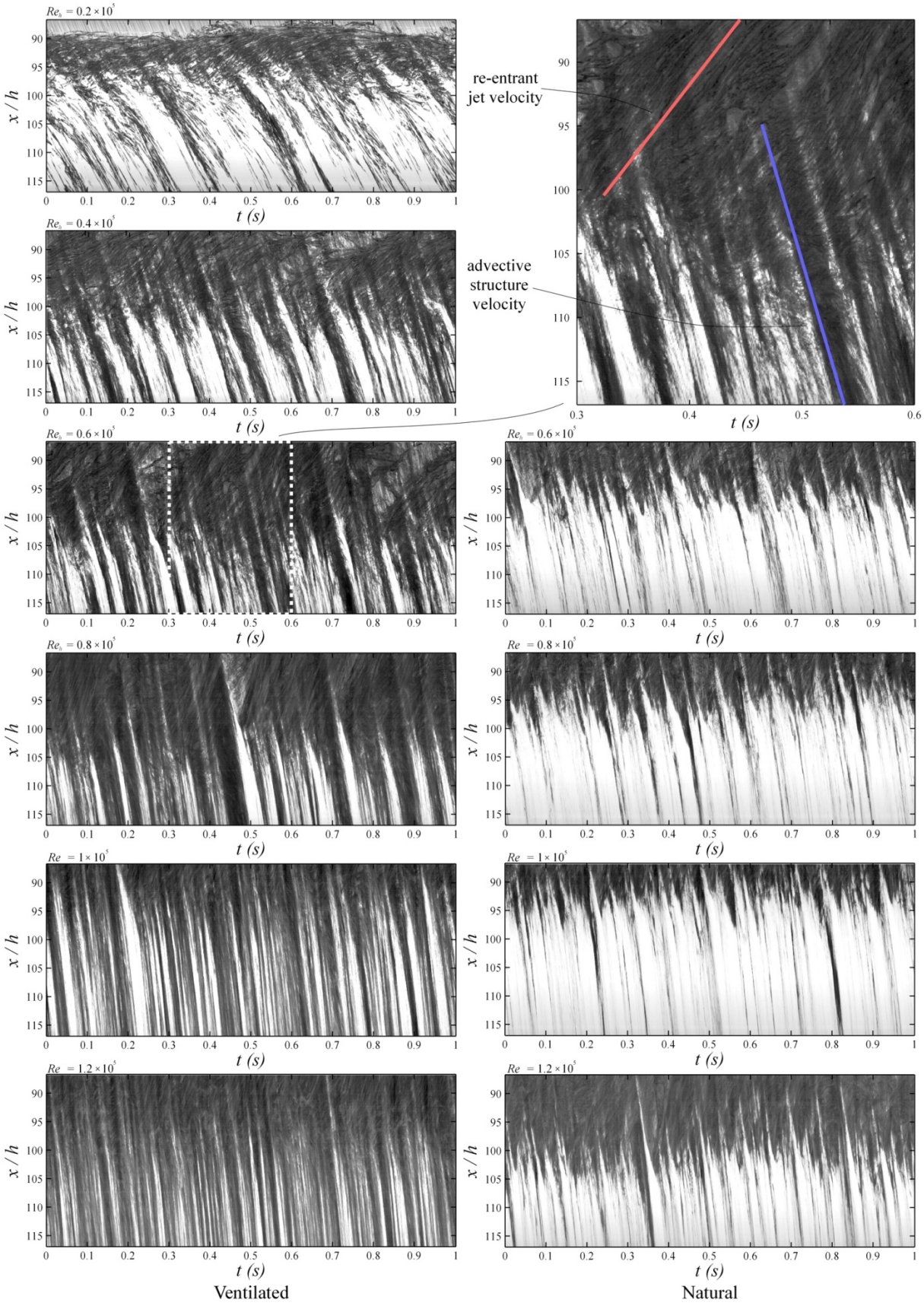

Figure 3.15: Space-time plots generated from a stream-wise line of single pixel width from high-speed shadowgraphy of 1 second duration recorded at 1 kHz. Plots are presented for ventilated and natural cavity flows across the range of investigated Re_h. A detail in the upper right corner is provided to define velocities of advected shed structures and re-entrant flows. (large-scale experiment)

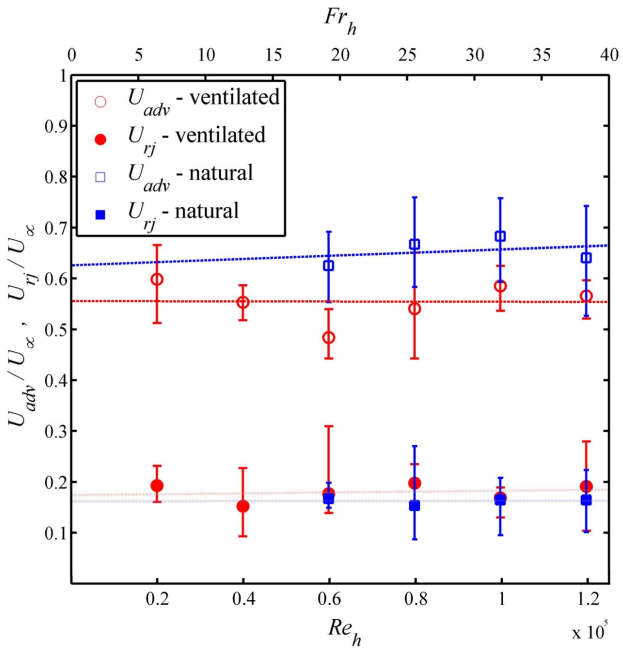

Figure 3.16: U_{adv}/U_∞ and U_{rj}/U_∞ ratios obtained from the space-time plots as a function of Re_h for ventilated and natural cavity flow. (large-scale experiment)

3.3.5 Spectral content of cavity flow over a 2-D wall-mounted fence

The power spectral densities (PSDs) of long sampled pressure signals from an array of six pressure sensors located in the cavity closure region were analysed using the Welch method (Welch, 1967). The pressure sensors are positioned on the test-section centre-line and are equi-spaced (at 60 mm intervals) in the stream-wise direction, with the nominal position of cavity closure approximately aligned with the third most upstream sensor. The time-series were recorded for 1000 s sampled at 1 kHz.

In figure 3.17 ventilated flow pressure spectra from each sensor is given for a constant $Re_h = 1 \times 10^5$. The data are presented in a non-dimensionalised form as St_h. Note there is the presence of 50 Hz mains supply noise (and higher harmonics) in the data due to the pressure fluctuations being small compared to the pressure sensor range (1 kPa fluctuations measured with a 15 bar sensor). Despite this noise the main spectral features related to the flow unsteadiness are easily discernible. Spectral content observed for each sensor is characterized by two broad-band peaks and a high-frequency roll-off that follows a power law behaviour ($\propto St_h^{-7/3}$). Interestingly, this behaviour in two-phase flow is similar to that observed in the single-phase flow over a forward-facing step, as presented by Camussi et al. (2008) and more recently by Graziani et al. (2017). Although, the similarity between the single-phase and cavitating flow is remarkable, a significant difference exists. For two-phase flow peaks in pressure fluctuations are observed at $St_h \approx 0.002$ and $St_h \approx 0.02$, whereas in single-phase flow these peaks occur an order of magnitude higher.

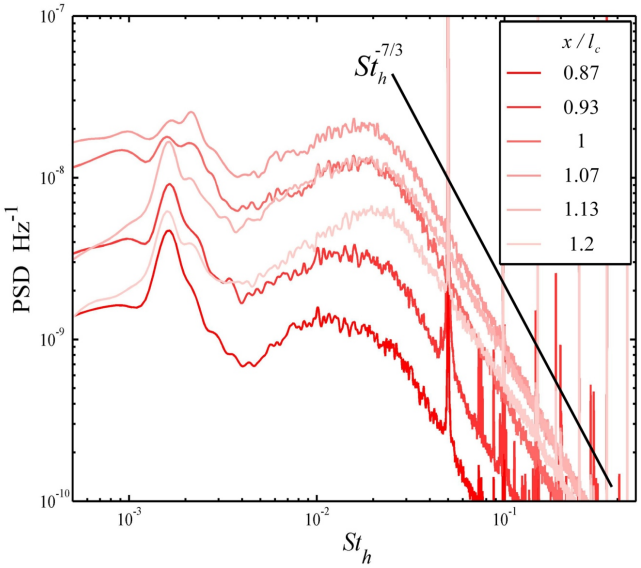

Figure 3.17: Wall pressure power spectra from six dynamic pressure sensors located on the test-section ceiling centre-line for ventilated flow at $Re_h = 1 \times 10^5$. A black line indicates the power spectra decay following a power law behaviour proportional to $St_h^{-7/3}$. (large-scale experiment)

This suggests that the presence of bubbles in the downstream separation zone induces a damping effect on the oscillating system, significantly reducing the frequencies.

If the ratio of energy contained in the low- and high-frequency peaks is analysed across the different sensors, it is evident that the contribution from the low frequency peak is dominant at the locations within the cavity, i.e. in the re-entrant jet region, while the high-frequency peak becomes more prominent as the sensor location moves downstream into the cavity wake. From this observation, the low-frequency peak can be associated with the previously discussed oscillations of the re-entrant jet length, while the high-frequency peak can be related to the cavity break-up induced by the large-scale structures contained within the overlaying turbulent boundary layer. The observed power law like high-frequency power spectra decay characterizes spectral content of pressure fluctuations within a turbulent boundary layer in a single-phase flow, which further supports the premise that cavity closure break-up is dominated by the characteristics of the overlaying boundary layer. The oscillations of the re-entrant jet can be considered analogous to the 'flapping' motion observed in single-phase flow, i.e. the extension and contraction of the separated zone originating from an upstream-downstream propagating wave (Hudy et al., 2003).

In figure 3.18 wall pressure spectra from the sensor nominally aligned with the cavity closure is given for both the ventilated and natural cavity cases. From figure 3.18a it can be seen for ventilated flow, that if the PSD is plotted against the Strouhal number defined using a constant length scale (i.e. fence height), the high frequency peak will collapse to a constant $St_h \approx 0.02$ value, leading to a conclusion that the frequency of

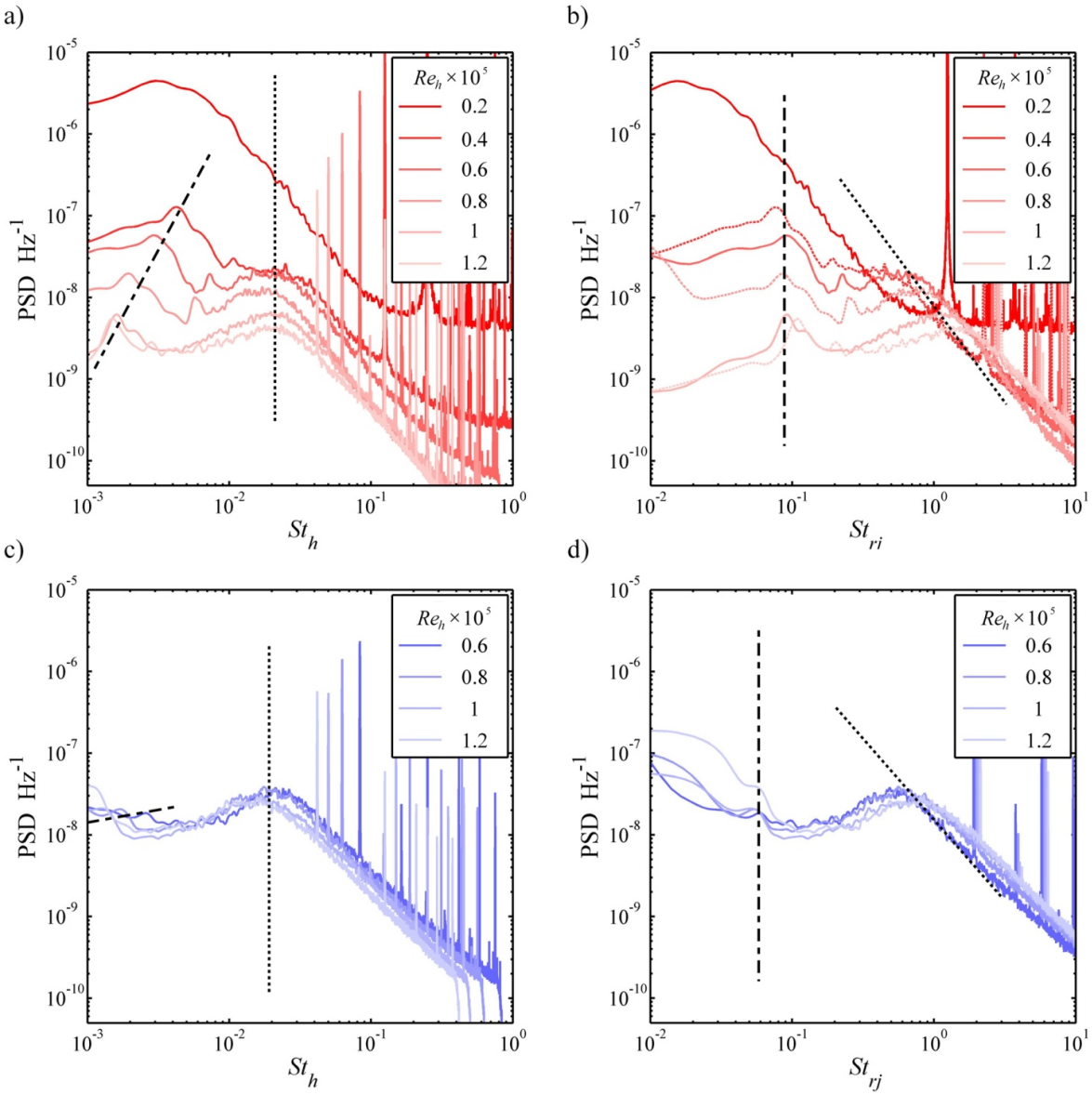

Figure 3.18: Wall pressure power spectra from the dynamic pressure sensor nominally aligned with the cavity closure. Data is presented for both ventilated (a,b) and natural (c,d) cavity flows with the frequency non-dimensionalised as St_h (a,c) and St_{rj} (b,d). The dash-dot lines are added to the plots to indicate the low-frequency peaks, while the dotted lines denote the high-frequency peaks. (large-scale experiment)

turbulent shedding is proportional to free-stream velocity. However, the location of the low-frequency peak does not collapse with the St_h. As previously noted, the low frequency peak is associated with the large-scale re-entrant jet oscillation, and given that the re-entrant jet length varies with free-stream speed, it may be useful to alternatively define a re-entrant jet length based Strouhal number, $St_{rj} = fl_{rj}/U_\infty$. When the pressure spectra is plotted against the St_{rj} (figure 3.18b) it can be seen that the low frequency peak collapses to a constant St_{rj} value of about 0.1. The high-frequency power law like decay is not affected by change in Re_h, which is consistent with the reasoning in section §3.3.1 that the cavity shedding is controlled by the overlying turbulent boundary layer. If the amount of energy contained within the low- and high-frequency peaks is compared across the range of Re_h, it is observable that peaks have approximately equal value at higher Re_h, but the low-frequency oscillation become increasingly more dominant with the decreasing Re_h. Note also that the low-frequency peak is not observed at the lowest Re_h in line with the minimal gas entrainment into the main flow in the sub-critical flow regime as discussed in section §3.3.2. That is, the broad peak in PSD for this Re_h apparently corresponds to turbulent cavity break-up, however this doesn't collapse with the higher Re_h spectra due to transition from sub- to super-critical regime. In the case of the naturally cavitating flow (figure 3.18c and d), a similar behaviour is observed. There is however a significant difference in the ratio of energy contained in the low-frequency and high-frequency peaks, where a more prominent role of high-frequency break-up is observed for natural cavity flow compared to ventilated flow where the peaks are of similar intensity. This leads to the conclusion that violent natural cavity break-up from condensation has sufficient energy to considerably interrupt the large-scale re-entrant jet oscillations, or at least filter them as they propagate from the re-entrant jet affected zone into the cavity wake. The collapse of low-frequency peak to a nominally constant St_{rj} in both two-phase flows is in contrast to the observations from single-phase flow, where the 'flapping' oscillation frequency occurs at a constant St_h. This difference can be attributed to the variation in re-entrant jet length (i.e. recirculating zone length) in the two-phase flows as described in section §3.3.2, in comparison to a nominally constant length of recirculating zone observed in single-phase flow for $Re_h > 0.085 \times 10^5$ (Graziani et al., 2017). On this basis, it may be concluded that the influence of gravity, arising from the presence of two phases with substantially different densities, in the recirculating region modulates its dynamic behaviour.

To analyse the intensity of pressure fluctuations in the cavity closure region the root-mean-square (RMS) value of the pressure signal is calculated. To exclude the contribution from mains electrical noise, the signal has been filtered using a series of high-order Butterworth 'stop-band' filters at the noise fundamental frequency and the harmonics. The filtered data was then reduced to a pressure coefficient $C_P = p/0.5\rho U_\infty^2$ and the RMS of the C_P ($C_{P_{RMS}}$) is calculated. In figure 3.19a $C_{P_{RMS}}$ values are plotted along the cavity closure region for both ventilated and natural flows with a constant $Re_h = 1 \times 10^5$. It

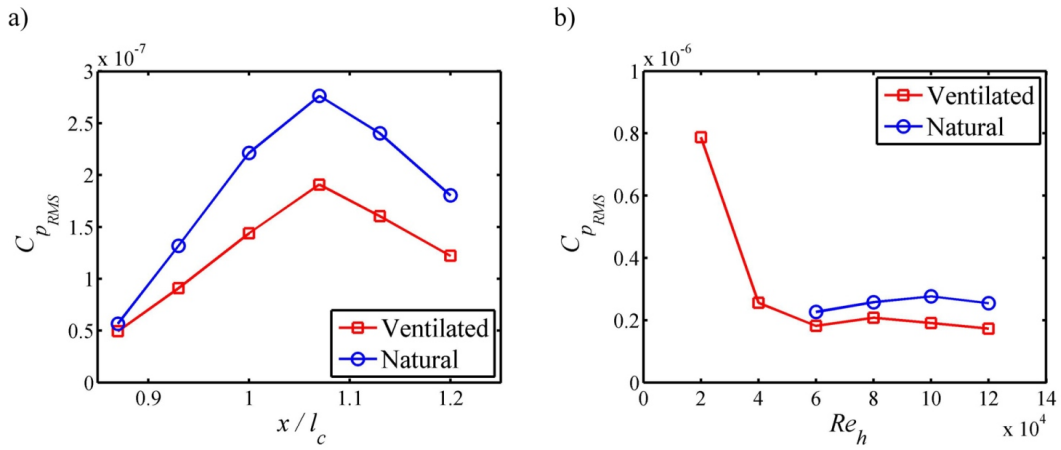

Figure 3.19: a) the distribution of root-mean-square (RMS) value of the pressure coefficient across the cavity closure for ventilated and natural cavity flows at $Re_h = 1 \times 10^5$, and b) the maximum $C_{P_{RMS}}$ value across the range of investigated Re_h for ventilated and natural cavity flow. (large-scale experiment)

can be observed that the most intense pressure fluctuations are detected just downstream of the cavity closure, and that the pressure fluctuation intensity decreases as the sensor is located further away from the closure. A more rapid decrease in pressure fluctuations is observed within the cavity, in comparison to that in the cavity wake. The pressure fluctuations at the cavity closure are about 5 times stronger than those within the cavity. Due to large sensor area (sensor diameter of 8.1 mm) the measured pressure fluctuations are small, dimensionally in the order of less than 1 kPa. Additionally, the $C_{P_{RMS}}$ values measured for natural cavity flow are about 50 % higher than those from the ventilated flow, confirming the more energetic and violent nature of the natural cavitation. From figure 3.19b it can be seen that the maximum pressure fluctuations are not significantly affected by the change in Re_h, apart from the case of ventilated flow at the lowest Re_h. Again, this discrepancy may be attributed to the differing cavity break-up mechanism in the sub-critical regime (see section §3.3.2).

3.3.6 Pressure-image cross-correlation

Time-series of averaged pixel intensity over an area corresponding to sensor size and location have been extracted from the forward-lit high-speed videos acquired simultaneously with the dynamic pressure measurements for comparison. It has been previously shown by de Graaf et al. (2016) that image and pressure signals from simultaneous acquisition have favourable correlation and that a lag between the two can be derived using cross-correlation. For cross-correlation, both signals have been normalised by subtracting the mean and dividing by the standard deviation. After this process, normalised image intensity (I') and pressure (p') are obtained. Additionally, the intensity signal is inverted as the dark areas in the image correspond to high pressure (i.e. high liquid content) and light areas correspond to low pressure (i.e. high gas content). After the lag between

the signals is determined one of the functions, in this case I' is shifted in time, with the adjusted signal labelled I'_s. Time, t, has been non-dimensionalised by $t' = U_\infty t/h$.

The above described process has been applied in the present study to cross-correlate the image intensity and the filtered pressure signal at the location of each sensor. In figure 3.20 a series of pressure and corresponding shifted image intensity time-series, along with a matching image sequence, is presented for ventilated cavity flow for $Re_h = 1 \times 10^5$. Starting with the most upstream location within the cavity, it can be observed that the signal is quite low for the majority of time as the break-up of bubbly structures at this position is quite rare. However, the signals correlate well for these rare events. Moving downstream it is possible to track the formation and evolution of shed structures through time. The further downstream the measurement is taken, the more structures start to appear, providing a basis for a stronger correlation between the image and pressure time-series. At the two most downstream positions, no emergence of new structures can be detected, and only the evolution of the upstream shed structures is observed.

A description of the life of a single structure and associated pressure disturbance can be provided from joint analysis of the time-series and image sequences. At time (a) the cavity surface does not appear to be broken and a number of structures already shed from the cavity can be observed in the wake. In (b) the disturbances caused by overlaying turbulence and the re-entrant jet flow induce the initiation of cavity break-up at the position of the most upstream sensor. A narrow high-intensity jump, related to liquid jet impingement on the wall and subsequent formation of a stagnation point, can be observed in both the pressure and image intensity signals. The structure is then advected into the wake with the velocity equal to U_{adv}. As the structure passes over subsequent sensors (b-g) a pressure signature is imparted. The pressure/image intensity peaks tend to have lower amplitude, but longer length, the further downstream the measurements are taken. This can be attributed to turbulent diffusion as can be seen from the image sequences. As the structures are advected downstream they are broken up by the turbulent flow (e-g), leading to increased mixing between the phases and a larger area covered by the resulting bubbly mixture. The now much larger extent of bubbly mixture dampens the pressure measured by the sensors located far downstream.

A similar sequence is provided for naturally cavitating flow in figure 3.21. The observations of the cavity break-up initiation (a-b) is the same as for ventilated flow. A difference is apparent however, in the evolution of the structures as they are advected downstream into the wake. The strongest correlation between the signals is detected just after the structure initially forms (c-d), but as the structure is advected downstream the correlation diminishes (e-g). This more pronounced decrease in the pressure/image correlation can be attributed to collapse and condensation of vaporous structures, providing less distinct features in the signals to correlate. From the given time-series it can be seen that the collapse of a cavity structure causes not only its disappearance from the consequent image

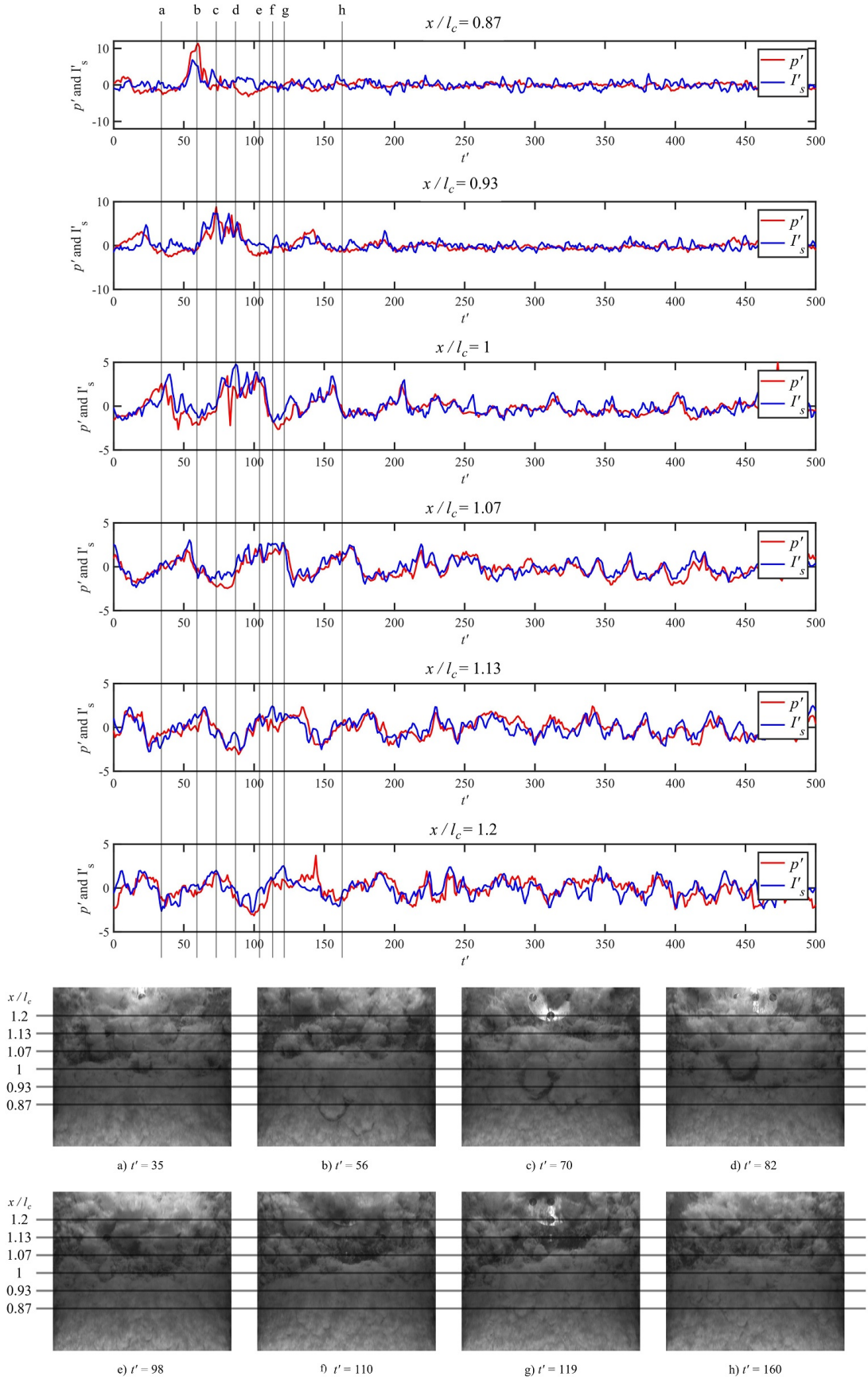

Figure 3.20: A series of pressure and corresponding shifted image intensity signals for each pressure sensor location showing the correlation between the two for ventilated cavity flow for $Re_h = 1 \times 10^5$. A matching image sequence provides the visualization of presented signals. (large-scale experiment)

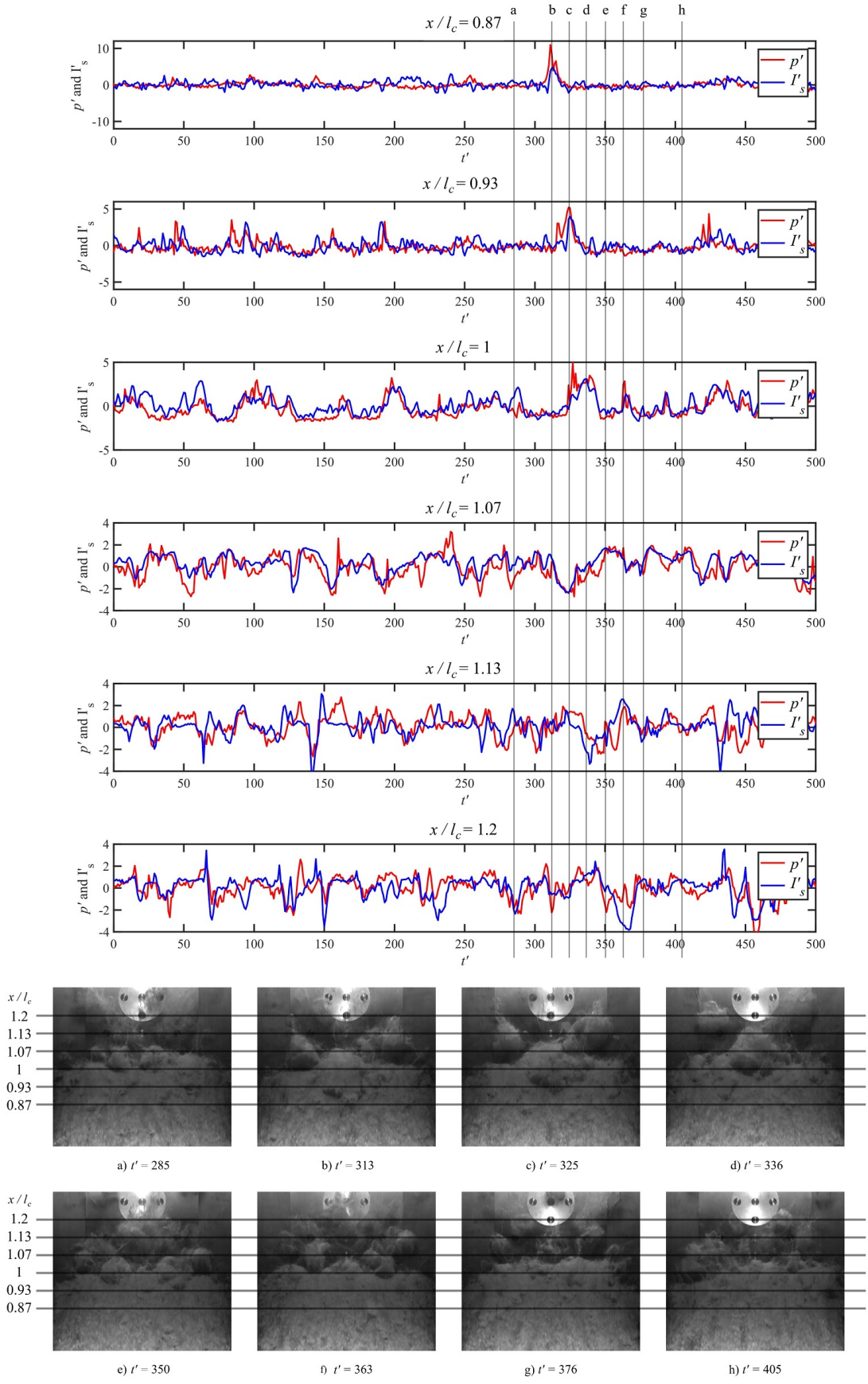

Figure 3.21: A series of pressure and corresponding shifted image intensity signals for each pressure sensor location showing the correlation between the two for natural cavity flow for $Re_h = 1 \times 10^5$. A matching image sequence provides the visualization of presented signals. (large-scale experiment)

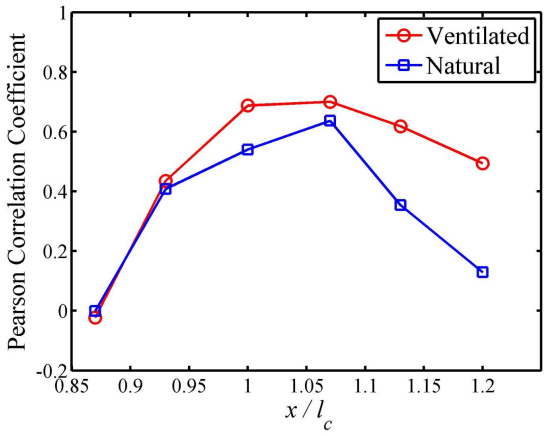

Figure 3.22: Pearson Correlation Coefficent between the image intensity and dynamic pressure signals at each sensor location for ventilated and natural cavity flow for $Re_h = 1 \times 10^5$. (large-scale experiment)

sequence, but also the cessation of any further related pressure disturbance. This suggests that the pressure fluctuation registered by the sensor used is mostly dependent on void fraction changes within the flow field.

To quantify the degree of correlation between the image intensity and pressure, the Pearson Correlation Coefficient (PCC) is calculated for the image/pressure sensor pairing for both the ventilated and natural cavity flows, with the results presented in figure 3.22. The trend confirms the qualitative observations discussed above, with the highest PCC value of about 0.7 registered just downstream of the nominal cavity closure and monotonically decreasing value moving away from this location. The more rapid decrease in PCC value can be seen as the region of interest moves upstream inside the cavity, where the PCC value tends to zero. In contrast to the ventilated flow, a severe drop in the PCC value (reaching almost zero) can be observed in the wake of a natural cavity. This drop is attributable to the condensation of vaporous structures and the extinction of the related pressure signature as described above.

The favourable correlation between the image intensity and pressure time-series suggests that a comparable power spectra should be obtained by analysing either signal. In figure 3.23, the power spectra obtained from pressure sensor measurement for 100 and 1000 seconds, is compared with that from shadowgraphy and forward-lit high-speed videos in the cavity wake recorded for 100 seconds for ventilated flow at $Re_h = 1 \times 10^5$. Additionally, the spectra of re-entrant jet oscillations is obtained from a forward-lit imaging by analysing the intensity of a pixel region near the re-entrant jet inner boundary. The PSD obtained from the wake imaging correlates well with the low- and high-frequency peaks from the pressure signal, suggesting the image analysis alone can be useful in characterizing the spectral content of the cavitating flows due to a strong image intensity/pressure coupling. A strong correlation in turbulent power decay is also evident between the pressure and shadowgraphy signal, with a slightly lesser correlation found with the forward-lit

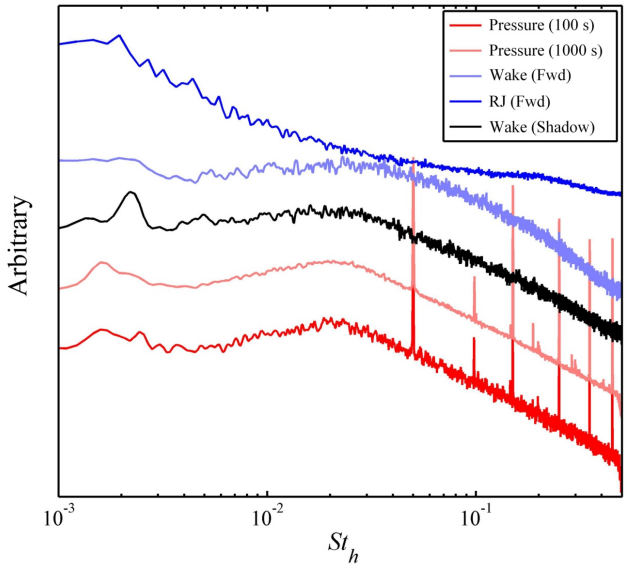

Figure 3.23: Power spectra of time-series from wall pressure measurements (100 and 1000 s) and image intensity from forward-lit (fwd) and shadowgraphy (shadow) imaging (100 s) in the cavity wake. The power spectra of image intensity signal extracted at the location of re-entrant jet inner boundary is also shown. The data is for ventilated flow at $Re_h = 1 \times 10^5$. (large-scale experiment)

imaging data. Furthermore, the correlation between the low-frequency peak in pressure spectra and spectra obtained from forward-lit imaging of re-entrant jet, confirms that the re-entrant jet oscillation is the mechanism driving the low-frequency fluctuations.

Based on the conclusions from the previous paragraph, a comparison of the power spectra obtained from the forward-lit high-speed imaging from both the large-scale and small-scale facilities is provided in figure 3.24. The spectra from small-scale measurements is smoothed by averaging the spectra at each span-wise pixel for a constant stream-wise location. It can be seen that a favourable agreement in the location of the low- and high-frequency peaks in the spectra from different facilities exists if the data is collapsed on St_h, i.e. in both data sets the peaks are located about $St_h \approx 0.002$ for low-frequency and $St \approx 0.02$ for high-frequency peak. This observation further supports the premise that the cavity break-up is predominantly governed by the overlying boundary layer turbulence, as the δ/h ratio was held approximately constant for both facilities. Due to the three-dimensional character of the re-entrant flow observed in the small-scale tests (see section §3.3.1) the re-entrant jet length could not be established and thus could not be used for data reduction as was the case in section §3.3.5.

In figure 3.25 a series of cross-correlation functions between the pressure measurements from the most downstream ($x/l_c = 1.2$) and third most downstream ($x/l_c = 1.07$) dynamic pressure sensor is presented for the whole range of investigated Re_h in ventilated flow. Two features of these curves can be used to provide additional flow characterization. Firstly, the position of the cross-correlation maxima on the horizontal axis defines the lag between the two signals ($\Delta t_1'$), from which the advective velocity can be calculated due

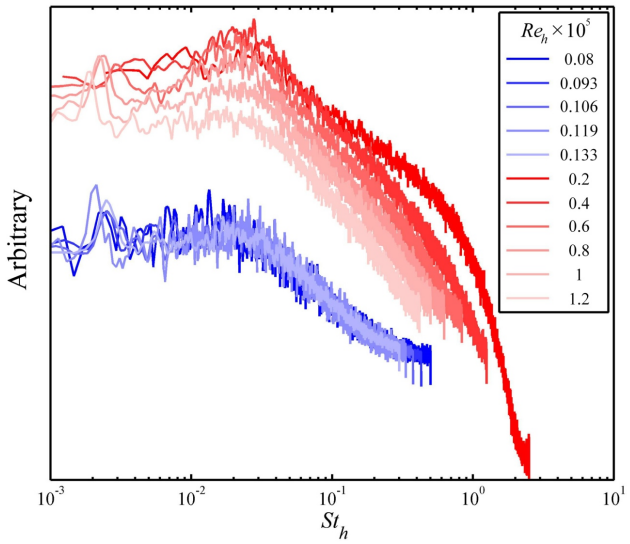

Figure 3.24: The wall pressure power spectra from forward-lit high-speed imaging across the range of Re_h investigated in the large-scale (red lines) and small-scale (blue lines) experiments. The image intensity of a single pixel in the cavity wake is extracted from 100 s high-speed imaging (acquired at 1 kHz) from large-scale test and 4 s high-speed imaging from small-scale test (acquired at 4 kHz). The spectra from small-scale test is smoothed by averaging the spectra at each span-wise pixel for a constant stream-wise location.

to known sensor separation. Secondly, the horizontal extent, i.e. the width, of the peak can be used to identify the dominant length scale of the structures shed into the cavity wake.

A comparison between the U_{adv}/U_∞ obtained from space-times plots and pressure sensor cross-correlation across the range of investigated Re_h values for ventilated flow is given in figure 3.26a. A strong correlation between the results from two methods can be observed, with approximately constant value of $U_{adv}/U_\infty \approx 0.56$ obtained in both cases. A discrepancy in the cases with two lowest Re_h values can be attributed to the absence of the high-frequency wall pressure spectra peak leading to insufficient number of events for the cross-correlation algorithm to provide a meaningful result.

The width of the main cross-correlation peak between the points with zero value of cross-correlation function (w_{st}) can be multiplied by U_{adv} to calculate the largest length scale of structures (l_{st}/h) from the turbulent cavity break-up. For comparison the length scales obtained from the POD second mode (first shedding mode) are presented. In both cases, the l_{st}/h decreases approximately as a linear function of Re_h. The l_{st}/h value for low Re_h obtained from the pressure cross-correlation differs from the observed trend, with the difference arising from the reduced cross-correlation between two pressure signals at low Re_h values. A favourable agreement between the results from the two methods can be seen from figure 3.26b, with the difference in the l_{st}/h absolute value influenced by the definition of the threshold parameter (i.e. the cross-correlation function threshold value) in the cross-correlation analysis.

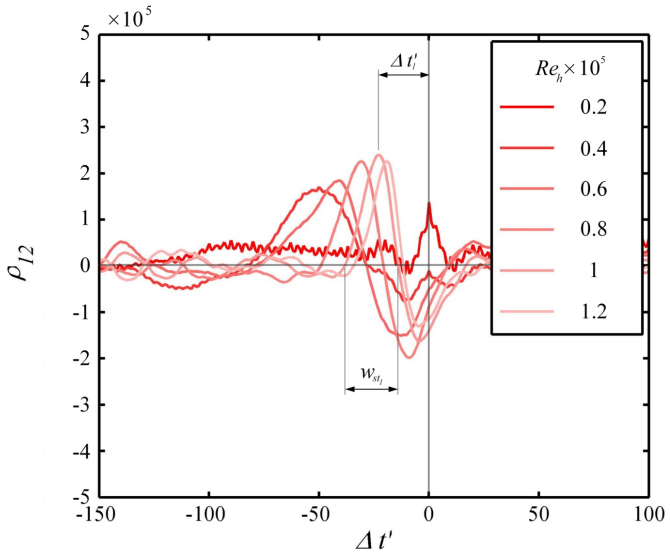

Figure 3.25: Cross-correlation function between the pressure signal from the most downstream and third most downstream dynamic pressure sensor for the investigated range of Re_h in ventilated cavity flow. The definition of lag between the sensors ($\Delta t_1'$) and the cross-correlation peak width (w_{st_1}) is denoted for $Re_h = 1 \times 10^5$. (large-scale experiment)

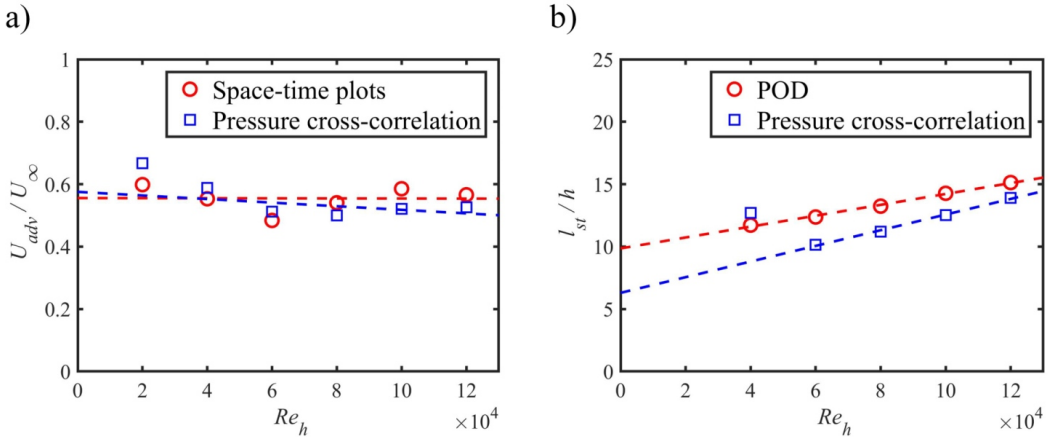

Figure 3.26: a) comparison of U_{adv}/U_∞ obtained from the space-time plots and the time-lag from cross-correlation of signals from pressure sensor mounted at fixed stream-wise distance across the range of Re_h. b) l_{st}/h obtained from the width of main peak of cross-correlation function between the two pressure sensors and POD technique across the range of Re_h. (large-scale experiment)

3.4 Conclusions

The topology and unsteady behaviour of ventilated and natural cavity flows over a fixed height 2-D wall-mounted fence were investigated for fixed length cavities using high-speed and still imaging, X-ray densitometry and dynamic surface pressure measurements in two experimental facilities. Based on the observations of cavity topology and shedding mechanisms, the examined flow is classified within the 'thin non-auto-oscillating cavity' regime (Callenaere et al., 2001). Two main features contributing to cavity unsteady behaviour were found, irregular small-scale shedding of gaseous/vaporous structures at the cavity closure and larger-scale oscillations in size of the re-entrant jet affected region. From the spectral analysis of wall pressure fluctuations, the small-scale shedding is associated with a high-frequency broad-band peak and a power law decay ($\propto St^{-7/3}$), analogous to that observed in a single-phase flow over a forward-facing step. The location of this peak collapsed for $St_h \approx 0.02$, showing that the cavity break-up is invariant of Re_h and Fr_h, and governed by the overlying turbulent boundary layer characteristics only. The re-entrant jet oscillation was observed as a low-frequency peak in wall pressure spectra, analogous to the 'flapping' instability of the recirculation zone in single-phase flow. The low-frequency peak was found to collapse for a Strouhal number based on the re-entrant jet length (of about 0.1). The re-entrant length jet was found to have a linear dependence on free-stream velocity, analogous to the recirculation zone length in gravity dominated super-critical open-channel flow. This similarity indicates that the low-frequency oscillation of the re-entrant jet is influenced by gravity (i.e. influence of buoyancy due to inclusion of the gaseous/vaporous phase of much lower density), which is in contrast with the observations from single-phase flow where it was found to be independent of free-stream velocity. Another gravity induced effect was observed through a significant change in the cavity break-up mechanism (wave pinch-off rather than turbulent break-up) and spectral content for $Fr_H \leq 1$ (the conditions analogous to sub-critical open-channel flow). In spite of the fundamental difference between the two flows, overall cavity flow over a wall-mounted fence was found to be similar in many respects to that in single-phase flow, where the difference in behaviour could be attributed mainly to the influence of buoyancy.

From the qualitative and quantitative (POD) wake analysis it was found that the number and size of shed structures increases following an increase in free-stream velocity for the ventilated case, but it remains nominally constant in naturally cavitating flow due to condensation of vaporous structures. Advective and re-entrant flow velocities were investigated using space-time plots and cross-correlation between the simultaneous pressure measurements from sensors positioned at different stream-wise locations along the test-section centre-line. From both methods, approximately constant U_{adv}/U_∞ ratio was found across the range of investigated Re_h, with the values about 0.56 for ventilated flow and 0.65 in the natural cavity case. Additionally, space-time plots from high-speed

shadowgraphy were used to obtain U_{rj}/U_∞, which was found to be about 0.18, for both ventilated and natural cavity flows.

Acknowledgements

The authors wish to acknowledge the assistance of Mr Robert Wrigley and Mr Steven Kent in carrying out the experiments in Univeristy of Tasmania cavitation tunnel, and Mr Kent Pruss and Miss Juliana Wu in carrying out the experiments in University of Michigan cavitation tunnel. The authors wish to acknowledge the financial support received through University of Tasmania Conference and Research Travel Funding Scheme for research trip to University of Michigan and the support of Australian Maritime College.

Chapter 4

Numerical Analysis of Ventilated Cavity Flow Over a 2-D Wall-Mounted Fence

This chapter is based on the article published in *Ocean Engineering*. The contributing authors are: L. Barbaca, B.W. Pearce and P.A. Brandner. The abbreviated version of this chapter was presented at the (peer-reviewed) 19^{th} *Australasian Fluid Mechanics Conference*, Melbourne, 8-11 December 2014. The conference paper is included in Appendix A.

The citation for the journal paper is:

Barbaca, L., Pearce, B. W., Brandner, P. A., 2017, Numerical analysis of Ventilated Cavity Flow Over a 2-D Wall-Mounted Fence, *Ocean Engineering*, **141**:143 - 153

The citation for the conference paper is:

Barbaca, L., Pearce, B. W., Brandner, P. A., 2014, Computational Investigation of Ventilated Cavity Flow Over a 2-D Wall-Mounted Fence, 2014, *in Proceedings of the* 19^{th} *Australasian Fluid Mechanics Conference, Melbourne, 8-11 December 2014*

Abstract

Ventilated cavity flow over a 2-D wall mounted fence is numerically investigated using a viscous approach. An implicit unsteady compressible solver was used with a RANS $k-\omega$ SST turbulence model and VOF approach to capture the cavity interface. The simulations

were carried out for a fixed fence height based Froude number and constant outlet pressure. Cavity topology, wall pressure distributions and the resulting hydrodynamic forces were determined as a function of ventilation rate, degree of fence immersion in the oncoming wall boundary layer and degree of confinement of the flow domain. It was found that with an increase in ventilation rate, lift increases and drag decreases resulting in a greater hydrodynamic efficiency (lift to drag ratio) of the fence-wall system. With increase in immersion of the fence in the boundary layer, both lift and drag decreased, while the lift to drag ratio increased. Variation in the degree of confinement had a large influence on the flow, with the reduction in lift and hydrodynamic efficiency observed for the more confined conditions.

4.1 Introduction

Ventilated (also termed 'artificial') cavities can be utilized for drag reduction in marine applications. Drag can be decreased by forming an air bubble/layer between the solid surface and water to reduce the skin friction (Ceccio, 2010), or by increasing the pressure on the downstream surface of the cavitating body to reduce the form drag (Franc and Michel, 2004). The main parameter used to characterize these flows is the cavitation number, $\sigma_c = (p_\infty - p_c)/0.5\rho U_\infty^2$, where p_∞ is the reference free-stream pressure, p_c is the pressure inside the cavity, ρ is the liquid density and U_∞ is the reference free-stream velocity. Similar cavities can be formed naturally (vapour filled) when the liquid is subjected to vapor pressure (p_v), with in this case $\sigma_c = \sigma_v = (p_\infty - p_v)/0.5\rho U_\infty^2$. It has been shown that, for the same σ_c value, natural and ventilated cavities exhibit comparable behaviour except for the differences in closure physics (May, 1975; Kunz et al., 1999).

To sustain a cavity long enough to be applicable for drag reduction purposes, σ_c has to be in the order of 0.1 (Kawakami and Arndt, 2011). As p_v is small, to naturally achieve such a low σ_c in a practical flow, a high free-stream velocity (i.e. $>$ 100 knots) is required. In the ventilated cavity case p_c is controlled by the flux of injected air, and such low σ_c values can be achieved independent of free-stream conditions. Consequently, devices utilising ventilation can be efficiently used at lower operating velocities and/or higher free-stream pressures (i.e. deeper submersion), leading to a much broader range of potential application.

Depending on the location of the cavity closure, a cavity is classified as either a 'partial' cavity or a 'supercavity'. The former is defined where the closure region is located on the surface of the body and if the closure is rather downstream in the wake it is termed a supercavity (Franc and Michel, 2004). The application of both ventilated partial and supercavitation to high-speed underwater bodies has been of particular interest post the second world war for military applications (Reichardt, 1946; Waid, 1957), but also there

has been some interest in a commercial context (Brentjes, 1962).

Past studies into ventilated flows have mainly focused on the reduction of skin friction in hydrodynamic applications. There has been extensive research into the use of axisymmetric ventilated cavities for drag reduction of underwater projectiles in the second half of last century, with an ongoing interest in the topic. A review of basic physical properties and calculation methods for axisymetric ventilated cavities is given by Semenenko (2002). The other application of substantial interest has been in the use of ventilated partial cavities on the underwater part of ship hulls, referred as 'air-lubrication'. The injection of air is used to create a stable cavity for ships operating in the range of speeds that are not sufficient to enable detachment of a natural cavity from a geometric discontinuity in the hull. To date several semi-displacement and planning boats using this phenomenon have been built, with a reported resistance decrease in the range of 10-30% (Latorre, 1997; Butuzov et al., 1999; Matveev et al., 2009). Additionally, some work has been done on implementing air-lubrication system on full displacement ships in a commercial context (Mizokami et al., 2010; Surveyor, 2011). A comprehensive overview of the work done in this field is presented in a review article by Ceccio (2010). Kopriva et al. (2008) proposed the use of ventilation on low-drag partially cavitating hydrofoils with a smooth cavity reattachment (Amromin et al., 2003) for application on high-speed vessels.

Alternatively, ventilation has been also applied as a form drag reduction technique. Based on this technique a class of lifting surfaces, described as base-ventilated hydrofoils, has been developed. These hydrofoils have a wedge shaped profile, with air injected through a thick trailing edge and a cavity detaching from the trailing edge geometric discontinuities. Such foils can be utilized on hydrofoil supported boats or for propulsion by ventilated propellers (Lang and Daybell (1961); Huang (1965); Verron and Michel (1984); Franc and Michel (2004)). More recently, a novel concept of an intercepted base-ventilated hydrofoil for ride control of a high-speed craft is proposed by Elms (1999). A related topic of the flow around a retractable fence fitted to the transom of a marine craft, also known as an 'interceptor' (Faltinsen, 1996), can be observed as a special case of an 'infinite' ventilated cavity. Some numerical investigations on interceptor flows are reported by Brizzolara (2003) and Molini and Brizzolara (2005).

Within the scope of the present study ventilated cavity flow over a 2-D wall mounted fence is investigated. This study is a continuation of the research on cavitating flow over a wall mounted fence that has been performed at the Australian Maritime College (AMC) Cavitation Research Laboratory (CRL). To date, a several reports on numerical (Pearce et al., 2010; Pearce and Brandner, 2014; Barbaca et al., 2014) and experimental (Barbaca et al., 2016) work have been published. The interest in this flow is based on the potential use of a retractable fence ('interceptor') attached to the trailing edge of a base-ventilated hydrofoil for a rapid generation of bi-directional lift with a minimum drag penalty. This topic has been of an ongoing interest at the AMC with a numerical (Pearce and Brandner,

2015b) and preliminary experimental (Pearce and Brandner, 2012a,b) studies reported.

The main objective of the present work is to investigate the effect of fence immersion within the oncoming wall boundary layer on the flow. As the fence is attached to a flat wall (i.e. isolated from the foil), these results are also relevant for flow over an interceptor attached to a ship hull (either used for lift generation, or ventilated cavity drag reduction). Furthermore, the case studied is a canonical cavitating flow (with nominal zero streamwise pressure gradient) of basic interest and suitable for comparison of experiment and computation, which has not previously been addressed in the published literature.

Cavity topology and resulting hydrodynamic forces are examined with respect to the flux of injected air, immersion of the fence in the upstream wall boundary layer and the degree of confinement of the flow. The results are compared with potential flow predictions obtained using a Boundary Element Method (Pearce and Brandner, 2014) and analytical predictions from free-streamline theory (Brennen, 1995). Some comparison with the experimental results from the cases with similar geometries is provided. The present numerical investigations will be complemented with a future experimental study in a cavitation tunnel.

4.2 Numerical modelling

A schematic representation of the ventilated cavity flow over a wall mounted fence of interest here is shown in figure 4.1. A fence of a height h is immersed in the oncoming wall boundary layer of thickness δ. δ is defined as the distance from the wall where U is 99% of the free-stream velocity U_∞. Air is supplied to the wake region of the flow through the downstream face of the fence. A ventilated cavity with re-entrant jet closure is shown detaching from the fence tip at the angle β to horizontal axis. The resulting pressure signature on the wall upstream of the fence is indicated.

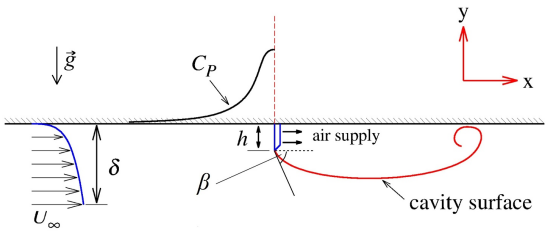

Figure 4.1: Sketch of a wall mounted fence immersed in the oncoming wall boundary layer with a ventilated cavity detaching from the sharp fence tip. Air is supplied from the downstream face of the fence. The pressure distribution on the upstream wall is shown. The origin of the coordinate system is at the fence/wall junction

In the case of ventilated cavities, for constant free-stream conditions, the cavitation

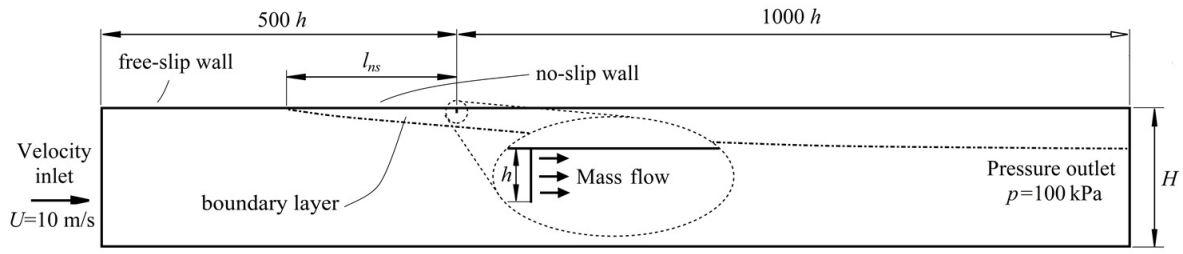

Figure 4.2: Computational domain with geometric parameters and boundary conditions shown

number, σ_c, is controlled by the air flow rate. Ventilated air flow data is presented in terms of a volumetric flow rate coefficient, $C_{Qv} = Q_m/\rho_{air}U_\infty S$, where Q_m is the air mass flow rate, ρ_{air} is the air density and S is the reference area (fence height multiplied by unit width). For the consideration of the effect of the fence immersion in the wall boundary layer an additional dimensionless parameter is defined, the boundary layer thickness to fence height ratio, δ/h. Influence of the confinement is evaluated through the use of the dimensionless ratio between domain and fence height (H/h). A Froude number based on fence height, $Fr = U_\infty/\sqrt{gh}$, where g is gravitational acceleration, is also applicable.

Commercial Computational Fluid Dynamics (CFD) software, CD Adapco STAR-CCM+, was used in the present study. For later comparison with experimental results a rectangular computational domain of finite height was chosen for the numerical analysis (figure 4.2). The domain height, H, was varied between $40h$ and $200h$, and the fence, modelled as 10 mm high and 0.1 mm thick, was attached to the upper domain boundary. The domain inlet and outlet were positioned sufficiently away from the fence to minimise their influence on the flow, located $500h$ and $1000h$ respectively. For spatial discretization, a structured hexahedral mesh with prism layer cells in the boundary layer region was used. To resolve the flow a first order implicit unsteady finite volume method with second order spatial accuracy was employed. Water was defined with constant density and air as an ideal compressible gas. The interface between the phases was captured using a VOF method based on the volume fraction equation (Hirt and Nichols, 1981). Surface tension and gravity effects were included in the model. For the consideration of viscous effects a RANS approach with the SST (Menter) $k-\omega$ turbulence model was used.

Water enters the domain through the constant velocity inlet, with the velocity set to 10 m/s ($Fr = 31.93$) for all cases. The flow rate of the air injected through the downstream face of the fence was varied between 0.01 kg/s and 0.09 kg/s (giving $0.084 < C_{Qv} < 0.751$), except for the cases with the thinnest boundary layer where additional air was needed for the cavity to achieve the 'infinite' length. The domain outlet was defined as a constant pressure outlet, with the pressure set to 100 kPa for all cases (giving a free-stream cavitation number, based on vapour pressure, $\sigma_v \cong 1.95$). A range of unperturbed boundary layer thicknesses at the fence position ($x = 0$) was achieved by changing the

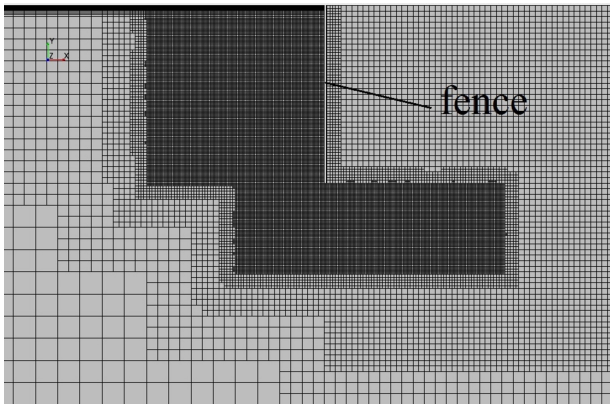

Figure 4.3: Local refinement of the mesh in front of the fence and in the cavity region. The prism layer on the upstream wall is also shown.

length of the no-slip wall condition (l_{ns}) upstream of the fence (figure 4.2). The part of the wall upstream of l_{ns} was prescribed as a free-slip wall with no boundary layer present. With this technique, δ/h values between 0 and 10 were achieved for a constant fence height and constant free-stream conditions. For investigating the effect of blockage four domains of different height H were created, giving confinement ratios, H/h, ranging between 40 and 200. The reference pressure (p_∞) was defined as the minimum pressure value on the tunnel wall upstream of the fence. Existence of minimum pressure value is due to the boundary layer growth imposed pressure signature. The reference free-stream velocity (U_∞) was chosen as the value on the domain centreline, $100h$ upstream of the fence.

A convergence analysis was undertaken for both temporal and spatial discretization for the case with $\delta/h = 2$, $C_{Qv} = 0.03$ and $H/h = 60$. Time steps ranging between 0.5 and 2 ms were analysed and a time step of 1 ms gave results (drag coefficient) within 1% of the independent solution (table 4.1). Spatial convergence was analysed with the number of cells varying between about 0.2 and 4×10^6. It was found that a mesh consisting of just over 1.8×10^6 cells gave results (drag coefficient) within 1% of the grid independent solution (table 4.2). Prism layer parameters were chosen to achieve $y^+ < 1$ for the lower wall (with the fence attached) and $y^+ \approx 30$ for the upper wall (without fence). The mesh was refined in the cavity region, with additional refinement upstream of the fence to resolve the separation bubble (figure 4.3). Computational time needed to obtain a solution, using 12 cores on a multi-node cluster, varied between 20 to 30 hours. This was mainly dependant on the time needed for the cavity to fully develop, the length of which was dependant on flow conditions and geometry.

Some comparison of the present viscous data has been made with results obtained using a potential flow analysis (Pearce and Brandner, 2014). Further explanation of the particular method used can be found in Pearce and Brandner (2015a).

Time step (ms)	C_D	Error (%)
2	0.623	2.52
1	0.608	0.57
0.5	0.611	-

Table 4.1: Results from the temporal convergence analysis for drag coefficient.

Cell count ($\times 10^6$)	C_D	Error (%)
0.2	0.602	2.49
0.6	0.618	1.63
1.8	0.608	0.67
4	0.612	-

Table 4.2: Results from the spatial convergence analysis for drag coefficient.

4.3 Results and Discussion

4.3.1 Cavity topology

A typical result for the flow topology in the region upstream of the fence is shown in figure 4.4. As is well-known from single phase flow studies of similar geometry, a separated flow region (separation bubble) is present upstream of the fence. A typical separation bubble consists of a main vortex accompanied by the secondary counter-rotating vortex present at the wall/fence junction. The separation zone size may be quantified using the location of stagnation points and it varies with the boundary layer thickness, but only for $\delta/h < 1$, with the largest separation zone present for $\delta/h = 0.1$ (figure 4.5). Stagnation points for the main vortex are found at $x \approx -1.73h$ on the upstream wall and $y \approx 0.57h$ on the fence for large δ/h. The largest separation zone (when $\delta/h = 0.1$) has stagnation points located at $x = -1.96h$ on the wall and $y = 0.71h$ on the fence. The size of the secondary vortex exhibits similar behaviour to the size of the main vortex. Typical stagnation points are positioned at $x \approx -0.1h$ on the wall and $y \approx 0.16h$ on the fence, with the larger values present for thin boundary layers. It was found that the size of the separation bubble was not affected by the rate of air ventilation (figure 4.5).

The cavity smoothly detaches from the fence tip and the gas-liquid interface is present as a smeared zone in contrast with the sharp free surface as represented in the potential flow formulation. In a physical flow the cavity surface can range from a glassy laminar interface to more turbulent broken-up thicker inter-facial regions (Pearce and Brandner, 2012b; Pearce et al., 2015; Barbaca et al., 2016).

The detachment angle, β (see figure 4.1), is defined here as the angle between the detachment streamline at the fence tip and the horizontal axis. The angle at which cavity detaches from the fence tip is in direct correlation with the size of the separation zone. It was found that the presence of a larger separation zone results in steeper cavity

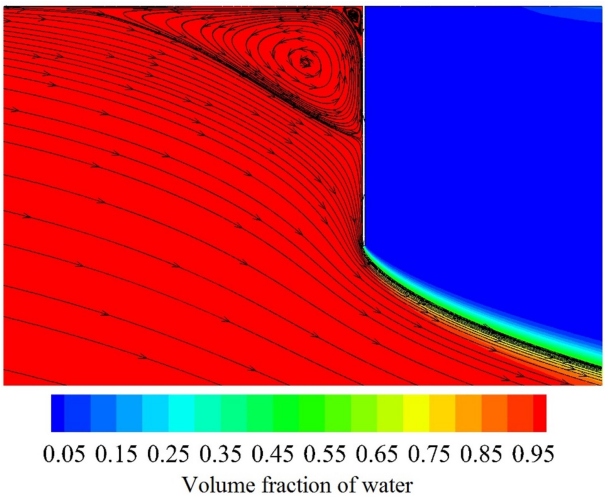

Figure 4.4: Streamlines depicting flow topology upstream of the fence ($\sigma_c = 0.2368, \delta/h = 2$) showing the region of flow separation which typically extends about $0.5h$ from the wall along the fence face. The cavity surface, detaching from the fence tip, is also shown from the plot of volume fraction contours.

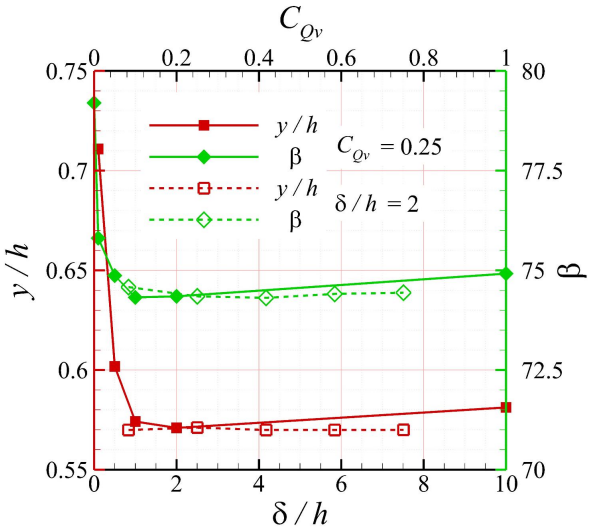

Figure 4.5: Location of the separation zone stagnation point along the fence face and the detachment angle value (β) with varying δ/h (solid lines, $C_{Qv} = 0.25$) and variable C_{Qv} (dashed lines, $\delta/h = 2$).

detachment (figure 4.5). The steepest detachment is present for the case with no boundary layer and no separation bubble, with the $\beta = 79.2°$. β decreases with increase in δ/h and remains relatively constant when δ/h reaches 1, with just the slight increase for the thickest boundary layer. The lowest value of the cavity detachment angle is found to be approximately 74.3°. β is found to be independent of the variation in C_{Qv} for constant δ/h (figure 4.5).

Unlike naturally forming cavities, i.e. vapour filled cavities forming solely due to flow conditions, the cavity topology of a ventilated cavity can be altered by varying the ventilation rate for otherwise constant flow conditions. The dependence of σ_c on volumetric flow-rate coefficient C_{Qv}, for a range of boundary layer thickness to fence height ratios is shown in figure 4.6a. A vertical asymptote is present in all conditions as

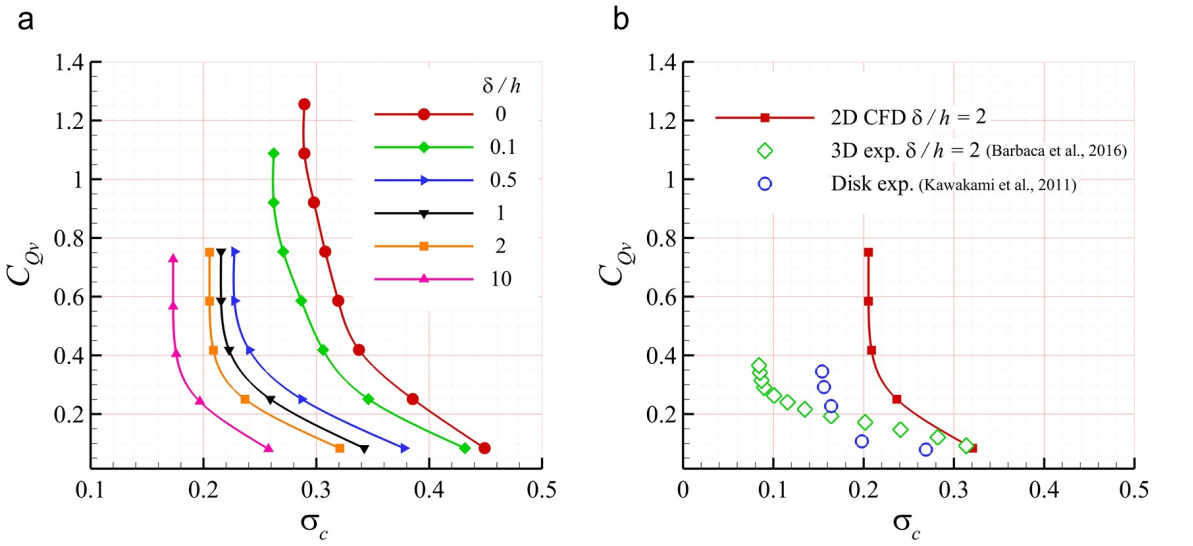

Figure 4.6: a) Relation between σ_c and C_{Qv} for various δ/h. All data are for a constant confinement, $H/h = 60$. The vertical part of the curves represents blocked flow conditions. A lower σ_c value is achieved for the same C_{QV} with the deeper immersion of the fence in the oncoming boundary layer; b) A comparison of the CFD results for 2D wall mounted fence with experimental data for a 3D wall mounted fence (Barbaca et al., 2016) with $\delta/h = 2$, and experimental data for a ventilated axisymmetric disk (Kawakami and Arndt, 2011).

σ_c reduces, representing a lower limit $\sigma_c = \sigma_{min}$, dependent on the prescribed geometry and flow conditions. When σ_{min} is reached the flow is described as 'blocked' (Brennen, 1995), analogous to the chocked condition of compressible flow through valves and orifices, and is a function of the degree of confinement of the flow domain. The blockage ratio for the present case was set to the value of $H/h = 60$. The further analysis of blockage effects will be discussed in section 4.4.

Typical cavity topologies, represented as volume fraction contours, for differing air ventilation rates are shown in figure 4.7. Here the reference flow velocity and pressure have been held constant and thus σ_c varies proportionally with C_{Qv}. The cavity closure on the downstream wall exhibits a typical re-entrant jet behaviour (Callenaere et al., 2001). This re-entrant jet flow diverts liquid back upstream along the wall into the cavity. For short cavities ($l_c/h < 50$) the re-entrant jet transports liquid almost up to the fence with most of the cavity consisting of a liquid/gas mixture. For the longer cavities, the re-entrant jet only extends a limited length, leaving the upstream cavity region filled with air only.

Depending on the flow conditions, gas discharge from the cavity closure consists of a constant stream of air entrained into the flow and discrete mixed-phase structures of a variable size detaching periodically from the cavity. For sufficiently long cavities ($l_c/h > 150$), the re-entrant jet is partially separated away from the wall (i.e. falling towards the cavity interface) at several points inside the cavity due to the effect of gravity. These points represent the inception zones from which detaching mixed-phase structures

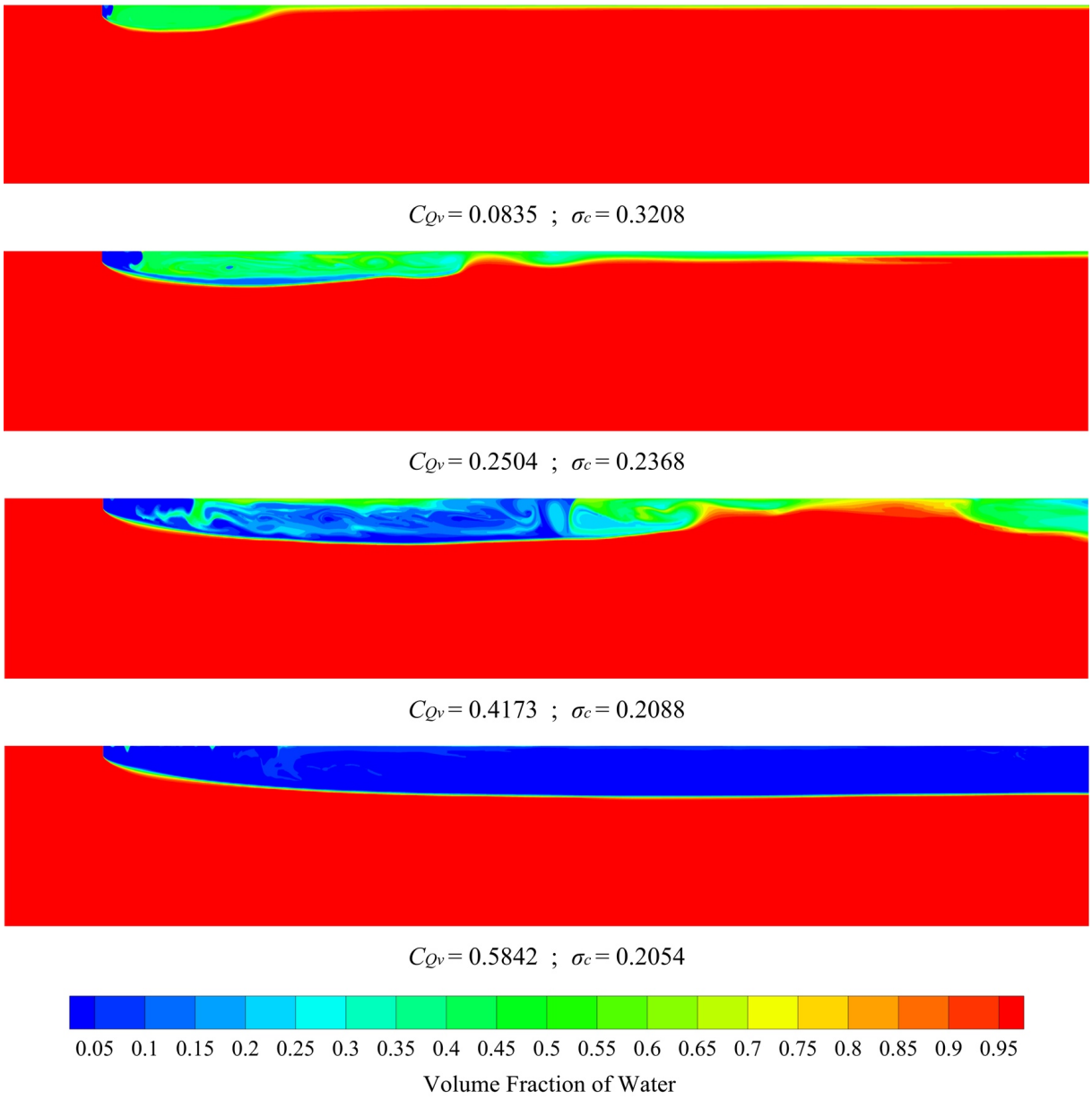

Figure 4.7: Cavity topologies represented with volume fraction contours throughout the range of cavitation numbers, for the constant $\delta/h = 2$ and $H/h = 60$. The evolution of the cavity with the decrease in σ_c can be seen. The re-entrant jet covers most of the short cavities, and just a portion of the length for the longer one. Cavity grows 'infinitely' when σ_{min} is reached. The plot vertical scale is twice the horizontal scale.

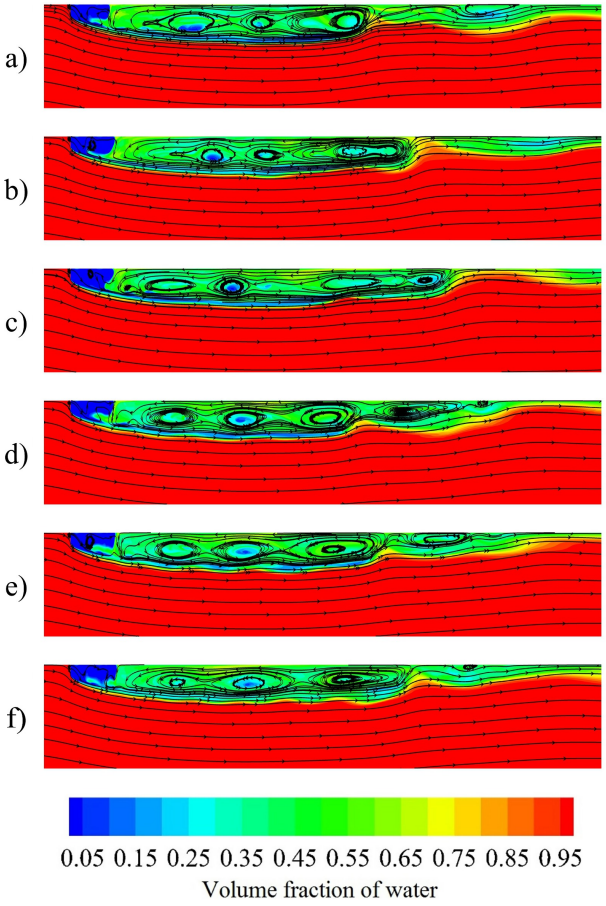

Figure 4.8: A typical example of the gas discharge process shown as a sequence, with instantaneous streamlines used for visualization ($\delta/h = 2$, $H/h = 60$, $C_{Qv} = 0.25$). The process starts just after the previous bubble is entrained into the flow (a). The cavity grows to its maximum length (b-c) and the bubble closest to the closure elongates, forming a neck with the next bubble upstream (d), until it is entrained (e-f). The recirculation zones within the re-entrant jet region represent the origins of future shedding events. The plot vertical scale is twice the horizontal scale.

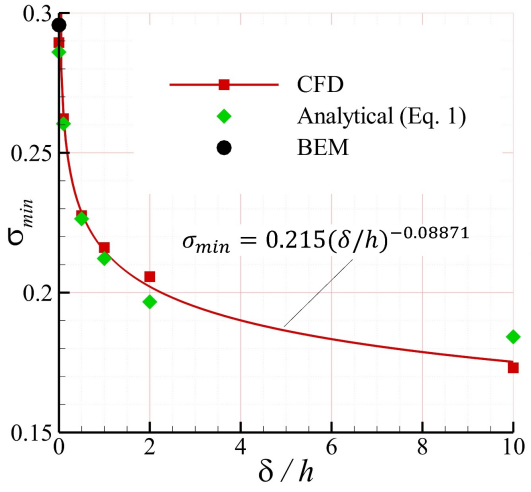

Figure 4.9: Dependence of σ_{min} on δ/h with a power law curve of best fit (for $H/h = 60$). The analytical data for the same blockage conditions is calculated from Eq. 4.1 using the cavity thickness obtained for the examined flow conditions (i.e. t_c value from the CFD data). BEM data (Pearce et al., 2010) for the case with no boundary layer (for $H/h = 60$) is also shown.

form. A typical example of the gas discharge process is shown as a sequence in figure 4.8. Instantaneous streamlines are used for visualization of the process dynamics. Figure 8a shows the cavity just after a large structure has been entrained into the flow. The cavity length is at minimum and within the large re-entrant jet zone several recirculating bubbles, which represent the origins of future shedding events, can be observed. After a shedding event, the cavity starts to re-grow (figure 4.8b-c) until it reaches a maximum length (figure 4.8d), just before the next shedding event occurs. During the growth phase, the recirculating bubble closest to the closure starts to elongate, forming a neck with the adjacent upstream bubble. The neck eventually disappears (figure 4.8e) and the separated bubble is entrained into the main flow (figure 4.8f). During the process a new recirculating bubble forms upstream inside the re-entrant jet zone and this cycle repeats. The mixed-phase structures detaching from the cavity vary in size and during a large bubble shedding event shown in the sequence a much smaller scale event can be also observed (figure 4.8c-d)(also see the video provided in supplementary data).

Figure 6a shows a consistent trend in the dependence of σ_c on C_{Qv} throughout the range of examined δ/h values. For a constant C_{Qv} value, a lower σ_c is achieved if the fence is immersed deeper in the oncoming boundary layer. The cases of $\delta/h = 0$ and 0.1 depart slightly from this trend, probably due to a change in the flow in the separation zone just upstream of the fence, described above.

From figure 4.6a it is apparent that for larger δ/h a lower σ_{min} value is obtained. σ_{min} is found to decrease following a power law trend ($\sigma_{min} = 0.215(\delta/h)^{-0.08871}$). In (Brennen, 1995), an analytical equation, derived from free-streamline theory, is given for a prediction of minimum cavitation number in blocked flow. Free-streamline methods tend to give reasonable approximations for developed cavitating flows (e.g. Mäkiharju et al. (2013a)), as long as the free-streamline detachment location is fixed by the geometry of the body. In the present case the detachment point is fixed at the fence tip. For this particular flow the equation can be written as

$$\sigma_{min} = 1 - \left(1 - \frac{t_c}{H}\right)^2 \tag{4.1}$$

where t_c/H is the ratio between the maximum cavity and the flow domain cross-sectional areas.

From figure 4.9 it can be seen that the results from CFD data and analytical prediction for σ_{min}, for the same blockage ratio ($H/h = 60$), are in good agreement. The difference becomes more pronounced with increased boundary layer thickness, which is not unexpected as the analytical prediction is based on inviscid computations. The σ_{min} obtained with $\delta/h = 0$ and $H/h = 60$ from CFD and BEM (Pearce et al., 2010) compare favourably, with values of 0.289 and 0.296 respectively.

As mentioned above, maximum cavity thickness is the parameter responsible for the

shift in σ_{min} in figure 4.6a. This suggests that t_c is controlling the shift in σ_c on C_{Qv} dependence throughout the entire range of C_{Qv} values. In figure 4.10, t_c as a function of σ_c is shown with similar behaviour observed for all cases examined. It can be seen that for the same σ_c, cavity thickness decreases with increase in fence immersion within the boundary layer. This decrease in the cavity thickness leads to a decrease in blockage, and subsequently a lower σ_c value can be achieved for the same C_{Qv}, as depicted in figure 4.6a. The increase in the cavity thickness for a lower δ/h value is a consequence of the steeper cavity detachment angle from the tip (β), already discussed above. Cavity thicknesses obtained with the potential flow analysis are larger than the ones obtained with the CFD analysis for the case with no boundary layer present (figure 4.10). A closer agreement exists for the low σ_c values, as the BEM formulation becomes less accurate for the smaller cavities present at the higher cavitation numbers.

As there are no published experimental data that can be used for direct validation of the present 2D numerical results, experimental data from similar 3D flows are used for a comparison. There are some differences between the 2D and 3D flows including cavity closure mechanisms at low Fr and blockage ratios and resulting effect. Despite these differences each of the flows have overall similar behaviour and reasonable comparison of the trends present in the mean data can be made. In figure 4.6b a comparison of the numerical results for a 2D wall mounted fence from the CFD simulations with experimental data for a 3D wall mounted fence (Barbaca et al., 2016) for the same $\delta/h = 2$, and experimental data for ventilated axisymmetric disk (Kawakami and Arndt, 2011) is shown. It can be seen that all curves follow approximately the same trend with vertical asymptotes present for the 'blocked' conditions. Due to a lesser confinement in the experimental studies, the reported cavitation number values are lower.

It is common that in drag reduction applications with ventilated backward facing steps (BFS) negative cavitation numbers occur (Lay et al., 2010; Matveev and Miller, 2011). In the present study only positive cavitation numbers are observed. Although these two flows may seem similar, the fundamental difference in the closure physics is responsible for this contrast in the resulting cavity pressure. Unlike large cavities with smooth and stable closure present in the BFS flows, the cavities in the present study are shorter and have an unsteady re-entrant jet closure. The existence of a re-entrant jet leads to continuous air entrainment into the main flow and ensures an under-pressure (positive cavitation number values) inside the cavity. On the other hand, the smooth cavity reattachment, achieved using a sloped beach positioned at the cavity closure region to control the cavity break-up, ensures limited to no air loss in a BFS flow, resulting in over-pressure inside the cavity and consequently negative cavitation numbers.

As the closure region consists of a mixed phase, volume fraction contours could not be used to reliably determine the cavity length. Instead, the location of the stagnation point (i.e. point of maximum pressure on the wall) has been used as the point of cavity

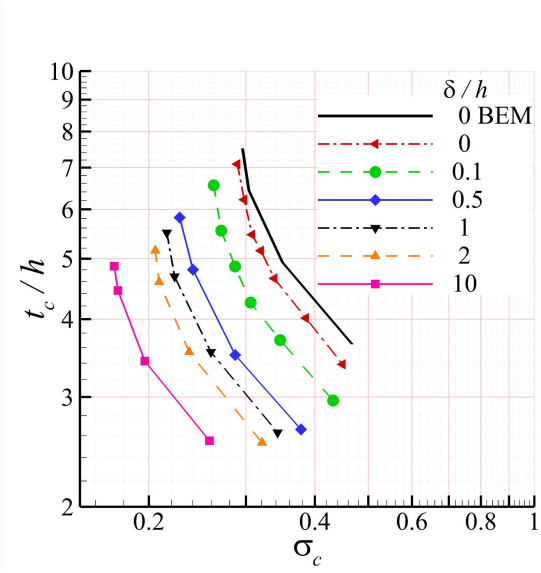

Figure 4.10: Cavity thickness as a function of σ_c for the cases with varying δ/h and for $H/h = 60$. Potential flow data (BEM) is shown for comparison.

closure. This location is where the flow divides forming the re-entrant jet/cavity and wake regions. Time averaging was necessary to establish a mean value of the length for the cavities with detaching structures. The cavity length oscillations were typically in the order of $20 - 25\%$ of the mean cavity length.

The dependence of cavity length on cavitation number is shown in figure 4.11a. The viscous data obtained from the CFD simulations exhibits a similar behaviour to the potential flow BEM (Pearce and Brandner, 2014). Due to the effect of confinement, cavity length becomes 'infinite' when σ_{min} is reached. In an unbounded flow the cavity length follows a power law as a function of σ_c (Franc and Michel, 2004; Pearce and Brandner, 2014). The effect of an increase in δ/h can be observed as a right to left translation of the curves, i.e. the same cavity length is achieved at a lower cavitation number. A slightly different behaviour can be observed in the CFD data with the thinnest boundary layer and for no boundary layer at all. The probable reason for such behaviour is, already mentioned, different upstream separation bubble topology. Also, it can be seen that results for the zero boundary layer cases obtained with CFD and potential flow analysis are in good agreement.

In figure 4.11b comparisons are made of the numerical results for the 2D wall mounted fence from CFD simulations with; inviscid data (BEM) for the infinite flow, experimental data for 3D wall mounted fence (Barbaca et al., 2016) for the same $\delta/h = 2$, experimental data for ventilated axisymmetric disk (Kawakami and Arndt, 2011) and experimental data for ventilated 2D wedge (Waid, 1957). It can be seen that curves approximately follow the same trend, with cavity length increasing 'infinitely' when the flow becomes 'blocked'. The shift along the σ_c axis is dependent on the confinement conditions of a particular flow, as discussed above.

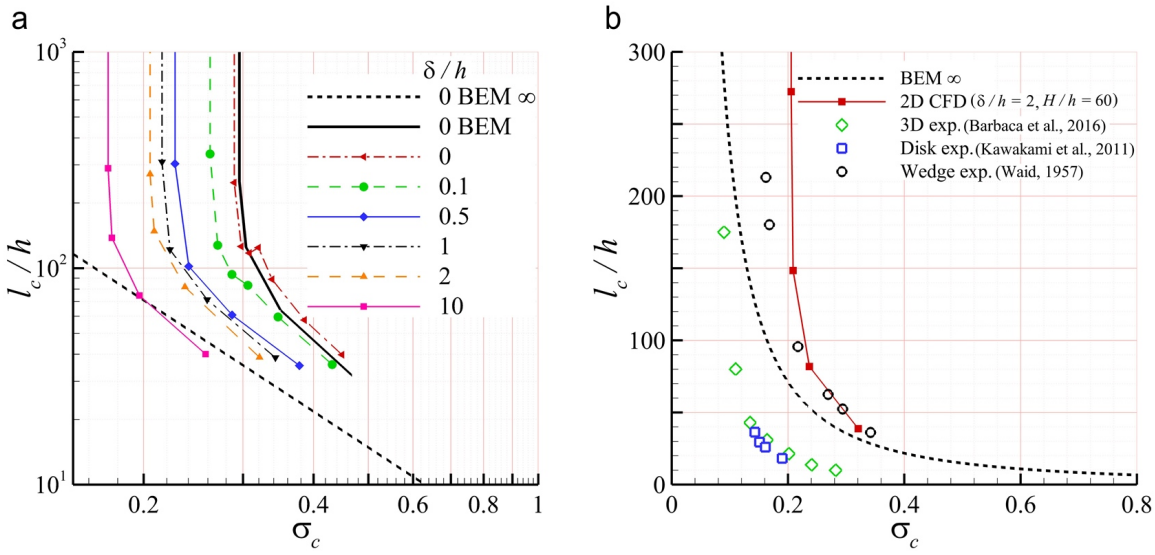

Figure 4.11: a) Cavity length as a function of σ_c for varying δ/h and constant $H/h = 60$. Inviscid data (BEM) for the same blockage ratio and the infinite flow cases ($l_c = 4.54\sigma_c^{-1.71}$ (Pearce et al., 2010)) are also shown; b) Comparisons of the CFD results for the 2D wall mounted fence with; inviscid data (BEM) for the same blockage ratio and the infinite flow, experimental data for a 3D wall mounted fence (Barbaca et al., 2016) for the same $\delta/h = 2$, experimental data for ventilated axisymmetric disk (Kawakami and Arndt, 2011) and experimental data for ventilated 2D wedge (Waid, 1957).

4.3.2 Upstream wall pressure signature

The influence of the ventilation rate on the wall pressure distribution upstream of the fence, and ultimately on the lift, is central to assessing the hydrodynamic performance of the wall/fence/cavity system. In the present study ventilated cavity flow over a wall mounted fence is investigated in the context of an 'interceptor' type device. The relatively short cavity length needed to achieve the primary goal of drag limitation (by ventilation) results in a large portion of the cavity being affected by an unsteady re-entrant jet. The unsteady and non-uniform pressure signature (i.e. pressure peaks and troughs) on the re-entrant jet affected part of the downstream wall results in a nominally zero lift contribution. On this basis an analysis of the downstream wall pressure distribution has not been presented.

In figure 4.12 a typical plot of the pressure distribution (with $C_p = (p - p_\infty)/0.5\rho U_\infty^2$), along the upstream wall, for a range of ventilation rates (with constant $\delta/h = 2, H/h = 60$) is shown. To normalize the results, the pressure gradient imposed by the boundary layer presence in the domain without the fence was subtracted from the resulting pressure distribution on the upstream wall. The general behaviour is for the pressure to be constant up to one fence height from the fence and then reduce exponentially to a nominal zero value ($C_p = 0.001$). A C_p of 0.001 was chosen as a limit to define the length of upstream wall (l_{wall}) affected by the presence of the fence under differing flow conditions. It was found that with increase in C_{Qv} l_{wall} increased, but the rate of increase reduces to zero as $\sigma_c \rightarrow \sigma_{min}$. Typical results show l_{wall} increasing by about 7% over the C_{Qv} range

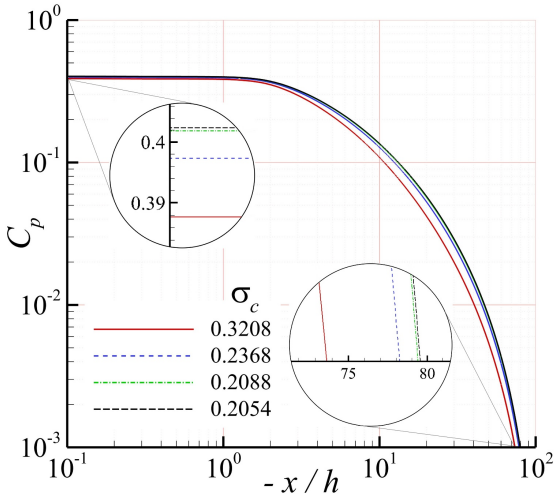

Figure 4.12: Wall pressure distribution upstream of the fence for varying C_{Qv} and constant $\delta/h = 2$ and constant $H/h = 60$. Insets provide more detailed information about $C_{p_{max}}$ and l_{wall} behaviour.

investigated up to maximum of about $80h$ (see lower inset in figure 4.12). Also, of interest is the maximum value of the pressure coefficient, $C_{p_{max}}$, at $x/h = 0$ (i.e. at the wall/fence junction). $C_{p_{max}}$ behaves similarly to l_{wall} with increasing C_{Qv}, reaching an asymptotic value with the $\sigma_c \to \sigma_{min}$. Overall increase in the $C_{p_{max}}$ is about 4%, with the maximum value just over 0.4 (see upper inset in figure 4.12). The $C_{p_{max}}$ is reduced in comparison with the inviscid flow prediction which has full stagnation point at the fence/wall junction, i.e. $C_{p_{max}} = 1$, consequently reducing the lift (normal force) generated on the wall.

Similarly, influence of the ventilation rate on the pressure distributions on the front and back faces of the fence, and therefore the resulting drag, was examined. In figure 4.13 the fence pressure distribution (front face) is presented for different ventilation rates (for $\delta/h = 2, H/h = 60$). Due to the presence of a separation zone upstream of the fence, the stagnation point, and hence the maximum pressure location, is located on the fence face and not at the wall/fence junction. The value of the pressure coefficient increases over the complete height of the fence. The difference in the value of the maximum pressure coefficient is around 3% for the range of ventilation rates examined. On the back face of the fence the pressure is nominally constant and is equal to the cavity pressure ($C_p = -\sigma_c$), which decreases with increase in ventilation rate.

The influence of fence immersion in the boundary layer on the upstream wall pressure distribution is shown in figure 4.14, both as a linear (14a) and a $log - log$ (14b) plot. The data presented is for a constant ventilation rate ($C_{Qv} \approx 0.25$) and constant blockage ratio ($H/h = 60$). The main effect that an increase in δ/h has on the upstream wall pressure distribution is a large decrease in the $C_{p_{max}}$ at the wall/fence junction. The $C_{p_{max}}$ value drops around 70%, from the $C_{p_{max}} = 1$, for the case with $\delta/h = 0$, to $C_{p_{max}} \approx 0.3$, for the case with $\delta/h = 10$. The relationship between $C_{p_{max}}$ and δ/h, has a trend that follows a power law, $C_{p_{max}} = 0.444(\delta/h)^{-0.182}$ (figure 4.15). Consequently, the pressure

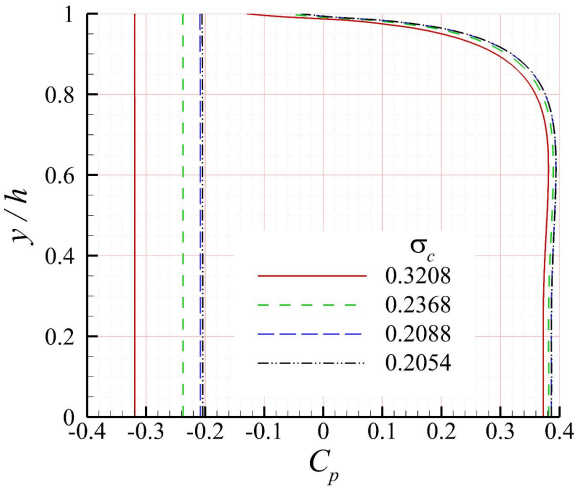

Figure 4.13: Pressure distribution on the front (positive) and back (negative) face of the fence for the range of C_{Qv} values and constant $\delta/h = 2$ and constant $H/h = 60$. Left hand side vertical curves are the pressure distributions (constant and equal to the cavity pressure) at the back face of the fence.

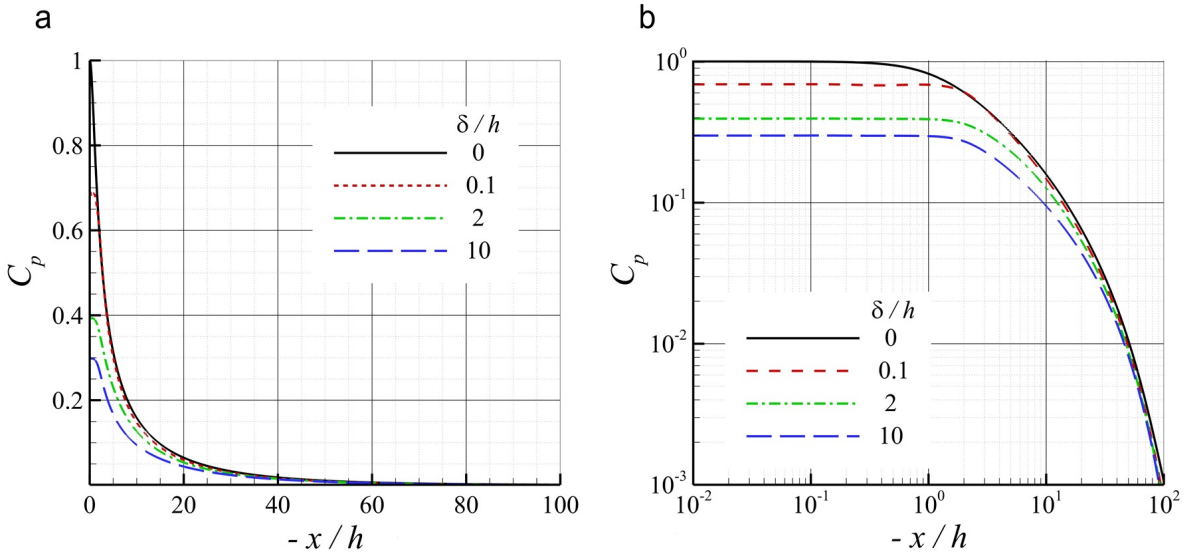

Figure 4.14: Wall pressure distribution upstream of the fence for varying δ/h with constant $C_{Qv} \approx 0.25$ and constant $H/h = 60$, presented as a linear (a) and $log - log$ (b) plot.

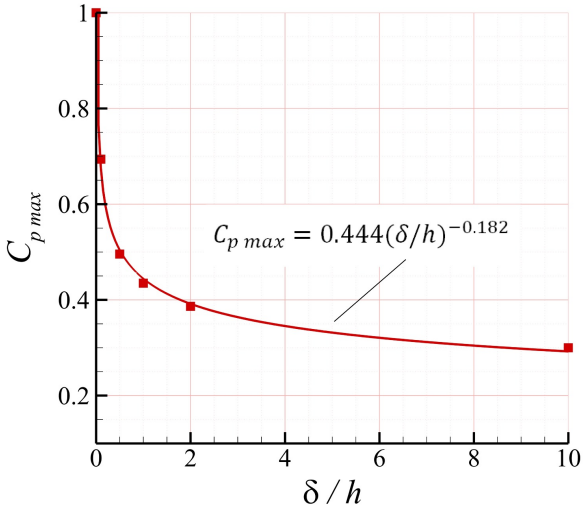

Figure 4.15: Dependence of $C_{p_{max}}$ on δ/h with the power law best fit curve for constant $C_{Qv} \approx 0.25$ and constant $H/h = 60$.

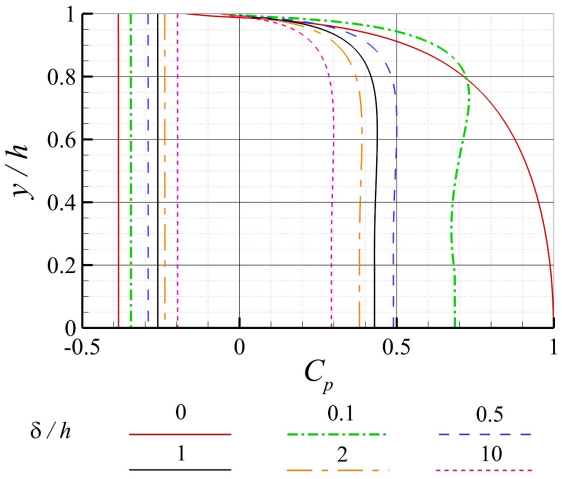

Figure 4.16: Pressure distribution on the front and back face of the fence for the range of δ/h values, constant $C_{Qv} \approx 0.25$ and constant $H/h = 60$.

coefficient values in the separation zone in front of the fence are higher for the cases with the lower δ/h value. Moving further upstream of the fence the difference in the C_p value with varying δ/h reduces. l_{wall} decreases with an increase in δ/h, but this effect is not as pronounced as the decrease in $C_{p_{max}}$. The difference in l_{wall} is around 10% for the range of δ/h values examined.

The pressure distribution on the front and back faces of the fence for different δ/h values and constant C_{Qv} and H/h is presented in figure 4.16 ($C_{Qv} \approx 0.25, H/h = 60$). The pressure distribution curves correlate with the size of the separation bubble upstream of the wall/fence junction. The C_p value decreases monotonically from the wall/fence junction to the fence tip for the case with no boundary layer. As discussed above, for the cases with an oncoming wall boundary layer, the C_p has a peak located at some

intermediate position along the fence face. This peak is associated with the stagnation point, present due to the existence of the separation bubble. The pressure peak is located furthest from the wall for the thinnest boundary layer ($\delta/h = 0.1$). The difference between the peak C_p value and that at the wall/fence junction decreases with increase in δ/h. The $C_{p_{max}}$ value shows a significant decrease (around 70%) with increase in δ/h.

4.3.3 Hydrodynamic forces

Hydrodynamic forces, i.e. drag (D) and lift (L), resulting from the pressure distributions over the fence and the upstream wall are of interest for many applications involving interceptors. The data presented here is only concerned with the forces generated due to the pressure field, as the idea of addition of a wall mounted fence is to provide a local pressure field change. The fences are relatively small compared to the body that they are attached to, e.g. $h/l \approx 1 - 2\%$, and so the additional skin friction due to the addition of the fence is small and has been neglected in this analysis. In common with the usual convention drag is the force normal to the fence and is obtained from the integral of pressure fields acting over the front and back faces of the fence. In this study, considering the fence/wall combined body, lift has been defined as the force normal to the wall, which is obtained from the integral of the pressure distribution on the wall upstream of the fence. In the present study a length of $100h$ has been chosen for the integration zone as sufficient to account for the presence of the fence as discussed in the section 3.2. It was found that the lift contribution from between $60h$ and $100h$ is less than 0.5% of the total. Lift and drag are non-dimensionalised using force coefficients based on the fence height and a unit width giving; lift coefficient $C_L = L/0.5\rho U_\infty^2 h$ and drag coefficient $C_D = D/0.5\rho U_\infty^2 h$.

The dependence of the force coefficients and hydrodynamic efficiency (L/D) on C_{Qv} and δ/h is shown in figure 4.17. All hydrodynamic parameters (C_L, C_D and L/D) are found to have a power law dependence on σ_c when varying the ventilation rate for a particular boundary layer thickness and blockage ratio. Increase in the ventilation rate (decrease in σ_c) leads to increase in lift, which is due to both a higher $C_{p_{max}}$ value and a greater l_{wall}. Lift increased $15 - 19\%$, for the range of constant δ/h values, over the examined C_{Qv} values. Drag reduces as σ_c decreases, with the maximum difference being $12 - 18\%$, depending on δ/h. The reduction in the drag stems from a decrease in pressure difference across the fence. These variations in the hydrodynamic forces contribute positively to an increase in the L/D with increasing C_{Qv}, reaching a maximum value for $\sigma_c = \sigma_{min}$. The lift to drag ratio increases by $25 - 30\%$ with increase in C_{Qv}, for the range of boundary layer thicknesses examined.

From figure 4.17, it can be seen that all curves (L, D and L/D) are moved to the lower cavitation numbers with increase in fence immersion in the oncoming boundary layer. Lift decreases with increase in δ/h mainly attributable to the decrease in $C_{p_{max}}$ value at the

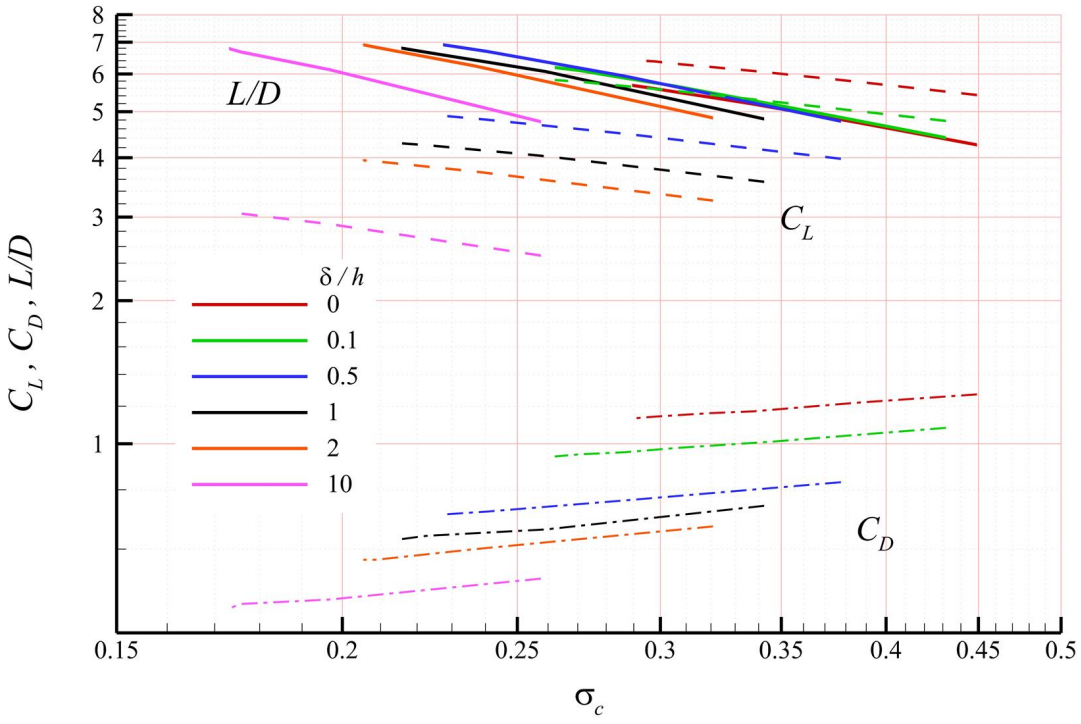

Figure 4.17: Dependence of hydrodynamic parameters C_L, C_D and L/D on σ_c and δ/h for constant $H/h = 60$ in $log - log$ plot.

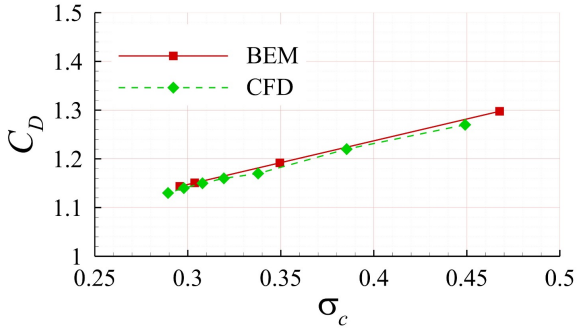

Figure 4.18: C_D curves obtained for varying σ_c with BEM and CFD with no oncoming boundary layer present for the same blockage conditions ($H/h = 60$).

wall/fence junction and associated lower C_p values in the separation bubble zone. The l_{wall} is also reduced, lowering the total lift, but this component has a lesser influence than the reduction in magnitude of the pressure field. The drop in the lift between the thickest boundary layer examined ($\delta/h = 10$) and the case with no boundary layer is approximately 55%. As with the reduction in σ_c, with an increase in δ/h drag is also reduced. The main contribution in the drag reduction is from a large (70%) drop in the $C_{p_{max}}$ value on the front face of the fence. Additionally, the absolute C_p value on the back face of the fence decreases due to the higher cavity pressure. The decrease in drag is around 55% between the minimum and maximum δ/h values. Such a drop in the drag is expected, due to the lower oncoming flow velocity and less momentum flux at the fence height with deeper immersion in the boundary layer.

In figure 4.18, a comparison between the drag coefficient results from BEM and CFD for varying cavitation number is shown. Results from inviscid BEM and CFD with no upstream wall boundary layer present, for the same blockage ratio ($H/h = 60$), show good agreement. Ultimately, the decrease in the drag is greater than decrease in the lift, and L/D is higher for larger values of δ/h. The difference between the highest and lowest values is around 15%.

4.3.4 Blockage Analysis

The degree of confinement of the flow domain, expressed through the blockage ratio H/h, has a large influence on the cavity flow. It has already been shown (figures 4.6a-b and 4.9) that the flow becomes 'blocked' and that the minimum achievable value of the cavitation number, σ_{min}, is a function of δ/h. After σ_{min} is reached, cavity lengths tends to infinity (figure 4.11) and the flow geometry remains unaffected with any further increase in ventilation rate. As the results from this study are going to be compared with experimental data, all simulations were conducted using a domain corresponding to the cavitation tunnel test section with blockage ratio of 60. To more generally investigate the effect of varying ventilation rate on the confined flow regime, three additional values of the blockage ratio ($40, 100$ and 200) were examined for one boundary layer thickness ($\delta/h = 2$).

Figure 19 shows the dependence of σ_c on C_{Qv} under varying blockage conditions. It can be seen that for the less confined flow, the range of cavitation numbers achievable for the same range of ventilation rate is greater and the slope of the curve is less. Also, the fully blocked flow condition (vertical part of the curve) is achieved at a higher ventilation rate (i.e. lower σ_c). Experimental data for a 3D wall mounted fence (Barbaca et al., 2016) is added to figure for a comparison. It can be seen that the results for 2D flow tend to become more similar to the less confined 3D flow with a less pronounced blockage effect (higher H/h value).

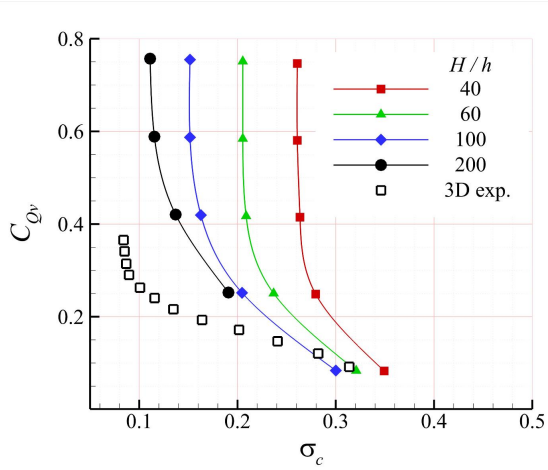

Figure 4.19: Relation between σ_c and C_{Qv} for varying H/h and constant $\delta/h = 2$. A lower σ_c value is achievable for greater blockage ratios. Experimental results for ventilated cavity flow over a 3D wall mounted fence (Barbaca et al., 2016) are shown for comparison.

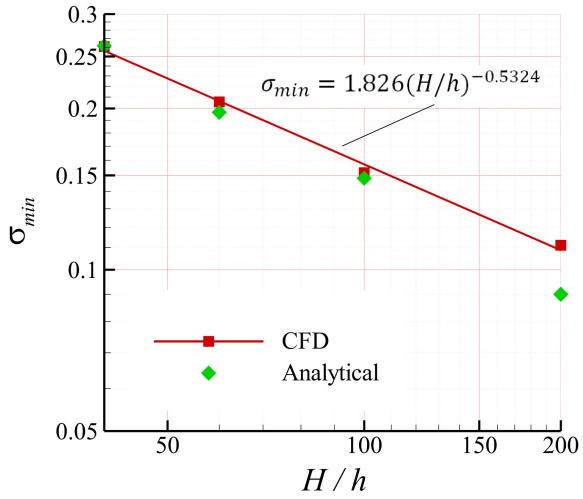

Figure 4.20: Dependence of σ_{min} on H/h with a power law best fit curve as a $log-log$ plot (for constant $\delta/h = 2$). The analytical data is calculated from Eq. 4.1 using the cavity thickness obtained for the flow conditions examined (i.e. t_c value from the CFD data).

The σ_{min} decreases following a power law trend ($\sigma_{min} = 1.826(H/h)^{-0.5234}$) with increase in H/h, as can be seen in figure 4.20. The CFD results compare favourably with the analytical predictions from free-streamline theory (Eq. 4.1), with a larger discrepancy present for the least blocked case.

In figure 4.21, the relation between the cavity length and cavitation number for the varying H/h ($\delta/h = 2$) is presented. The shift of the curves to the left with decrease of confinement is similar to the σ_c dependence on C_{Qv}. The fully blocked flow conditions, where the cavity grows 'infinitely' for a small increase in C_{Qv} (represented with the vertical part of the curves), is shifted to lower σ_c values with increase in H/h. The slope of the curve is gentler and is approaching the power law behaviour, which is characteristic of unbounded cavity flows (Franc and Michel, 2004; Pearce and Brandner, 2014).

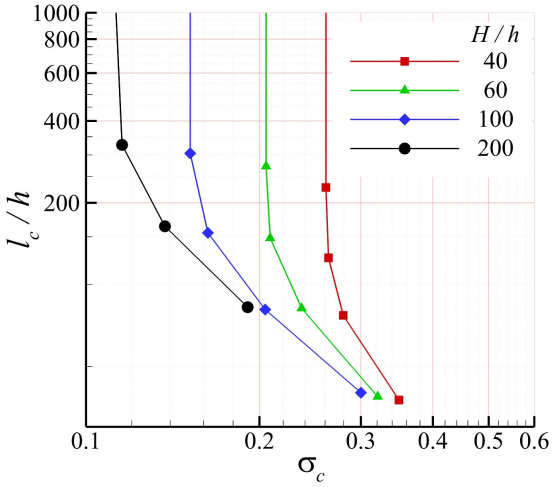

Figure 4.21: Cavity length as a function of σ_c for the cases with varying H/h and constant $\delta/h = 2$.

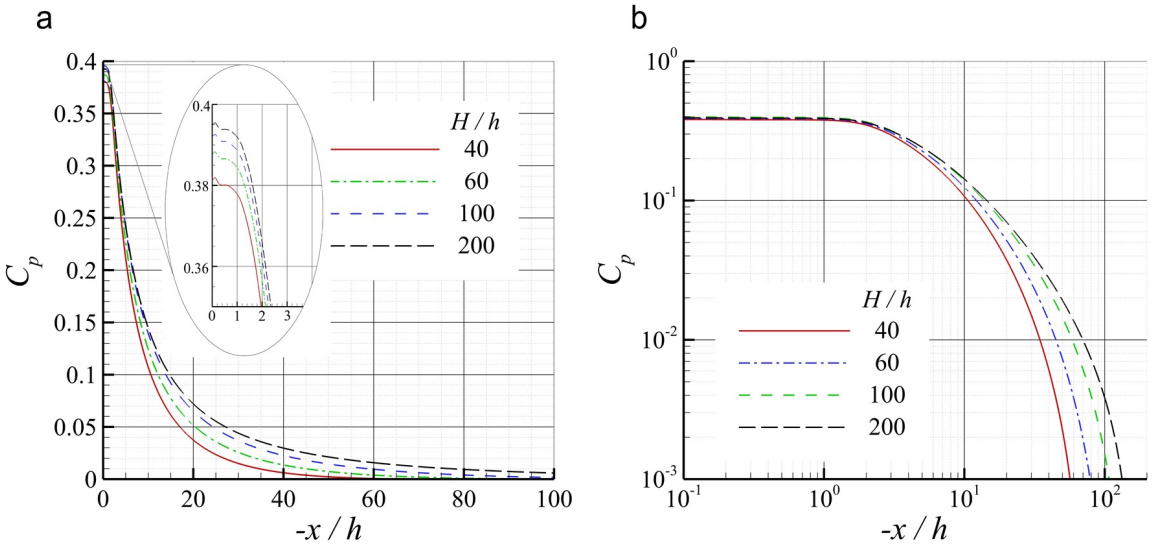

Figure 4.22: Wall pressure distribution upstream of the fence for varying H/h, constant $C_{Qv} \approx 0.25$ and constant $\delta/h = 2$, presented as a linear (a) and $log - log$ (b) plot. Inset provides a magnified view in the near wall region highlighting the difference in $C_{p_{max}}$ values.

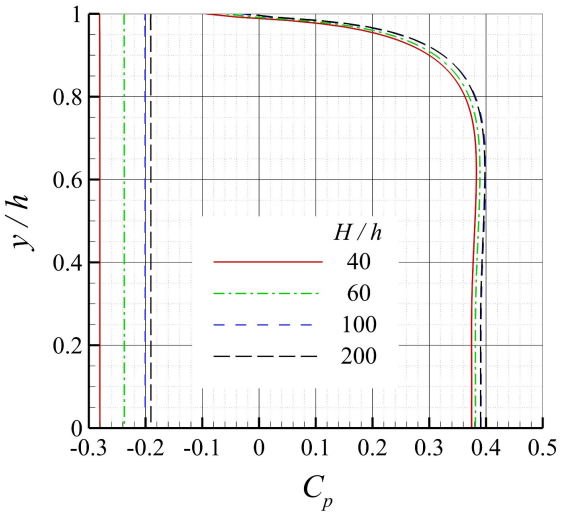

Figure 4.23: Pressure distribution on the front and back face of the fence for the range of H/h values, constant $C_{Qv} \approx 0.25$ and constant $\delta/h = 2$.

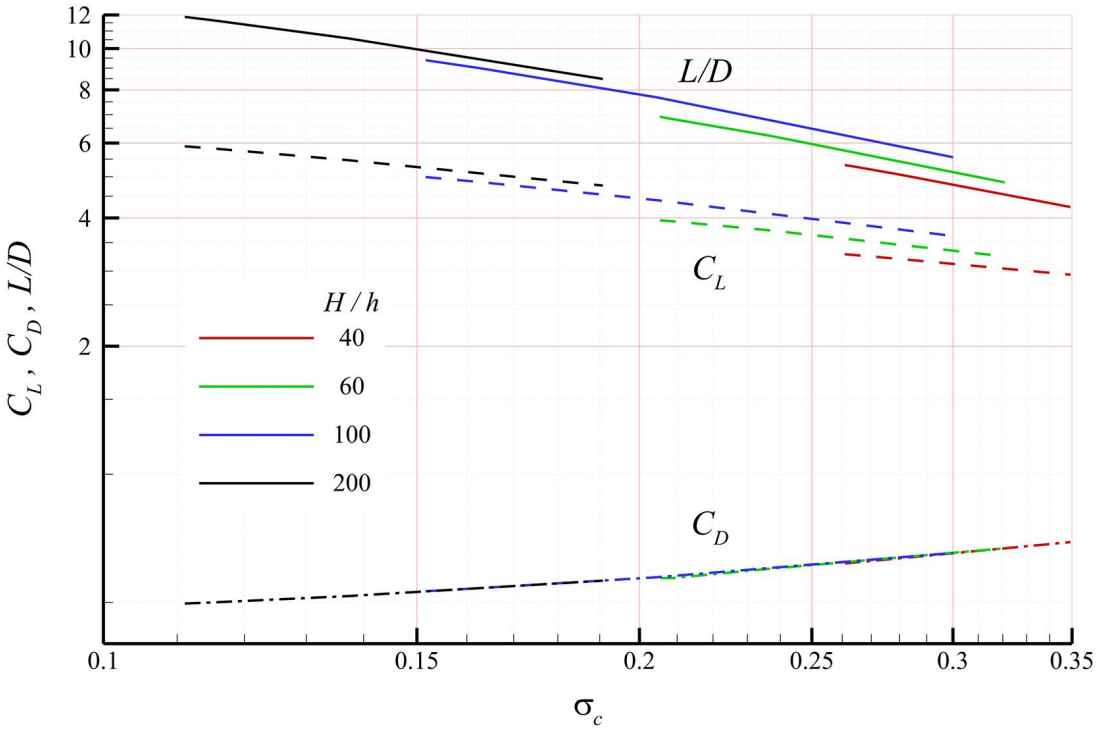

Figure 4.24: Dependence of hydrodynamic parameters C_L, C_D and L/D on σ_c and H/h for constant $\delta/h = 2$.

The effect that a change in blockage ratio has on the upstream wall pressure distribution for the cases with a constant $C_{Qv} \approx 0.25$ (and $\delta/h = 2$) is shown in figure 4.22. The $C_{p_{max}}$ value slightly increases with a greater blockage ratio and it tends to an asymptotic value as the flow approaches unbounded conditions (see inset in figure 4.22a). The main effect of the reduced confinement is the increase in l_{wall}. The dependence of l_{wall} on H/h approximately follows a power law relation, with the minimum value (for $H/h = 40$) being around 43% of the maximum value (for $H/h = 200$).

The pressure distribution on the fence, for constant δ/h and C_{Qv} values, shows similar behaviour through the range of examined blockage ratios (figure 4.23). The maximum $C_{p_{max}}$ value is found on the upper half of the fence and corresponds to the location of a stagnation point. $C_{p_{max}}$ shows a slight increase with the increase in H/h.

The influence of blockage ratio on the hydrodynamic parameters is shown in figure 4.24. All curves are shifted to the lower cavitation numbers (translation to the left) with increase in H/h. C_L increases with reduced confinement due to the larger area under the influence of the fence. The maximum increase in lift is around 44% for the range of H/h investigated. It can be seen that the C_D data fall onto one curve, i.e. there is no difference in drag for a constant cavitation number across the range of blockage ratios examined. Due to the increase in lift, with drag unaffected, hydrodynamic efficiency is improved as the flow becomes less confined. The L/D increases about 55% for the range of investigated H/h values.

4.4 Conclusions

Ventilated cavity flow over a 2-D wall mounted fence was investigated numerically using computational fluid dynamics for a fixed fence height based Froude number ($Fr = 31.93$) and constant free-stream cavitation number ($\sigma_v \cong 1.95$). The flow was examined for a range of air ventilation rates (C_{Qv}) and oncoming boundary layer thickness to fence height ratios (δ/h). The flow topology was examined, with a separation bubble immediately upstream of the fence and a re-entrant jet cavity closure captured. Dependence of cavitation number (σ_c) on ventilation rate is established with a shift towards lower cavitation numbers with an increase in δ/h. A blocked flow condition is observed through the existence of a minimum cavitation number (σ_{min}). Cavity length (l_c) grows with decrease in σ_c, extending to an 'infinite' length when σ_{min} is reached. Correspondingly, cavity thickness (t_c) also increases, approaching an asymptotic value in the blocked flow condition. The same l_c and t_c are obtained at a lower cavitation number with increase in δ/h.

Upstream wall and fence pressure distributions were investigated. With the respect to the upstream wall distribution, the general trend was consistent under all flow conditions.

The main differences were observed in $C_{p_{max}}$ at the wall/fence junction and the length of the wall influenced by the presence of the fence (l_{wall}). With increase in the ventilation rate both parameters show slight increase. The $C_{p_{max}}$ value decreased around 70% between the cases without and with the thickest boundary layer, while the l_{wall} reduced slightly. Pressure distribution on the front face of the fence has a peak value on the outer half of the fence due to the stagnation point associated with the separation bubble. The pressure coefficient on the back face of the fence is constant and equal to the absolute value of cavitation number (i.e. $C_p = -\sigma_c = const.$).

The lift (wall normal) force, resulting from the upstream wall pressure distribution, increases up to 19% with increase in C_{Qv} and decreases about 55% with increase in δ/h. The drag (streamwise) force, caused by the pressure difference between the front and back face of the fence, decreases up to 18% with increase in C_{Qv} and about 55% with the increase in δ/h. Correspondingly, hydrodynamic efficiency increased about 30% and 15% with the increase in C_{Qv} and δ/h, respectively.

The dependence of σ_c on C_{Qv}, and l_c on σ_c, as a function of the blockage ratio (H/h) is established. The main effect of increasing H/h on pressure distributions is an increase in l_{wall}. Due to this increase in l_{wall}, the lift increases with increasing H/h, while drag remains approximately the same. This leads to an increase in the lift to drag ratio of around 55% through the range of H/h values examined.

Some comparison is made with potential flow results from a boundary element method, analytical predictions from free-streamline theory and experimental data from similar flows available in the published literature. The values for σ_{min}, l_c, t_c and drag obtained from CFD with no oncoming boundary layer present compare favourably with BEM data. Analytical predictions are in good agreement with CFD results for small δ/h. Approximately the same trends are observed in the present numerical results and experimental data from similar flows available in literature. A companion experimental study in a cavitation tunnel is planned for a comparison with the numerical data.

Chapter 5

Experimental Study of Ventilated Cavity Flow Over a 3-D Wall-Mounted Fence

This chapter is based on the article published in *International Journal of Multiphase Flow*. The contributing authors are: L. Barbaca, B.W. Pearce and P.A. Brandner. The abbreviated version of this chapter was presented at the (peer-reviewed) 16^{th} *ISROMAC Conference*, Honolulu, Hawaii, US, 10 - 15 April, 2016. The conference paper is included in Appendix B.

The citation for the journal paper is:

Barbaca, L., Pearce, B. W., Brandner, P. A., 2017, Experimental Study of Ventilated Cavity Flow Over a 3-D Wall-Mounted Fence, *International Journal of Multiphase Flow*, **97**:10 - 22

The citation for the conference paper is:

Barbaca, L., Pearce, B. W., Brandner, P. A., 2016, Experimental Investigation of Ventilated Cavity Flow Over a 3-D Wall-Mounted Fence, *in Proceedings of 16th International Symposium on Transport Phenomena and Dynamics of Rotating Machinery ISROMAC-16*, Honolulu, Hawaii, 10-15 April, 2016

Abstract

Ventilated cavity flow over a fixed height 3-D wall-mounted fence is experimentally investigated in a cavitation tunnel for a range of free-stream conditions. The impact of 3-D effects on cavity topology is examined, along with the dependence of the cavitation number and drag on the volumetric flow rate coefficient, fence height based Froude number and vapour pressure based cavitation number. Three different flow regimes are identified throughout the range of cavitation numbers for a particular free-stream condition. Generally, the cavity has a typical re-entrant jet closure the intensity of which is found to increase linearly with increasing Froude number. This increase in re-entrant jet intensity causes an increase in drag with Froude number for constant volumetric flow rate coefficient. At low Froude numbers the closure mechanism transitions from a single to a split re-entrant jet. The parameters used to characterize the cavity topology show a linear dependence on Froude number irrespective of the closure mode. The cavity topology and drag are found to be independent of vapour pressure based cavitation number.

5.1 Introduction

In high-speed marine applications the occurrence of cavitation will generally have a detrimental effect on the device performance. The presence of cavitation bubbles or larger cavities attached to the body will result in a performance loss and greater flow instability. If the cavity extends downstream of the body (termed a 'supercavity') these negative effects will be largely diminished and the existence of a gaseous bubble/layer between the body and surrounding water will result in a decrease in skin friction (Acosta, 1973). To achieve a natural (i.e. vaporous) cavity of such extent the required flow speed is impractically high for most applications (Kawakami and Arndt, 2011). When a particular geometry is utilized to induce flow separation and cavity formation this is commonly referred to as a 'cavitator'. An 'artificial' or 'ventilated' supercavity, with largely similar behaviour to that formed naturally (May, 1975), may be formed at a lower flow velocity by admission or forced injection of incondensable gas into the wake of a cavitator.

Ventilated flows have been extensively studied in the context of drag reduction techniques since mid-last century for various marine applications (Swanson and O'Neill, 1951; Schiebe and Wetzel, 1961). Prominent examples of using an incondensable gas bubble/layer to reduce drag include axisymmetric ventilated supercavitating underwater projectiles (e.g. Brennen, 1995; Semenenko, 2002), air bubble injection into turbulent boundary layers (e.g. Murai, 2014) and ventilated cavity flow over a backward-facing step (e.g. Latorre, 1997; Ceccio, 2010; Matveev et al., 2009; Lay et al., 2010; Mäkiharju et al., 2013a). A related technique, referred as 'base-ventilation', is used on lifting surfaces to

limit the form drag (e.g. Franc and Michel (2004)). Air injected through the downstream face (base) of the body results in an increase in the wake pressure, thus reducing the streamwise differential pressure across the body, consequently reducing the form drag. A recent comprehensive review on ventilation of lifting bodies, both natural and forced, has been authored by Young et al. (2017). In addition to its hydrodynamic applications, ventilation has also found use in hydraulics to prevent surface erosion through the application of aeration devices on dam spillways (Chanson, 1989) and also in hydro turbines to attenuate pressure fluctuations (e.g. Papillon et al., 2002).

A basic flow that has potential use in a range of high-speed marine applications is the ventilated cavity flow from a cavitator in the form of a wall-mounted fence. Amongst the wealth of literature published on cavitating and ventilated flows the particular flow stemming from this form of cavitator has not had any comprehensive focus. Some analytical results have been published on 2-D lifting surfaces with trailing edge fences (e.g. Fridman, 1998) and some recent 2-D inviscid and viscous numerical analysis has been reported by Pearce and Brandner (2014) and Barbaca et al. (2014). This study aims to contribute to the topic with new experimental data on a 3-D flow configuration.

The use of fixed and adjustable wall-mounted fences in single-phase flow is a well established method for lift enhancement and active control in a range of aerospace, automotive and wind engineering applications (e.g. Storms and Jang, 1994; Jeffrey et al., 2000; Timmer and Van Rooij, 2003; Kinzel et al., 2010). The use of trailing edge 'cupping' on propeller blades is an example of fence use in a marine context (Denny et al., 1989). A similar multiphase flow associated with fences (also termed 'interceptors') fitted to the bottom and sides of a ship's transom (Brizzolara, 2003; Faltinsen, 1996), can be considered as an 'infinite' (i.e. nominally zero cavitation number) ventilated cavity flow over a wall-mounted fence, with the back face of the fence subjected to atmospheric pressure.

Within the scope of the present study, ventilated cavity flow over a 3-D wall-mounted fence is experimentally investigated in a cavitation tunnel for a range of free-stream conditions. The impact that the 3-D flow geometry has on the closure physics is examined, along with the dependence of the cavitation number and drag on the mass flux of injected air. In addition to gaining understanding of the physics associated with a canonical multiphase flow, this flow is also of practical interest in the application of a wall-mounted fence as an interceptor type device in high-speed flows.

A schematic representation of ventilated cavity flow over a wall-mounted fence is shown in figure 5.1. A fence, of height h, is immersed in the upstream wall boundary layer of thickness δ. The latter is defined as the distance from the wall where the local mean velocity, U, is 99% of the free-stream velocity U_∞. Air is supplied to the wake region of the resulting bluff-body flow through a manifold on the downstream face of the fence. A ventilated cavity, with re-entrant jet closure, is shown detaching from the sharp fence tip.

The fundamental dimensionless parameter characterizing cavitating flows is the cavi-

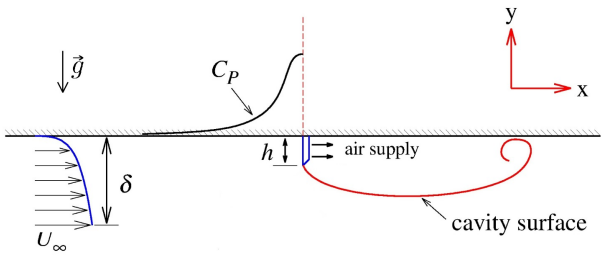

Figure 5.1: Sketch of a wall-mounted fence immersed in the oncoming wall boundary layer with a ventilated cavity detaching from the sharp fence tip. Air is supplied from the downstream face of the fence. The pressure distribution on the upstream wall is shown. The origin of the coordinate system is at the fence/wall junction

tation number, which in general form can be expressed as $\sigma_c = (p_\infty - p_c)/0.5\rho U_\infty^2$, where p_c is the pressure inside the cavity, p_∞ is the reference free-stream pressure measured at the test section mid-height upstream of the fence, ρ is the liquid density and U_∞ is the reference free-stream velocity. The experimental setup was developed to examine the dependence of cavitation number on the flux of injected air, fence height based Froude number ($Fr = U_\infty/\sqrt{gh}$, where g is the gravitational acceleration) and vapour pressure, p_v, based free-stream cavitation number ($\sigma_v = (p_\infty - p_v)/0.5\rho U_\infty^2$). Alternatively, a Froude number based on the test section depth, H, is defined by $Fr_H = U_\infty/\sqrt{gH}$. The rate at which air is injected in the flow is characterized by a volumetric flow rate coefficient $C_{Qv} = Q_m/\rho_{air} U_\infty S$, where Q_m is the mass flow of the injected air, ρ_{air} is the air density and S is the reference area (for the present case it is the surface of the fence face). Alongside the cavitation number, the drag D is examined with the respect to the aforementioned parameters. The drag is expressed in its non-dimensionalised form, as the drag coefficient $C_D = D/0.5U_\infty^2 \rho S$. The cavity length, l_c, dependence on σ_c was also investigated.

The present report follows on from work undertaken over recent years at the Australian Maritime College (AMC) Cavitation Research Laboratory (CRL). As a part of a research project on intercepted base-ventilated hydrofoils (Elms, 1999; Pearce and Brandner, 2015b,c), several numerical studies of naturally cavitating (Pearce et al., 2010; Pearce and Brandner, 2014) and ventilated (Barbaca et al., 2014) flow over a wall-mounted fence in isolation have been reported on. The work presented here will be accompanied with a future experimental study of a ventilated cavity flow over a 2-D wall-mounted fence.

5.2 Experimental setup

The experiments were performed in the University of Tasmania variable pressure water tunnel. The tunnel design incorporates a large tank downstream of the test section for bubble coalescence and separation (Brandner et al., 2015). This feature, combined with the auxiliary systems for the rapid degassing and continuous evacuation of the large

quantities of incondensable gas, enables efficient conduct of tests involving ventilation (i.e. injection and continuous removal of large quantities of air). The tunnel test section measures 0.6 × 0.6 m square, by 2.6 m long. The operating velocity and pressure are controlled independently, with ranges from 2 to 12 m/s and 4 to 400 kPa absolute respectively. The tunnel volume is 365 m^3 and is filled with demineralised water. Optical access is provided through acrylic windows on each side of the test section.

The experimental setup has been developed to study ventilated cavity flow over 2-D (spanning the whole test section width) and 3-D (spanning only a portion of the test section width) wall-mounted fences. For the present study only the results obtained with the 3-D fence model are presented. The fence model (figure 5.2), equipped with an internal manifold for air distribution, is machined from a single stainless steel bar. The fence is 156 mm wide × 10 mm high, with a V-notch machined around the sides and outer edge providing a 'sharp' tip to ensure a stable cavity detachment. The model spans nominally a quarter of the test section, resulting in a blockage ratio (based on cross-sectional area) of $< 0.5\%$. The shape of the rear part of the fence does not have an influence on the flow, as it is located completely inside the cavity. The air distribution system consists of an internal channel and 10 equi-spaced streamwise outlets distributing air into the wake of the fence. To facilitate drag measurement the model is attached to a six-component force balance, and mounted to the test section ceiling with the fence located, symmetric about the vertical centre line, 0.7 m from the entrance as indicated in figure 5.3. The oncoming wall boundary layer thickness at this position is 19 mm (Belle et al., 2016), which results in boundary layer thickness to fence height ratio of $\delta/h = 1.9$. The mounting disk on the force balance had an outside diameter of 160 mm and the model remained within disk and did not have any contact with the test section ceiling. A flexible tube is routed through the balance for the air supply.

A multiplexing valve system used for pressure measurement is represented schematically in figure 5.3. This setup allows the use of a single pressure transducer for all measurements, eliminating the need to apply corrections arising from transducer zero and span errors. The free-stream dynamic pressure and pressure inside the cavity are measured relative to the free-stream static pressure, from which σ_c can be derived. The cavity pressure is measured with a wall taping located just downstream of the model, with a tube routed through the balance. The gas/liquid interface, set at the tunnel ceiling height allows for the gas filled cavity pressure to be measured with the liquid/liquid differential pressure transducer. Prior to each cavity pressure measurement the gas side is purged to ensure that the passage is free from liquid.

The test section absolute pressure is measured, depending on the value, from high or low range Siemens Sitransp absolute pressure transducers models 7MF4333-1FA02-2AB1 and 7MF4333-1GA02-2AB1 with estimated precision of 0.13 and 0.48 kPa respectively. The test section velocity is measured from the calibrated contraction differential pres-

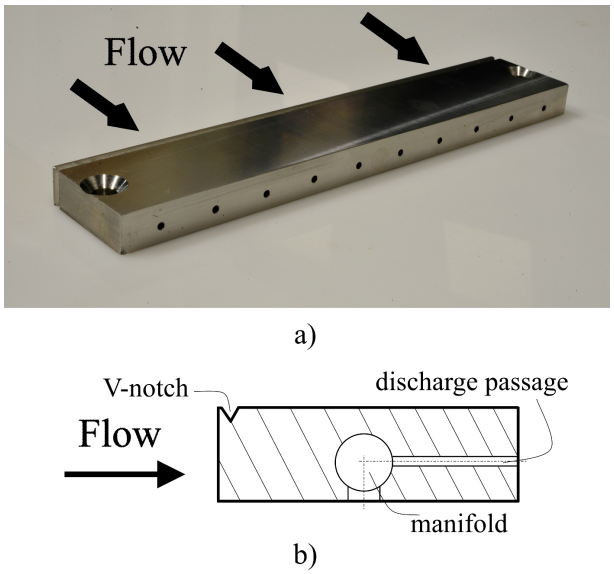

Figure 5.2: a) A rear view of the stainless steel fence model. Ten equi-spaced passages for the air supply can be seen on the downstream face of the fence. b) A cross-section of the fence model. A V-notch is machined around the sides and outer edge providing a 'sharp' tip to ensure a stable cavity detachment.

sure. Depending on the value, either high or low range Siemens Sitransp differential pressure transducers models 7MF4433-1DA02-2AB1-Z and 7MF4433-1FA02-2AB1-Z are used, with estimated precision of 0.007 and 0.018 m/s respectively. The air mass flow rate is controlled and measured using an Alicat Scientific model MCR-500-SLPM-D (flow rate range 0-500 SLPM) mass flow meter with an estimated precision of 3 SLPM. The ventilated cavitation number is measured using a Validyne model DP15TL differential pressure transducer (estimated precision of 0.2 kPa) via Swagelok model SS-43Z6FS1 7 way valve actuated using a stepper motor controlled from the data acquisition system. The force balance used to measure the model drag has a maximum rated load of 2 kN and an estimated precision of 0.15 N (for additional description see Zarruk et al., 2014). The dissolved gas content of the water is measured using an Endress+Hauser OxyMax WCOS 41 membrane sensor.

The three independently prescribed variables that control ventilated cavity flow over a fence are; air ventilation rate, free-stream Froude number and free-stream cavitation number. The combination of the latter two, being held at particular constant values, giving a particular free-stream condition. Due to the air flow rate being measured via a mass flow meter, the volumetric flow rate coefficient could not be prescribed (it depends on the gas pressure inside the cavity and the free-stream conditions), and it had to be calculated using the cavity pressure derived from the measured ventilated cavitation number. Due to the limited extent of the test section, an upper bound on the air flow rate needed to be determined (for a particular free-stream condition) where the cavity length would extend out of the test section into the diffuser (see figure 5.3). Approximately ten Q_m values were examined for each set of free-stream conditions.

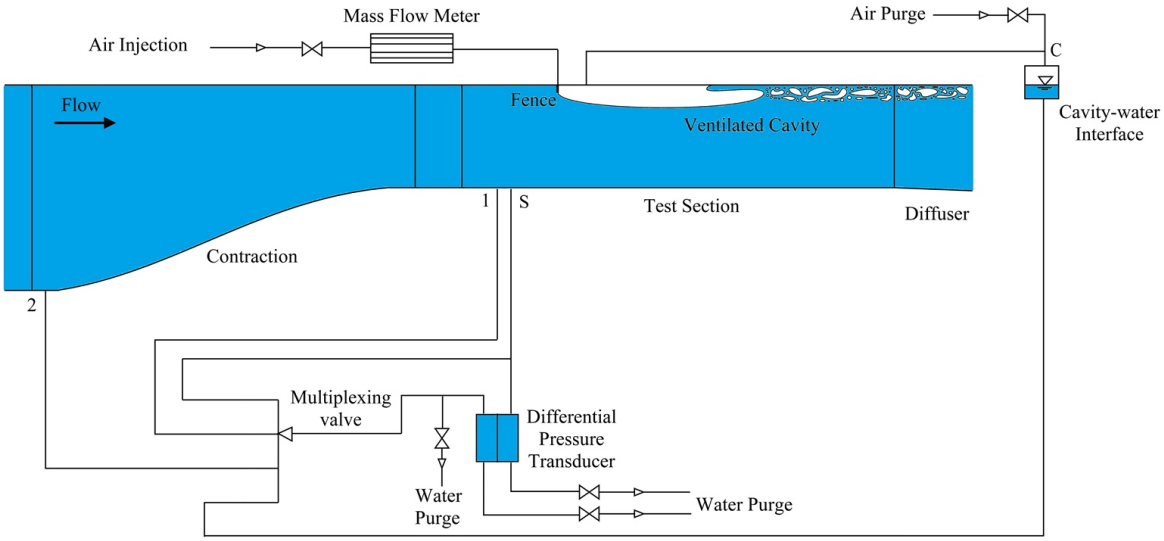

Figure 5.3: Schematic of the multiplexing valve system used for obtaining the cavitation number, σ_c. Air injection is via a mass flow meter. Gas pressure measured from the taping inside the ventilated cavity is converted to a liquid pressure (necessary for the differential pressure transducer operation) using the cavity-water interface.

Tests were conducted for three main Fr values (controlled with test section velocity) and three values of σ_v (controlled with the test section static pressure for a particular flow velocity). The tested conditions were 20.1, 25.3 and 30.3 for the Fr and 0.55, 0.75 and 0.95 for the σ_v. Additional Fr values were used to investigate the cavity closure behaviour in more detail. For all investigated free-stream speeds, Fr_H was greater than one, resulting in super-critical flow for all cases (Ohtsu et al., 2001). All tests were conducted with a dissolved O_2 content between 2 and 6 ppm.

Cavity length has been obtained using still forward-lit photography as the average from at least ten images. Images were taken using a Nikon D800E SLR camera with either a Nikon AF Nikkor 24 mm f/2.8D or Nikon AF Nikkor 50 mm f/1.8D lens, depending on the desired field of view. The exposure was controlled using a triggered stroboscopic flash (Drello 1018/LE4040).

5.3 Results and discussion

5.3.1 General cavity topology and closure physics

Air entrainment into the main flow and the related unsteadiness of cavity closure are among the most detailed features studied with ventilated cavity flow. Considerable effort has been applied to create cavities with minimal or no gas loss by insuring a smooth cavity reattachment (see for example Arndt et al., 2009), but understanding unsteady cavity closure behaviour is still of ongoing interest for various applications.

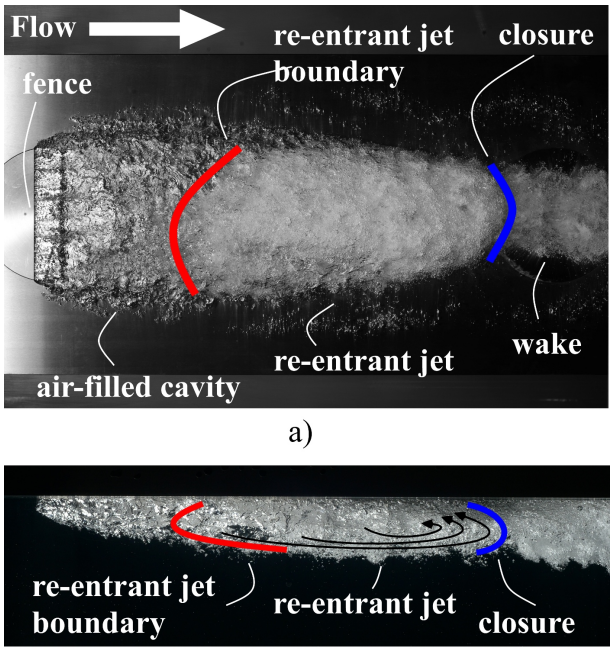

Figure 5.4: Typical geometry of a fully developed ventilated cavity shown as: a) bottom view and b) side view. The upstream region of the cavity is filled with air and has a relatively sharp cavity/water interface. The closure region exhibits re-entrant jet behaviour. The re-entrant jet causes cavity break-up and these bubbles are entrained in the main flow predominantly through the unsteady shedding cycle and, to a lesser extent, also via the significantly more turbulent re-entrant jet affected cavity/water interface region. The relatively narrow and thicker wake consist of a dense stream of entrained bubbles.

A typical geometry of a fully developed ventilated cavity is shown in figure 5.4. The cavity has a stable detachment from both the sharp side and outer (or tip) edges of the fence upstream face. Two distinct regions are evident along the length of the cavity. The region closer to the fence is almost entirely filled with air and it can be seen as the zone with a relatively sharp cavity/water interface and a transparent appearance. The rear or closure of the cavity exhibits re-entrant jet behaviour, observed as an opaque region, which is a predominant mode of air entrainment observed in cavitating flows with unsteady closure (Callenaere et al., 2001).

The re-entrant jet can be described as a wave penetrating into the cavity and transporting liquid upstream along the wall. The liquid jet falls under gravity, impinging on the cavity surface, shedding a portion of the cavity as a dense bubbly mixture into the main flow. To a lesser degree, some entrainment is also evident via the turbulent cavity interface. Depending on the cavity length and free-stream conditions, the re-entrant jet can extend all the way to the fence, or be contained to only a portion of the cavity. The detached bubbles on the sides of the cavity stem from the three-dimensionality of the flow with vortices entraining a small portion of the ventilated air into the flow. These vortices also cause cavity necking (reduction in width) along the cavity length.

5.3.2 The influence of ventilation rate

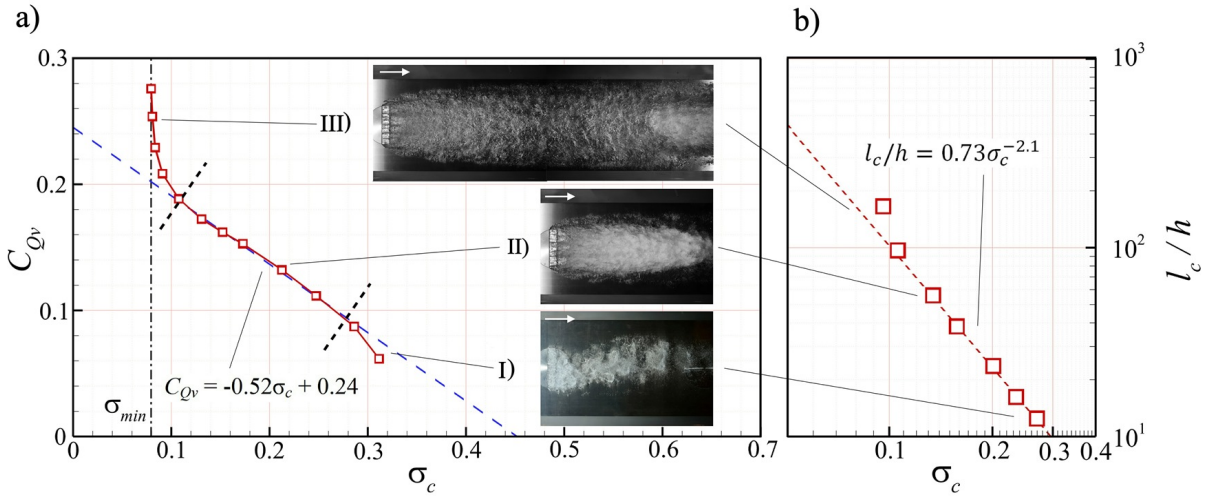

Figure 5.5: a) Dependence of cavitation number on the volumetric flow rate coefficient (for $Fr = 25.3$, $\sigma_v = 0.95$). Three regimes can be differentiated along the curve: I) shear layer cavitation, II) fully formed cavity with a linear dependence and III) cavity in 'blocked' conditions. The vertical asymptote represents a minimum cavitation number obtainable under the examined conditions. b) The relation between the cavity length and cavitation number, as a $log - log$ plot. The data approximately follows a power law trend, except for the very long cavities, when the flow is influenced by the tunnel diffuser approaching the blocked condition.

For ventilated cavity flow, at a particular free-stream condition, σ_c is controlled solely by the air ventilation rate, C_{Qv}. The dependence of σ_c on C_{Qv} is shown in figure 5.5a (with $Fr = 25.3$, $\sigma_v = 0.95$), where three regimes can be identified. In regime (I), a ventilated cavity is not yet fully formed. The short cavity present has a typical shear layer cavitation appearance with periodic oscillations in the span-wise direction due to alternate vortex shedding, similar to that associated with bluff body single-phase flow (Matsumoto, 1999). In regime (II), the cavitation number has a linear dependence on the ventilation rate. A ventilated cavity is fully formed and a re-entrant jet closure is present. Re-entrant jet formation stabilises the span-wise oscillation of the cavity tail, as the streamwise momentum associated with the jet overcomes the span-wise perturbation induced by the three-dimensional flow around the fence sides. Initially, the re-entrant jet impinges on the downstream face of the fence, but ceases to do so with reduction in cavitation number and subsequent increase in cavity length. The linear dependence of σ_c on C_{Qv} was found to be unaffected by the extent of the re-entrant jet. In regime (III), the cavity flow is being affected by confinement where a limiting $\sigma_c = \sigma_{min}$ is reached irrespective of any further increase in air flow. This 'blockage' effect is solely a function of the geometry of the confined flow (Brennen, 1995). When this lower bound is approached cavity growth is very sensitive to a change in ventilation rate where the length increases 'infinitely' with a slight increase in C_{Qv}.

The relation between the cavity length (l_c/h) and σ_c, for constant free-stream condi-

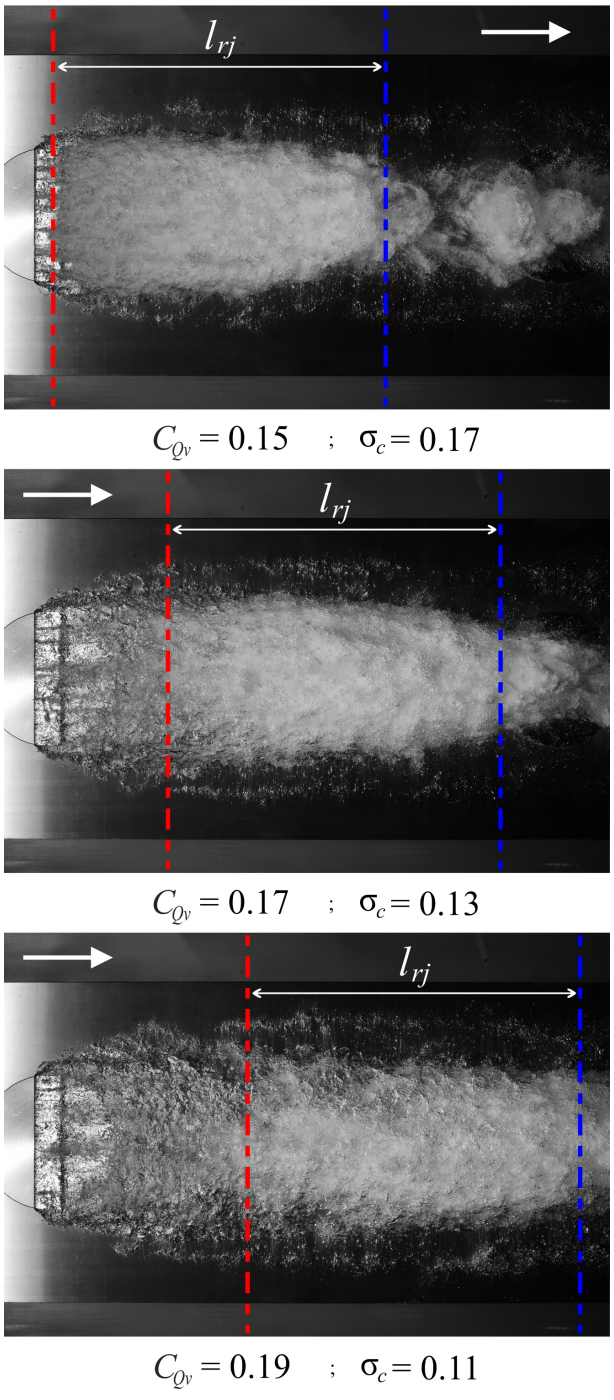

Figure 5.6: Cavity development with an increase in ventilation rate is shown for constant free-stream conditions ($Fr = 25.3$, $\sigma_v = 0.95$). The re-entrant jet impinges on the fence for the short cavity (a), but ceases to impinge as the cavity grows (b-c). Once the re-entrant jet detaches from the fence, its length (l_{rj}) remains unchanged as the ventilation rate increases.

tions, ($Fr = 25.3$, $\sigma_v = 0.95$) is shown in figure 5.5b. It can be seen that the data, away from the blocked lower bound condition, follows a power law trend ($l_c/h = 0.73\sigma_c^{-2.1}$), which is characteristic of unbounded cavitating flow (Franc and Michel, 2004). This indicates that the confinement of the flow domain does not significantly affect the results obtained. The cavity growth deviates from the power law trend and becomes more rapid as the cavity length approaches the test section outlet and the flow becomes more influenced by the tunnel diffuser.

For the developed cavity regime (II) a more detailed representation of the cavity evolution, with increase in air injection rate, is shown for a constant free-stream condition ($Fr = 25.3$, $\sigma_v = 0.95$) in figure 5.6. As stated above, during the initial phase of cavity growth, the re-entrant jet impinges on the downstream face of the fence (figure 5.6a), but as the cavity length increases the re-entrant jet also moves downstream (figure 5.6b-c). Once the re-entrant jet is no longer in contact with the fence its length remains constant as the overall length of the cavity increases with higher ventilation rate. This suggests that the re-entrant jet intensity is independent of the ventilation rate for a particular set of free-stream conditions.

5.3.3 The influence of free-stream Froude number

The influence of a change in free-stream speed, i.e. Fr, on the dependence of σ_c on C_{Qv} has been investigated. In figure 5.7 curves of σ_c versus C_{Qv} are shown for three Fr values (for $\sigma_v = 0.95$). It can be seen that with the increase in Fr, a higher C_{Qv} is needed to obtain the same σ_c, i.e. more air needs to be injected into the cavity and that the slope of the linear region is increased. σ_{min} also increases with an increase in Fr, which suggests a higher degree of confinement with increased free-stream velocity. The more pronounced blockage is a consequence of an increase in maximum cavity cross-sectional area $S_c = t_c w_c$, where t_c and w_c are the maximum cavity thickness and width, respectively, as shown in figure 8. As t_c/h increases with an increase in Fr ($\approx 20\%$), w_c/h decreases, but at a relatively slower rate ($\approx 6\%$), the combined effect results in an increase in S_c/S.

To investigate the effect that a change in free-stream speed has on the re-entrant jet intensity, fixed length cavities are examined for a range of Fr values. In figure 5.9, cavities of a constant length ($l_c/h \approx 70$) are shown for varying Fr ($15.9 \leq Fr \leq 38.3$) and constant σ_v ($= 0.95$). In all instances the cavity closure is located on the right side of the image. It can be seen that with a decrease in Fr the length of re-entrant jet reduces, reflecting a less intense re-entrant jet at lower Fr. This behaviour can be quantified using a re-entrant jet to cavity length ratio, l_{rj}/l_c. For three cavity lengths ($l_c/h \approx 40, 70\,\&\,100$) it is shown in figure 5.10 that l_{rj}/l_c has a linear dependence on Fr. From extrapolation, l_{rj}/l_c reaches a zero value for a non-zero $Fr = Fr_0$, indicating that a complete extinction of re-entrant jet occurs for a non-zero flow velocity. The re-

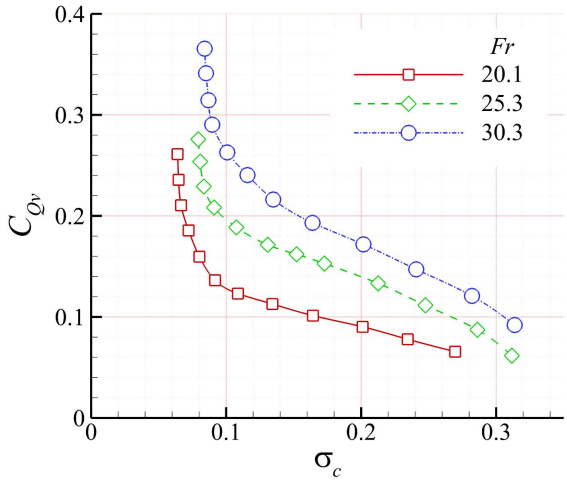

Figure 5.7: Relation between σ_c and C_{Qv} for the cases with different Froude number and constant free-stream cavitation number ($\sigma_v = 0.95$)

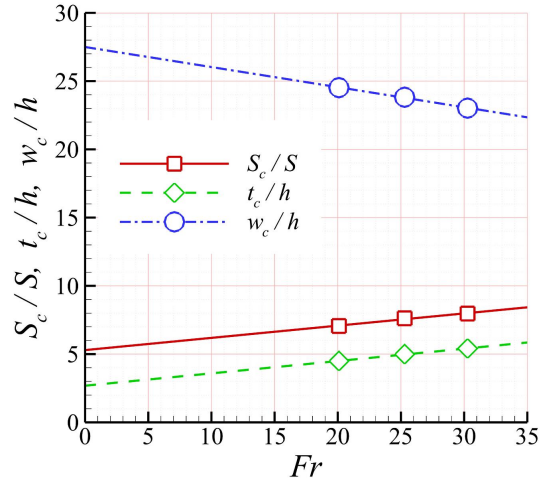

Figure 5.8: Dependence of S_c/S, t_c/h and w_c/h on Fr for constant cavity length ($l_c/h \approx 70$) and constant free-stream cavitation number ($\sigma_v = 0.95$).

entrant jet extinction is a consequence of smooth cavity reattachment to the downstream wall, promoting a stable closure with minimal air leakage into the main flow, which is now governed by the wave pinch-off mechanism (Mäkiharju et al., 2013a). Such a phenomenon is commonly observed in the ventilated backward facing step flow, where low Fr (usually coupled with a sloped beach placed in the cavity closure region) ensures minimal air loss (Arndt et al., 2009; Lay et al., 2010; Matveev and Miller, 2011), for which Matveev (2003) has provided a theoretical basis. Note that the free-stream condition at which re-entrant jet extinction is predicted coincides with the transition from super-critical to sub-critical flow, i.e. $Fr_H \approx 1$, as shown in figure 5.10.

From figure 5.11 it can be seen that for a higher Fr more air has to be injected to achieve a particular cavity length, with a linear increase in C_{Qv} over the investigated range of Fr. This increase in air injection is associated with a more intense re-entrant jet, resulting in greater air entrainment into the main flow. Similarly, σ_c increases linearly with an increase in Fr for fixed length cavities. Both C_{Qv} and σ_c decrease to zero for a non-zero Fr, supporting the inference drawn above that the re-entrant jet ceases to exist for $Fr \leq Fr_0$. The Fr_0 value in this case is about 4.0 which is less than that corresponding to $Fr_H \approx 1$ as was the case for l_{rj}/l_c shown in figure 10. This difference can be attributable to air entrainment mechanisms other than the re-entrant jet as discussed earlier, including turbulence mixing on the cavity/water interface and bubbles detaching from the vortical flows at the edges of the fence, both of these contributing to a non-zero σ_c and C_{Qv} at $Fr_H \approx 1$.

With a decrease in Fr and related weakening of the re-entrant jet flow, the influence of the three-dimensional effects on the cavity topology becomes more pronounced. The vortical flow originating from the fence sides becomes increasingly dominant in determining the cavity closure behaviour as the streamwise momentum associated with the main flow (and the high air injection rates required to maintain the cavity) declines. This change results in a transformation of the cavity closure topology from a well defined single re-entrant jet regime, through a phase of gradual re-entrant jet widening to the complete split of the re-entrant jet into two separate branches. A similar phenomenon is well documented for ventilated axisymmetric cavity flow, where a re-entrant jet closure transitions into twin vortex closure at low Fr and σ_c values (Karn et al., 2016). With free surface flows a similar topology is also observed for ventilated transom stern flow (Doctors, 2005) and supercritical flow behind chute piers (Reinauer and Hager, 1994).

In figure 5.12 a series of images depicting the transformation of the cavity closure for a fixed length cavity ($l_c/h \approx 125$) is presented for varying Fr ($10.9 \leq Fr \leq 20.6$). A complementary schematic of cavity cross-section at the distance l_{cs} from the fence (noted in figure 5.12a) is shown in figure 5.13 for the same Fr values. For the highest Fr the closure exhibits the single re-entrant jet behaviour, with the most intense air shedding along the flow centreline (figure 5.12a). On each side of the cavity a streak of air bubbles

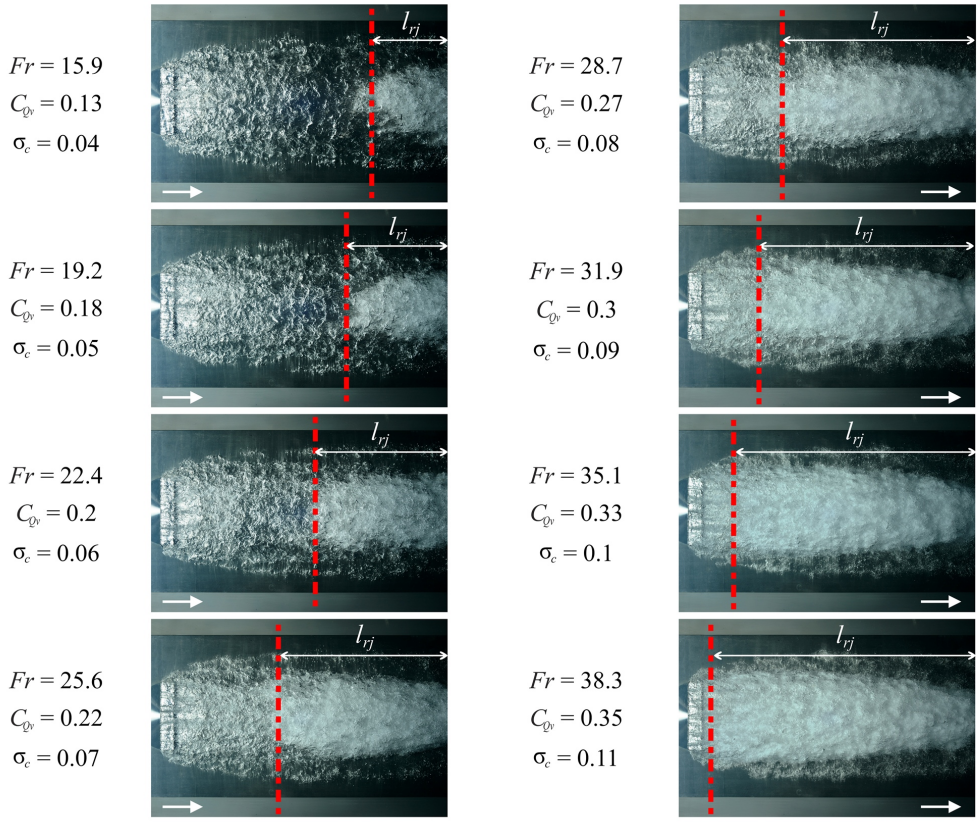

Figure 5.9: Cavities of a constant length ($l_c/h \approx 70$) are shown for varying Fr ($15.9 \leq Fr \leq 38.3$) and a constant σ_v ($\sigma_v = 0.95$). In all instances the cavity closure is located on the right border of an image. With a decrease in Fr the length of region occupied by the re-entrant jet reduces.

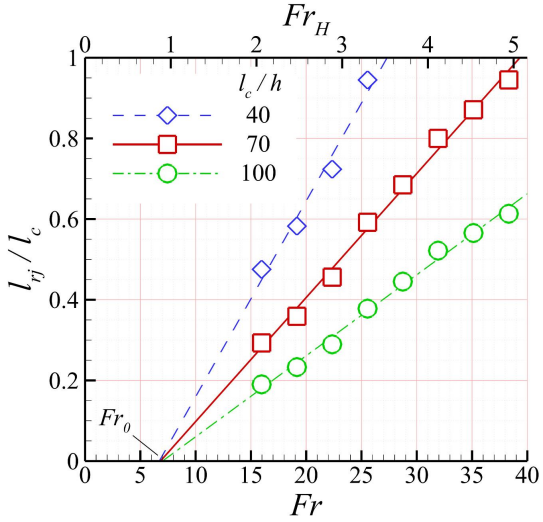

Figure 5.10: Dependence of the re-entrant jet to cavity length ratio on Fr for a fixed length cavities ($l_c/h \approx 40, 70\,\&\,100$) and constant σ_v ($\sigma_v = 0.95$). The data follows a linear trend and l_{rj}/l_c reaches a common zero value (i.e. extinction of the re-entrant jet) for a non-zero $Fr = Fr_0 \approx 7.0$, which corresponds to a Fr_H value of about 1.0, that is, the transition between super and sub-critical flow.

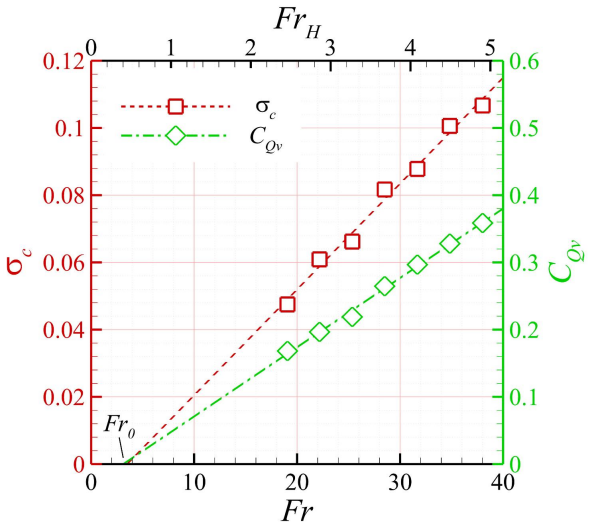

Figure 5.11: C_{Qv} and σ_c as a function of varying Fr for fixed length cavities ($l_c/h \approx 70$) depicted in figure 5.9. Both variables decrease linearly with an decrease in Fr, and reach zero value for a non zero $Fr = Fr_0 \approx 4.0$.

associated with the vortical flow from the fence sides can be observed (figure 5.13a). With a decrease in Fr the rear part of the re-entrant jet widens, leading to formation of a triangular (Δ-shaped) re-entrant jet (figure 5.12b). As the thickness of the cavity sides increase (figure 5.13b-c), shedding starts to occur along the full span of the jet, with the gradual relocation of the high intensity shedding zone from the centre to the sides and an indent appearing in the downstream cavity boundary (figure 5.12c). The cross-section of the rear part of the cavity becomes divided into a middle zone and two side pockets with a trough appearing between them (figure 5.13b-d). Initially, the middle section contains most of the cross-sectional area, but with a decrease in Fr there is a redistribution to the sides. A notch starts to appear in the re-entrant jet downstream boundary and the majority of the shedding occurs symmetrically from the sides (figure 5.12d). Once Fr reaches a critical value (Fr_c), the closure region splits into two symmetric branches with a separate re-entrant zone in each. A bifurcation point is established on the centreline at the root of the split (figure 5.12e) and the cavity middle zone is no longer present at the examined cross-section location (figure 5.13e-f). The distance between the fence tip and the bifurcation point is labelled as critical length (l_{cr}). Once the bifurcation has occurred, all air entrainment now occurs via the branch closure zones and no leakage occurs near the root. With a further decrease in Fr the length of the re-entrant jets in the branches decreases, similar to the behaviour already discussed for the single re-entrant jet regime, and the bifurcation point moves closer to the fence (figure 5.12f-g). With a decrease in re-entrant jet length, a clear air-filled region between the bifurcation point and the re-entrant jet upstream boundary appears, as shown in figures 5.12g and 5.13g. For a constant Fr, l_{cr} is independent of ventilation rate, i.e. the bifurcation point remains fixed following any increase in the ventilation rate after the split has occurred (figure 5.12h).

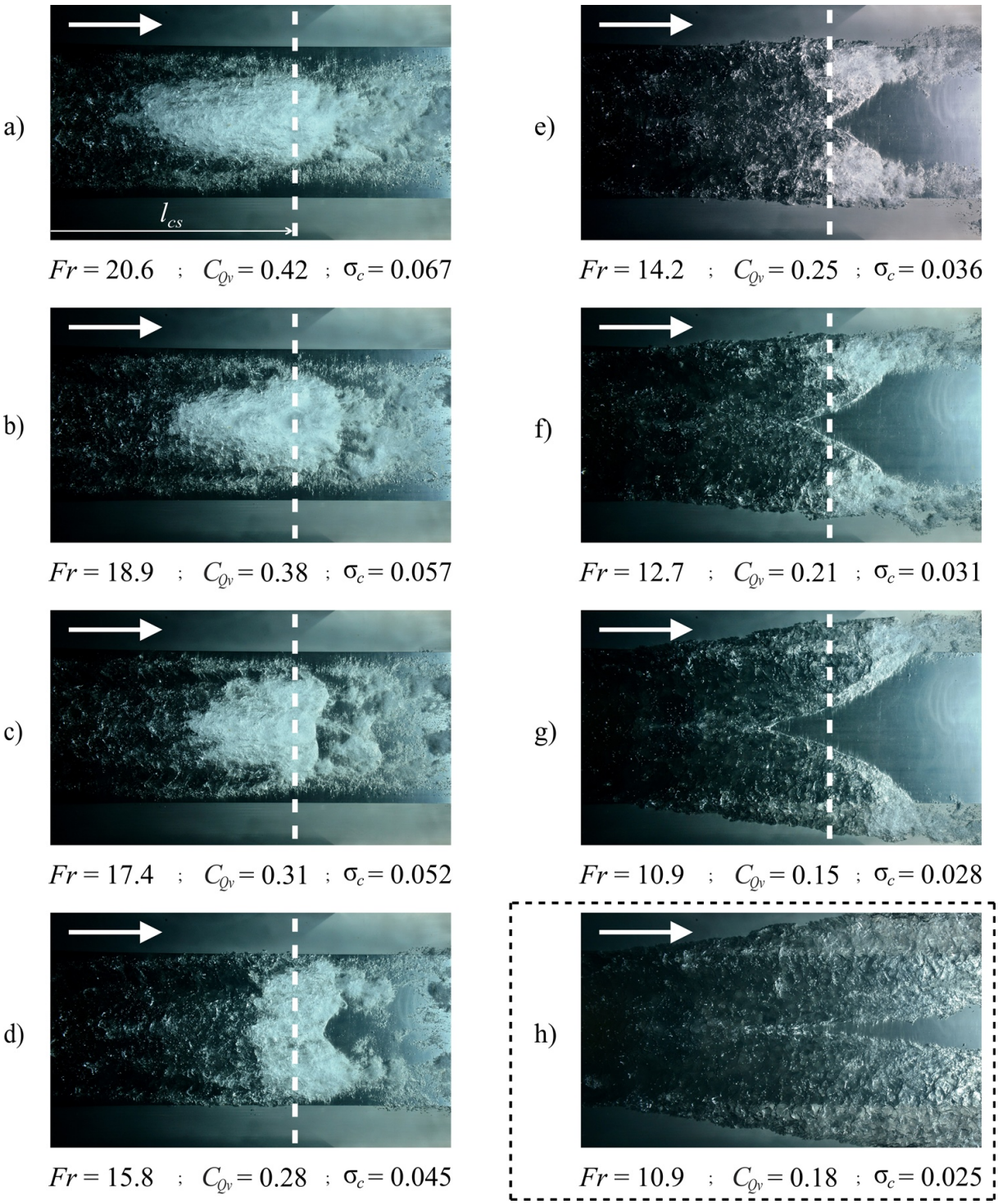

Figure 5.12: Cavity closure transformation for the fixed length cavities $l_c/h \approx 125$ and varying Fr ($10.91 \leq Fr \leq 20.6$). With a decrease in Fr the single re-entrant jet regime present for the high Fr (a) starts to gradually widen and forms into a Δ-shape (b-c). A notch appears on the re-entrant jet outer boundary (d) leading to the eventual complete split of the cavity closure into two symmetrical branches with a re-entrant jet present in each of them (e-f). With a further decrease in Fr the re-entrant jet length decreases and bifurcation point (i.e. the root of the split) moves closer to the fence (g). For the constant Fr (highlighted by dashed box), the bifurcation point remains fixed following any increase in the ventilation rate after the split has occurred (h).

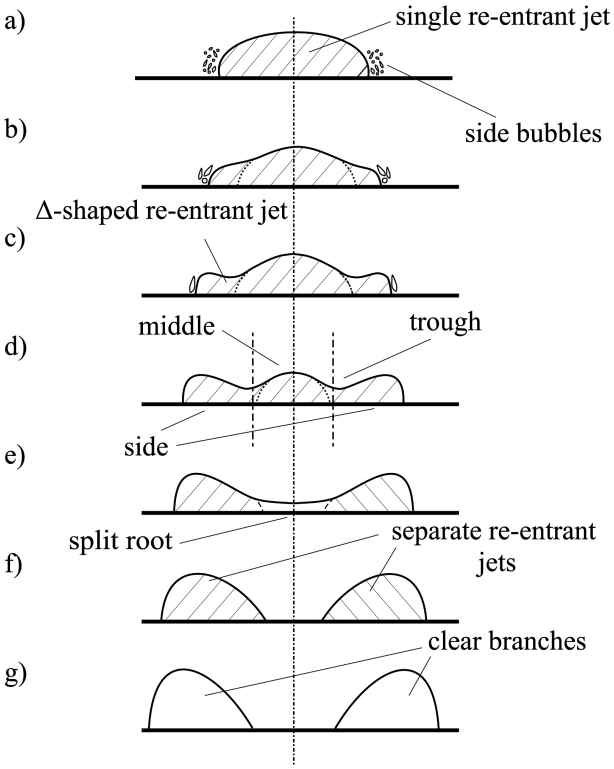

Figure 5.13: A schematic of the evolution of cavity cross-section at the location l_{cs} downstream of the fence tip (figure 5.12) following a decrease in Fr. The cross-section shows a single re-entrant jet at high Fr (a). With a decrease in Fr the cross-section initially divides in the middle section and side pockets (b-c), with the latter becoming more dominant at lower Fr (d). After the split in re-entrant jet has occurred (e) two separate branches are visible (f-g).

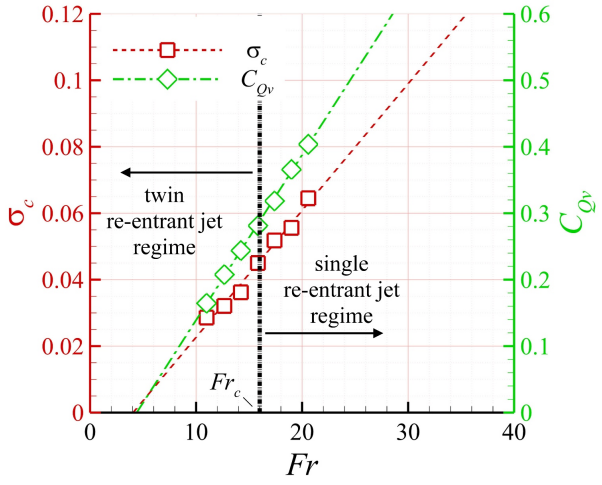

Figure 5.14: C_{Qv} and σ_c as a function of varying Fr for fixed length cavities. Both variables decrease linearly with a decrease in Fr. No discontinuity, or a change in the slope of the curve is apparent in the vicinity of Fr_c (i.e. across the cavity closure transformation process).

Although, the closure topology changes significantly throughout the range of Fr examined, no discontinuities or changes in the dependence of C_{Qv} on Fr are apparent in the vicinity of Fr_c, and a linear behaviour similar to one presented for the single re-entrant jet cavities (figure 5.11) can also be observed. Likewise, σ_c decreases linearly with a decrease in Fr, and is also unaffected by the closure transformation (figure 5.14).

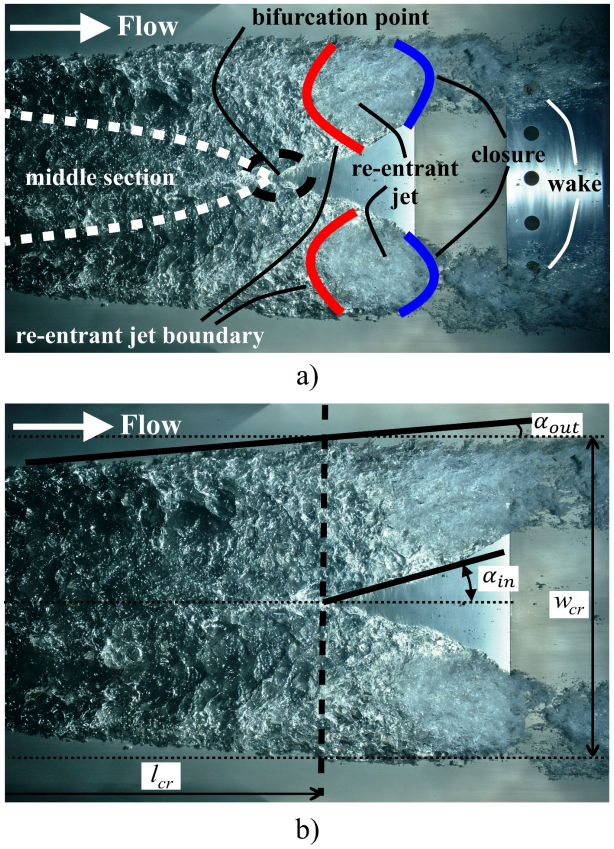

Figure 5.15: a) A typical topology of the cavity with a split re-entrant jet closure present. The cavity closure is split into two symmetrical branches with a re-entrant jet present in each of them. Troughs in the cavity surface, dividing the cavity upstream of the bifurcation point into a middle and side sections, are indicated by white dashed lines. b) Definition of l_{cr}, w_{cr}, α_{in} and α_{out} parameters for characterisation of the split re-entrant jet geometry.

In figure 5.15a a typical topology of the cavity with a split re-entrant jet closure is shown. Shedding is confined to the tip portion of the branches only, with no entrainment through the root zone. Upstream of the bifurcation point the cavity can be differentiated into two regions. A middle section which is symmetrical about the streamwise centreline is differentiated by depressions or troughs in the cavity surface from an outside region or pocket on each side. The latter are formed by vortical flow structures originating from the fence sides, i.e. 3-D end effects. Moving downstream from the fence the middle section reduces in thickness and width, until it completely disappears at the bifurcation point as depicted in figure 5.13. With decrease in the volume within the middle section, the side pockets grow until they become cavity branches downstream of the bifurcation point.

The evolution of a growing cavity encompassing the transition from a single to a

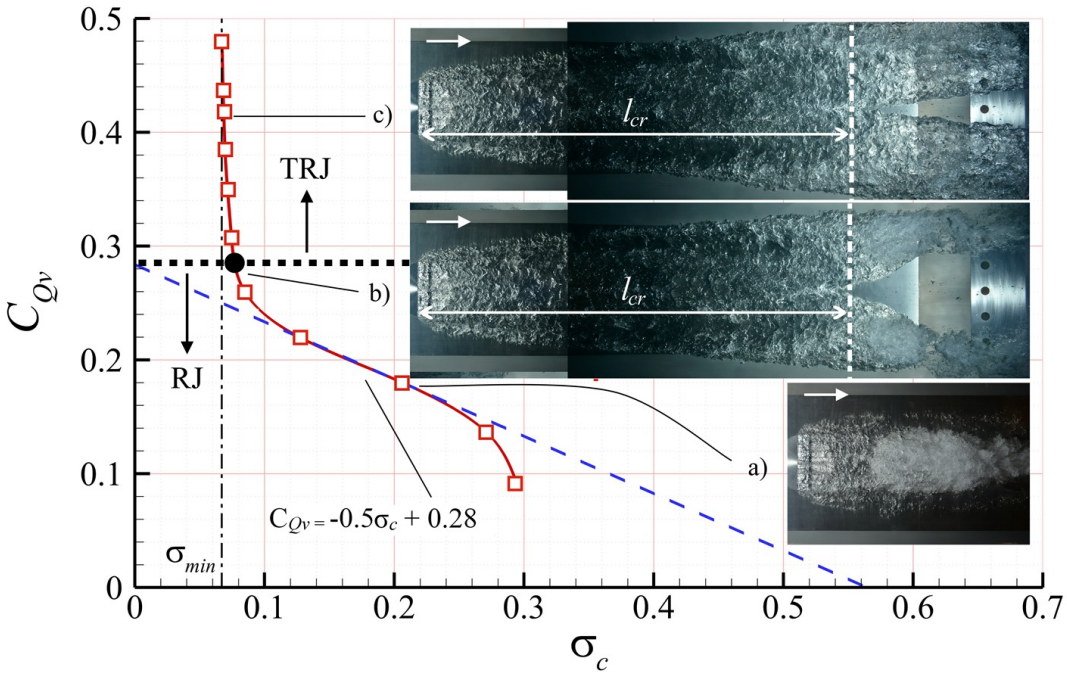

Figure 5.16: Development of the cavity with the split re-entrant jet closure present following an increase in C_{Qv}, for the constant free-stream conditions ($Fr = 15.9$, $\sigma_v = 0.95$). The transition point from single to split re-entrant jet closure is shown as a black filled circle.

split re-entrant jet closure, as the ventilation rate is increased for a constant set of free-stream conditions ($Fr = 15.9$, $\sigma_v = 0.95$), is shown in figure 5.16. The behaviour is similar to that found at higher Fr, i.e. without transition (figure 5.5a), so the significant change in closure topology does not affect the universal dependence of σ_c on C_{Qv}. In the example given, the bifurcation occurs at a σ_c value close to σ_{min}, as the corresponding l_{cr} is relatively long. Note that depending on Fr the point of transition will vary along the curve.

Topologies of split re-entrant jet cavities are shown in figure 5.17 for various Fr. The bifurcation point moves towards the fence with a decrease in Fr, with the critical length l_{cr}/h showing a linear dependence on Fr (figure 5.18a). From figure 5.18a it can also be seen that l_{cr}/h extrapolates to nominally zero for $Fr = 0$. This suggests that for very low flow speeds a split in the re-entrant jet would occur even for the shortest cavities. The parameter $(l_{cr}/h)/Fr$ can be used as a criterion for the transition, with $(l_{cr}/h)/Fr \approx 7.7$ as the critical value. For the cavities with $(l_{cr}/h)/Fr \leq 7.7$ a single re-entrant jet closure will be present, otherwise a split re-entrant jet exists. The non-dimensional cavity width at the position of bifurcation point (w_{cr}/h) increases linearly with a decrease in Fr due to the stronger influence of the spanwise momentum on the cavity with a decrease in the ventilation rate (figure 5.18a).

Two useful parameters which provide additional characterization of the split cavity

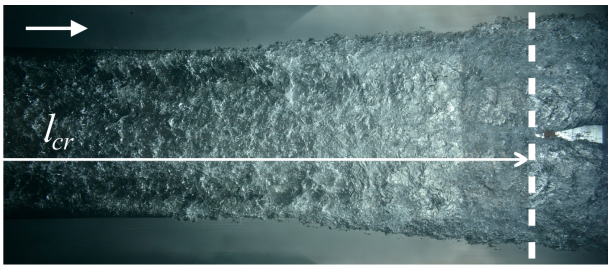

$Fr = 20.6$; $C_{Qv} = 0.42$; $\sigma_c = 0.067$

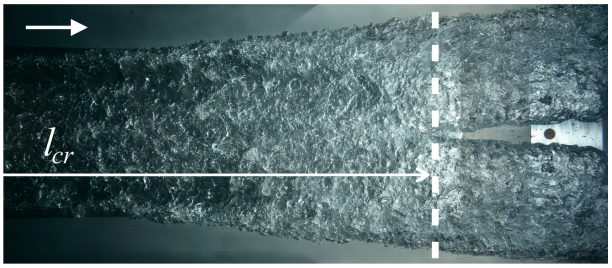

$Fr = 17.4$; $C_{Qv} = 0.32$; $\sigma_c = 0.051$

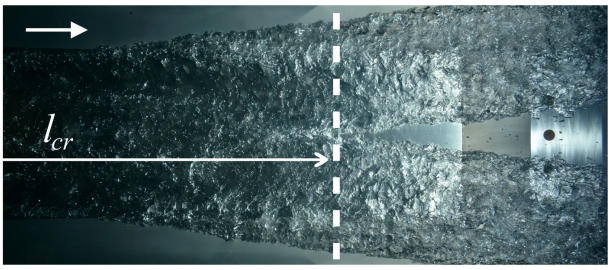

$Fr = 14.2$; $C_{Qv} = 0.25$; $\sigma_c = 0.043$

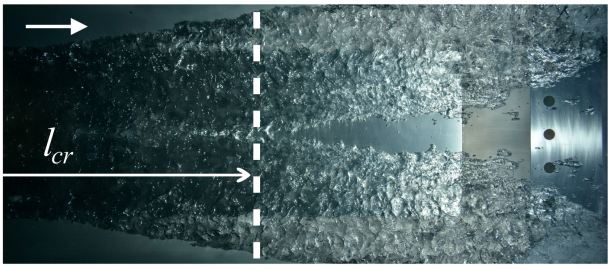

$Fr = 10.9$; $C_{Qv} = 0.15$; $\sigma_c = 0.034$

Figure 5.17: Split re-entrant jet cavities for varying Fr. Note that l_{cr} decreases as Fr is reduced.

topology are the interior angle between the cavity branches and the centreline (α_{in}), and the angle between the cavity side boundary and the centreline α_{out} (figure 5.15b). For consistency both angles are measured at the location of the bifurcation point for a particular Fr (i.e. l_{cr} downstream of the fence). From figure 5.18b, α_{in} increases linearly following an increase in Fr, while α_{out} experiences a linear decrease. α_{in} is always greater than α_{out} across the range of Fr investigated, with the difference reducing as Fr decreases, i.e. the topology of the branches changes from tapered (triangular) to more parallel with reduction in Fr (and consequent increase in cavity length).

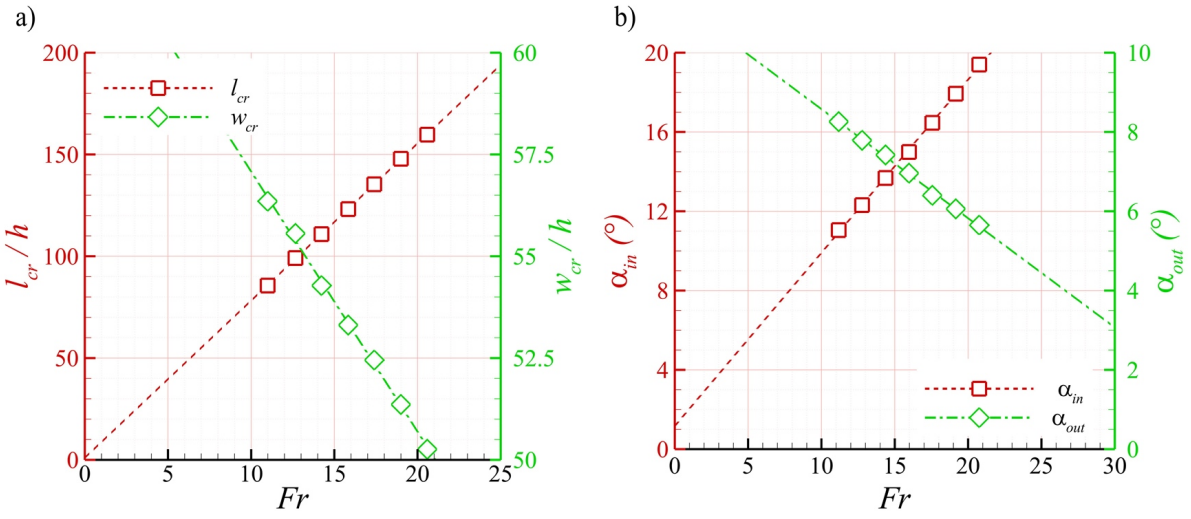

Figure 5.18: a) Dependence of l_{cr}/h and w_{cr}/h on Fr. l_{cr}/h increases linearly, while w_{cr}/h decreases linearly with an increase in Fr. b) Dependence of l_{cr}/h and w_{cr}/h on Fr. l_{cr}/h increases linearly, while w_{cr}/h decreases linearly with an increase in Fr

Following the discussion above, a schematic overview of cavity development is presented in figure 5.19. For very low C_{Qv} typical shear layer type cavitation is present, with the bubbles following the trail of alternate vortices forming at the fence sides (figure 5.19a). As C_{Qv} increases a fully developed cavity with re-entrant jet closure is established. Initially, the re-entrant jet impinges on the fence downstream face (figure 5.19b), but with an increase in cavity length the re-entrant jet moves downstream away from the fence (figure 5.19c). The re-entrant jet length remains constant once it moves from the fence and shedding is contained to the zone near the centreline. As the cavity length approaches l_{cr}, the re-entrant jet begins to widen (figure 5.19d) and develops a Δ-shaped appearance. Once past l_{cr}, the spanwise momentum associated with the vortical flow of the fence sides prevails over the streamwise momentum and a split in the cavity closure occurs (figure 5.19e). The re-entrant jet is now divided into two branches and no entrainment occurs in the vicinity of the bifurcation point. The cavity middle section outlines the zone that is largely unaffected by the three-dimensional flow. With a further increase in C_{Qv} the branches continue to elongate, but the location of bifurcation point remains unchanged

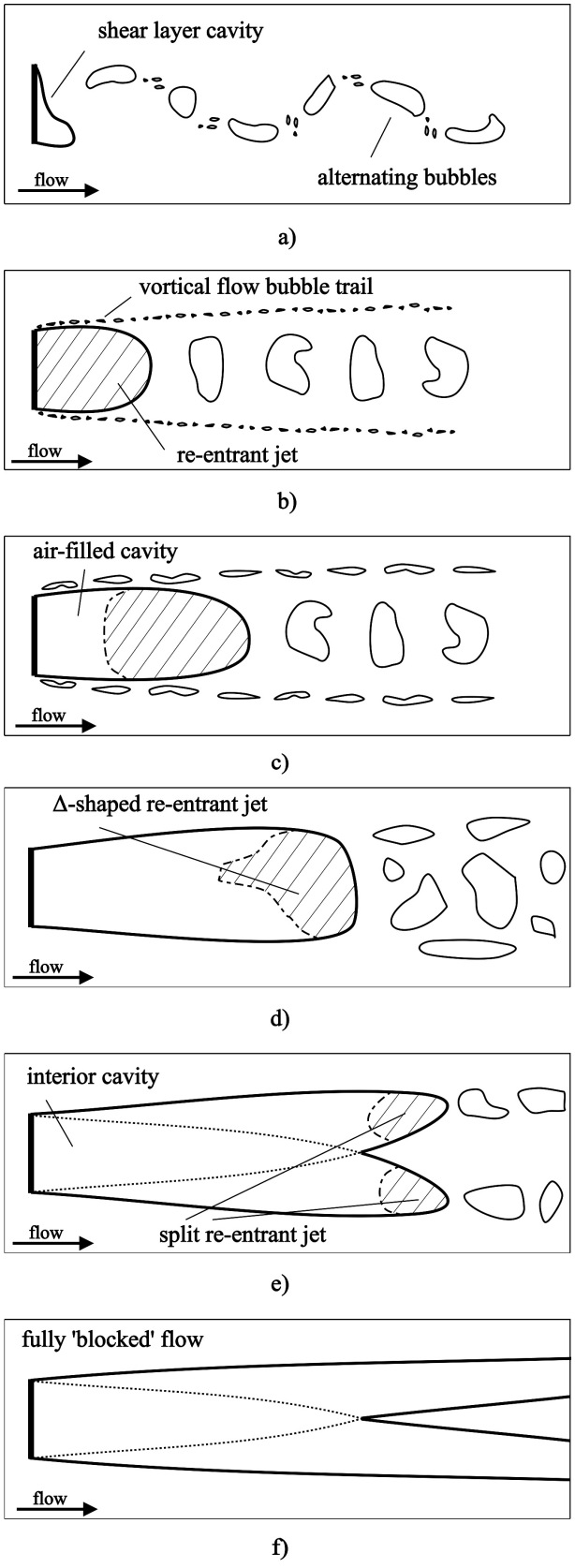

Figure 5.19: A schematic showing the evolution of the cavity with an increase in C_{Qv} for constant free-stream conditions. The detected regimes are: (a) shear layer cavitation; (b-c) fully developed cavity with the single re-entrant jet closure; (d) developed cavity with Δ-shaped re-entrant jet; (e) developed cavity with the split re-entrant jet closure; (f) cavity with the split re-entrant jet closure in a 'blocked' flow condition. This depiction of cavity development is applicable for all free-stream conditions.

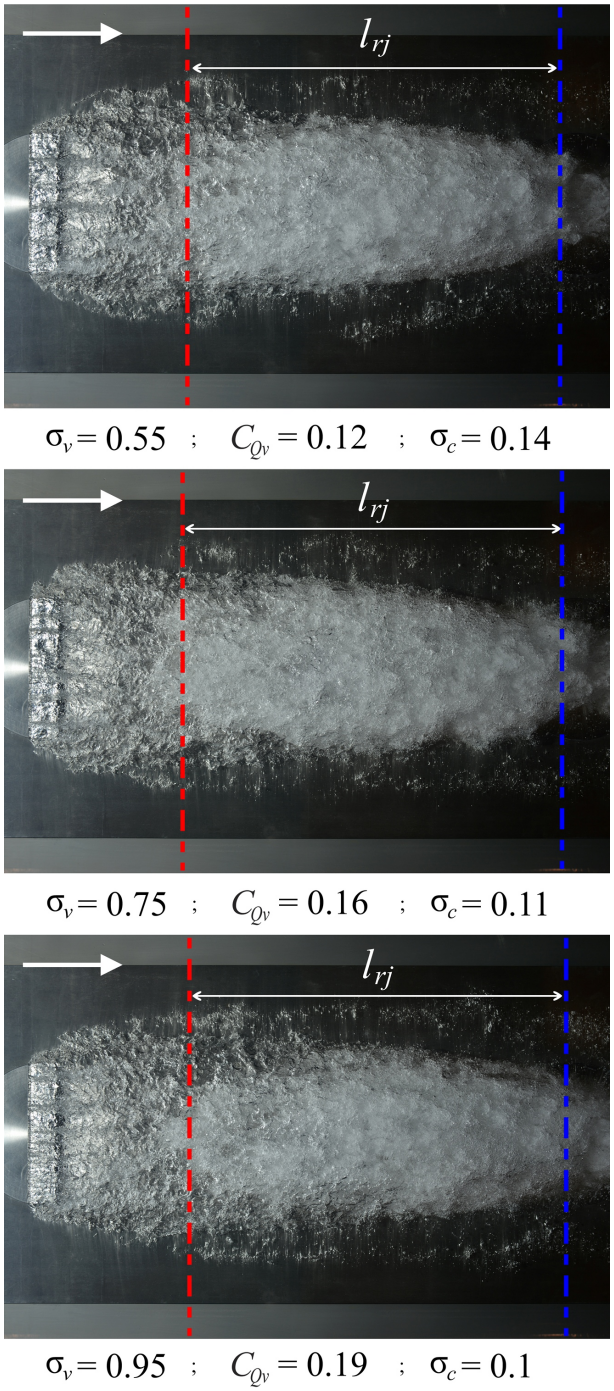

Figure 5.20: Fixed length cavities for variable free-stream σ_v. The re-entrant jet length remains constant and there are no significant changes in the cavity topology observed for the range of σ_v examined.

(figure 5.19f). This depiction is applicable for all free-stream conditions, with the only difference being the location of bifurcation point (i.e. different l_{cr}). The schematic depicts the complete evolution of the cavity from shear layer cavitation to one largely dominated by two-dimensional effects, and finally into a fully three-dimensional cavity. The latter topology resembles the flow associated with air-injection through a single hole described in a recent study (Mäkiharju and Ceccio, 2016).

5.3.4 The influence of free-stream cavitation number

The cavity topology was investigated for the alternative case of varying free-stream cavitation number σ_v (at a constant Fr). In figure 5.20 cavities of a constant length ($l_c/h \approx 70$) are shown for three σ_v values ($\sigma_v = 0.55, 0.75 \,\&\, 0.95$). It can be seen that no significant change in the re-entrant jet length or appearance can be observed. Although re-entrant jet intensity remains unchanged, C_{Qv} has to be altered to maintain a constant cavity length in order to compensate for the change in the free-stream pressure.

In figure 5.21 the dependence of σ_c on C_{Qv} for the case of varying σ_v and a fixed Fr ($Fr = 25.3$) is shown. With the increase in σ_v more air has to be injected to achieve the same σ_c value. The linear part of the curve has a relatively constant slope for all σ_v values. σ_{min} is approximately constant, which is expected as the free-stream velocity is held constant.

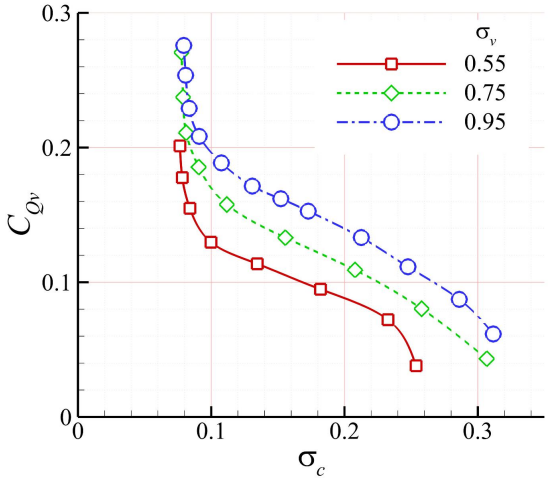

Figure 5.21: Relation between σ_c and C_{Qv} for different free-stream cavitation numbers and constant Froude number value ($Fr = 25.3$)

5.3.5 Drag

Traditionally, the main interest in devices utilizing ventilated cavities has been for drag reduction. In figure 5.22a the dependence of C_D on σ_c is shown for three values of Fr

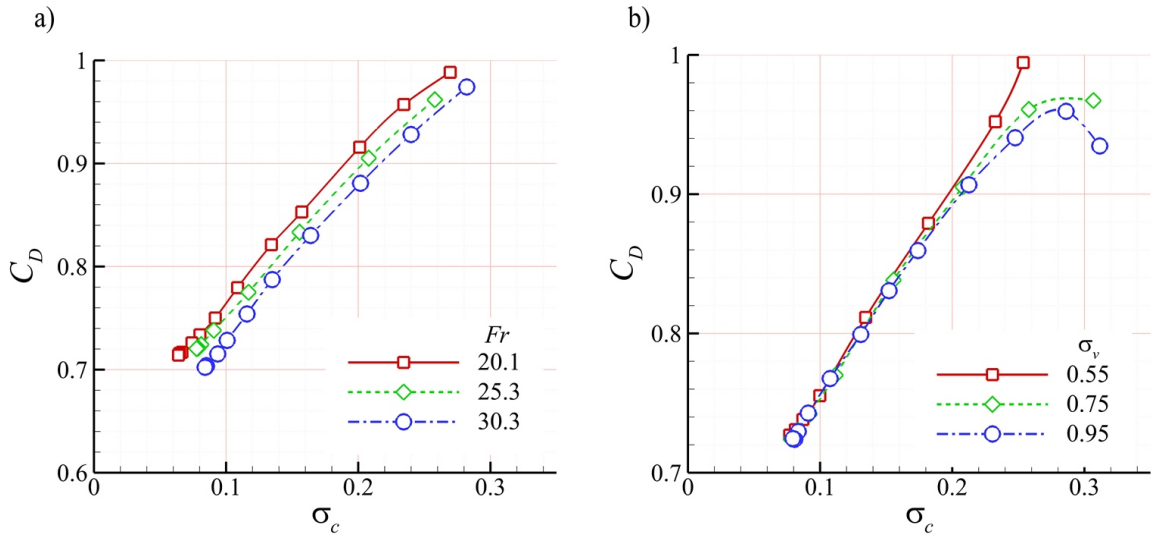

Figure 5.22: a) Drag coefficient as a function of cavitation number for three values of Froude number and constant free-stream cavitation number ($\sigma_v = 0.95$). b) Drag coefficient as a function of cavitation number for three values of free-stream cavitation number and constant Froude number value ($Fr = 25.3$).

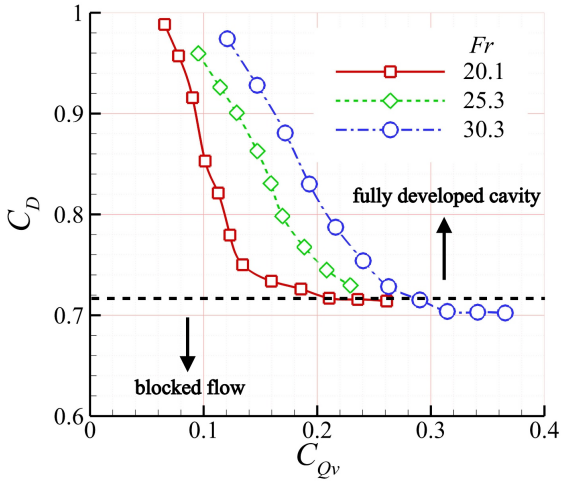

Figure 5.23: Dependence of C_D on C_{Qv} for variable Fr and constant σ_v. The higher intensity re-entrant jet present at higher Fr is causing an increase in C_D at a constant C_{Qv}.

(for $\sigma_v = 0.95$). The drag coefficient decreases approximately linearly with the decrease in cavitation number. The non-linearity present for high σ_c is due to shear layer cavity behaviour, as a fully formed cavity is not yet present. It can be seen that for $\sigma_c = \sigma_{min}$ the drag also has a minimum value ($C_{D_{min}}$). Drag decreases with increase in Fr (figure 5.22a), mainly due to the change in blockage resulting from cavity thickness variation discussed in section 3.2 (figure 5.8). The difference in C_D, for constant σ_c, across the range of examined Fr is around 5%.

In figure 5.22b the alternate case of varying σ_v, for a fixed Fr (= 25.3), is presented. It can be seen that C_D is independent of σ_v in the region where a ventilated cavity is fully formed. A slight difference exists for high σ_c values, again where the shear layer cavitation regime is present.

In the drag reduction context it is common to link a high C_D with the presence of a high intensity re-entrant jet and subsequent high ventilation rates needed to maintain the ventilated cavity. To illustrate this, the dependence of C_D on C_{Qv} is shown in figure 5.23 for cases with three Fr values. As already discussed, a higher C_{Qv} is needed to achieve the same cavity length at a higher Fr, which conversely means that if the C_{Qv} is held constant, a higher σ_c and a shorter cavity will be achieved at high Fr. As presented in figure 5.22a a higher σ_c is related to a higher C_D, so it is not unexpected to see that C_D is increasing with an increase in Fr for a constant C_{Qv}. From figure 5.23 it can be seen that in the region where a fully developed cavity is present a difference of up to 25% in C_D can be observed. For blocked flow, the drag behaviour is asymptotic, with $C_{D_{min}}$ controlled by the blockage ratio.

5.4 Conclusions

Ventilated cavity flow over a fixed height three-dimensional wall-mounted fence has been investigated experimentally in a cavitation tunnel. An experimental setup has been developed to examine the influence of air ventilation rate and free-stream conditions on the cavitation number, cavity topology and drag. A typical cavity geometry features two distinct regions along the length; the air-filled region with a transparent appearance closer to the fence and an opaque mixed-phase closure region. The closure exhibits a re-entrant jet behaviour which is the primary mechanism of air entrainment into the main flow. To a lesser extent, air is also entrained via the turbulent cavity/water interface and detached bubbles from the vortical flows each side of the cavity.

Three different flow regimes were identified following a decrease in σ_c for a constant set of free-stream conditions: (I) shear layer cavitation with alternate vortex shedding process for high σ_c values, (II) developed cavity with a re-entrant jet closure and a linear dependence of σ_c on C_{Qv} for intermediate σ_c values and (III) 'blocked' cavity flow where

$\sigma \to \sigma_{min}$. Cavity length as function of σ_c follows a power law behaviour until the cavity approaches the test-section outlet, where the cavity growth is very sensitive to any further small increase in ventilation rate. The re-entrant jet intensity was found to be independent of ventilation rate for any particular free-stream condition. With an increase in Fr and/or σ_v, significantly more air is needed to obtain the same σ_c value.

To investigate the effect of a change in free-stream conditions on re-entrant jet intensity, fixed length cavities were examined for a range of free-stream Fr and σ_v. The re-entrant jet becomes less intense as Fr decreases, with l_{rj}/l_c exhibiting a linear dependence on Fr. Similarly, C_{Qv} and σ_c decrease linearly as Fr decreases. As a consequence of the re-entrant jet weakening, the influence of three-dimensional effects on the cavity topology becomes more pronounced. With a decrease in Fr, the cavity closure behaviour goes through a transformation from a well defined single re-entrant jet regime, through a phase of gradual re-entrant jet widening to a complete split of the re-entrant jet into two separate branches (i.e. split re-entrant jet closure). Although, a change in the air entrainment mode is present, the relations between the governing parameters remain unaffected.

After the re-entrant jet divides, any further increase in C_{Qv} leads to the elongation of the cavity branches only, while the location of the bifurcation point (i.e. root of the split) remains constant. The length from the fence tip to the bifurcation point, l_{cr}/h, decreases linearly with decreasing Fr. For the alternate case of varying σ_v at a constant Fr no change in the re-entrant jet intensity was observed.

With a decrease in σ_c, the drag coefficient decreases linearly until it reaches a minimum value when $\sigma_c = \sigma_{min}$. Drag decreases with an increase in Fr, with a difference of around 5% for a constant σ_c across the range of Fr investigated. However, due to the more intense re-entrant jet present at high Fr values, an increase of up to 25% in C_D was observed across the range of Fr investigated if the C_{Qv} was held constant. The drag is found to be independent of σ_v.

A companion study is planned to investigate the effect of fence immersion in the upstream wall boundary layer. A series of unsteady measurements in the closure region are also to be conducted, coupled with high-speed imaging, to gain deeper insight into the re-entrant jet closure dynamics. These 3-D wall-mounted fence results will also be compared with a future study of ventilated cavity flow over a 2-D wall-mounted fence.

Acknowledgements

The authors wish to acknowledge the assistance of Mr Robert Wrigley and Mr Steven Kent in carrying out the experiments and the support of the Australian Maritime College.

Chapter 6

General Conclusions and Future Recommendations

6.1 Conclusions

Within this thesis, experimental and numerical investigations of cavity flow over a wall-mounted fence immersed in a turbulent boundary layer are presented. The basic understanding of this canonical flow is gained experimentally through a systematic study of ventilated and natural cavity flows over 2-D and 3-D wall-mounted fences in a cavitation tunnel.

Irrespective of the origin, i.e. natural or ventilated, two distinct regions are evident along the length of a fully developed cavity: a transparent air/vapour filled zone closer to the fence and an opaque, re-entrant jet affected, closure region. Although, a re-entrant jet closure was observed, the cavities did not exhibit large-scale oscillations, but irregular shedding of small scale structures. From the qualitative analysis of the flow mean topology, the re-entrant jet was identified as the primary driving mechanism of cavity break-up. However, quantitative unsteady analysis showed that, although the interaction between the re-entrant jet and cavity water/interface affects the cavity surface break-up, the characteristics of the overlying turbulent boundary layer govern the break-up and subsequent entrainment of bubbly structures at the cavity closure. This turbulence governed small-scale cavity break-up was associated with a high-frequency broad-band peak and a power law decay in the wall pressure spectra, similar to observations from single-phase flow over a forward-facing step. The location of this peak collapsed for $St_h = 0.02$, showing that cavity-break-up is invariant of free-stream velocity. Another unsteady feature was observed as larger-scale oscillations in the size of the re-entrant jet affected region. This oscillation was observed as a low-frequency peak in the wall pressure spectra, anal-

ogous to the 'flapping' instability of the recirculation zone in single-phase flow. The low-frequency peak was found to collapse for a Strouhal number based on the re-entrant jet length (of about 0.1). The re-entrant jet length was found to have a linear dependence on free-stream velocity, analogous to the recirculation zone length in gravity dominated super-critical open-channel flow. This similarity indicates that the low-frequency oscillation of the re-entrant jet is modulated by gravity (i.e. influence of buoyancy due to inclusion of the gaseous/vaporous phase of much lower density compared to water). Likewise, a significant change in cavity behaviour was observed as the flow underwent transition analogous to transition from sub- to super-critical regime in open-channel flow. In spite of the fundamental difference between the two flows, the unsteady behaviour of cavity flow over a wall-mounted fence was found to be similar in many respects to that in single-phase flow, where the difference in behaviour could be attributed mainly to the influence of buoyancy.

Following a decrease in cavitation number from inception three flow regimes were identified: shear layer cavitation, fully developed cavitation and blocked flow conditions when $\sigma_c \to \sigma_{min}$. In ventilated cavity flow a nominally linear dependence of σ_c on C_{Qv} is observed in the fully developed cavity regime. The cavity length exhibits a power law like increase following a decrease in σ_c, up until $\sigma_c \approx \sigma_{min}$ where a vertical asymptote representing 'infinite' cavity growth is present. The dependence of cavity length on cavitation number was found to be independent of free-stream conditions.

The upstream wall pressure distribution is characterized by a zone of almost constant C_P within one fence height of the fence, followed by a slow decrease in C_P between one h and $5h$ and a power law like reduction in the far field. For a constant set of free-stream conditions, drag decreased linearly following a decrease in cavitation number, reaching the asymptotic value for $\sigma_c \to \sigma_{min}$. The decrease in drag, coupled with increase in lift leads to an increase in hydrodynamic efficiency of the fence/wall system with decreasing σ_c. The drag is found to be independent of free-stream conditions and to decrease with an increase in fence immersion in the oncoming wall boundary layer.

The experimental data are compared with numerical results from CFD analysis. An implicit unsteady compressible solver is used with a RANS $k-\omega$ SST turbulence model and VOF approach to capture cavity interface. The simplified numerical model was observed to have clear limitations. However, depending on the parameter of interest a reasonable agreement between the experimental and numerical results has been shown confirming the utility of the simulation method used. Additionally, numerical analysis is used to evaluate the effect of confinement on the flow, which is shown to significantly alter the relations between the flow parameters.

Despite the significant differences observed in the 2-D and 3-D cavity geometries the general trend behaviour across various parameters was found to be quite similar, and only affected by reduced blockage for the 3-D configuration. The main effect of 3-D flow was

observed through reduction in cavity width towards the closure at higher free-stream Fr. With a decrease in Fr, and a related decrease in the re-entrant jet intensity, the cavity closure goes through a transformation from a well defined single re-entrant jet regime, through a phase of gradual re-entrant jet widening to a complete split of the re-entrant jet into two separate branches. Although, a change in the closure topology is present, the relations between the governing parameters remain unaffected.

The basic understanding of cavity flow over a wall-mounted fence gained from this study provides a good basis for further research of fence flows in a more applied context. These results may benefit the development of novel concepts of base-ventilated hydrofoils equipped with a retractable fence at the trailing edge, from which the initial interest in this topic originated. Additionally, these results are also relevant for flow over a fence attached to a ship hull, used either for force generation or ventilated drag reduction.

6.2 Future recommendations

Recommendations for future work are primarily in the context of extending unsteady investigations to a broader range of parameters. In addition to the effect of free-stream velocity reported within this thesis, the effect of change in cavity length, free-stream pressure and fence immersion in the overlying boundary layer on the unsteady behaviour of cavity flow over a 2-D wall-mounted fence should be addressed. In addition, an unsteady study of cavity flow over a 3-D wall-mounted fence would be of interest. Improvements in the dynamic pressure measurements could be made by using more sensitive sensors. The effect of confinement, determined from the numerical analysis, should be investigated experimentally by testing fences of different height. The numerical analysis could be improved by using 3-D solver and employing more sophisticated CFD modelling techniques, such as Large Eddy Simulation or Detached Eddy Simulation, which could be a useful tool for additional characterization of the flow unsteady behaviour.

Bibliography

A. J. Acosta. Hydrofoils and hydrofoil craft. *Annual Review of Fluid Mechanics*, 5(1): 161–184, 1973.

E. L. Amromin, J. Hansberger, R. E. A. Arndt, and M. Wosnik. Investigation of a low-drag partially cavitiating hydrofoil. In *Cav-2003 Symposium*, 2003.

R. E. A. Arndt, W. T. Hambleton, E. Kawakami, and E. L. Amromin. Creation and maintenance of cavities under horizontal surfaces in steady and gust flows. *Journal of Fluids Engineering*, 131(11):111301–1 – 111301–10, 2009.

M. Awasthi, W. Devenport, S. Glegg, and J. Forest. Pressure fluctuations produced by forward steps immersed in a turbulent boundary layer. *Journal of Fluid Mechanics*, 756:384–421, 2014.

L. Barbaca, B. W. Pearce, and P. A. Brandner. Computational investigation of ventilated cavity flow over a 2-D fence. In *The Proceedings of the 19th Australasian Fluid Mechanics Conference*, 2014.

L. Barbaca, B. Pearce, and P. Brandner. Experimental investigation of ventilated cavity flow over a 3D wall mounted fence. In *16th International Symposium on Transport Phenomena and Dynamics of Rotating Machinery, Honolulu, Hawaii, April 10-15, 2016*, 2016.

L. Barbaca, B. W. Pearce, and P. A. Brandner. Experimental study of ventilated cavity flow over a 3-D wall-mounted fence. *International Journal of Multiphase Flow*, 97: 10–22, 2017a.

L. Barbaca, B. W. Pearce, and P. A. Brandner. Numerical analysis of ventilated cavity flow over a 2-D wall mounted fence. *Ocean Engineering*, 141:143–153, 2017b.

L. Barbaca, B. W. Pearce, and P. A. Brandner. An experimental study of cavity flow over a 2-D wall-mounted fence in a variable boundary layer (article in press). *International Journal of Multiphase Flow*, 2018.

A. Belle, P. A. Brandner, B. W. Pearce, K. L. de Graaf, and D. B. Clarke. Artificial thickening and thinning of cavitation tunnel boundary layers. *Experimental Thermal and Fluid Science*, 78:75–89, 2016.

P. Brandner, B. Pearce, and K. de Graaf. Cavitation about a jet in crossflow. *Journal of Fluid Mechanics*, 768:141–174, 2015.

P. A. Brandner, Y. Lecoffre, and G. J. Walker. Design considerations in the development of a modern cavitation tunnel. In *Proceedings of the 16th Australasian Fluid Mechanics Conference, 16AFMC*, pages 630–637, 2007.

P. A. Brandner, G. J. Walker, P. N. Niekamp, and B. Anderson. An experimental investigation of cloud cavitation about a sphere. *Journal of Fluid Mechanics*, 656:147–176, 2010. ISSN 1469-7645.

C. Brennen. *Cavitation and Bubble Dynamics*. Oxford University Press, New York, 1995.

J. Brentjes. Free-surface water tunnel studies of a family of base-ventilated hydrofoils. Technical report, Hydrodynamics Laboratory, Laboratory of Fluid Mechanics and Jet Propulsion, California Institute of Technology, 1962.

S. Brizzolara. Hydrodynamic analysis of interceptors with CFD methods. In *Seventh International Conference on Fast Sea Transportation - FAST 2003, Naples, Italy*, pages 49–56, 2003.

A. Butuzov, A. Sverchkov, A. Poustoshny, and S. Chalov. High speed ships on the cavity: scientific base, design pecularities and perspectives for the Mediterranean Sea. In *Proceedings of the 5th Symposium on High Speed Marine Vehicles*, 1999.

M. Callenaere, J. P. Franc, J. M. Michel, and M. Riondet. The cavitation instability induced by the development of a re-entrant jet. *Journal of Fluid Mechanics*, 444:223–256, 2001.

R. Camussi, M. Felli, F. Pereira, G. Aloisio, and A. D. Marco. Statistical properties of wall pressure fluctuations over a forward-facing step. *Physics of Fluids*, 20(7):075113, 2008.

S. L. Ceccio. Friction drag reduction of external flows with bubble and gas injection. *Annual Review of Fluid Mechanics*, 42(1):183–203, 2010.

H. Chanson. Study of air entrainment and aeration devices. *Journal of Hydraulic Research*, 27(3):301–319, 1989.

K. L. de Graaf, P. A. Brandner, and B. W. Pearce. Spectral content of cloud cavitation about a sphere. *Journal of Fluid Mechanics*, 812, 2016.

D. F. de Lange, G. J. de Bruin, and L. van Wijngaarden. On the mechanism of cloud cavitation - experiment and modelling. In *2nd International Syposium on Cavitation, Tokyo, 1994*, 1994.

S. B. Denny, L. T. Puckette, and E. N. Hubble. A new usable propeller series. *Marine Technology and SNAME News*, 26:173–191, 1989.

G. Dimaczek, C. Tropea, and A. B. Wang. Turbulent flow over two-dimensional, surface-mounted obstacles: Plane and axisymmetric geometries. In *Advances in Turbulence 2: Proceedings of the Second European Turbulence Conference, Berlin, August 30 – September 2, 1988*, pages 114–121, 1989.

L. J. Doctors. The separation of the flow past a transom stern. In *First International Conference on Marine Research and Transportation (ICMRT '05) , Ischia, Italy*, 2005.

D. M. Driver, H. L. Seegmiller, and J. G. Marvin. Time-dependent behavior of a reattaching shear layer. *AIAA Journal*, 25(7):914–919, 1987.

F. Durst and A. K. Rastogi. *Turbulent Flow over Two-Dimensional Fences, Turbulent Shear Flows 2*, pages 218–232. Springer-Verlag, 1980.

B. R. Elbing, S. Mäkiharju, A. Wiggins, M. Perlin, D. R. Dowling, and S. L. Ceccio. On the scaling of air layer drag reduction. *Journal of Fluid Mechanics*, 717:484–513, 2013.

A. Elms. Improved hydrofoil device. International patent number WO 99/57007, 1999.

O. Faltinsen. *Hydrodynamics of high speed vehicles*, volume 5. Cambridge University Press, Cambridge, England, 1996.

F.-M. Fang and D. Y. Wang. On the flow around a vertical porous fence. *Journal of Wind Engineering and Industrial Aerodynamics*, 67:415–424, 1997.

T. M. Farabee and M. J. Casarella. Measurements of fluctuating wall pressure for separated/reattached boundary layer flows. *Journal of Vibration, Acoustics, Stress, and Reliability in Design*, 108(3):301–307, 1986.

J. Franc and J. M. Michel. *Fundamentals of Cavitation*, volume 76 of *Fluid Mechanics and Its Applications*. Kluwer Academic Publishers, Dordrecht, 2004.

J. P. Franc. Partial cavity instabilities and re-entrant jet. In *Fourth International Symposium on Cavitation - CAV2001, Californian Institute of Technology, Pasadena, California, U.S.*, 2001.

G. M. Fridman. Matched asymptotics for two-dimensional planing hydrofoils with spoilers. *Journal of Fluid Mechanics*, 358:259–281, 1998.

R. A. Furness and S. P. Hutton. Experimental and theoretical studies of two-dimensional fixed-type cavities. *Journal of Fluids Engineering*, 97(4):515–521, 1975.

H. Ganesh, S. A. Mäkiharju, and S. L. Ceccio. Bubbly shock propagation as a mechanism for sheet-to-cloud transition of partial cavities. *Journal of Fluid Mechanics*, 802:37–78, 2016a.

H. Ganesh, J. Wu, and S. Ceccio. Investigation of cavity shedding dynamics on a NACA0015 hydrofoil using time resolved X-ray densitometry. In *31st Symposium on Naval Hydrodynamics, 11-16 September 2016, Monterey, California, USA*, 2016b.

M. C. Good and P. Joubert. The form drag of two-dimensional bluff-paltes immeresed in turbulent boundary layers. *Journal of Fluid Mechanics*, 31(3):547–582, 1968.

S. Gopalan and J. Katz. Flow structure and modeling issues in the closure region of attached cavitation. *Physics of Fluids*, 12(4):895–911, 2000.

A. Graziani, M. Lippert, D. Uystepruyst, and L. Keirsbulck. Scaling and flow dependencies over forward-facing steps. *International Journal of Heat and Fluid Flow*, 67(Part A):220–229, 2017.

W. H. Hager, R. Bremen, and N. Kawagoshi. Classical hydraulic jump: length of roller. *Journal of Hydraulic Research*, 28(5):591–608, 1990.

C. W. Hirt and B. D. Nichols. Volume of fluid VOF method for the dynamics of free boundaries. *Journal of Computational Physics*, 39(1):201–225, 1981.

T. Huang. Investigation of base vented hydrofoils. Technical report, Hydronautics, Inc., 1965.

L. M. Hudy, A. M. Naguib, and W. M. H. Jr. Wall-pressure-array measurements beneath a separating/reattaching flow region. *Physics of Fluids*, 15(3):706–717, 2003.

M. Insel, S. Gokcay, and I. Helvacioglu. Flow analysis of an air injection through discrete air lubrication. In *International Conference on Ship Drag Reduction SMOOTH-SHIPS*, 2010.

C. O. Iyer and S. L. Ceccio. The influence of developed cavitation on the flow of a turbulent shear layer. *Physics of Fluids*, 14(10):3414–3431, 2002.

D. Jeffrey, X. Zhang, and D. W. Hurst. Aerodynamics of Gurney flaps on a single-element high-lift wing. *Journal of Aircraft*, 37(2):295–301, 2000. ISSN 0021-8669. doi: 10.2514/2.2593.

A. Karn, R. E. A. Arndt, and J. Hong. An experimental investigation into supercavity closure mechanisms. *Journal of Fluid Mechanics*, 789:259–284, 2016. doi: 10.1017/jfm.2015.680.

E. Kawakami and R. E. A. Arndt. Investigation of the behavior of ventilated supercavities. *Journal of Fluids Engineering*, 133(9):091305–1 – 091305–11, 2011.

Y. Kawanami, H. Kato, and H. Yamaguchi. Three-dimensional characteristics of the cavities formed on a two-dimensional hydrofoil. In *3rd International Symposium on Cavitation, Grenoble, France*, volume Vol 1, pages 191–196, 1998.

H. B. Kim and S. J. Lee. Time-resolved velocity field measurements of separated flow in front of a vertical fence. *Experiments in Fluids*, 31(3):249–257, 2001.

M. P. Kinzel, M. D. Maughmer, and E. P. N. Duque. Numerical investigation on the aerodynamics of oscillating airfoils with deployable gurney flaps. *AIAA Journal*, 48(7): 1457–1469, 2010. ISSN 0001-1452. doi: 10.2514/1.J050070.

J. Kopriva, R. E. A. Arndt, and E. L. Amromin. Improvement of hydrofoil performance by partial ventilated cavitation in steady flow and periodic gusts. *Journal of Fluids Engineering, Transactions of the ASME*, 130(3):0313011–0313017, 2008.

R. F. Kunz, D. R. Stinebring, T. S. Chyczewski, D. A. Boger, H. J. Gibeling, and T. R. Govindan. Multi-phase CFD analysis of natural and ventilated cavitation about submerged bodies. In *Proceedings of the 1999 3rd ASME/JSME Joint Fluids Engineering Conference, FEDSM'99, San Francisco, California, USA, 18-23 July 1999*, 1999.

K. R. Laberteaux and S. L. Ceccio. Partial cavity flows. Part 1. Cavities forming on models without spanwise variation. *Journal of Fluid Mechanics*, 431:1–41, 2001a.

K. R. Laberteaux and S. L. Ceccio. Partial cavity flows. Part 2. Cavities forming on test objects with spanwise variation. *Journal of Fluid Mechanics*, 431:43–63, 2001b.

T. Lang and D. Daybell. Water tunnel tests of three vented hydrofoils in two-dimensional flow. *Journal of Ship Research*, 5(3):1–15, 1961.

R. Latorre. Ship hull drag reduction using bottom air injection. *Ocean Engineering*, 24 (2):161–175, 1997.

W. Lauterborn and H. Bolle. Experimental investigations of cavitation-bubble collapse in the neighbourhood of a solid boundary. *Journal of Fluid Mechanics*, 72(2):391–399, 1975.

K. A. Lay, R. Yakushiji, S. Mäkiharju, M. Perlin, and S. L. Ceccio. Partial cavity drag reduction at high Reynolds numbers. *Journal of Ship Research*, 54(2):109–119, 2010.

Q. Le, J. P. Franc, and J. M. Michel. Partial cavities: Global behavior and mean pressure distribution. *Journal of Fluids Engineering*, 115(2):243–248, 1993.

I. H. Lee, S. A. Mäkiharju, H. Ganesh, and S. L. Ceccio. Scaling of gas diffusion into limited partial cavities. *Journal of Fluids Engineering*, 138(5):051301–051301, 2016.

I.-H. R. Lee. *Scaling of gas diffusion into limited partial cavity and interaction of vertical jet with cross-flow beneath horizontal surface*. PhD thesis, 2015.

J. B. Leroux, J. A. Astolfi, and J. Y. Billard. An experimental study of unsteady partial cavitation. *Journal of Fluids Engineering*, 126(1):94–101, 2004.

S. A. Mäkiharju and S. L. Ceccio. Experimental study on the formation of an air layer with gas injection from discrete sources. In *31st Symposium on Naval Hydrodynamics, Monterey, CA, USA, 11-16 September 2016*, 2016.

S. A. Mäkiharju and S. L. Ceccio. On multi-point gas injection to form an air layer for frictional drag reduction. *Ocean Engineering*, 147:206–214, 2018.

S. A. Mäkiharju, B. R. Elbing, A. Wiggins, S. Schinasi, J. M. Vanden-Broeck, M. Perlin, D. R. Dowling, and S. L. Ceccio. On the scaling of air entrainment from a ventilated partial cavity. *Journal of Fluid Mechanics*, 732:47–76, 2013a.

S. A. Mäkiharju, C. Gabillet, B. G. Paik, N. A. Chang, M. Perlin, and S. L. Ceccio. Time-resolved two-dimensional X-ray densitometry of a two-phase flow downstream of a ventilated cavity. *Experiments in Fluids*, 54(7), 2013b.

S. A. Mäkiharju, M. Perlin, and S. L. Ceccio. Time resolved X-ray densitometry for cavitating and ventilated partial cavities. *International Shipbuilding Progress*, 60(1-4): 471–494, 2013c.

S. A. Mäkiharju, H. Ganesh, and S. L. Ceccio. The dynamics of partial cavity formation, shedding and the influence of dissolved and injected non-condensable gas. *Journal of Fluid Mechanics*, 829:420–458, 2017a.

S. A. Mäkiharju, I.-H. R. Lee, G. P. Filip, K. J. Maki, and S. L. Ceccio. The topology of gas jets injected beneath a surface and subject to liquid cross-flow. *Journal of Fluid Mechanics*, 818:141–183, 2017b.

M. Matsumoto. Vortex shedding of bluff bodies: A review. *Journal of Fluids and Structures*, 13(7):791–811, 1999.

K. I. Matveev. On the limiting parameters of artificial cavitation. *Ocean Engineering*, 30 (9):1179–1190, 2003.

K. I. Matveev and M. J. Miller. Air cavity with variable length under a model hull. *Proceedings of the Institution of Mechanical Engineers, Part M: Journal of Engineering for the Maritime Environment*, 225(2):161–169, 2011.

K. I. Matveev, T. J. Burnett, and A. E. Ockfen. Study of air-ventilated cavity under model hull on water surface. *Ocean Engineering*, 36(12–13):930–940, 2009.

A. May. Water entry and the cavity-running behaviour of missiles. Report 75-2, NAVSEA Hydroballistics Advisory Comitee, 1975.

S. Mizokami, C. Kawakita, Y. Kodan, S. Takano, S. Higasa, and R. Shigenaga. Experimental study of air lubrication method and verification of effects on actual hull by means of sea trial. Report, Mitsubishi Heavy Industries Technical Review Vol. 47 No. 3, 2010.

A. Molini and S. Brizzolara. Hydrodynamics of interceptors: a fundamental study. In *International Conference on Maritime Research and Transportation ICMRT 2005*, 2005.

Y. Murai. Frictional drag reduction by bubble injection. *Experiments in Fluids*, 55(7): 1773, 2014.

F. Murzyn and H. Chanson. Free-surface fluctuations in hydraulic jumps: Experimental observations. *Experimental Thermal and Fluid Science*, 33(7):1055–1064, 2009.

B. R. Noack, K. Afanasiev, M. Morzynsky, G. Tadmor, and F. Thiele. A hierarchy of low-dimensional models for the transient and post-transient cylinder wake. *Journal of Fluid Mechanics*, 497:335–363, 2003.

I. Ohtsu, Y. Yasuda, and H. Gotoh. Hydraulic condition for undular-jump formations. *Journal of Hydraulic Research*, 39(2):203–209, 2001.

B. W. v. Oudheusden, F. Scarano, N. P. v. Hinsberg, and D. W. Watt. Phase-resolved characterization of vortex shedding in the near wake of a square-section cylinder at incidence. *Experiments in Fluids*, 39(1):86–98, 2005.

B. Papillon, M. Sabourin, M. Couston, and C. Deschenes. Methods for air admission in hydroturbines. In *Proc. of the XXIst IAHR Symp. on Hydraulic Mach. and Syst (Lausanne, Switzerland)*, 2002.

B. Pearce. *Ventilated Supercavitating Hydrofoils for Ride Control of High-Speed Craft (Ph.D. thesis)*. PhD thesis, 2011.

B. W. Pearce and P. A. Brandner. The effect of vapour cavitation occurence on the hydrodynamic performance of an intercepted base-ventilated hydrofoil. In *18th Australasian Fluid Mechanics Conference*, 2012a.

B. W. Pearce and P. A. Brandner. Experimental investigation of a base-ventilated supercavitating foil with interceptor. In *8th International Symposium on Cavitation, Cav 2012*, 2012b.

B. W. Pearce and P. A. Brandner. Inviscid cavity flow over a wall-mounted fence. *Ocean Engineering*, 80:13–24, 2014.

B. W. Pearce and P. A. Brandner. Numerical analysis of basic base-ventilated supercavitating hydrofoil sections. *Proceedings of the Institution of Mechanical Engineers, Part M: Journal of Engineering for the Maritime Environment*, 229(3):291–302, 2015a.

B. W. Pearce and P. A. Brandner. Numerical analysis of base-ventilated intercepted supercavitating hydrofoil sections. *Ocean Engineering*, 104:63–76, 2015b.

B. W. Pearce and P. A. Brandner. Numerical analysis of basic base-ventilated supercavitating hydrofoil sections. *Proceedings of the Institution of Mechanical Engineers, Part M: Journal of Engineering for the Maritime Environment*, 229(3):291–302, 2015c.

B. W. Pearce, P. A. Brandner, and J. R. Binns. A numerical investigation of the viscous 2-D cavitating flow over a wall-mounted fence. In *17th Australasian Fluid Mechanics Conference*, pages 660–663, 2010.

B. W. Pearce, P. A. Brandner, and S. J. Foster. Ventilated cavity flow over a backward-facing step. *Journal of Physics: Conference Series*, 656(1):012164, 2015. ISSN 1742-6596.

T. M. Pham, F. Larrarte, and D. H. Fruman. Investigation of unsteady sheet cavitation and cloud cavitation mechanisms. *Journal of Fluids Engineering*, 121(2):289–296, 1999.

S. Prothin, J. Y. Billard, and H. Djeridi. Image processing using proper orthogonal and dynamic mode decompositions for the study of cavitation developing on a NACA0015 foil. *Experiments in Fluids*, 57(10):157, 2016.

H. Reichardt. The laws of cavitation bubble at axially symmetrical bodies in a flow. Technical report, Ministry of Aircraft Production Volkenrode, MAP-VG, 1946.

R. Reinauer and W. H. Hager. Supercritical flow behind chute piers. *Journal of Hydraulic Engineering*, 120(11):1292–1308, 1994.

G. E. Reisman, Y.-C. Wang, and C. E. Brennen. Observations of shock waves in cloud cavitation. *Journal of Fluid Mechanics*, 355:255–283, 1998.

G. L. Richard and S. L. Gavrilyuk. The classical hydraulic jump in a model of shear shallow-water flows. *Journal of Fluid Mechanics*, 725:492–521, 2013.

P. S. Russell, D. R. Giosio, J. A. Venning, B. W. Pearce, and P. A. Brandner. Microbubble generation from condensation and turbulent breakup of sheet cavitation. In *31st Symposium on Naval Hydrodynamics, 11-16 September 2016, Monterey, California, USA*, pages 1–13, 2016.

F. R. Schiebe and J. M. Wetzel. Ventilated cavities on submerged three-dimensional hydrofoils. Report No. 36, Series B, St. Anthony Falls Hydraulic Laboratory, 1961.

V. Semenenko. Artificial supercavitation, physics and calculation. In *Lecture Notes from the RTO AVT/VKI Special Course on Supercavitating Flows, von Karman Institute for Fluid Dynamics*, 2002.

R. L. Simpson. Turbulent boundary-layer separation. *Annual Review of Fluid Mechanics*, 21(1):205–232, 1989.

L. Sirovich. Turbulence and the dynamics of coherent structures. *Quarterly of Applied Mathematics*, 45:561–590, 1987.

B. L. Storms and C. S. Jang. Lift enhancement of an airfoil using a Gurney flap and vortex generators. *Journal of Aircraft*, 31(3):542–547, 1994.

Surveyor. Airship of the sea. *Surveyor, A Quarterly Magazine from AMS*, pages 10–15, 2011.

W. M. Swanson and J. P. O'Neill. The stability of an air-maintained cavity behind a stationary object in flowing water. Report M-24.3, Hydrodynamics Laboratory, California Institute of Technology, 1951.

W. A. Timmer and R. P. J. O. M. Van Rooij. Summary of the Delft University wind turbine dedicated airfoils. *Journal of Solar Energy Engineering, Transactions of the ASME*, 125(4):488–496, 2003.

J. Verron and J.-M. Michel. Base-vented hydrofoils of finite span under a free-surface: An experimental investigation. *Journal of Ship Research*, 28(2):90–106, 1984.

O. Vigneau, S. Pignoux, J. L. Carreau, and F. Roger. Influence of the wall boundary layer thickness on a gas jet injected into a liquid crossflow. *Experiments in Fluids*, 30 (4):458–466, 2001.

R. L. Waid. Water tunnel investigation of two-dimensional cavities. Technical Report Hyd. Rpt. E-73.6, CIT, 1957.

P. Welch. The use of fast Fourier transform for the estimation of power spectra: A method based on time averaging over short, modified periodograms. *IEEE Transactions on Audio and Electroacoustics*, 15(2):70–73, 1967.

S. C. Yaragal, H. S. Govinda Ram, and K. K. Murthy. An experimental investigation of flow fields downstream of solid and porous fences. *Journal of Wind Engineering and Industrial Aerodynamics*, 66(2):127–140, 1997.

Y. L. Young, C. M. Harwood, F. Miguel Montero, J. C. Ward, and S. L. Ceccio. Ventilation of lifting bodies: Review of the physics and discussion of scaling effects. *Applied Mechanics Reviews*, 69(1):010801–1 – 010801–38, 2017.

P. W. Yu and S. L. Ceccio. Diffusion induced bubble populations downstream of a partial cavity. *Journal of Fluids Engineering*, 119(4):782–787, 1997.

G. A. Zarruk, P. A. Brandner, B. W. Pearce, and A. W. Phillips. Experimental study of the steady fluid–structure interaction of flexible hydrofoils. *Journal of Fluids and Structures*, 51:326–343, 2014.

Appendices

Appendix A

Computational Investigation of Ventilated Cavity Flow Over a 2-D Wall-Mounted Fence

This paper was presented at the (peer-reviewed) 19^{th} *Australasian Fluid Mechanics Conference*, Melbourne, 8-11 December 2014.

The citation for the conference paper is:

Barbaca, L., Pearce, B. W., Brandner, P. A., 2014, Computational Investigation of Ventilated Cavity Flow Over a 2-D Wall-Mounted Fence, 2014, *in Proceedings of the* 19^{th} *Australasian Fluid Mechanics Conference, Melbourne, 8-11 December 2014*

19th Australasian Fluid Mechanics Conference
Melbourne, Australia
8-11 December 2014

Computational Investigation of Ventilated Cavity Flow Over a 2-D Fence

L. Barbaca, B.W. Pearce and P.A. Brandner

Australian Maritime College
University of Tasmania, Launceston, Tasmania 7250, Australia

Abstract

Ventilated supercavitating flow over a 2-D wall mounted fence is numerically investigated using a viscous approach. Flow was simulated using an implicit unsteady compressible solver with a RANS *k*-ω SST turbulence model and VOF approach for cavity interface tracking. All simulations were carried out for a fixed fence height based Reynolds number of 50,000. The effect of ventilation rate on the flow characteristics is investigated. The effects of the wall boundary layer were examined by comparing results with inviscid potential flow from a boundary element method. The relationship between ventilation rate and the lift and drag resulting from the respective wall and fence pressure distributions is determined. It was found that, lift increases and drag decreases with increasing ventilation rate thus increasing hydrodynamic efficiency. These numerical results will be compared with future experimental investigations to be performed in a cavitation tunnel.

Introduction

A ventilated supercavity is a gaseous cavity formed when incondensable gas is introduced into the low pressure region of a liquid flow. There are several marine applications where use of this phenomenon can lead to the significant performance improvements. The most extensively investigated application of ventilated supercavitation is its use on the axisymmetric underwater projectiles as a method to achieve drag reduction. Drag is reduced due to the formation of a gaseous bubble surrounding the body, limiting its contact with liquid, thus largely reducing skin friction. A summary of knowledge is presented by Semenenko [13]. A similar method for drag reduction is used for an application referred to as air-lubrication of the wetted part of the ship hull. Drag reduction is achieved by injecting air through specially designed devices on the ship hull bottom. This creates a partial air-ventilated cavity under the ship hull, significantly reducing friction resistance ([3] and [8]).

Ventilation can be used on base-ventilated hydrofoils to create a stable supercavity under the conditions where a natural supercavity, i.e. from vapour alone, will not form. This enables drag reduction for foils designed to operate in the natural supercavitating regime, well before conditions required for natural supercavitation to occur are reached. Also, a novel concept of an intercepted base-ventilated hydrofoil for the ride control of a high-speed vessel is proposed by Elms [5]. In the present study some basic aspects of air-ventilated cavity flow over a wall mounted fence are investigated. Separated flow over a fence protruding from the wall has been extensively investigated within the field of aerodynamics. A fence fitted to the trailing edge of an aerofoil, also known as a Gurney flap, is used as a lift enhancement device [14] in aerospace and automotive applications. Similarly, fences attached to the bottom and sides of the ship transom, also called interceptors, are used for ride and steering control, respectively [6]. Some numerical investigation on the interceptors are reported by Brizzolara [2] and Molini and Brizzolara [9], and this topic is still of interest with a recent experimental study published by Day and Cooper [4].

The present study is a part of ongoing work on base-ventilated hydrofoils involving numerical [10, 12] and experimental [11] investigations. Within this study a further step in the numerical modelling is presented. Ventilated cavity flow over a wall-mounted fence is investigated with a viscous approach. The effect of ventilation rate on the flow physics and hydrodynamic performance is investigated. Effects of the viscosity are evaluated through a comparison with inviscid potential flow data, obtained using a numerical boundary element method [12].

A sketch of the ventilated cavity flow over a wall mounted fence investigated is shown in figure 1. The fence, of height h, is immersed within the wall boundary layer of thickness δ, where U is 99% of the freestream velocity, U_∞. To ventilate the flow air is supplied to the wake region through the downstream face of the fence. Cavity detachment is from the fence tip and a typical re-entrant jet closure regime is illustrated. The resulting pressure distribution is indicated on the wall upstream of the fence.

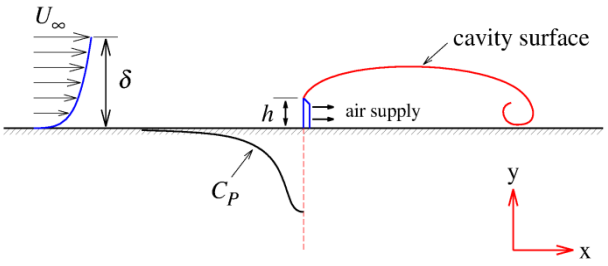

Figure 1: Sketch of a wall mounted fence immersed within the boundary layer with a ventilated cavity detaching from the sharp outer edge. Gas is supplied from the downstream face of the fence. The pressure distribution on the upstream wall is shown. The origin of the coordinate system is at the fence/wall junction.

The main dimensionless parameter governing a ventilated cavity flow is the cavitation number, $\sigma_c = (p_\infty - p_c)/0.5\rho U_\infty^2$, where p_c is the pressure inside the cavity, p_∞ is the reference freestream pressure, ρ is the liquid density and U_∞ is the reference freestream velocity. In the case of ventilated cavities, for constant free stream conditions, σ_c is determined by the air flow rate which is characterized by a volumetric flow coefficient $C_{Qv}=Q_m/\rho_{air}U_\infty S$, where Q_m is the mass flow of the supplied air, ρ_{air} is the air density and S is the surface area of the fence. A Reynolds number based on fence height, $Re_h=U_\infty h/\nu$, where ν is the kinematic viscosity, is also applicable.

Modelling

The commercial Computational Fluid Dynamics software, CD Adapco STAR-CCM+, was used for the present study. For later comparison with experimental results a rectangular computational domain was created to represent the University of Tasmania cavitation tunnel test section. The domain height was set at 60h and a fence, modelled as 10 mm high and 0.1 mm thick, was attached to the test section floor. The domain inlet and outlet were positioned sufficiently away from the fence to avoid their influence on the flow, located at 500h and 1000h respectively. For the spatial discretization, a structured hexahedral mesh with prism layer cells in the boundary layer region was used. To resolve the flow a first order implicit unsteady finite volume method was employed. Water was defined with constant density and air as an ideal compressible gas. The interface between the phases was tracked using a VOF method based on the volume fraction equation. Surface tension and gravity effects were included in the model. Gravitational acceleration was directed upwards to enable comparison with the future experimental data where the fence will be located on the test section ceiling. For the consideration of viscous effects a RANS approach with the SST (Menter) k-ω turbulence model was used.

Water enters the domain through the constant velocity inlet, with the velocity set to 10 m/s (Re_h=1×10^5) for all cases. The flow rate of injected air was varied between 0.01 kg/s and 0.09 kg/s (giving $0.084 < C_{Qv} < 0.751$). The domain outlet was defined as a constant pressure outlet, set to 50 kPa for all cases. An unperturbed boundary layer thickness at the fence position ($x = 0$) of $\delta/h = 2$ was achieved by setting the length of the free slip boundary condition on the wall upstream of the fence. The reference pressure used was defined as the minimum pressure on the wall upstream of the fence. The reference freestream velocity was chosen as the value at the vertical centreline 100h upstream of the fence.

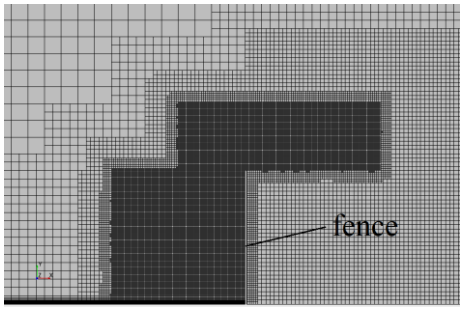

Figure 2: Local refinement of the mesh in front of the fence and in the cavity region. The prism layer on the upstream wall is also shown

A convergence analysis was done for both temporal and spatial discretization. Time steps ranging between 0.5 and 2 ms were analysed and a time step of 1 ms gave results within 1% of the independent solution. Spatial convergence was analysed with the number of cells varying between about 0.2 and 4×10^6. It was found that a mesh consisting of just over 1.8×10^6 cells gave results within 1% of the grid independent solution. Prism layer parameters are chosen to achieve y^+<1 for the wall with the fence attached and $y^+ \approx 30$ for the wall without the fence. Mesh refinement is used in the region where the cavity is expected with additional refinement upstream of the fence to resolve the separation bubble. Computational time needed to obtain a solution, using 12 cores on a multinode cluster, varied between about 20 to 30 hours. This was mainly dependent on the time needed for a cavity to fully develop, i.e. the length of the resulting cavity which was a function of the ventilation rate.

Results and Discussion

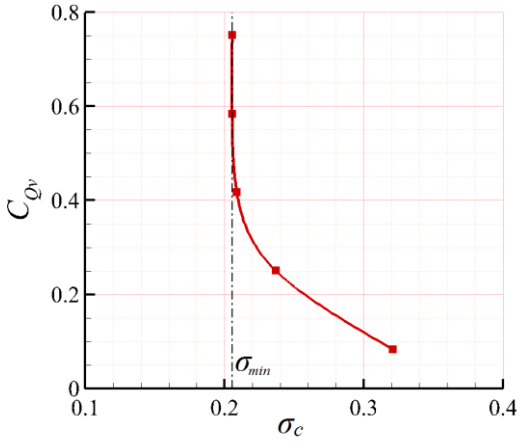

Figure 3: Relation between cavitation number, σ_c, and volumetric flowrate coefficient, C_{Qv}, for δ/h=2.

The dependence of σ_c on C_{Qv} is shown in figure 3. On the left hand side of the curve a vertical asymptote is present representing a minimum σ_c value achievable under the prescribed geometric and flow conditions. At $\sigma_c = \sigma_{min,}$ the flow is said to be 'blocked' [1], analogous to the choked condition of compressible flow though valves and orifices, and is a function of the degree of confinement of the flow domain. The extent of the confinement/blockage is expressed in terms of the ratio of the domain height, H, and the fence height, which for the present study was a value of H/h=60. Significantly lower values of σ_{min} are achieved for the cases with a boundary layer present compared to the potential flow case with the same blockage conditions, with the values of σ_{min} being 0.2054 and 0.2957, respectively.

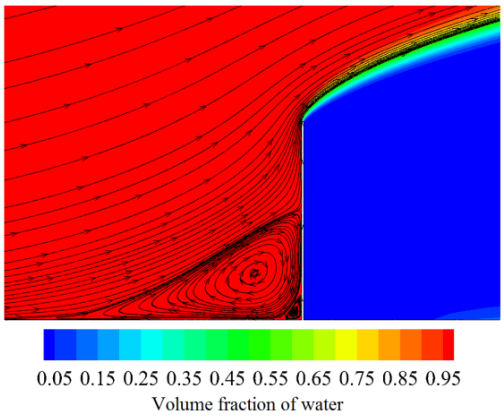

Figure 4: Streamlines depicting flow topology upstream of the fence (σ_c = 0.2368, δ/h = 2) showing the upstream separation zone. The cavity surface, including the detachment from the fence tip, is also shown as contours of volume fraction.

The flow topology upstream of the fence is shown in figure 4. A separation bubble is present as would be expected for a viscous flow over a forward-facing step. It can be seen that under the main vortex, at the fence/wall junction, a secondary counter-rotating vortex is present. It was found that the size of the separation zone doesn't vary significantly with respect to σ_c. Stagnation points were located at $x = -1.73h$ on the wall and $y = 0.57h$ on the fence for the main vortex, and $x = -0.1h$ on the wall and $y = 0.16h$ on the fence for the secondary vortex. The cavity detaches from the fence and the gas-liquid interface is

represented as a smeared zone in contrast with the defined free surface present in the potential flow formulation.

Closure of a ventilated cavity on the downstream wall exhibits re-entrant jet behaviour. Depending on the flow conditions gas discharge from the cavity closure may be continuous or as large bubbly structures detaching from the cavity periodically. The latter regime is described as a pulsating cavity [7]. A typical example of the closure region of a pulsating cavity is shown in figure 5. The streamlines show that a bubble is close to detachment with the formation of a new bubble upstream. A re-entrant jet flow can be observed diverting liquid upstream along the wall into the cavity. For short cavities the re-entrant jet transports liquid almost up to the fence, with most of the cavity consisting of a liquid/gas mixture. For the longer cavities, the re-entrant jet only extends a limited extent leaving the upstream cavity region completely filled with air only. When σ_c reaches σ_m, the cavity length becomes 'infinite' extending to the domain outlet. With a further increase in C_{Qv} the cavity geometry remains unchanged, but the computational time needed for the cavity to reach the domain outlet is shortened.

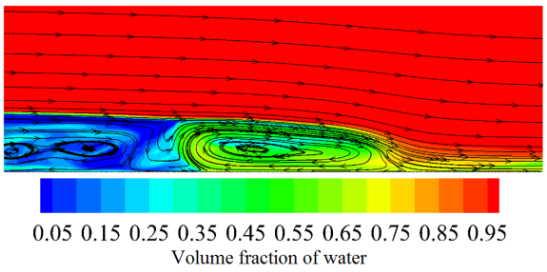

Figure 5: Closure region of the cavity represented with volume fraction contours (σ_c = 0.2368, δ/h = 2). Streamlines show a bubble about to detach and a new bubble starting to form in the cavity upstream.

As the closure region consists of a mixed phase, volume fraction contours could not be used to determine cavity length. Instead, the location of the stagnation point downstream of the cavity, where the flow divides into the re-entrant jet and wake region, is used to determine cavity length. The stagnation point manifests as a peak in the wall pressure distribution downstream of the fence. For the pulsating regime, several peaks were present due to the bubbles already detached from the cavity and the one associated with the main cavity closure was used to determine cavity length. Time averaging was necessary to establish a mean value of the length for the pulsating cavities. The cavity oscillations were typically in the order of 20% of the mean length. The dependence of cavity length on cavitation number is shown in figure 6. The viscous (δ/h=2) and potential flow data exhibit similar behaviour, with cavities growing infinitely when σ_m is reached. In an unbounded flow the cavity length behaves in accordance with a power law with respect to σ_c ([7], [12]). The effect of the boundary layer can be observed as a left hand translation of the potential flow curve, i.e. same cavity length is achieved for a lower cavitation number.

The influence of the ventilation rate on the wall pressure distribution upstream of the fence, and ultimately on the lift, is of interest. Figure 7 shows a double log plot of the pressure distribution (with $C_p = (p - p_\infty)/0.5\rho U_\infty^2$), along the upstream wall. The wall pressure distributions for all cases display an exponential like reduction with upstream distance. A C_p of 0.001 was chosen as a level to determine a length of influence of the fence. It was found that with an increase in C_{Qv}, the length of influence increased, but the rate of increase reduces to zero as $\sigma_c \rightarrow \sigma_m$. The length of influence increases by about 7% over the C_{Qv} range investigated up to maximum of about 80h (see lower inset in figure 7).

Also of interest is the maximum value of the pressure coefficient, $C_{p\,max}$, for x/h=0. $C_{p\,max}$ behaves similarly to the length of influence with increasing C_{Qv} reaching an asymptotic value with $\sigma_c \rightarrow \sigma_m$. Overall increase in $C_{p\,max}$ is about 4%, with the maximum value just over 0.4 (see upper inset in figure 7). The boundary layer effect lowers $C_{p\,max}$ by approximately 60% compared with the potential flow result (where $C_{p\,max}$=1). This is due to the fence immersion within the boundary layer resulting in a locally lower velocity at the fence height compared with the uniform velocity profile in the potential flow solution.

For the range of ventilation rates investigated the hydrodynamic parameters (lift, drag and lift to drag ratio) have a power law dependence on σ_c as shown in figure 8. Lift and drag are non-dimensionalised using the fence height giving, $C_L = L/0.5\rho U_\infty^2 h$ and $C_D = D/0.5\rho U_\infty^2 h$. Lift was calculated as the integral of the pressure distribution on the wall upstream of the fence over a

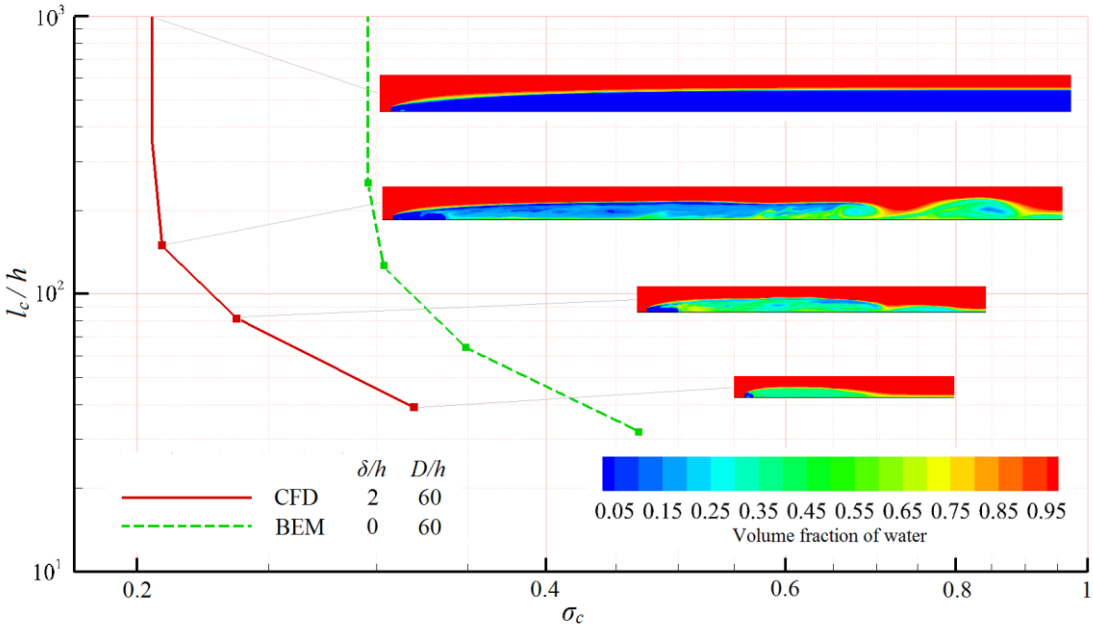

Figure 6: Cavity length (l_c/h) as a function of cavitation number (σ_c) for the viscous (δ/h=2) and potential flow cases with the same blockage ratio, H/h=60. Cavity topology for all viscous cases is shown using contours of volume fraction.

length of 100h. As discussed above this distance is sufficient to determine the lift. The lift added between 60h and 100h is limited to below 0.5% of the total. Increase in the ventilation rate leads to increase in the lift, which can be attributed to the higher value of the $C_{p\,max}$ and greater length of influence of the upstream wall pressure. Lift increased 18% over the range of ventilation rates investigated. Drag was calculated from the integral of the pressure distribution over the front and back faces of the fence. Drag decreases with decrease in σ_c, with the difference between highest and lowest values being about 15%. This can be attributed to the effect of cavity pressure on the back face of the fence as the ventilation rate increases. Both of these aspects contribute positively to an increase in the lift to drag ratio with increasing ventilation rate, reaching the maximum value for σ_c= σ_m. The lift to drag ratio increases by about 30% over the range of ventilation rates investigated.

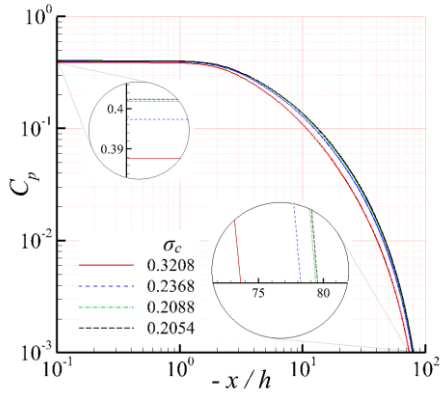

Figure 7: Wall pressure distribution upstream of the fence (with δ/h=2).

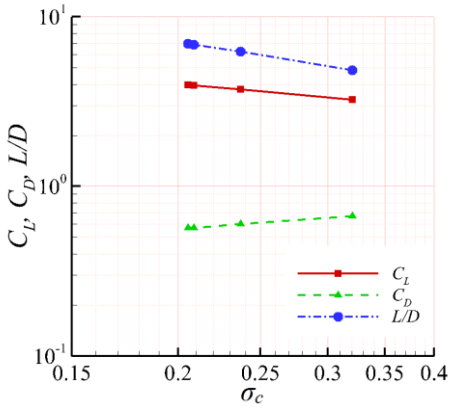

Figure 8: Dependence of hydrodynamic parameters C_L, C_D and L/D on σ_c

Conclusions

Ventilated cavity flow over a 2-D wall mounted fence was investigated numerically using a viscous approach with some comparison made with potential flow results from a boundary element method analysis. Dependence of the cavitation number on volumetric flow rate coefficient is established. Cavity flow topology was determined, with a separation zone in front of the fence and a re-entrant jet closure captured. Cavity length exhibits similar general behaviour with the respect to cavitation number for both the viscous and potential analyses, with the same cavity length occurring at a lower cavitation number with a boundary layer present. Upstream wall pressure data shows that maximum pressure (i.e. stagnation at the fence/wall junction) and the length of wall influenced by the presence of the fence varies with respect to C_{Qv}. A lift (spanwise) force results from the imposed pressure distribution due to the addition of a fence which increases with ventilation rate. The drag (streamwise) force on the fence also reduces as ventilation is increased resulting in an increase in hydrodynamic efficiency

Further numerical investigation into the effects of the overlying boundary layer and flow confinement on cavity geometry and hydrodynamic performance is required. A companion experimental investigation is also planned for comparison with the numerical study.

References

[1] Brennen, C. E. (1995). Cavitation and Bubble Dynamics, Oxford University Press, New York.

[2] Brizzolara, S. (2003). Hydrodynamic analysis of interceptors with CFD methods Seventh International Conference on Fast Sea Transportation - FAST 2003. Naples, Italy**:** 49-56.

[3] Ceccio, S. L. (2010). Friction drag reduction of external flows with bubble and gas injection, *Annu. Rev. Fluid Mech.* **42:** 183-203.

[4] Day, A. H. and C. Cooper (2011). "An experimental study of interceptors for drag reduction on high-performance sailing yachts." Ocean Engineering **38**(8–9): 983-994.

[5] Elms, A. R. (1999). Improved Hydrofoil Device. International Patent Number WO 99/57007. W. I. P. Organization.

[6] Faltinsen, O. (1996). Hydrodynamics of high speed vehicles. Cambridge, England, Cambridge University Press.

[7] Franc, J. P. and J. M. Michel (2004). Fundamentals of Cavitation. Dordrecht, Kluwer Academic Publishers.

[8] Matveev, K. I., T. J. Burnett and A. E. Ockfen (2009). "Study of air-ventilated cavity under model hull on water surface." Ocean Engineering **36**(12–13): 930-940.

[9] Molini, A. and S. Brizzolara (2005). Hydrodynamics of interceptors: a fundamental study. International Conference on Maritime Research and Transportation ICMRT 2005. Ischia, Italy.

[10] Pearce, B. W., P. A. Brandner and J. R. Binns (2010). A numerical investigation of the viscous 2-D cavitating flow over a wall-mounted fence. 17th Australasian Fluid Mechanics Conference, Auckland, New Zealand.

[11] Pearce, B. W. and P. A. Brandner (2012). Experimental investigation of a base-ventilated supercavitating foil with interceptor. 8th International Symposium on Cavitation, Cav 2012, Singapore.

[12] Pearce, B. and P. Brandner (2014). "Inviscid cavity flow over a wall-mounted fence." Ocean Engineering **80**: 13-24.

[13] Semenenko, V. N. (2001). Artificial Supercavitation, Physics and Calculation. Lecture Notes from the RTO AVT/I Special Course on Supercavitating Flows, von Karman Institute for Fluid Dynamics, Rhode Saint Genese, Belgium.

[14] Storms, B. L. and C. S. Jang (1994). "Lift enhancement of an airfoil using a Gurney flap and vortex generators." Journal of Aircraft **31**(3): 542-547.

Appendix B

Experimental Investigation of Ventilated Cavity Flow Over a 3-D Wall-Mounted Fence

This paper was presented at the (peer-reviewed) 16^{th} *ISROMAC Conference*, Honolulu, Hawaii, US, 10-15 April 2016.

The citation for the conference paper is:

Barbaca, L., Pearce, B. W., Brandner, P. A., 2016, Experimental Investigation of Ventilated Cavity Flow Over a 3-D Wall-Mounted Fence, *in Proceedings of 16th International Symposium on Transport Phenomena and Dynamics of Rotating Machinery ISROMAC-16*, Honolulu, Hawaii, 10-15 April, 2016

Experimental Investigation of Ventilated Cavity Flow Over a 3D Wall Mounted Fence

Luka Barbaca[1]*, Bryce W. Pearce[1], Paul A. Brandner[1]

ISROMAC 2016

International Symposium on Transport Phenomena and Dynamics of Rotating Machinery

Hawaii, Honolulu

April 10-15, 2016

Abstract

Ventilated cavity flow over a 3-D wall mounted fence is experimentally investigated in a cavitation tunnel. The influence of air ventilation rate, fence height based Froude number and vapour pressure based cavitation number on the resulting cavity and associated drag coefficient is determined. Three different flow regimes are identified throughout the range of cavitation numbers for a constant set of free-stream conditions. The geometry of a fully formed ventilated cavity is described. The re-entrant jet cavity closure is observed as the primary mechanism for entrainment of ventilated air into the flow.

Keywords

Ventilated cavity — Wall mounted fence — Cavitation tunnel

[1]*Australian Maritime Collage, University of Tasmania, Launceston, Tasmania, Australia*

***Corresponding author**: Luka.Barbaca@utas.edu.au

INTRODUCTION

The need for faster and more efficient sea transport is more prominent than ever in today's world. As vessel speed increases the occurrence of cavitation becomes unavoidable. Cavitation in this context being the formation and interaction of vaporous volumes (or cavities) with the flowing liquid. The phase change occurs in regions where the liquid is subjected to pressures at or below vapor pressure. It is mostly an undesirable phenomenon as it can lead to performance loss, vibration, noise and surface erosion of the cavitating body. Depending on the application, various techniques have been investigated to minimize these detrimental effects. One of the techniques that has been extensively studied is the use of artificial ventilation.

Ventilated supercavities (also termed 'artificial') are created when incondensable gas (typically air) is injected into the low pressure region of the liquid flow. The injection of gas induces the creation of a ventilated supercavity with the closure located in the wake of the cavitating body. Two main benefits from ventilated cavities are drag reduction and increased flow stability. The use of ventilated cavities has been investigated extensively from the middle of last century for mainly military, but also for commercial application [1, 2, 3].

Axisymmetric ventilated supercavities have been investigated for drag reduction purposes on underwater projectiles (i.e. torpedoes). By enveloping the body in an air bubble, and thereby reducing its wetted area, the skin friction is significantly reduced. A comprehensive review of axisymmetric ventilated cavity flow is presented in [4]. 'Air-lubrication' is a similar method used for hull drag reduction where an air layer is created to reduce the contact area between the hull and water [5].

The injection of air on the downstream face of a wedge shaped hydrofoil (i.e. a 'base-ventilated hydrofoil') was first proposed as a method to reduce drag in the 1950's [6]. Due to the increased pressure on the blunt base, the resulting streamwise pressure integral over the foil surface is reduced. More recently, Elms [7] proposed an intercepted base-ventilated hydrofoil, equipped with a rotating tail section, for ride control of high-speed craft. Also, the flow around a transom mounted interceptor [8], can be considered as a ventilated cavity flow with an 'infinite' cavity, subjected to atmospheric pressure, detaching from the interceptor tip.

Ventilated cavity flows have been of interest at the Australian Maritime College (AMC) Cavitation Research Laboratory (CRL) in recent years. The cavitating flow over a wall mounted fence has been investigated numerically, both using a potential flow Boundary Element Method (BEM) [9] and Computational Fluid Dynamics (CFD) [10]. A comprehensive numerical study (using BEM) of intercepted base-ventilated hydrofoils has been reported by Pearce and Brandner [11] and a limited set of experimental data has been presented by the same authors [12].

In this report, ventilated cavity flow over a 3D wall mounted fence has been examined experimentally in the CRL cavitation tunnel. This flow is of interest for the generation of forces

from geometric discontinuities/interceptor type devices as well as being a cavitating flow of basic interest. The parameters that control cavity geometry are investigated and basic cavity physics are described.

1. EXPERIMENTAL OVERVIEW

A schematic representation of ventilated cavity flow over a wall mounted fence is shown in figure 1. A fence, of a height h, is immersed in the upstream wall boundary layer of thickness δ. δ is defined as the distance from the wall where U is 99% of the freestream velocity U_∞. Air is supplied to the wake region of the flow through a manifold on the downstream face of the fence. A ventilated cavity, with re-entrant jet closure, is shown detaching from the sharp fence tip.

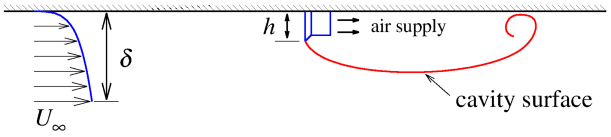

Figure 1. Sketch of a wall mounted fence immersed in the upstream wall boundary layer with a ventilated cavity detaching from the sharp tip. Air is supplied through the downstream face of the fence.

The fundamental dimensionless parameter characterizing cavitating flows is the cavitation number, which in general form can be expressed as $\sigma_c = (p_\infty - p_c)/0.5\rho U_\infty^2$, where p_c is the pressure inside the cavity, p_∞ is the reference free-stream pressure, ρ is the liquid density and U_∞ is the reference freestream velocity. The experimental setup was developed to examine the dependence of cavitation number on the flux of injected air, fence height based Froude number ($Fr = U_\infty/\sqrt{gh}$, where g is the gravitational acceleration) and vapour pressure, p_v, based free-stream cavitation number ($\sigma_v = (p_\infty - p_v)/0.5\rho U_\infty^2$). The rate at which air is injected in the flow is characterized by a volumetric flowrate coefficient $C_{Qv} = Q_m/\rho_{air} U_\infty S$, where Q_m is the mass flow of the injected air, ρ_{air} is the air density and S is the reference area (for the present case it is the surface of the fence face). Alongside the cavitation number, the drag D is examined with respect to the aforementioned parameters. The drag is expressed in its non-dimensionalised form, as the drag coefficient $C_D = D/0.5U_\infty^2 \rho S$. The cavity length l_c dependence on C_{Qv} was also investigated.

The experiments were performed in the CRL water tunnel. The tunnel design [13, 14] incorporates a large tank downstream of the test section for bubble coalescence and separation. This feature, combined with auxiliary systems for the rapid degassing and continuous evacuation of the large quantities of incondensable gas, enables efficient conduct of tests involving ventilation (i.e. injection and continuous removal of large quantities of air). The tunnel test section measures 0.6 x 0.6 m square, by 2.6 m long. The operating velocity and pressure ranges are 2 to 12 m/s and 4 to 400 kPa absolute respectively. The tunnel volume is 365 m^3 and is filled with demineralised water. Optical access is provided through acrylic windows on each side of the test section.

The experimental setup has been developed to study ventilated cavity flow over 2D and 3D wall mounted fences. For the present study only results obtained with the 3D fence model are presented. The fence model (figure 2), equipped with an internal manifold for air distribution, is machined from a single stainless steel bar. The fence is 10 mm high, with a V-notch machined at the fence front tip to ensure a stable cavity detachment. The model is 0.156 m wide and spans approximately a quarter of the test section. The shape of the rear part of the fence does not have an influence on the flow, as it is located completely inside the cavity. The air distribution system consists of an internal channel and 10 equi-spaced streamwise outlets distributing air into the wake of the fence. The model is mounted on a six-component force balance, attached to the test section ceiling. A tube is routed through the balance for the air supply.

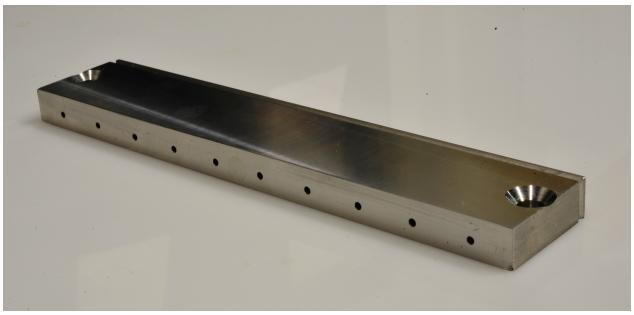

Figure 2. A rear view of the fence model. Ten equi-spaced passages for the air supply can be seen on the downstream face of the fence. A V-notch is machined at the fence front tip to ensure a stable cavity detachment.

A scani-valve system used for pressure measurement is represented schematically in figure 3. This setup allows use of a single pressure transducer for all measurements, eliminating the need to apply corrections arising from transducer zero and span errors. The freestream dynamic pressure and pressure inside the cavity are measured relative to the freestream static pressure, from which σ_c can be derived. The cavity pressure is measured with a wall taping located just downstream of the model, with a tube routed through the balance.

The test section absolute pressure is measured, depending on the value, from high or low range Siemens Sitransp absolute pressure transducers models 7MF4333-1FA02-2AB1 and 7MF4333-1GA02-2AB1 with estimated precision of 0.13 and 0.48 kPa respectively. The test section velocity is measured from the calibrated contraction differential pressure. Depending on the value, a high and low range Siemens Sitransp differential pressure transducers models 7MF4433-1DA02-2AB1-Z and 7MF4433-1FA02-2AB1-Z are used, with estimated precisions of 0.007 and 0.018 m/s respectively. The air mass

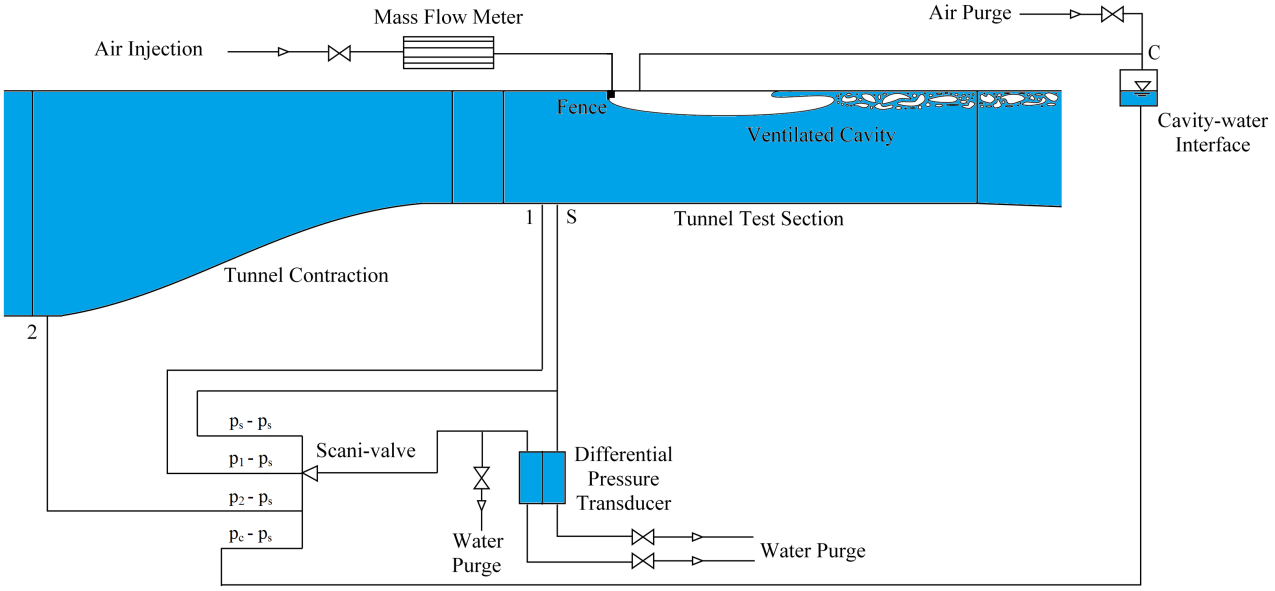

Figure 3. Schematic of the scani-valve system used for obtaining the cavitation number, σ_c. Air injection is via a mass flow meter. Gas pressure measured from the taping inside the ventilated cavity is converted to a liquid pressure (necessary for the differential pressure transducer operation) using the cavity-water interface.

flow rate is controlled and measured using an Alicat Scientific model MCR-500-SLPM-D (flow rate range 0-500 SLPM) mass flow meter with an estimated precision of 3 SLPM. The ventilated cavitation number is measured using a Validyne model DP15TL differential pressure transducer (estimated precision of 0.2 kPa) via Swagelok model SS-43Z6FS1 7-way valve actuated using a stepper motor controlled from the data acquisition system. The force balance used to measure the model drag has a maximum rated load of 2 kN and an estimated precision of 0.15 N. The dissolved gas content of the water is measured using an Endress+Hauser OxyMax WCOS 41 membrane sensor.

The three independently prescribed variables that control ventilated cavity flow over a fence are; air ventilation rate, Froude number and free-stream cavitation number. Due to the air flow rate being measured via a mass flow meter , the volumetric flowrate coefficient could not be prescribed (it depends on the gas pressure inside the cavity and the free-stream conditions), and it had to be calculated using the cavity pressure derived from the measured ventilated cavitation number. To determine the range of Q_m values (for a particular free-stream condition), cavity length was increased beyond the test section outlet to establish the Q_m upper bound. Approximately ten Q_m values were examined for each set of the free-stream conditions.

Tests were conducted for three Fr values (controlled with the test section velocity) and three values of σ_v (controlled with the test section static pressure). The examined values were 20.1, 25.3 and 30.3 for the Fr and 0.55, 0.75 and 0.95 for the σ_v. The fence model was fully immersed in the oncoming upstream wall boundary layer, with the boundary layer thickness to fence height ratio of approximately 1.9. The tests were conducted with a dissolved O_2 content between 2 and 6 ppm. Cavity length has been obtained using still forward-lit photography as the average from at least ten images.

2. RESULTS AND DISCUSSION

2.1 Cavity geometry

A typical geometry of a fully formed ventilated cavity is shown in figure 4. The cavity has a stable detachment from the fence upstream face sharp tip and sides. The cavity can be divided into two regions along its length. The region closer to the fence is almost entirely filled with air and the zone with a smooth cavity/water interface. In the rear part of the cavity injected air is entrained into the main flow. The closure of the cavity exhibits re-entrant jet behaviour [15]. The re-entrant jet can be described as a wave penetrating into the cavity and transporting liquid upstream along the wall. The liquid falls under gravity, engulfing air into bubbles. These are then entrained into the main flow predominantly through the shedding process at the cavity closure and, to a lesser extent, via the re-entrant jet/water interface. Depending on the cavity length and free-stream conditions, the re-entrant jet can extend all the way to the fence, or be contained to only a portion of the cavity length. In figure 4, re-entrant jet region can be seen as a chaotic region with a broken cavity/water interface. The wake of the ventilated cavity consists of a continuous stream of air bubbles entrained in the main flow. The unattached bubbles on the sides of the cavity illustrate

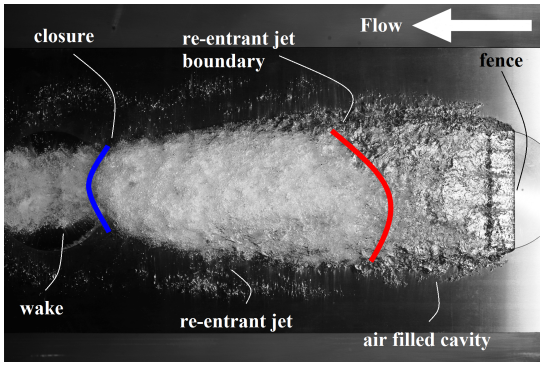

Figure 4. A typical geometry of a fully formed ventilated cavity. The upstream region of cavity is filled with the air and has a smooth cavity/water interface. The closure region exhibits re-entrant jet behaviour. The re-entrant jet causes cavity break-up and resulting bubbles are entrained in the main flow predominantly through shedding process at the closure and, to a lesser extent, via the re-entrant affected cavity interface. The wake consists of a constant stream of entrained bubbles.

the effect of three-dimensional flow with vortices entraining a small portion of the ventilated air into the flow. These vortices also cause cavity necking (reduction in width) along the cavity length.

For ventilated cavity flows, at particular free-stream conditions, σ_c is controlled solely by the air ventilation rate, C_{Qv}. The dependence of σ_c on C_{Qv} can be derived from figure 5 (with $Fr = 25.3, \sigma_v = 0.95$). Along the curve, three regimes can be identified. In regime (a), a ventilated cavity is not yet fully formed. The short cavity present has a typical shear layer cavitation appearance. In regime (b), cavitation number has a linear dependence on the ventilation rate. A ventilated cavity is fully formed and a re-entrant jet closure is present. At the beginning of this region the re-entrant jet impinges on the downstream face of the fence. With reduction in cavitation number and increase in cavity length, the re-entrant jet no longer impinges on the fence.Despite these differences there remains a linear relationship between σ_c and C_{Qv}. In regime (c), the flow is said to be 'blocked' [16]. On the left hand side of the curve a vertical asymptote is present, representing the minimum cavitation number value obtainable, σ_{min}. When this minimum cavitation number is reached the cavity grows 'infinitely' with even the slightest increase in C_{Qv}. The blocked cavitation number is a function of the degree of confinement of the flow domain, which in this case is the ratio between the maximum cavity and tunnel test section cross-sectional areas normal to the flow direction.

Figure 6 shows the relation between l_c/h and σ_c (for $Fr = 20.1, \sigma_v = 0.95$). It can be seen that the data follows a power law ($l_c/h = 0.7369\sigma_c^{-2.142}$). This power law behaviour is characteristic of an unbounded flow [17]. This indicates that any blockage effect present does not significantly affect the results obtained.

The influence of a change in free-stream conditions, i.e. Fr and σ_v, on the dependence of σ_c on C_{Qv} has also been investigated. In figure 7 curves of σ_c versus C_{Qv} are shown for three Fr values (for $\sigma_v = 0.95$). It can be seen that with the increase in Fr a higher C_{Qv} is needed to obtain the same

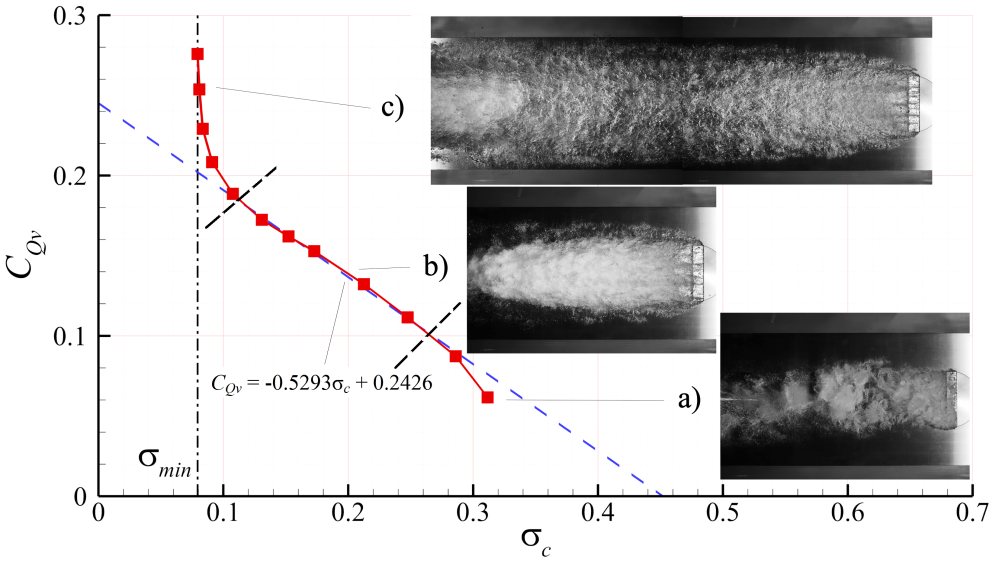

Figure 5. Dependence of cavitation number on the volumetric flowrate coefficient (for $Fr = 25.3, \sigma_v = 0.95$). Three regimes can be differentiated along the curve: a) shear layer cavitation, b) fully formed ventilated cavity with a linear dependence and c) cavity in 'blocked' conditions. The vertical asymptote represents a minimum cavitation number obtainable under the examined conditions.

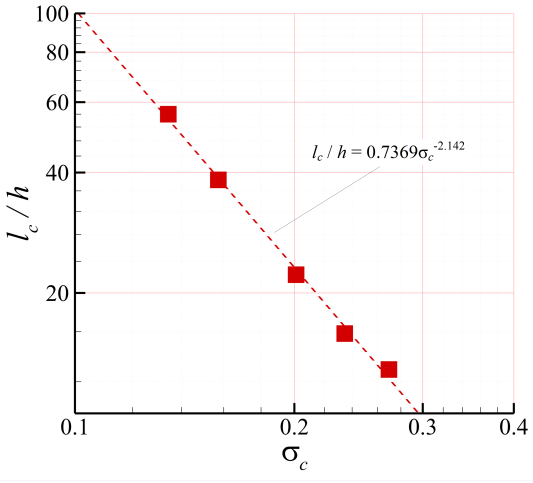

Figure 6. Non-dimensional cavity length as a function of cavitation number (for $Fr = 20.1, \sigma_v = 0.95$). The curve exhibits a power law behaviour ($l_c/h = 0.7369\sigma_c^{-2.142}$), which is characteristic of an unbounded flow.

σ_c, i.e. more air needs to be injected into the cavity. With the increase in Fr the slope of the linear region is increased. σ_{min} also increases with an increase in Fr, which suggests a higher degree of confinement with increased free-stream velocity. This may be attributable to an increase in the cavity thickness due to the higher vertical velocity component at the detachment point at the fence tip.

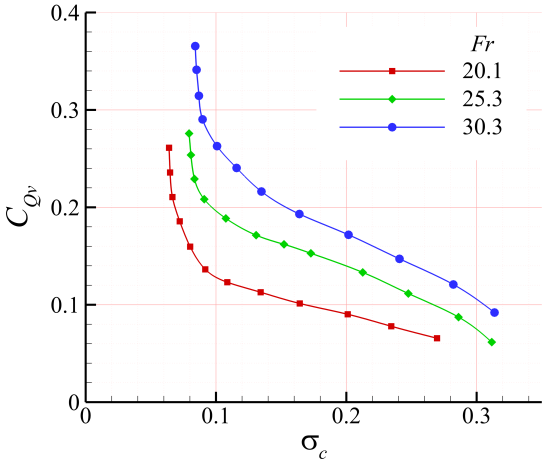

Figure 7. Relation between σ_c and C_{Qv} for the cases with different Froude number and constant free-stream cavitation number ($\sigma_v = 0.95$)

Figure 8 shows the alternate case of varying σ_v for a fixed Fr ($Fr = 25.3$). With the increase in σ_v more air has to be injected to achieve the same σ_c value. The linear part of the curves has relatively constant slope for all σ_v values. σ_{min} is approximately constant, which is expected as the free stream velocity is held constant.

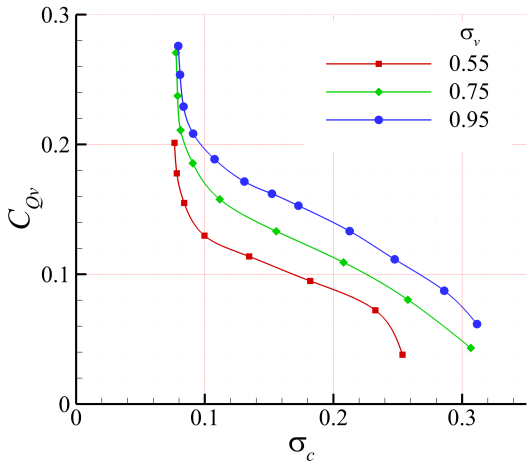

Figure 8. Dependence of σ_c on C_{Qv} for different free-stream cavitation number and constant Froude number value ($Fr = 25.3$).

2.2 Drag

Traditionally, the main interest in devices utilizing ventilated cavities has been for drag reduction. In figure 9 the dependence of C_D on σ_c is shown for three values of Fr (for $\sigma_v = 0.95$). The drag coefficient decreases approximately linearly with the decrease in cavitation number. The non-linearity present for high σ_c is due to the shear layer cavity behaviour, as a fully formed cavity in not yet present. It can be seen that for $\sigma_c = \sigma_{min}$ the drag also has a minimum value ($C_{D_{min}}$). Drag slightly decreases with increase in Fr (figure 9). The difference in $C_{D_{min}}$ through the range of examined Fr is approximately 1.5%. Figure 10 gives the alternate case of varying σ_v for a fixed Fr ($Fr = 25.3$). It can be seen that C_D is independent of σ_v in the region where ventilated cavity is fully formed. A slight difference is exists for high σ_c values, again where the shear layer cavitation regime is present.

3. CONCLUSIONS

Ventilated cavity flow over a three-dimensional wall mounted fence has been investigated experimentally in a cavitation tunnel. An experimental setup has been developed to examine the influence of air ventilation rate and free-stream conditions on the cavitation number, cavity length and drag. It was found that three flow regimes can be differentiated as cavitation number varies: a) shear layer cavitation for high σ_c values, b) for intermediate σ_c values, a fully formed ventilated cavity with a linear dependence of σ_c on C_{Qv}, and c) 'blocked' cavity flow when $\sigma_c \to \sigma_{min}$. In the case of a fully formed ventilated cavity the cavity closure exhibits a re-entrant jet behaviour. The re-entrant jet shedding is primarily responsible for air entrainment into the flow. Cavity length as function of σ_c follows a power law behaviour.

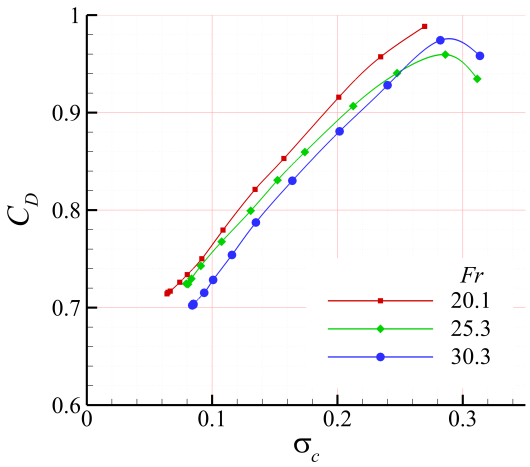

Figure 9. Drag coefficient as a function of cavitation number for three values of Froude number and constant free-stream cavitation number value ($\sigma_v = 0.95$).

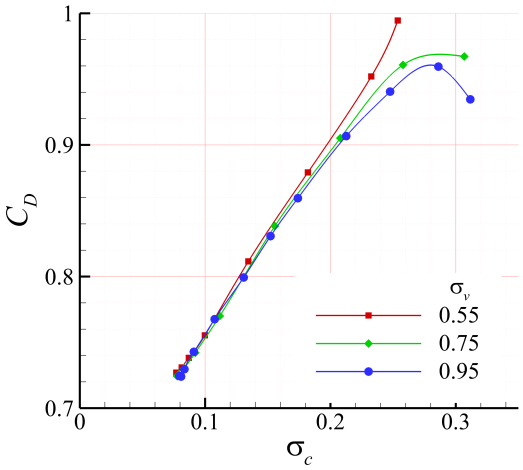

Figure 10. Drag coefficient as a function of cavitation number for three values of free-stream cavitation number and constant Froude number value ($Fr = 25.3$).

With an increase in Fr and/or σ_v, significantly more air is needed to obtain the same σ_c value. With a decrease in σ_c, drag coefficient decreases linearly until it reaches a minimum value when $\sigma_c = \sigma_{min}$. The C_D shows a mild dependence with Fr and is independent of σ_v.

A companion study is planned to investigate the effect of fence immersion in the upstream wall boundary layer. A series of unsteady pressure measurements in the closure region is also to be conducted, coupled with the high-speed camera imaging, to gain a deeper insight into the re-entrant jet closure physics. These 3-D wall mounted fence results will also be compared with a future study of ventilated cavity flow over a 2-D wall mounted fence.

ACKNOWLEDGMENTS

The authors wish to acknowledge the assistance of Mr Robert Wrigley and Mr Steven Kent in carrying out the experiments and the support of the Australian Maritime College.

REFERENCES

[1] T. G. Lang and D. A. Daybell. Water tunnel tests of three vented hydrofoils in two-dimensional flow. *Journal of Ship Research*, 5(3):1–15, 1961.

[2] A. Rowe. Evaluation study of a three-speed hydrofoil with wetted upper side. *Journal of Ship Research*, 23(1):55–65, 1979.

[3] T.T. Huang. Investigation of base vented hydrofoils. Technical report 465-1, Hydronautics, Inc., 1965.

[4] V.N. Semenenko. Artificial supercavitation, physics and calculation. In *Lecture Notes from the RTO AVT/VKI Special Course on Supercavitating Flows, von Karman Institute for Fluid Dynamics*, 2001.

[5] S. L. Ceccio. Friction drag reduction of external flows with bubble and gas injection. *Annual Review of Fluid Mechanics*, 42:183–203, 2010.

[6] M.P. Tulin. Steady two-dimensional cavity flows about slender bodies. Report 834, DTMB, 1953.

[7] A.R. Elms. Improved hydrofoil device. International patent number, WO 99/57007, W.I.P. Organization, 1999.

[8] A. Molini and S. Brizzolara. Hydrodynamics of interceptors: a fundamental study. In *International Conference on Maritime Research and Transportation ICMRT 2005*, Ischia, Italy, 2005.

[9] B. Pearce and P. Brandner. Inviscid cavity flow over a wall-mounted fence. *Ocean Engineering*, 80:13–24, 2014.

[10] L. Barbaca, B.W. Pearce, and P.A. Brandner. Computational investigation of ventilated cavity flow over a 2-d fence. In *The Proceedings of the 19th Australasian Fluid Mechanics Conference*, Melbourne, Australia, 2014.

[11] B. W. Pearce and P. A. Brandner. Numerical analysis of base-ventilated intercepted supercavitating hydrofoil sections. *Ocean Engineering*, 104:63–76, 2015.

[12] B. W. Pearce and P. A. Brandner. Experimental investigation of a base-ventilated supercavitating foil with interceptor. In *8th International Symposium on Cavitation, Cav 2012*, Singapore, 2012.

[13] P.A. Brandner, Y. Lecoffre, and G.J. Walker. Development of an australian national facility for cavitation research. In *In Sixth International Symposium on Cavitation - CAV 2006*, 2006.

[14] P. A. Brandner, Y. Lecoffre, and G. J. Walker. Design considerations in the development of a modern cavitation

tunnel. In *Proceedings of the 16th Australasian Fluid Mechanics Conference, 16AFMC*, pages 630–637, 2007.

[15] M. Callenaere, J. P. Franc, J. M. Michel, and M. Riondet. The cavitation instability induced by the development of a re-entrant jet. *Journal of Fluid Mechanics*, 444:223–256, 2001.

[16] C.E. Brennen. *Cavitation and Bubble Dynamics*. Oxford University Press, New York, 1995.

[17] J.P. Franc and J. M. Michel. *Fundamentals of Cavitation*, volume 76 of *Fluid Mechanics and Its Applications*. Kluwer Academic Publishers, Dordrecht, 2004.